# A study of physical processes in galaxies and circumgalactic medium

*by*

**Mukesh Singh Bisht R**




Jawaharlal Nehru University, New Delhi




Raman Research Institute

Supervisor : **Biswajit Paul**

Co-Supervisor : **Biman B. Nath**

Submitted: December, 2025

This thesis is submitted for the degree of Doctor of Philosophy

# DECLARATION

I, **Mukesh Singh Bisht R** (Enrolment No.: RRI/2020/016), declare that the work reported in this thesis titled '**A study of physical processes in galaxies and circum-galactic medium**', is entirely original. This thesis is composed independently by me at **Raman Research Institute (RRI)** under the supervision of **Prof. Biswajit Paul** and **Prof. Biman B. Nath** and is the result of my own work unless otherwise stated. I further declare that the subject matter presented in this thesis has not previously formed the basis for the award of any degree, diploma, membership, associateship, fellowship or any other similar title of any university or institution. I also declare, this thesis has been checked through the plagiarism software DrillBit.

Biswajit Paul
Signature of Supervisor
**Prof. Biswajit Paul**
Professor, RRI

Signature of Candidate
**Mukesh Singh Bisht R**
Research Fellow, RRI

Biman Nath
Signature of Co-Supervisor
**Prof. Biman B. Nath**
Professor, RRI

Astronomy & Astrophysics Group
Raman Research Institute (RRI)
Bengaluru 560080, Karnataka, India

Date: 23.12.2025
Place: Bengaluru

## CERTIFICATE

This is to certify that the work contained in the thesis titled '**A study of physical processes in galaxies and circumgalactic medium**', submitted by **Mukesh Singh Bisht R** (Enrolment No.: RRI/2020/016) to the Jawaharlal Nehru University for the award of the degree of **Doctor of Philosophy (Ph.D.)** in Physical Sciences, is the bonafide record of orginal research work carried out by the candidate from February 2021 — December 2025, under my guidance and supervision at **Raman Research Institute (RRI)**, Bengaluru, India. The results embodied in the thesis have not been submitted to any other University or Institute for the award of any degree or diploma.

Signature of Director
**Prof. Tarun Souradeep**
Director & Professor, RRI

अध्यक्ष/CHAIRPERSON
शैक्षणिक समिति/Academic Committee
रामन अनुसंधान संस्थान
Raman Research Institute
बेंगलूरु/Bengaluru - 560 080

Astronomy & Astrophysics Group
Raman Research Institute (RRI)
Bengaluru 560080, Karnataka, India

Signature of Supervisor
**Prof. Biswajit Paul**
Professor, RRI

Signature of Co-Supervisor
**Prof. Biman B. Nath**
Professor, RRI

Date: 23.12.2025
Place: Bengaluru

# ACKNOWLEDGEMENTS

Being born in the small village of Syuni Malli in Chamoli district, Uttarakhand, with limited facilities and connectivity, I am deeply grateful to my dadi, Late Hyunka Devi, and dada Late Kalam Singh, who enrolled me in a private school in the nearby town so that I could receive a good education. I sincerely thank my maa Chandra Devi and papa Ranjeet Singh, who continued to support my studies after my grandparents. They worked tirelessly throughout their lives to ensure that my higher education was never compromised. Without their support, I could never have continued my studies. I am also thankful for the kind support of my family and all the people from my village, whose continuous encouragement keeps me motivated to do well in life. To all my teachers—from pre-school to post-graduation—I express my heartfelt gratitude for your wonderful teaching, which helped me understand my subjects in depth. I especially thank my chacha Kundan Singh, my mama Jeet Singh, and my big brother Rajendra Singh for their constant motivation and support, because of whom I have been able to pursue a path in research.

For my PhD, I have been fortunate to conduct my research in the Astronomy and Astrophysics group at RRI. I am deeply grateful to Biman, who guided me at both professional and personal levels and shaped my research in ways that made it possible for me to complete this thesis. I am also thankful to Biswajit for kindly agreeing to be my official supervisor after Biman's retirement. I thank my committee members, Shiv and Saurabh, for consistently evaluating my research, and Tarundeep Saini for serving as the external examiner in my comprehensive exam. I am grateful to all my collaborators, without whom I would not have learned as much or published my work. I thank Projjwal and Yuri for their invaluable help on my 'supernova' project, and Prateek and Alankar for their important inputs and discussions on my 'mCC' work. I am especially thankful to Smita and Sanskriti for introducing me to X-ray observations and analysis, and to Manami, Yair, and Anjali for their valuable contributions to my X-ray project. I also thank Biman, Prateek, Smita, and Sanskriti for providing recommendation letters for my postdoctoral applications. I am grateful to Kartick, with whom I am working on 3D simulations, for his many technical and non-technical insights. I also thank Jasjeet, Arif, and Rahul for their useful discussions on cosmological simulations, which significantly helped me in understanding the subject. I sincerely thank all of you for being a part of

my research journey and for helping me whenever I was stuck.

The people on the Astro Floor have been truly amazing and supportive throughout my PhD journey. I am especially grateful to my colleagues from L-219—Manami, Naren, Gunjan, Manish, Sovan, Sourav, and Ashwin—for fostering a healthy and research-focused environment that helped me stay focused and productive. I would also like to thank Rahul, Manish, and Kinjal for their substantial help with my X-ray project. I am deeply thankful to my seniors—Naren, Anjan, Hemanth, Ketan, Tanuman, Anirban, and Sandeep—for creating such a lively, cheerful, and inspiring atmosphere. My thanks also go to others on the Astro Floor, including Vikram, Mayuri, and Nayantara, as well as my juniors—Suva, Tamang, Vaishali, Ajit, Yash, Aritra, Patil, Naren, Boxi, Aman, Akash, and Ujjwal—for their companionship and support. I am grateful to the AA secretaries—Mamta, Harini, and Manjunath—for their constant assistance throughout my PhD. I would also like to thank the RRI administration, particularly Naresh, Suresh, Vidya, Radha, and Gayathri, for their help and cooperation. I also thank the IT, Library, and Canteen staff at RRI for their constant support and help. I am particularly grateful for the in-house HPC cluster, which I used extensively throughout my research.

Extra-curricular activities, especially outdoor sports, have been an integral part of my PhD life. I am truly grateful to everyone who taught me, encouraged me, and supported me in various sports. RRI Sports has been remarkably inclusive, always welcoming juniors without any hesitation. I would like to thank all my sports companions in cricket, badminton, and volleyball—Saurabh, Anand, Marie, Anindya, Chandeshwar, Shreyas, Snehal, Vishnu, Abhishek, Soumya, Yogesh, Arun, Vardhan, Sharath, Akhil, Vaibhav, Sebanti, Sukhveer, Ketan, Sagar, Irla, Yadu, Bhadra, Deepak, Abhijeet, Aman, Amit, Aritra, DK, Faraz, Kinjal, Kiran, Maitri, Manish, Makarand, Naren, Nikhil, Pooja, Raghu, Sayantan, Shashank, Suva, Siddharth, Soumen, Soumyajit, Boxi, Vishnu, Suraj, Vaibhav, Vijay, Rudra, Abinash, Alen, Subbu, Naresh, Sachin, Arunima, and Brandy. I would especially like to thank Kartick for helping me learn Table Tennis. I am also grateful to the RRI Sports Committee for organizing all the tournaments, and I extend my sincere thanks to Saurabh, Sachin, Subbu, Chetan, Munneswaran, and all the ground staff for their immense effort and support in making these events successful.

I would like to thank all the RMV Hostel members for providing a wonderful and peaceful stay throughout my PhD. My heartfelt thanks go to the cooks—Padmaji, Shardaji, Saumyaji, Deepaji, Sudhaji, and Ratnaji—for their delicious food and the warm, family-

like environment they created. I am also truly grateful to Naren, Chandeshwar, Nancy, Akhil, Alka, Yogesh, Anusrita, Manish, Rupak, Alen, Abinash, Maitri, Saurvah, Palak, Vaibhav, Kinjal, Kiran, Anand, Anirban, Patil, Suva, DK, Soumyajit, Imran, Sukhveer, Rudra, and Shashank for celebrating festivals such as Diwali and Holi together, making the hostel feel like home.

I would also like to thank all my batchmates from the 2020 batch—Manish, Kinjal, Rupak, Shashank, Vaibhav, Anirban, Pooja, Susovan, Anson, Sayari, Gourab, Srijit, and Swarnava—for their excellent organization of In-House 2023 and for all their help and efforts throughout my PhD. Lastly, I would like to thank you, Maitri, for your constant support and encouragement, which kept me motivated and helped me complete my thesis.

I would like to confess that this part of my thesis has been the toughest to write, and I am sure I may have unintentionally missed someone—my sincere apologies for that. Thank you all!

# SYNOPSIS

## Introduction

The circumgalactic medium (CGM) is a vast reservoir of multiphase gas surrounding galaxies. It regulates the inflow of material from the intergalactic medium (IGM) and reprocesses gas expelled in galactic outflows. Depending on the physical processes at play (heating/cooling), the gas may either remain in the CGM or accrete onto the interstellar medium (ISM), where it can contribute to star formation. The CGM is therefore a key component in shaping the evolutionary pathways of galaxies (Tumlinson et al. 2017).

Observations of the Milky Way's (MW) CGM indicate multiphase gas with temperatures ranging from the cool phase ($\sim 10^4$ K) to the warm-hot phase ($\sim 10^6$ K). While the origin and distribution of these phases are relatively well understood, the recent discovery of an even hotter gas ($\sim 10^7$ K) in the MW's CGM is particularly intriguing. This hot or 'super-virial' (SV) gas is detected in both X-ray emission (Das et al., 2019a) and absorption (Das et al., 2019b). In X-ray emission, it is observed in both hemispheres, and it covers $\approx 80\%$ of the sightlines along which it is looked for (Bluem et al., 2022; Gupta et al., 2023). However, the X-ray absorption studies are limited to only three sightlines (towards 1ES 1553+113 (Das et al., 2019b), Mrk 421 (Das et al., 2021), and NGC 3783 (McClain et al., 2024a); all in the northern hemisphere).

Observations also suggest that the emitting and absorbing hot X-ray gas have distinct origins. Emission at $\sim$ 1 keV is dominated by the K and L shell transitions of Fe (Bhattacharyya et al., 2023), thereby Fe is abundant, whereas absorbing gas is found to be $\alpha-$enhanced. The inferred column density ($\propto nL$) and emission measure ($\propto n^2L$) imply a $\sim$Mpc length-scale, if both phases are assumed to originate from the same region, far exceeding the possible size of the MW's CGM. Thus, the emitting and absorbing hot X-ray gas should be modeled separately. For my PhD thesis, in the first two projects, I proposed models to explain the origin and spatial distribution of the emitting and absorbing hot gas. In my third project, I developed a model of cool gas ($\sim 10^4$ K) in the CGM, treating it as a collection of 'misty' clouds embedded within the hotter medium.

This model explains the column density and equivalent width distribution of ions tracing the cool gas, such as MgII. In the fourth project, I used *Chandra* and *XMM-Newton* grating data to detect the ions tracing the hot gas in the MW's CGM towards the blazar PKS 2155-304.

## Origin of X-ray emitting 'super-virial' gas in the Circumgalactic medium of the Milky Way

In Bisht et al. 2024b, we proposed that a puffed-up, disk-like region around the Milky Way, with a typical scale radius of $\approx 5$ kpc and a scale height of $\approx 1$ kpc, can explain the observed properties of the hot X-ray emitting gas. Our disk model successfully reproduced the observed correlation between the EM of the hot gas and that of the warm–hot or virial-temperature ($\sim 10^6$ K) gas along different sightlines. The mass of this hot phase, estimated from the disk model, is $\sim 4 \times 10^7\, M_\odot$, significantly lower than that of the mass-dominant warm–hot phase. To investigate the origin of the hot X-ray–emitting gas, we performed an idealized 2D hydrodynamical simulation of the Milky Way using a toy model of stellar outflows in the *PLUTO* code. Our simulation showed that disk-wide stellar outflows can produce a puffed-up, disk-like region, suggesting that stellar feedback could be a plausible origin of the hot X-ray emitting gas.

## Can supernovae from Runaway stars mimic the signatures of 'super-virial' gas in X-ray absorption?

In Bisht et al. 2024a, we modeled the hot X-ray absorbing gas observed along three lines of sight. The absorbing gas is characterized by a high column density of highly ionized species such as OVIII, NeX, and SiXIV, indicative of high temperatures, $\alpha$-element enhancement, super-solar ionic abundance ratios, and significant non-thermal broadening. We proposed that the shock-heated ejecta from core-collapse supernovae in the extra-planar regions of the Milky Way can account for these observed properties, provided that such remnants lie along the corresponding sightlines. The reverse shock in a supernova remnant can heat the ejecta to super-virial temperatures, while the $\alpha$-enriched compo-

sition of the ejecta naturally explains the observed abundance patterns. Our models suggest that a supernova with a blast energy of $\sim 10^{51}$ erg, ejecta mass of $\sim 10\,M_{\odot}$, and ambient density of $\approx 0.1$ cm$^{-3}$ can reproduce the observed high ion column densities on timescales of a few $\sim 100$ kyr. Massive runaway stars located in the extra-planar regions of the Milky Way are likely progenitors of such supernovae along the three sightlines. However, the covering fraction of such events across the sky is estimated to be $\lesssim 1\%$; therefore, this model would face challenges if future observations reveal that the absorbing gas has a large sky covering fraction.

## Misty, patchy, and turbulent: constraining the cool gas in the Circumgalactic medium

In Bisht et al. 2025, we modeled the cool gas ($\sim 10^4$ K) in the CGM. Observations, simulations, and theoretical studies consistently suggest that the cool gas occupies only a tiny fraction of the CGM volume ($\lesssim 1\%$). Observations of cool gas tracer ions such as MgII, CaII, and CII show a large scatter in column density at similar impact parameters. A comparable scatter has also been observed in the CGM of M31 using multiple background quasars (Lehner et al., 2020). Motivated by these findings, we proposed that the cool gas in the CGM exists in clumpy structures, referred to as cloud complexes (CCs), each composed of numerous tiny cool cloudlets embedded within the hotter medium. We further posited that adopting a 'mist-limit' assumption within a CC—i.e., assuming a unit area covering fraction of cool gas—simplifies the computation of observables such as EW and column density, which would otherwise be computationally expensive if the cool cloudlets were modeled from first principles. Using Monte Carlo realizations of $\sim 10^3$ CCs distributed throughout the CGM following a power-law distribution ($dN_{\rm CC}/dR \propto R^{-1}$), each with a characteristic size of $\approx 10$ kpc, we found that COS-Halos (Werk et al., 2013) galaxies (Milky Way–like galaxies) typically have a cool gas mass of $\sim 10^{10}\,M_{\odot}$. We also demonstrated that the blending of absorption lines from individual cloudlets along a sightline with distinct line of sight velocities produces the turbulent broadening at the CC scale.

## Detection of 'super-virial' gas in the Circumgalactic medium of the Milky Way towards PKS 2155-304

Along with modeling hot gas in the CGM of the MW, we also observed hot gas using X-ray absorption lines towards PKS 2155-304 using the archival grating data of *Chandra* and *XMM-Newton* (Singh Bisht et al. 2025). We detected MgXII K$\alpha$ for the first time in the CGM of the MW and SiXIV K$\alpha$ line, which are the tell-tale signatures of the absorbing hot gas. With detected and non-detected ions, we inferred four distinct temperature phases in the CGM of the MW along this sightline: SV or hot phase ($\approx 5 \times 10^7$ K; MgXII, SiXIV), 'virial' or warm-hot phase ($\approx 2 \times 10^6$ K; OVII, NeIX), 'sub-virial' or warm phase ($\approx 2 \times 10^5$ K; CV, NVI), and cool phase ($< 1.7 \times 10^5$ K; OIV, OV). We further found that the low-ionization lines are blueshifted, whereas high-ionization lines are redshifted, suggesting a scenario with infalling sub-virial gas, quasi-static virial gas, and outflowing super-virial gas. As this sightline lies in the southern hemisphere (the previous three were in the northern hemisphere), it likely indicates a widespread distribution of X-ray absorbing hot gas. An order of magnitude variation in the inferred temperature and distinct ions detected along different sightlines indicates an inhomogeneous nature of the hot gas.

# LIST OF PUBLICATIONS

1. *On the Origin of the* $10^7$ *K Hot Emitting Gas in the Circumgalactic Medium of the Milky Way*
   **Mukesh Singh Bisht**, Biman B. Nath, Smita Mathur, ApJ, 975, 49B
   DOI: 10.3847/1538-4357/ad77c0, arXiv: 2408.14344

2. *Can Supernovae from Runaway Stars Mimic the Signs of Absorbing "Supervirial" Gas?*
   **Mukesh Singh Bisht**, Projjwal Banerjee, Biman B. Nath, Yuri Shchekinov, ApJ, 975, 26B
   DOI: 10.3847/1538-4357/ad77be, arXiv: 2408.14351

3. *Misty, patchy, and turbulent: constraining the cool circumgalactic medium with mCC*
   **Mukesh Singh Bisht**, Prateek Sharma, Alankar Dutta, Biman B Nath, MNRAS, 542, 1573B
   DOI: 10.1093/mnras/staf1319, arXiv: 2411.17173

4. *Detection of 'super-virial' gas in the Circumgalactic medium of the Milky Way towards PKS 2155-304*
   **Mukesh Singh Bisht**, Sanskriti Das, Smita Mathur, Manami Roy, Yair Krongold, Anjali Gupta, submitted to ApJ [under review]
   DOI: 10.48550/arXiv.2509.02019, arXiv: 2509.02019

# Contents

**1 Introduction** **1**

1.1 Circumgalactic Medium . . . . . 1

1.2 Observations . . . . . 5

1.2.1 X-ray emission . . . . . 5

1.2.2 Optical/UV . . . . . 11

1.2.3 Radio . . . . . 14

1.3 Simulations . . . . . 15

1.4 Analytical models . . . . . 19

1.5 Motivation of the thesis . . . . . 23

1.6 Structure of the thesis . . . . . 24

**2 On the Origin of the $10^7$ K Hot Emitting Gas in the Circumgalactic Medium of the Milky Way** **27**

2.1 Introduction . . . . . 29

2.2 Disk-shaped profile of the virial and super-virial gas . . . . . 34

2.3 Simulation setup . . . . . 39

2.4 Simulation Results . . . . . 43

2.4.1 Hot gas in the extra-planar region . . . . . 44
2.5 Discussion . . . . . 45
2.6 Summary . . . . . 47

**3 Can Supernovae from Runaway Stars Mimic the Signs of Absorbing "Supervirial" Gas? 48**

3.1 Introduction . . . . . 50
3.2 Simulation of Core-Collapse Supernova and Evolution of the Remnant . . 52
3.2.1 Modelling Massive Star Evolution and Nucleosynthesis in CCSNe 52
3.2.2 Modelling the Supernova Remnant . . . . . 53
3.3 Results . . . . . 58
3.3.1 Overall Evolution of the Ejecta . . . . . 58
3.3.2 Evolution of Pressure, Density, and Temperature of Shocked Ejecta 62
3.3.3 Comparing Timescales . . . . . 63
3.3.4 Evolution of Column Density . . . . . 67
3.3.5 Comparison with Observations . . . . . 68
3.4 Discussion . . . . . 72
3.5 Summary . . . . . 78

**4 Misty, patchy, and turbulent: constraining the cool circumgalactic medium with mCC 79**

4.1 Introduction . . . . . 81
4.2 Observational Data . . . . . 84
4.3 Misty cloud complexes in the CGM . . . . . 85

4.3.1 Analytical estimates . . . 87
4.3.2 Physical number density profile of cool gas . . . 90
4.3.3 Understanding analytical results . . . 91
4.3.4 Monte Carlo realizations of CCs in the CGM . . . 94
4.3.5 Comparing MgII column density with observations . . . 99
4.3.6 Comparing MgII Equivalent Width and covering fraction with observations . . . 101
4.3.7 Estimating cool gas mass in the CGM . . . 102
4.3.8 'Advanced' Model: varying size and mass of CCs . . . 105
4.4 Line blending with smaller cloudlets . . . 108
4.5 Direct modeling of cloudlets & CCs across CGM . . . 113
4.5.1 Comparing with observations . . . 117
4.6 Discussion . . . 122
4.6.1 Utility of CC-like approaches to model multiphase CGM . . . 122
4.6.2 Modeling intermediate temperature gas . . . 124
4.6.3 Astrophysical Implications . . . 125
4.6.4 Caveats & future directions . . . 129
4.7 Summary . . . 131
4.8 Data Availability . . . 133

**5 Detection of 'super-virial' gas in the Circumgalactic medium of the Milky Way towards PKS 2155-304 134**

5.1 Introduction . . . 136

5.2 Data Reduction and Analysis . . . 137
5.2.1 Data Reduction . . . 139
5.2.2 Data Analysis . . . 141
5.2.3 Model-independent Analysis . . . 145
5.2.4 `PHASE` model . . . 146
5.3 Results . . . 149
5.3.1 Temperature . . . 150
5.3.2 Equivalent H column density . . . 153
5.3.3 Abundance Ratios . . . 153
5.4 Discussion . . . 157
5.4.1 Comparison with previous studies . . . 157
5.4.2 Origin of the super-virial gas . . . 159
5.5 Conclusion . . . 162

**6 Conclusion & Future Directions** **164**

6.1 Origin of X-ray Emitting Super-Virial Gas . . . 164
6.2 Supernovae From Runaway Stars as Sources of X-ray Absorbing Super-Virial Gas . . . 165
6.3 Structure of the Cool CGM: Misty Cloud Complexes (mCC) . . . 165
6.4 Detection of Super-Virial Gas Toward PKS 2155-304 . . . 166
6.5 Future Directions . . . 166

**A The mist limit** **182**

A.0.1 Terminal velocity of cloudlets within a CC . . . 184

A.1 MgII ion fraction estimates . . . . . 184

A.2 Standard deviation estimates . . . . . 186

# List of Figures

1.1 CGM illustration. The CGM contains both inflowing gas from the intergalactic medium (IGM), which supplies fuel for star formation, and outflowing gas from galaxies, which can heat and enrich the existing circumgalactic gas. . . . . 4

1.2 EM correlation of the warm-hot (x-axis) and hot (y-axis) gas for various lines of sight from Bluem et al. 2022 using *HaloSat*. . . . . 8

1.3 Ion fraction of H and He like ions of various elements in Collisional Ionization Equilibrium (CIE) computed using the radiative transfer code `CLOUDY` (Ferland et al., 2017). . . . . 10

1.4 This illustration shows how absorption lines can be used to detect cool/warm gas in the CGM. . . . . 12

1.5 Baryon fraction as a function of normalized radial distance from the halo center for different halo masses ($M_{200c}$) and simulations, adapted from Ayromlou et al. 2023. Feedback processes redistribute baryons to much larger distances, extending well beyond the virial radius of the galaxy. . . 17

1.6 Log-normal temperature probability distribution function at a radial distance of 20 kpc from the center of a galaxy (Dutta et al., 2024a). The two peaks correspond to the warm-hot and warm phases. Similarly, multiple peaks can be constructed corresponding to the individual phases of the CGM. . . . . 21

2.1 The Emission Measure (EM) data from various authors (Bluem et al. 2022,Bhattacharyya et al. 2023, Gupta et al. 2021,Ponti et al. 2023, and Gupta et al. 2023) is plotted as a function of $\sin(b)$, where $b$ is the galactic latitude. The figure contains two sets of data. The top set of points, with EM $\approx 10^{-3} - 10^{-1}$ cm$^{-6}$ pc, corresponds to the virial phase while lower data points with EM $\approx 10^{-5} - 10^{-3}$ cm$^{-6}$ pc correspond to the super-virial phase. The solid black lines show the mean EM calculated in a bin size of $\Delta\sin(b) = 0.1$ for both virial and super-virial datasets. Note the anti-correlation between EM and $\sin(b)$ for both virial and super-virial phases as can be seen by the trend in the black solid lines. . . . . 31

2.2 The cartoon representation of the structure of the gaseous components of the MW. The blue region in the center shows the Interstellar medium (ISM). The magenta and the yellow regions show the extent of the super-virial and virial temperature-emitting disks, respectively. The extended region in green shows the Galactic virialized Halo. Note that the size of different regions is not to scale; it simply represents the overall structure of the extraplanar gas around the MW. . . . . 32

2.3 This figure shows the results of the MCMC analysis. The *left* and *right* panel shows the corner plot of parameters for virial and super-virial phases, respectively. The three vertical dashed black lines in the 1-D histogram mark the $16^{\text{th}}$, $50^{\text{th}}$, and $84^{\text{th}}$ percentiles of the samples. The three contour levels plotted with black solid lines contain 32, 64, and 96 percent of the samples, respectively. The blue line shows the initial guess value and is visible only in the case of $z_{\text{v}}$ as the guess values for other parameters are out of the plot ranges. The values on the top of each 1-D histogram show the $50^{\text{th}}$ percentile value (median) and the error shown corresponds to $16^{\text{th}}$ and $84^{\text{th}}$ percentile which is equal to $1\sigma$ error if the resulting 1-D histogram is Gaussian which is the case for most of the parameters. We performed the analysis using 32 walkers and 50,000 steps with Gaussian priors for all the parameters. We ensured the convergence of samples as the total number of steps is larger than 50 times the autocorrelation time. Note that the width in the Gaussian prior (see Table 2.1) is sufficiently larger than the width in the resulting histogram of the respective parameters. This shows that the resulting values are well-constrained. . . . . 33

2.4 The correlation between the Emission Measure (EM) of the virial temperature gas and the EM of the super-virial temperature gas based on our models overplotted on observed EM. The black open circles show the EM correlation for the virial halo profile and super-virial gas in the disk. The blue circles show the EM correlation with the virial and super-virial gas around the disk. The circles in cyan correspond to the virial gas in the halo + the virial gas in the disk and the super-virial gas in the disk. The EM values from our model are plotted for the observed lines of sight. The observational data points from various authors are shown in other colors with error bars. All the observed EM values are rescaled to the metallicity of 0.3 solar for virial gas and solar for super-virial gas. The narrow range in the black points compared to cyan points along the X-axis shows the importance of having a 'disk-shaped' virial phase profile. . . . . 38

2.5 The initial temperature, density, and pressure maps. There are temperature and density gradients in both $R$ and $z$ directions, as a result of the hydrostatic equilibrium in which the gravitational force is balanced by gas pressure combined with the rotation of the gas. . . . . 40

2.6 Temperature maps at three epochs, at 5, 10 and 15 Myr, from left to right. As the energy is injected in the disk, the hot SV-temperature gas is pushed up, generating an extraplanar region (shown in blue). Above this region, a virial temperature extraplanar region is formed (shown in yellow-green). Shock heating of the halo gas leads to another hot region at higher $z$ (shown in light green). . . . . 41

2.7 This figure shows the simulation results at 15 Myr. The *top left* and *right* panels show the temperature and particle number density maps, respectively. The *bottom left* and *right* panels show the pressure and metallicity maps, respectively. . . . . 42

3.1 Temporal evolution of the position of the reverse shock front in Eulerian coordinate $r_{\rm RS}$ (dashed lines) and Lagrangian coordinate $m_{\rm RS}$ (solid lines) for the different density profiles in characteristic coordinates. The red, green, magenta, and blue lines show the variation for $\beta = 0, 0.15, 0.3$ and 0.5 respectively. . . . . 57

3.2 Pressure, mass density, and radius profile as a function of $M/M_{\rm ej}$ at three epochs in the characteristic unit. The solid and dashed line shows the case with *core+envelope* ($\beta = 0.5$) and *no core*, respectively. The blue color shows the mass density profile (right y-axis). The red and green color shows the pressure and radius profile (left y-axis), respectively. The *top panel* shows the initial setup at $t^* = 0.01$. The *middle panel* shows the profiles at $t^* = 0.34$ when the reverse shock is about to hit the core for *core+envelope* case. The *bottom panel* shows the profiles when the reverse shock has hit the center of the ejecta at $t^* = 3.09$ for *core+envelope* case. For *no core* case, the reverse shock has already hit the center by $t^* = 3.09$ and the secondary shock wave has started traveling outwards, as can be seen by the jump in pressure (dashed red line) and density profile (dashed blue line). . . . . 59

3.3 Mean molecular weight profile as a function of $M/M_{\rm ej}$ calculated using KEPLER. The black, green, blue, and red lines show the mean molecular weight profile for $\beta = 0, 0.15, 0.30$, and 0.50, respectively. . . . . 60

3.4 Temperature (solid lines) and velocity profiles (dashed lines) for different values of $\beta$ when the reverse shock hits the center of the ejecta in the respective cases. Red, green, magenta, and blue colors show the cases with $\beta = 0, 0.15, 0.3$, and 0.5, respectively. The profiles are plotted for the fiducial case with $E = 10^{51}$ erg, $M_{\rm ej} = 10\ M_\odot$ and $n_0 = 0.1\,{\rm cm}^{-3}$. . . . . 61

3.5 This figure shows the ratio of "minimum" radiative cooling, recombination, and ionization timescale to the dynamical time as a function of time. The "minimum" timescale corresponds to the mass shell which has minimum radiative cooling/ionization/recombination time within $M/M_{\rm ej} \leq 0.2$ and $T \geq 4 \times 10^6$ K. The green line shows the ratio of radiative cooling to dynamical time calculated using the cooling function for core composition with CLOUDY (Ferland et al. 2017). The magenta and cyan lines show the ratio of the recombination timescale (Verner & Ferland 1996) to the dynamical timescale for OVII and OVIII, respectively. The purple and red lines show the ratio of the ionization timescale (Voronov 1997) to the dynamical time for OVI and OVII, respectively. The above timescales are plotted for $E = 10^{51}$ erg, $M_{\rm ej} = 10\ M_\odot$, $n_0 = 0.1{\rm cm}^{-3}$ and $\beta = 0.3$. . . . . 64

3.6 Mass fraction of different elements as a function of $M/M_{\rm ej}$ obtained using KEPLER. The magenta, red, blue, and green lines show Oxygen, Neon, Magnesium, and Silicon mass fraction profiles, respectively. The solid, dashed, and dotted lines refer to the case with $\beta = 0.5, 0.3$ and 0.15 corresponding to 25, 18, and 11 $M_\odot$ mass models, respectively. . . . . 65

3.7 Evolution of Oxygen column density of the shocked ejecta with time for density profiles with different core sizes of $\beta = 0, 0.15, 0.3$, and 0.5 shown in red, green, magenta, and blue, respectively. For *no core* case ($\beta = 0$), we use a constant Oxygen mass fraction of 0.15 throughout the ejecta. The dotted vertical lines in the respective color show the time when the reverse shock hits the center of the ejecta. The curves correspond to the adopted fiducial values of $E = 10^{51}$ erg, $M_{\rm ej} = 10\,M_\odot$, and $n_0 = 0.1\,{\rm cm}^{-3}$. . . . . 66

3.8 Ionization of a Oxygen gas at $T = 5$ keV with initial OI abundance of $0.001\,\mathrm{cm}^{-3}$ and initial $n_e = 10^{-5}\,\mathrm{cm}^{-3}$. . . . . 69

3.9 Column density of ions as a function of time for three lines of sight. The *top (a), middle (b)* and *bottom (c)* panel shows the column density towards Mrk421 (Das et al. 2021), IES1553+13 (Das et al. 2019b), and NGC3783 (McClain et al. 2024b) respectively. The magenta, green, and blue bands show the column density range of OVIII, NeX, and SiXIV, respectively, calculated from our model. The dashed lines in the same color show the upper and lower limits of the observed column density of respective ions. 71

3.10 The final position of 1000 runaway massive stars where they explode as core-collapse supernovae: (a) latitude $b$ versus distance $d$ from the Sun, (b) Height $z$ from the Galactic plane versus $d$, and (c) $z$ versus $b$. . . . . 76

4.1 The line of sight (LOS) projected distribution of $10^3$ CCs each of radius 10 kpc in the CGM of radius 280 kpc with a power-law CC distribution of index $\alpha = 1$ (Eq. 4.7). Notice that there are numerous empty regions towards the outer regions of CGM and comparatively fewer empty regions in the center. The LOSs passing through CGM outskirts will, therefore, not produce strong ion absorption in contrast with the central sightlines intersecting multiple CCs. . . . . 84

4.2 The *top panel* shows the mean MgII column density as a function of normalized impact parameter. The black line shows the baseline column density from D24. The blue line shows the mean MgII column density for uniform distribution, while magenta and orange lines show the same for power-law distribution of CCs in the CGM with power-law index of 1 and 2 respectively (Eqs. 4.6, 4.9). The baseline column density predicted by D24 shows no trend with the impact parameter, while the uniform and power-law distributions show a declining trend, which is observationally observed. However, the column density values for the power-law index of $\alpha = 1$ (magenta line) better match the typical values from observations. So we choose a power-law distribution with index $\alpha = 1$ as our fiducial parameter. The solid magenta line in the *bottom panel* shows the mean MgII column density for the fiducial value of $\alpha = 1$. The dotted magenta lines show the expected standard deviation (see Appendix A.2) from the average. The data points are from the COS-Halos survey (Werk et al. 2013). Even the data with smaller redshift $(0.15 - 0.25)$ and stellar mass bins $(10.5 - 11$ in $\log_{10}$; encircled with black color) show intrinsic scatter in the column density data. . . . . 92

4.3 Variation in MgII EW with MgII column density. The black lines show the EW for various $b_{\rm turb}$ values. The solid blue, red, and magenta lines show the analytical relation between EW and column density in the optically thin limit, and in the flat and damped portions of the curve of growth. These analytic relations are from Draine 2011 (see Chapter 9). We assume thermal broadening at $T = 10^4$ K for MgII, which gives $b_{\rm thermal} = 2.6\,{\rm km\,s^{-1}}$. In the flat portion (applicable to most of our CCs, see Fig. 4.2), the EW increases with increasing turbulent broadening. . . . . 96

4.4 Contours of equal (in $\log_{10}$) maximum MgII column density (corresponding to LOS passing through the center of a CC; black lines) and equivalent width (magenta lines, in units of Å) in the parameter space of $N_{\rm CC}$ and $R_{\rm CC}$ for a single cloud complex with $M_{\rm cool} = 10^{10} M_{\odot}$. For MgII column densities $\gtrsim 10^{13}$ cm$^{-2}$, the EW saturates in the flat part of the curve of growth (see Figure 4.3) and the curves of constant EW are no longer parallel to the constant column density contours. The EW increases with $R_{\rm CC}$ for a fixed MgII column density because of a larger $b_{\rm turb,CC}$ (see Fig. 4.3). . . . . 98

4.5 Variation in the MgII column density along $10^4$ sightlines with the cool gas mass (top panels), and number and radius of CCs (bottom $3 \times 3$ panels) for a power-law ($\alpha = 1$) distribution of CCs in the CGM. Only non-zero values are shown with circles, resulting in a smaller number of them when the covering fraction is small. The data points shown in green color are from the COS-Halos survey (Werk et al. 2013). It is evident from the top panels that cool CGM mass of $\sim 10^{10}\, M_{\odot}$ best matches the observed data. The bottom panels show the variation in MgII column density with $R_{\rm CC}$ and $N_{\rm CC}$ for a fixed cool gas mass of $10^{10}\, M_{\odot}$. Notice that the increase in the size of CC results in less scatter in the column density because with larger CCs, the volume fraction of CCs is larger, and a similar number of CCs is intersected along different sightlines. A similar trend is observed for a larger number of CCs in the CGM. For the range of parameters we explored, $N_{\rm CC} = 10^3$ CCs with $R_{\rm CC} = 10$ kpc and $M_{\rm cool} = 10^{10} M_{\odot}$ best explain the observed MgII column density distribution. . . . . 100

4.6 The *top panel* shows the MgII EW distribution as a function of the normalized impact parameter for our fiducial *mCC* model. The grey points (note that empty sightlines are not shown) show the total MgII EW as a function of the impact parameter for $10^4$ sightlines. The black solid line shows the mean EW. The solid and dotted orange lines show the best-fit relation and $1\sigma$ spread based on observations from Huang et al. 2021. The green points are the EW data points from the COS-Halos survey (Werk et al. 2013). The *bottom panel* shows the covering fraction as a function of the normalized impact parameter: the solid black line for an EW threshold of 0.3 Å and the dashed black line for 0.1 Å. The orange points show the covering fraction values from Huang et al. 2021 for the EW threshold of 0.3 Å. Our mCC model with the fiducial parameters reproduces the EW distribution and covering fractions. . . . . 103

4.7 The average MgII column density as a function of the area covering fraction of CCs for various combinations of the cool gas mass, $N_{\rm CC}$ and $R_{\rm CC}$ (see Figure 4.5). The colored points with solid, dashed, and dotted black lines on their borders are for a cool gas mass of $10^9$, $10^{10}$, and $10^{11}\,M_\odot$ respectively. The error bars on each point show the standard deviation on the column densities. The dotted, dashed, and solid black lines show the contours of constant average MgII column density times the covering fraction for three different values $\langle N_{\rm mgII}\rangle \times f_{\rm A}^{\rm CC} = 10^{11.3}, 10^{12.3}$, and $10^{13.3}$ cm$^{-2}$, respectively. The product of these two quantities closely tracks the cool CGM mass and hence can be used as an observable proxy for the cool CGM mass. To compute the above quantities, we selected 100 random sightlines (so that the probability of selection is proportional to the projected CGM area) out of $10^4$ to be statistically consistent with the typical size of observational samples. The green point represents the result from the COS-Halos (Werk et al. 2013) survey, the position of which indicates a cool gas mass of $\sim 10^{10}\,{\rm M}_\odot$ for the COS-Halos galaxies. . . . . 104

4.8 The grey and blue points show the MgII column density for the 'basic' and 'advanced' (considering the size, mass, and realistic radial distribution of CCs in the CGM) models, respectively, along a total of $10^4$ sightlines (empty sightlines are not shown). The solid lines in the respective colors show the average MgII column density. The green data points are from the COS-Halos survey (Werk et al. 2013). Notice a slight decrement in the average column density for the 'advanced' model and therefore a larger covering fraction, since the product of average column density and covering fraction is fixed for the fixed total cool gas mass in the CGM. The scatter is larger in the case of the 'advanced' model due to the size and mass variation of the CCs. . . . . 108

4.9 Normalized MgII absorption profile for increasing (decreasing) number (size) of cloudlets in a CC along a LOS. The dashed grey lines show the absorption profile from individual intersected cloudlets. The orange lines show the overall absorption profiles from the intersected cloudlets along the LOS. The blue lines show the overall absorption profile smoothed with a velocity resolution of $6\,\mathrm{km\,s^{-1}}$. The magenta lines show the absorption profile for the misty CC model along the sightline passing through the CC center smoothed with a velocity resolution of $6\,\mathrm{km\,s^{-1}}$ (see section 4.3.4 on how to calculate the CC absorption profile in the mist limit). As the size of cloudlets decreases from 10 to 0.1 pc (top to bottom panels), more and more cloudlets are intersected along the LOS. With an increase in the intersected cloudlets, the overall absorption profiles become broader with fewer absorbing components. For cloudlet size $\lesssim$ 0.1 pc, our misty CC model (magenta line, smoothed to a resolution of 6 km $\mathrm{s^{-1}}$) is roughly matching the total absorption profile. . . . . 111

4.10 In the *top panel*, the lines in different colors (total 16) show the MgII absorption profile from individual cloudlets intersected along a LOS through a CC (same as top panel of Fig 4.9 except that we only consider 16 out of 25 cloudlets for clarity). The solid orange line shows the overall/total absorption profile from all the intersected cloudlets. Due to the blending of absorption profiles, only 8 absorbing components are seen in the overall absorption profile. In the *bottom panel*, we show the $z$ coordinate and the LOS velocity of the intersected cloudlets. The color of the points corresponding to individual cloudlets is consistent with the top panel. Based on the position and velocity distribution, the cloudlets will be blended in the absorption spectrum. This illustration shows that cloudlets that are far apart in physical space may be blended due to similar LOS velocity, whereas cloudlets that are very close in physical space may have disparate LOS velocities, which makes it very difficult to infer 3D information from the 2D observations. . . . . 112

4.11 LOS projected distribution of CCs and cloudlets in the CGM for $M_{\rm cool} = 10^{10}\,{\rm M}_{\odot}$, $N_{\rm cc} = 10^3$, and $\alpha = 1$. Due to the power-law nature of the distribution of CCs and the projection effect, more CCs are found in the central region than in the outskirts. The inset shows the cloudlets within one of a CC for $\beta = 0$ and $\gamma = 1$ (fiducial parameters; see Table 4.2). In this fiducial case, $\approx 5 \times 10^8$ total cloudlets are generated, with $\approx 5 \times 10^5$ cloudlets per CC. Note that we only show $2 \times 10^3$ cloudlets in the inset to better highlight the variety of cloudlets with different sizes and orientations. Also, we do not explicitly show the distribution of cloudlets within all the CCs. The distribution of these cloudlets shows qualitative similarity to Figure 7 of Ramesh & Nelson 2024 that shows a snapshot from a high-resolution simulation of a Milky Way-like CGM. . . . . 115

4.12 The *top panel* shows the normalized histogram of the number of intersected cloudlets, $\log_{10} N_{\rm MgII}$, and MgII EW along $10^4$ LOSs (empty sightlines are not shown for number of intersected cloudlets and column density although they are taken into account for normalization). The blue, magenta, and grey colors correspond to $\gamma = 0, 1, 2$, the power-law index of the semi-axes distribution of ellipsoidal cloudlets. Note that the larger the $\gamma$, the larger the number of cloudlets, keeping other parameters fixed. The total number of cloudlets generated for $\gamma = 0, 1, 2$ is $\sim 5 \times 10^6, 5 \times 10^7, 10^9$ respectively. The rightmost panel shows the MgII covering fraction as a function of normalized impact parameter for an EW threshold of 0.3 Å. The data points are from Huang et al. 2021 while the dotted black line is from our misty CC model (see Fig. 4.6) with fiducial parameters. In the *bottom panel*, the colored scatter points show the total EW along all the LOSs as a function of the normalized impact parameter for the different values of $\gamma$, respectively. The color of the points is consistent with the top panel. The solid black lines show the mean EW, while the dotted black line in the middle panel shows the mean EW for our fiducial misty CC model (see top panel of Fig. 4.6). The solid orange and dashed lines show the best-fit relation and $1\sigma$ uncertainty from Huang et al. 2021 while data points in green are from the COS-Halos survey (Werk et al. 2013). The observed EW trend and covering fraction match better for the $\gamma = 1$ case. 118

4.13 This figure shows the histograms of the number of intersected cloudlets, MgII column density, MgII EW, and MgII covering fraction (same as the top left panels in Figure 4.12) to show variation with different parameters. We vary a single set of parameters for each row and hold the other parameters fixed to their fiducial values. . . . . 119

4.14 Column density distribution of OVI along $10^4$ sightlines, as predicted by our fiducial CC model with a simple prescription for warm gas (see section 4.6.2). Moreover, we assume the OVI ion fraction from photo+collisional ionization equilibrium at $10^{5.5}$ K, and assume similar cool and warm gas masses. The observed data points are from the COS-Halos (Werk et al. 2013) survey. The spread of OVI columns from our Monte Carlo model matches well with the observed spread. . . . . 126

5.1 Normalized absorption profile of the detected (green) and non-detected (red) ions. The dotted black vertical line in each panel shows the $z = 0$ value of the line center of the respective ions. The shaded blue region in each panel indicates the resolution element of the respective instrument relative to the $z = 0$ value of the line center of the ion. . . . . 142

5.2 Temperature ranges estimated from the column density ratio of two adjacent ions of the same metal probed in X-ray absorption. It clearly shows the multiphase nature of the CGM with *temperature valleys* (hatched region) in between. The dashed magenta and purple lines show the temperature estimated from the column density ratios of O VI (detected in UV absorptions by Collins et al. 2004), O V (non-detection in this work), and O VII (this work), O VI (Collins et al., 2004) respectively. . . . . 144

5.3 Individual contribution of different temperature phases for detected ions. The grey color shows the best-fit `PHASE` model, while blue, green, and red colors show the contribution of sub-virial ($T_1$), virial ($T_2$), and super-virial ($T_3$) phases, respectively. . . . . 151

5.4 Comparison of best-fit temperatures and associated $1\sigma$ uncertainties from previous studies along various lines of sight (Mrk 421, green, Das et al. 2021; stacked, grey, Lara-DI et al. 2024a; 1ES 1553+113, yellow, Das et al. 2019b; NGC 3783, red, McClain et al. 2024b). The temperature ranges from our study (PKS 2155-304) are plotted in blue. The left arrow shows the cool gas temperature estimated from the column density ratios of O V (non-detections) and O IV (detections) in our study. Therefore, we detect four temperature phases along PKS 2155-304. This is the first time that 4 temperature phases are inferred in such studies using X-ray absorption lines. This plot shows the multiphase nature of CGM along various lines of sight and within specific phases as well. . . . . 154

5.5 Non-solar abundance ratios of C, Ne, Mg, and Si relative to O in the respective phases. . . . . 155

5.6 *Top panel*: The green line shows the normalized spectrum for the Solar abundance ratio of Ne to Fe in the warm-hot phase. *Bottom panel*: The dotted, dashed, and dashed-dotted red lines show the normalized spectrum for solar abundance ratios of O to Fe, Mg to Fe, and Si to Fe in the hot phase. This shows the $\alpha-$enhancement in virial and super-virial phases. . 156

5.7 line of sight velocity of detected ions . . . . . 160

A.1 Projected cloudlet distribution (top 3×3 panels) in a cubical volume with $N_{\rm cl}$ cubical cloudlets uniformly covering a volume fraction $f_V$. The size of vacancies equals the cloudlet size. As expected from simple estimates, the area covering fraction becomes of order unity when $N_{\rm cl} \gtrsim f_V^{-2}$. The panels farther from the diagonal (toward the bottom-left) are deeper into the mist limit. The bottom panels show the normalized histogram of the number of cloudlets along different sightlines. The histogram is very well fit by a Poisson distribution (shown by dashed lines) with a mean $f_V^{2/3} N_{\rm cl}^{1/3}$. Note that the number of sightlines with zero and one cloudlet becomes comparable for $N_{\rm cl} \sim f_V^{-2}$, corresponding to the approach toward the mist limit with a unity area covering fraction. . . . . 183

A.2 MgII ion fraction as a function of total number density at $10^4$ K. The purple line shows the MgII fraction for the Collisional Ionization Equilibrium, while the green, blue, and orange colors show the values for Photoionization Equilibrium at the redshifts of 0.1, 0.2, and 0.3, respectively. The solid and dashed colored line shows the ion fraction with the HM12 (Haardt & Madau 2012) and KS18 (Khaire & Srianand 2019) background radiation field. We computed the ion fraction values using the radiative transfer code `CLOUDY` (Ferland et al. 2017). MgII ion fraction values vary by $\sim 2$ orders of magnitude from $\approx 0.01$–$0.6$ for $n \approx 10^{-3}$-$10^{-1}\,{\rm cm}^{-3}$ at $z \sim 0.2$. . 185

# List of Tables

2.1 Parameters, allowed ranges, Gaussian priors, and MCMC results for the virial (V) and super-virial (SV) phases. The reported values correspond to the median ($50^{\text{th}}$ percentile) with $1\sigma$ uncertainties given by the $16^{\text{th}}$ and $84^{\text{th}}$ percentiles. . . . . 35

3.1 This table shows the observed column density of OVIII, NeX, and SiXIV from Das et al. 2019b, Das et al. 2021, and McClain et al. 2024b towards IES1553+113, Mrk421, and NGC3783, respectively. . . . . 53

4.1 Symbols used in this paper and their description. Our *fiducial parameters* are $R_{\rm CGM} = 280$ kpc, $R_{\rm CC} = 10$ kpc, $M_{\rm cool} = 10^{10} M_{\odot}$, $N_{\rm CC} = 10^3$, and $\alpha = 1$. . . . . 88

4.2 Model parameters, fiducial values, tested ranges, and brief descriptions for direct modeling of cloudlets within cloud complexes distributed throughout the CGM. . . . . 114

5.1 Detected/non-detected ions and their EW for various instruments. . . . . 138

5.2 Parameters of the absorption lines used for our analysis. Fourth column: detected EW; fifth, sixth, and seventh columns: column density contribution from the three distinct temperature phases calculated using hybrid-ionization modeling; eighth column: total column density across three phases; ninth column: column density from detected EW using the linear part of the curve of growth. . . . . 140

5.3 Best fit `PHASE` model parameters. . . . . 149

# Chapter 1

# Introduction

## 1.1 Circumgalactic Medium

The Universe is believed to be homogeneous and isotropic on large scales. This feature of spatial homogeneity and isotropy, which is a fundamental postulate of Cosmology, provides the foundation for describing the Universe using the Friedmann-Lemaître-Robertson-Walker (FLRW) metric within the framework of General Relativity (Weinberg, 1972). The scale of homogeneity has been tested using various galaxy surveys. For example, Yadav et al. 2005 analyzed the Sloan Digital Sky Survey SDSS DR1 galaxy survey using multifractal analysis and found that the galaxy distribution is homogeneous on scales larger than $60 - 70h^{-1}$ Mpc, where $h = H_0/(100 \text{ km s}^{-1} \text{ Mpc}^{-1})$ and $H_0$ is the Hubble constant. Considering $h$ to be $0.674 \pm 0.005$ (Planck Collaboration et al., 2020), the typical scale of homogeneity is $\gtrsim 100$ Mpc.

The widely accepted ΛCDM model of Cosmology consists of three major constituents of the Universe: matter (comprising pressureless dark matter and baryonic matter), radiation, and dark energy, where dark energy currently dominates the energy budget of the Universe (Planck Collaboration et al., 2020). While this background model of the universe works well with many observations, for example, that of the Cosmic Microwave Background Radiation (CMBR), a monotonically decreasing uniform density field cannot account for the formation of various structures in the Universe, such as galaxies, the cosmic web, and the cosmic voids that are observed today. It is believed that these structures in the Universe have formed due to fluctuations in the density field. These fluctuations

produce over-dense and under-dense regions, which become the sites for structures at different scales. The origin of these density fluctuations remains uncertain, although it is widely believed that primordial perturbations in the early Universe, during the inflationary era, seeded these density fluctuations at all scales (Peebles, 1980).

Over time, overdense regions are unable to keep up with the expansion of the Universe and eventually collapse under their own gravity. Overdense regions with larger density contrast compared to the background density collapse at earlier epochs, while less overdense regions collapse at later times. During this collapse, particles in these regions approach equilibrium through a process known as 'violent relaxation', ultimately leading to the formation of a self-gravitating dark matter halo. Baryons, which interact gravitationally with dark matter, fall into the potential wells of dark matter halos and eventually reach virial equilibrium (Mo et al., 2010). The baryonic temperature is then determined by the virial theorem, $2KE + PE = 0$, where $KE$ and $PE$ denote the kinetic and potential energies, respectively. Baryons, unlike dark matter, can dissipate energy through radiative processes. The typical cooling time of a thermal plasma is $t_{\rm cool} \propto T/(n\Lambda(T))$, where $n^2\Lambda$ is the radiative cooling efficiency (with the dimensions of energy lost per unit time per unit volume), and $n$ is the particle number density of plasma. At $z \gtrsim 7$, the Compton cooling of energetic electrons by CMBR photons is also significant. The gaseous system for which the cooling time is shorter than the gravitational free-fall time ($t_{\rm ff} \propto 1/\sqrt{G\rho}$) can cool and collapse further. The ratio of the cooling time to the free-fall time sets the limits on the characteristic sizes and masses of galaxies (Rees & Ostriker, 1977; Silk, 1977; Binney, 1977). Thus, within these dark matter halos, galaxies—- which are the building blocks of the Universe——are formed. Over cosmic time, galaxies grow in mass and size through mergers with other galaxies (Lacey & Cole, 1993), as well as through cosmological gas accretion (Dekel & Birnboim, 2006; Tollet et al., 2022).

Baryons, which serve as the fuel for star formation, undergo further cooling in the central regions of galaxies via molecular cooling processes. This enables the gravitational collapse of molecular clouds, leading to the formation of stars. The resulting stellar populations constitute the visible component of a galaxy, typically concentrated in the central regions of the dark matter halo. For example, the half-light radius of the Milky Way is observed to be $5.75 \pm 0.38$ kpc (Lian et al., 2024), while its virial radius is $\approx 210$ kpc, considering its virial mass to be $10^{12} M_\odot$ (Bland-Hawthorn & Gerhard, 2016). Traditionally, the size of a galaxy– referring to its visible component–has been associated with

the extent of its stellar disk, largely because early observations were limited to telescopes operating in the optical band. However, multi-wavelength observations in radio, infrared, and X-rays have revealed more extended structures, such as neutral hydrogen (HI) disks, stellar halos, and gas in the much larger dark matter halos in which galaxies are embedded.

In particular, X-ray telescopes have uncovered the presence of an extended and massive hot gaseous medium surrounding the MW, commonly referred to as the Circumgalactic medium (CGM) (Tumlinson et al., 2017; Faucher-Giguère & Oh, 2023). It is reasonable to expect that a similar medium is present around other galaxies as well, as evidenced by absorption line studies in external galaxies. It was Spitzer 1956 who first drew attention to the fact that gas in the MW extends far beyond the stellar disk after having detected the presence of OVI and CIV absorption lines at high Galactic latitudes, which he called 'galactic corona'. Observational evidence indicates that gaseous halos not only exist around galaxies but also contain a large reservoir of mass that can account for the so-called 'missing baryons'. The term 'missing baryons' refers to the discrepancy between the observed baryon content within galaxies and the cosmic baryon fraction. In the framework of ΛCDM cosmology, the baryon density and total matter density are $\Omega_b h^2 = 0.0224 \pm 0.0001$ and $\Omega_m = 0.315 \pm 0.007$, respectively (Planck Collaboration et al., 2020), corresponding to a cosmological baryon fraction of $f_b \approx 0.16$. However, the total baryonic inventory within galaxies—including stars, interstellar gas, and dust—falls significantly short of this value. This discrepancy, together with observational evidence, suggests that a significant fraction of baryons resides in the CGM, which thus serves as a natural reservoir for the missing baryons.

Although its boundaries are not well defined, the CGM is typically considered to extend from the stellar and gaseous disk out to the virial radius of the halo. In systems with strong outflows—driven by stellar feedback or active galactic nucleus (AGN) activity—the CGM may even extend beyond the virial radius (Shull, 2014). By contrast, in galaxies with low star-formation activity and quiescent SMBH, such as the present-day Milky Way, the CGM is generally assumed to be confined within the virial radius. The CGM plays a crucial role in galaxy evolution, acting as both a reservoir of baryons and a regulator of gas inflows and outflows that shape the galaxies over cosmic time.

The gas in the CGM is multiphase and diffuse, as suggested by observations, theoretical works, and numerical simulations. In order to systematically study the physical

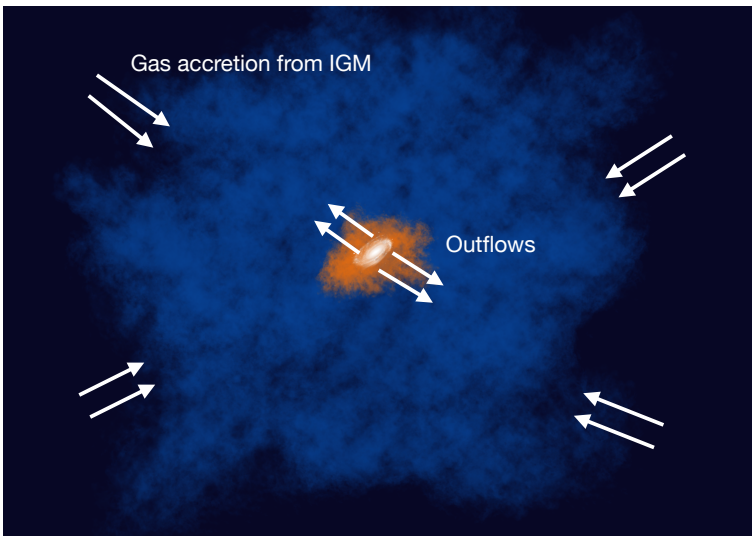



Figure 1.1: CGM illustration. The CGM contains both inflowing gas from the intergalactic medium (IGM), which supplies fuel for star formation, and outflowing gas from galaxies, which can heat and enrich the existing circumgalactic gas.

state of the CGM, it is typically divided into various temperature phases. These include the warm-hot phase (virial phase; $\sim 10^6$ K), warm phase ($\sim 10^5$ K), and cool phase ($\sim 10^4$ K), etc. While these are the temperature phases of typical MW-like CGM, similar phases are expected to be present in the CGM of other galaxies as well. The number density of gas in the CGM also varies by $\approx 2-3$ orders of magnitude, typically ranging between $10^{-5}$-$10^{-1}$ cm$^{-3}$ across various phases. Clearly, the CGM is tenuous compared to the ISM. This diffuse nature of this tenuous gas makes it harder to observe in emission since the detected flux scales as $n^2L$, where $n$ is the density of gas and $L$ is the extent of the emitting region. Therefore, sensitive telescopes are required to detect this gas in Optical/UV/X-rays. However, CGM is routinely observed in X-ray/optical/UV absorption, as absorption depends on the column density of the ion, which scales as $N_{\rm ion} \propto n_{\rm ion}L$, where $n_{\rm ion}$ is the number density of ion and $L$ is the size of the system harbouring these ions. Even though $n_{ion}$ is small, $L$ can be large enough (of the order of a few 100 kpc), so that the product of these two quantities can be significant for the ion to be detected in absorption.

## 1.2 Observations

### 1.2.1 X-ray emission

Several X-ray observatories have been set up in space to observe and study various astrophysical objects in the universe, such as galaxy clusters, Active Galactic Nuclei (AGN), X-ray binaries, etc, including the diffuse gas in the CGM. These observatories include *Chandra* (Weisskopf et al., 2000), *XMM-Newton* (Jansen et al., 2001), *Suzaku* (Mitsuda et al., 2007), *HaloSat* (Kaaret et al., 2019), *eROSITA* (Predehl et al., 2021), *XRISM* (Tashiro et al., 2025), etc, and future observatories like *ATHENA*, *HUBS* (Bregman et al., 2023), etc. These X-ray probes have detected the presence of CGM gas in both emission and absorption, as described below.

#### X-ray emission

Although it is natural for the 'virial' or warm–hot phase ($\sim 10^6$ K) of the MW's CGM to emit X-rays, detecting this emission is challenging due to the low gas density, as the flux scales with the square of the density. However, with the advent of more sensitive X-ray observatories, this diffuse emission has recently become detectable. The total emission is primarily dominated by metal line emission, while free–free (Bremsstrahlung) processes contribute to the underlying continuum. Owing to the limited energy resolution of Charge-Coupled Device (CCD) detectors used in these observatories, most individual emission lines remain unresolved (except for the brightest ones), causing the total emission to appear as a 'quasi-continuum' rather than a true continuum.

The total X-ray emission observed along a given line of sight, or over a region of the sky, arises from multiple components in addition to the CGM emission (Ponti et al., 2023). To isolate the diffuse CGM contribution, these components need to be carefully modeled. The total flux includes emission from the Local Hot Bubble (LHB; Liu et al. 2017), the soft X-ray background (SXB; McCammon & Sanders 1990), variable solar wind charge exchange (SWCX; Kuntz 2019), and the instrumental background. After accounting for or subtracting these components, the residual signal represents the intrinsic emission from the diffuse CGM of the Milky Way. Contributions from bright point sources within the Galaxy and from extragalactic sources are also removed to avoid contamination.

The diffuse gas emission is modeled using a single temperature collisionally ionized plasma model `APEC` (Astrophysical Plasma Emission Code; Smith et al. 2001) in software such as `XSPEC` (Arnaud et al., 1999). This emission model has three parameters: temperature, metallicity, and normalization. Normalization is proportional to the product of the solid angle subtended in the given patch of the sky by the telescope and the Emission Measure ($EM = \int^{los} n_e n_i dl$; where $n_e$ and $n_i$ are the electron and ion number densities). Since the solid angle is fixed by the telescope's field of view, one gets the best-fit temperature and EM from the analysis. Metallicity is usually fixed to either solar or 0.3 solar (Prochaska et al., 2017) in such analysis, since typical $\sim$ ks duration observations cannot constrain the metallicity. X-ray emission studies can thus constrain the temperature and EM along various lines of sight, which can be further used to constrain the analytical models of the CGM of the MW. Apart from the total emission, lines of highly emissive ions at the virial temperature, such as OVII, have also been observed by various authors and used to constrain the density and temperature of the CGM. These X-ray emission analysis results along various lines of sight are therefore key in constraining the models of the CGM.

Henley & Shelton 2013 detected the presence of warm-hot or virial gas in the MW's CGM using *XMM-Newton* along 110 sightlines and inferred the median temperature to be $2.22\times10^6$ K (interquartile range $0.63\times10^6$ K) and EM that varies by an order of magnitude 0.4-7 $\times$ $10^{-3}$ cm$^{-6}$ pc between different sightlines. Nakashima et al. 2018 observed the MW's CGM along 107 sightlines using *Suzaku* and found the median temperature to be $3.0 \times 10^6$ K. They also showed that the observed EM is better modeled with a disk and an extended profile morphology. They further showed using the OVII, FeXVII lines that the median [O/Fe] is $\sim$ 0.25, which signifies enrichment due to core-collapse supernovae.

Kaaret et al. 2020 analyzed the *HaloSat* (a CubeSat-based X-ray observatory with a field of view of 10°, especially optimized to study diffuse X-ray emitting gas; Kaaret et al. 2019) data along various fields in the CGM of the MW in the Southern hemisphere. They found that the EM is best modeled by a disk component along with an extended halo profile as previously suggested by Nakashima et al. 2018. The extended halo profile is required in order to explain the high column density of ions detected in absorption studies. They explored various disk models along with various extended halo models (see their Extended Data Fig. 4). Moreover, they showed that the CGM is clumpy on angular scales of $\sim$ 10°.

All of these observations were analyzed assuming emission from a single temperature thermal plasma, and the best-fit temperature obtained in these studies is roughly the warm-hot or virial temperature of the MW. However, Das et al. 2019a, for the first time, modeled the total emission from the MW's CGM using a two-temperature thermal plasma model in the direction of the blazar 1ES 1553+113 using *XMM-Newton*. The best-fit two temperatures correspond to the virial (warm-hot; $10^{6.25} - 10^{6.42}$ K) and super-virial (hot; $10^{6.68} - 10^{6.92}$ K) phases. Thus, they found the presence of an additional higher temperature gas than the virial gas in the CGM of the MW. They also performed the F-test analysis and found that this additional temperature component is required with very high confidence to better fit the data. According to them, this is strong evidence for X-ray emitting super-virial or hot gas in the CGM of MW along 1ES 1553+113.

A similar analysis with two temperature components has then been carried out by various authors along a large number of sightlines. Gupta et al. 2021 used *Suzaku* and *Chandra* observations along 4 sightlines to characterize the X-ray emitting gas in the MW's CGM. They again found that the emitting X-ray gas is well fitted by a two-temperature plasma model with the best-fit virial temperature of $0.176 \pm 0.008$ keV and super-virial temperature in the range $0.65 - 0.90$ keV. Using *HaloSat* data, Bluem et al. 2022 analyzed a large number of sightlines in the Northern and Southern hemispheres of the MW's CGM, and modeled the emission using two `APEC` models. They also found that a second component was required along a large number of sightlines (80% of the total sightlines) to better fit the emission data. For the warm-hot gas, they obtained an average temperature of $0.179^{+0.005}_{-0.007}$ keV and $0.184 \pm 0.009$ keV in the Northern and Southern latitudes, respectively. For the hot gas, the average temperatures in the Northern and Southern hemispheres are $0.69^{+0.05}_{-0.06}$ and $0.75 \pm 0.08$ keV, respectively. This result also showed that the average temperature in the Southern hemisphere was larger than in the Northern hemisphere. With data from a larger number of sightlines, they found a strong correlation between the EM of the warm-hot and hot gas (see Fig. 1.2). Note that such a correlation does not exist between the warm-hot and hot gas temperatures.

Ponti et al. 2023 observed the MW halo in the eFEDS field ($l \sim 220°$-$235°, b \sim 20°$-$40°$) using *eROSITA*. Unlike other studies, where metallicity is fixed, they allowed a variation in metallicity. Their best-fit results showed that the warm-hot gas metallicity is 0.068 $Z_\odot$, less than 0.3 $Z_\odot$, which is often considered to be a typical value in CGM (Prochaska et al., 2017). However, they fixed 0.7 solar metallicity for the hot gas.

Figure 10. from
Jesse Bluem et al 2022 Astrophys. J. 936 doi:10.3847/1538-4357/ac8662
https://dx.doi.org/10.3847/1538-4357/ac8662
© 2022. The Author(s). Published by the American Astronomical Society.

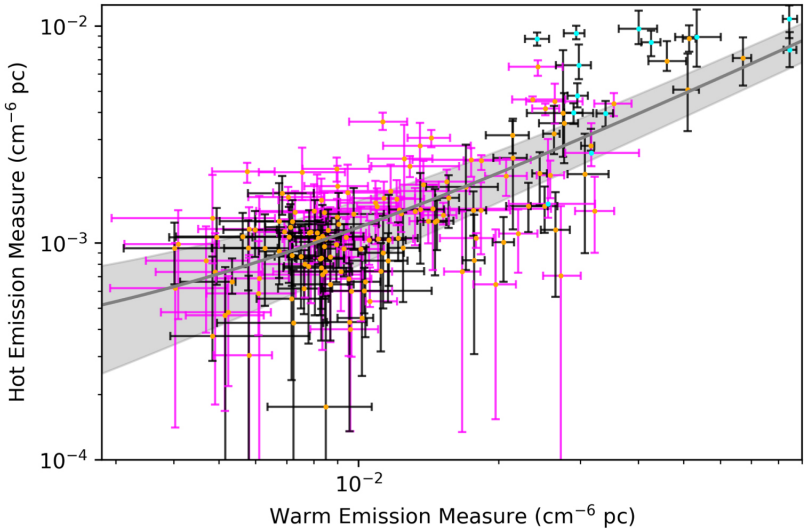



Figure 1.2: EM correlation of the warm-hot (x-axis) and hot (y-axis) gas for various lines of sight from Bluem et al. 2022 using *HaloSat*.

Bhattacharyya et al. 2023 used *XMM-Newton* observation towards the Blazar Mrk 421 ($l = 179°.83, b = 65°.03$) and 5 other fields near the blazar to study the X-ray emitting CGM. They found the temperature of two phases to be 0.14–0.192 keV and 0.66–1.14 keV. They further found the correlation in the EM of the two phases, whereas such a correlation was absent for the temperatures. They also showed that at the hot gas temperatures ($\sim 10^7$ K), emission was dominated by Fe emission lines. This suggested that the hot gas in emission was Fe-abundant.

Further, Sugiyama et al. 2023 used 130 *Suzaku* observations to study the diffuse gas in CGM. They found the median EM of the hot gas to be $3\times10^{-4}$ cm$^{-6}$ pc with $(1-8)\times10^{-6}$ cm$^{-6}$ pc as 16$^{\text{th}}$ and 84$^{\text{th}}$ percentile range. Lastly, Gupta et al. 2023 using 230 *Suzaku* archival observations, found that the temperature of warm-hot and hot gas to be $\sim 0.2$ and $\sim 0.4 - 1.1$ keV, respectively. All these observations show the presence of a hot phase in the MW's CGM for most of the sightlines, along with widespread warm-hot gas. This confirms the ubiquitous nature of X-ray-emitting hot gas across the Northern and Southern hemispheres. The EMs of the warm-hot and hot gas show a strong correlation, whereas the temperatures of the warm-hot and hot gas are uncorrelated. This correlation in EM suggests a correlation in the density structure of the two gaseous phases, as the emission is dominated by the nearby region.

### X-ray absorption

Apart from X-ray emission, the CGM of the MW has also been studied in X-ray absorption using the tracer ions. The warm-hot or 'virial' gas ($\sim 10^6$ K) is traced mainly using the absorption lines of OVII K$\alpha$ (21.61 Å), OVII K$\beta$ (18.63 Å), and OVIII K$\alpha$ (18.97 Å). Figure A.2 shows the ion fraction of H and He-like ions of various elements as a function of temperature for Collisional Ionization equilibrium (CIE), computed using the radiative transfer code `CLOUDY` (Ferland et al., 2017). It can be inferred from the figure that OVII is the ideal tracer of warm-hot gas in the CGM, whereas OVIII traces a slightly higher temperature gas in CIE. Oxygen lines are easily detected in X-ray absorption because of the relatively higher abundance of Oxygen relative to the other elements, even though the ionic fraction of different ions is significant at the warm-hot temperatures. These $z = 0$ absorption lines from the CGM of the MW have been detected in the spectra of bright background sources, typically quasars along various sightlines. The transmission grating in *Chandra* (HETG, LETG) and the reflection grating in *XMM-Newton* (RGS1, RGS2) have been mainly used to detect X-ray absorption lines. However, even with the current X-ray gratings, these absorption profiles cannot be resolved, although the line itself can be detected. For example, the resolution element of HEG in *Chandra* is $\Delta\lambda = 0.012$ Å, which corresponds to the velocity resolution of $\approx 170$ km s$^{-1}$ for OVII K$\alpha$ at 21.6 Å. The Doppler b parameter ($\sqrt{2k_BT/m_i}$; where $T$ is the temperature and $m_i$ is the mass of the ion) for OVII at $10^6$ K is $\approx 33$ km s$^{-1}$. Since the widths of these absorption lines are generally smaller than the velocity resolution of the instruments, the absorption profiles cannot be resolved.

Several authors observed the MW's CGM using X-ray absorption lines of OVII, OVIII, NeIX, etc, together with UV observations to study the temperature and density structure in the CGM along various lines of sight (Nicastro et al., 2002; Williams et al., 2005; Fang et al., 2006; Gupta et al., 2012). Unlike emission, the CGM of external galaxies is also probed using X-ray absorption (Mathur et al., 2023). All these observations were focused on detecting the warm-hot gas in the CGM. However, Das et al. 2019b using the grating data of *XMM-Newton* detected the presence of $z = 0$ NeX absorption line along with other ions in the spectra of 1ES 1553+113 ($l = 21°.91, b = 43°.96$). Detection of NeX suggests the presence of hotter temperature gas than the warm-hot gas in the MW's CGM. This can be noted from Fig. A.2, where NeX traces a higher temperature gas than warm-hot gas in CIE. Further using the `PHASE` model (models of collisionally

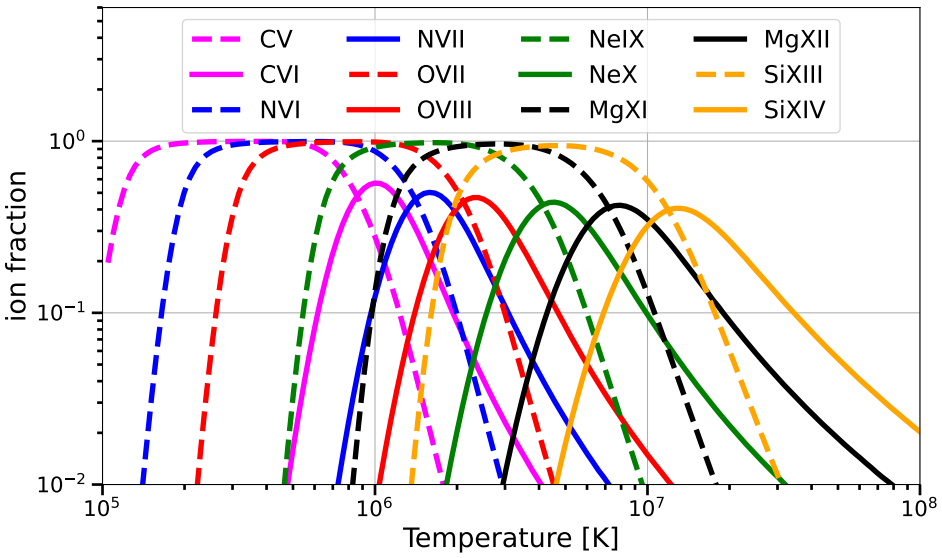



Figure 1.3: Ion fraction of H and He like ions of various elements in Collisional Ionization Equilibrium (CIE) computed using the radiative transfer code `CLOUDY` (Ferland et al., 2017).

ionized gas perturbed by photoionization by the meta-galactic radiation field, at a given redshift), they found the temperatures of the warm-hot and hot gas to be $1.29^{+0.71}_{-0.87} \times 10^6$ K and $1.15^{+6.09}_{-0.93} \times 10^7$ K, respectively. The corresponding equivalent Hydrogen column density (for solar metallicity of Oxygen) for the warm-hot and hot gas is $13.3^{+5.0}_{-4.5} \times 10^{18}$ and $2.9^{+2.4}_{-2.0} \times 10^{20}$ cm$^{-2}$ respectively. Additionally, they inferred that the hot gas is $\alpha-$enriched with [O/Fe] $= 0.9^{+0.7}_{-0.3}$, which suggests the enrichment due to core-collapse supernovae. Note that the hot gas detected in emission was inferred to be Fe-abundant. Therefore, absorbing and emitting X-ray hot gas appear to have distinct origins. These authors also found non-solar composition from the ratio of ions.

Next, Das et al. 2021 analyzed the deep high S/N *Chandra* data along Mrk 421. They detected various absorption lines of H and He-like ions along with NeX and SiXIV absorption lines, which trace the hot gas in the CGM, assuming CIE. Using these absorption lines, they inferred three distinct temperature phases, namely, the virial phase, super-virial phase, and sub-virial phase. Again, they found the super-solar composition of the ratio of ions and $\alpha$-enhancement in both virial and super-virial phases. McClain et al. 2024b followed a similar analysis towards NGC 3783 and found the presence of super-virial gas along with virial gas. They detected NeX along with other ions. Lastly, Lara-DI et al. 2023 detected SiXIV and SXVI absorption lines by stacking the X-ray data along 47 lines of sight. In the follow-up paper (Lara-DI et al., 2024b), they inferred three

temperature phases (virial, super-virial, and sub-virial) from the stacked data, which is similar to what is inferred along Mrk 421.

A few points regarding the nature of the $\sim 10^7$ K gas detected in X-ray emission and absorption are as follows: Unlike hot gas in emission, which is detected in $\approx 80\%$ of the sightlines, the X-ray absorbing hot gas is detected only along three lines of sight (1ES 1553+113, Mrk 421, and NGC 3783). Hot X-ray emission has a significant contribution from Fe line emission, while the absorbing X-ray hot gas is found to be $\alpha$-enhanced. Moreover, the absorbing hot gas is inferred to have a super-solar composition of the ratios of ions with dominant non-thermal broadening. The typical EM and equivalent H column density values obtained from these studies suggest a length scale of a few Mpc, if both emission and absorption are assumed to come from the same region! Thus, the X-ray emitting hot gas and X-ray absorbing hot gas ought to have distinct origins. Therefore, these two phases have to be treated and modeled distinctly.

### 1.2.2 Optical/UV

The CGM is also routinely observed in Optical/UV using absorption lines. These absorption lines include MgII, SiII, CaII, CIV, OVI, etc. Depending on the ionization conditions in the CGM, these ions trace various phases of the CGM, namely, the cool ($\sim 10^4$ K) and warm phase ($\sim 10^5$ K). Unlike warm-hot or virial gas in the CGM, which is believed to be in CIE, the lower temperature gas ($\sim 10^{4-5}$ K) is likely to be in Photo-ionization equilibrium (PIE). Therefore, the density of cool and warm gas is a key parameter in determining the ion fraction, unlike in CIE, where the ion fraction depends exclusively on the temperature. Background radiation fields such as HM12 (Haardt & Madau, 2012) and KS18 (Khaire & Srianand, 2019) are typically used to estimate the ion fraction in PIE.

Using optical and UV telescopes, the CGM of external galaxies has been extensively studied through absorption-line spectroscopy. Several surveys have been conducted to probe the photoionized cool and warm gas in the CGM of external galaxies. In these studies, quasars are observed spectroscopically, and their spectra are analyzed to identify absorption lines of various ions. Once the absorbers are detected at specific redshifts, they are associated with nearby galaxies by cross-matching with galaxy surveys to find the galaxy that lies closest to the absorber in both redshift and sky position. This

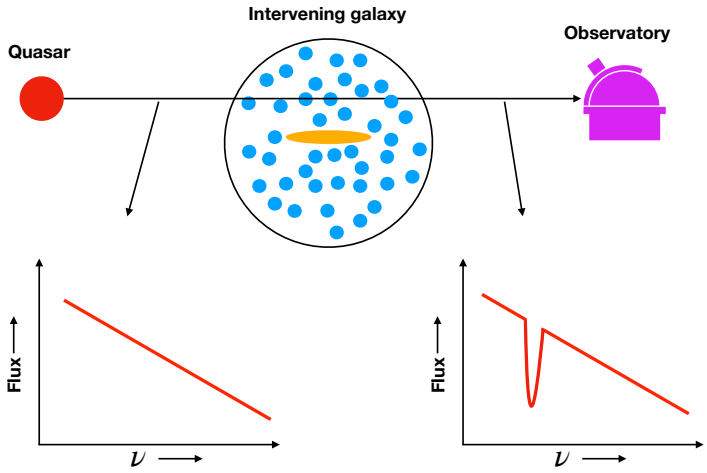



Figure 1.4: This illustration shows how absorption lines can be used to detect cool/warm gas in the CGM.

method—where quasars are observed first, absorbers are identified, and then matched with galaxies—is known as the 'absorber-centric' approach. In contrast, the 'galaxy-centric' approach begins by selecting a galaxy and then searching for quasars whose sightlines pass close to it, followed by a search for absorption lines at the galaxy's redshift. Because multiple quasar sightlines intersecting the CGM of the same galaxy are rare, it remains challenging to map the CGM of a single galaxy using absorption-line observations. Consequently, most studies rely on identifying individual (foreground) galaxy–(background) quasar pairs.

These surveys and database include MAGIICAT (Nielsen et al., 2013), COS-Halos survey (Tumlinson et al., 2011), MAGG (Dutta et al., 2020), SDSS DR16 (Anand et al., 2021), M3 Halo project (Huang et al., 2021), CUBS (Qu et al., 2023), MEGAFLOW (Cherrey et al., 2025), etc. The cool gas in the CGM is mainly observed using MgII doublet $\lambda\lambda 2796, 2803$ because of its wavelength advantage and its considerable oscillator strength. The Cosmic Origins Spectrograph (COS) onboard the Hubble Space Telescope (HST), operating in the UV band, enables the detection of MgII absorption lines up to a redshift of $z \sim 0.14$. At higher redshifts, MgII becomes accessible in the optical regime and is routinely observed using instruments such as MUSE ($z \sim 0.7$-$2.3$). Owing to this broad redshift coverage by various instruments, MgII absorption is among the most commonly detected tracers in the cool CGM surveys. The galaxies associated with

absorbers in these surveys span a wide range in redshift, stellar mass, galaxy type (star-forming or quiescent), and orientation angle with respect to the major axis of the galaxy. Consequently, a large spectroscopic survey such as DESI (DESI Collaboration et al., 2025) is essential to systematically investigate the distribution of cool gas in the CGM as a function of galaxy properties, including stellar mass, redshift, and galaxy type.

The primary observable in absorption-line analysis is the equivalent width (EW), which is subsequently converted into the column density of the absorbing ion using various techniques. The commonly employed techniques include the curve of growth analysis, which relates EW to column density; Voigt-profile fitting, where the absorption profile is modeled by convolving thermal and natural broadening effects; and the apparent optical depth (AOD) method, which derives the column density directly from the observed optical depth as a function of velocity. In the curve-of-growth (COG) analysis, if the measured EW is below a threshold value ($EW_0$), the linear (optically thin) regime of the curve is used to convert EW into column density. For stronger lines with EW larger than $EW_0$, the flat (saturated) portion of the curve is applicable, where the derived column density depends sensitively on the Doppler b-parameter, which accounts for both thermal and non-thermal (turbulent) broadening of the line. The expression for $EW_0$ is

$$EW_0 \approx 4.1 \times \left(\frac{b}{1\,\mathrm{km\,s^{-1}}}\right)\left(\frac{\lambda}{1000\,\text{Å}}\right)\ \text{mÅ} \tag{1.1}$$

where $\lambda$ is the transition wavelength of the ion. If the $b$ parameter is unknown, then an extrapolation of the linear part of the COG is used to estimate column density from the EW instead of the flat part of the COG. This results in an upper limit on the column density. Multiple ions detected for a single galaxy can be used to obtain the physical conditions of the gas bearing these ions in a detailed modeling (Sameer et al., 2024). Such a detailed model includes photoionization at the observed redshift to obtain the ion fraction, temperature, number density of H, H column density, and metallicity. Then a Bayesian analysis is performed to obtain the minimum number of clouds with best-fit parameters to explain the observation of all the detected ions.

This analysis yields the typical size of the clouds (along the line of sight) in the CGM ($l \sim N_H/n_H$), where $N_H$ is the column density and $n_H$ is the number density of hydrogen. It is, however, difficult to determine the transverse size of clouds directly from the observations. This makes it challenging to infer the 3D information of cool gas clouds from the 2D information using the absorption lines. However, with an extended background source and integral field spectroscopy instruments such as MUSE, it is possible to esti-

mate the coherence length of absorbers. In a rare case of a gravitationally lensed system, using background gravitational arcs, Dutta et al. 2024b measured the coherence length of Mg II absorbers to be approximately $\sim$ 10 kpc. This represents a characteristic size of MgII absorbing clouds in the CGM. Nevertheless, such systems are exceedingly rare, and it remains infeasible to map the CGM of an external galaxy using absorption-line measurements alone.

### 1.2.3 Radio

Apart from X-rays, optical, and UV, the CGM of MW has also been probed and studied in the radio band. Fast Radio Bursts (FRBs; Petroff et al. 2019), which are typically millisecond-duration radio bursts, can be used to study the CGM of the MW. These radio bursts, when travelling through the CGM of MW, get dispersed by free electrons in it. This 'dispersion' results in higher frequency photons reaching earlier than photons with lower frequencies. Effectively, the oscillations of free electrons in the CGM slow down the waves with lower frequencies more than those with higher frequencies. This dispersion is quantified by a parameter known as 'Dispersion Measure' or DM, which is the line of sight integral of free electrons ($\int^{los} n_e dl$). Free electrons are contributed by the various thermal phases of the CGM; therefore, FRBs cannot be used to disentangle the individual phases of the CGM. However, they provide a powerful probe to constrain the total baryonic mass contained within the CGM (Ravi, 2019; Ravi et al., 2025).

Since most of the FRBs are extra-galactic in origin, the total DM observed has contributions from several components along the line of sight. These include the following:

$$DM_{tot} = DM_{source} + DM_{host} + DM_{IGM} + DM_{MW,ISM} + DM_{MW,CGM} \tag{1.2}$$

where, $DM_{source}$ is the contribution of the source that gives rise to these radio pulses, $DM_{host}$ is the contribution of the host galaxy, $DM_{IGM}$ is the contribution of IGM, $DM_{MW,ISM}$ is the contribution of ISM of MW, and $DM_{MW,CGM}$ is the contribution of CGM of the MW. Once the contribution of the individual components is known, the contribution of the CGM of the MW can be obtained. However, it is difficult to obtain the contribution of the individual components. Therefore, only nearby FRBs can be used to put tighter limits on the DM contribution of the CGM of MW since the contribution of the IGM is minimal in these cases. Similarly, Rotation Measure (RM $= \int n_e B_{||} dl$) can be used to constrain the (line-of-sight component of) magnetic field in the CGM. Moreover,

the radio signals from FRBs can also be used to estimate the size of cool clouds in the CGM as a result of scintillation (Mas-Ribas et al., 2025).

## 1.3 Simulations

The CGM has been extensively studied using numerical simulations, including large-scale cosmological simulations such as Illustris-TNG, SIMBA, FIRE, ROMULUS, and EAGLE, as well as various idealized simulations designed to isolate specific physical processes. Cosmological simulations generally start at very high redshifts with appropriate initial conditions and are evolved forward to the present epoch. The simulation outputs at different redshifts are then analyzed to study the evolution of galaxies and their CGM. These studies typically find that the CGM is primarily shaped by outflows driven by SMBH activity and stellar feedback, in addition to being influenced by cosmological gas accretion and galaxy mergers. However, due to limitations in dynamic range, large-volume cosmological simulations (with box sizes of order $\sim$ (100 Mpc)$^3$) cannot adequately resolve the ISM of individual galaxies.

The implementation of AGN feedback varies among different simulations. Typically, AGN feedback is modeled in two modes: the thermal (or quasar) mode and the kinetic (or radio) mode. The radio mode corresponds to a low-accretion state, during which jets are launched, while the thermal mode operates during high BH accretion rates, where large amounts of energy are thermally deposited into the surrounding gas. In both modes, mass and energy are injected into the CGM, altering its thermal structure. Since the CGM serves as a reservoir of cold gas that replenishes the ISM and fuels star formation, AGN feedback significantly influences the star formation activity within galaxies. The feedback-driven heating of the CGM increases its radiative cooling time, thereby suppressing gas inflow into the galaxy. As a result, the galaxy becomes quenched, typically characterized by a specific star formation rate (sSFR) below $\sim 10^{-11}$ yr$^{-1}$.

In general, stellar feedback is primarily responsible for quenching galaxies at the low-mass end, while AGN feedback dominates the quenching of massive galaxies with halo masses $\gtrsim 10^{12}\,M_\odot$. Because different cosmological simulations implement AGN feedback in distinct ways, the effects on star formation and galaxy quenching also vary among them. Zinger et al. 2020 investigated the impact of AGN feedback on the CGM of massive

galaxies at $z = 0$ in the TNG100 and TNG300 simulations, and found that the entropy of the CGM gas is a sensitive indicator of the feedback energy injection. They concluded that AGN feedback in the TNG operates in both an 'ejective' and a 'preventative' manner: it is ejective in the sense that it expels cold gas from the ISM—thereby depleting the fuel for star formation—and preventative, because it heats the CGM gas, increasing its radiative cooling time and thus suppressing the accretion or condensation of gas back into the ISM.

Terrazas et al. 2020 studied AGN feedback in the TNG100 simulation as a function of sSFR, stellar mass, and black hole mass. They found that the sSFR sharply decreases once the energy of the kinetic winds from the SMBH exceeds the gravitational binding energy of the gas within the stellar radius of the galaxy. This transition occurs above a threshold black hole mass, beyond which galaxies become 'quenched'. Ayromlou et al. 2023 investigated the effect of feedback on the redistribution of baryons in the CGM and beyond, comparing results from the TNG, EAGLE, and SIMBA simulations. They found that SMBH feedback can eject baryons to distances up to several tens of virial radii, thereby reducing the baryon fraction within the virial radius of galaxies. To quantify this, they defined a 'closure radius' ($R_c$) as the radius within which the cumulative baryon fraction equals the cosmic baryon fraction ($\approx 0.16$), and derived a relation between $R_c$ and $M_{200c}$ for individual halos, groups, and clusters across the three simulations.

Thus, AGN feedback can redistribute baryons within and beyond the CGM (see Fig. 1.5), influencing observables such as the thermal and kinematic Sunyaev–Zel'dovich (tSZ and kSZ) effects, X-ray emission, and ion column densities at distances extending far beyond the virial radius. This redistribution also drives mass and metal flows into the IGM, thereby enriching its chemical composition and altering its thermodynamic structure, depending on the strength of the outflows. Morgan & Bailin 2025 examined the mass and metal flows in TNG galaxies under different feedback conditions—classified by radio mode (radio-quiet or radio-loud), sSFR, and galaxy morphology. By analyzing the mass flow rates, metal flow rates, and mass accumulation rates as functions of galactocentric radius, they identified a characteristic radius of $\sim 0.2\,R_{\rm v}$ (where $R_{\rm v}$ is the virial radius) that marks a transition region where significant dynamical changes occur. This radius effectively separates the inner and outer regions of galaxies. Consistent with these findings, several other cosmological simulations also emphasize the key role of AGN feedback in driving and regulating baryon redistribution in galaxies.

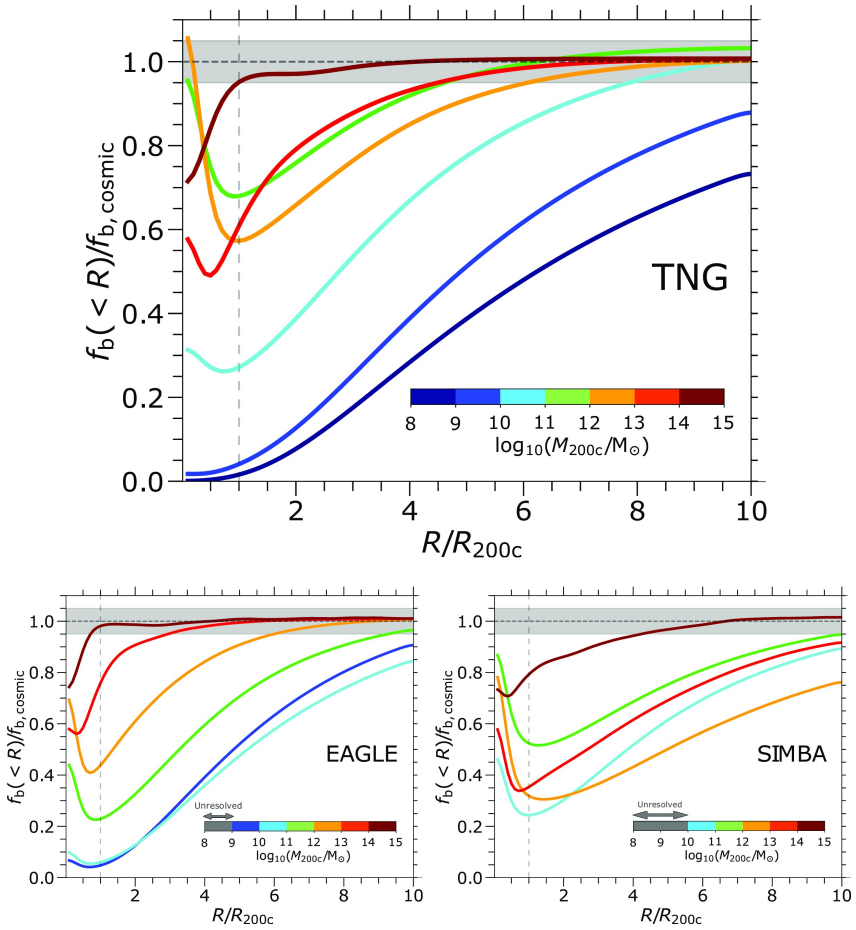



Figure 1.5: Baryon fraction as a function of normalized radial distance from the halo center for different halo masses ($M_{200c}$) and simulations, adapted from Ayromlou et al. 2023. Feedback processes redistribute baryons to much larger distances, extending well beyond the virial radius of the galaxy.

Apart from cosmological simulations, various idealized simulations have also been conducted to study the impact of feedback on the ISM and CGM. These simulations help to establish sub-grid prescriptions for mass and energy loading factors that are implemented in large-scale cosmological simulations, where the ISM cannot be fully resolved. Li & Bryan 2020 compiled recent small-box simulation results, after quantifying the mass, energy, and metal loading factors of supernova (SN)-driven outflows into the ISM and CGM. They found that hot outflows are substantially stronger than cool outflows, carrying higher specific energy and energy flux. Furthermore, they showed that hot outflows cannot escape from dark matter halos with masses $\gtrsim 10^{12}\,M_{\odot}$, thereby reinforcing the picture that AGN feedback, rather than stellar feedback, is primarily responsible for quenching star formation in massive halos.

Li & Tonnesen 2020 performed an idealized simulation of an MW-like galaxy, incorporating stellar feedback over a period of 8 Gyr. The stellar feedback prescription was based on results from small-box simulations, including the mass, energy, and metal loading factors. They found that at low specific star formation rate densities, stellar feedback cannot drive outflows that escape the halo, instead producing a fountain-like structure around the galactic disk. At later times, the hot outflows become saturated, as the radiative cooling rate balances the outflow rate, resulting in the formation of a metal-enriched halo with a universal density profile. The total baryon and metal masses in the CGM were found to be lower than the cosmic baryon and metal fractions, suggesting that past feedback episodes may have ejected baryons and metals to much larger distances. Vijayan & Li 2022 further analyzed this simulation to study the X-ray spectra and, by comparing with observations, found that the spectra are best described by a log-normal temperature distribution. Their results also revealed the presence of super-virial gas ($\sim 10^7$ K) in the CGM of an MW-like galaxy, but with a high SFR of $\sim 10\,M_{\odot}\,\mathrm{yr}^{-1}$, significantly higher than the current MW value (Elia et al., 2022).

Other idealized simulations have focused on large-scale Galactic structures. Sarkar et al. 2015, 2017 used central energy injection to model the MW's Fermi and eROSITA bubbles, concluding that star formation activity in the Galactic center can reproduce the observed bubble characteristics. Vijayan et al. 2018 studied disk-wide stellar outflows, finding that they create a chimney-like structure near the disk. The mass and energy ejection rates were tied to the SFR, computed via the Kennicutt–Schmidt relation (Kennicutt, 1998).

Apart from large-scale and idealized simulations, small-scale simulations have been conducted to study the survival of cool gas clouds ($\sim 10^4$ K) in the CGM. As these clouds travel through the hot CGM ($\sim 10^6$ K), they are subject to various hydrodynamical instabilities (Gronke et al., 2022; Das & Gronke, 2024; Tan & Fielding, 2024). Complementary studies using zoom-in cosmological simulations have investigated the morphology, mass, size, and density distribution of cool clouds in the CGM (Ramesh & Nelson, 2024; Ramesh et al., 2025). However, these works are still limited by resolution, making it challenging to accurately constrain the properties of lower-mass and smaller-size clouds.

## 1.4 Analytical models

In order to interpret the various observational signatures of the CGM, to predict how these signatures vary along different sightlines, and to constrain its underlying physical conditions, analytical models have been constructed. In such models, the CGM is commonly assumed to be in hydrostatic equilibrium with the dark matter halo and to be spherically symmetric. While these assumptions are idealized, they provide a tractable framework for linking theoretical predictions with observations. The differential equation for hydrostatic equilibrium in one-dimensional spherical coordinates is given by:

$$\frac{dP(r)}{dr} = -\rho(r)\frac{d\phi(r)}{dr} \tag{1.3}$$

where $P$ is the total pressure, including contributions from thermal gas, cosmic rays, magnetic fields, etc.; $\rho$ is the gas mass density; and $\phi$ is the gravitational potential of the dark matter halo. The self-gravity of the gas is neglected for simplicity. The dark matter density profile is generally assumed to follow the NFW profile (Navarro et al., 1997) or a modified NFW profile. Assuming only thermal gas pressure and an ideal gas, the above equation can be written as,

$$nk_B\frac{dT}{dr} + k_BT\frac{dn}{dr} = -\rho\frac{d\phi}{dr} \tag{1.4}$$

where $n$ is the particle number density and $k_B$ is the Boltzmann constant. For a polytropic gas, the pressure and density are related by:

$$P = K\rho^{\Gamma} \tag{1.5}$$

where $K$ is often referred to as the entropy of the gas, and $\Gamma$ is the polytropic index. A value of $\Gamma = 1$ corresponds to an isothermal gas, while $\Gamma = 5/3$ represents an adiabatic

gas. Using the polytropic relation, the hydrostatic equilibrium equation becomes:

$$\rho^{\Gamma}\frac{dK}{dr} + K\Gamma\rho^{\Gamma-1}\frac{d\rho}{dr} = -\rho\frac{d\phi}{dr} \tag{1.6}$$

This equation can be solved to obtain the density profile of the gas, assuming constant entropy ($K$=constant) or when the entropy profile is known. Once the density profile is known, the pressure and temperature profiles can be computed using the polytropic relation and the ideal gas equation. From this starting point, various analytical CGM models can be constructed based on additional assumptions, such as isothermal CGM, adiabatic CGM, or precipitation models. The simplest case is the isothermal model (for example Sarkar et al. 2015), in which the CGM gas is assumed to have a fixed temperature—typically corresponding to the mass- and volume-dominated warm-hot phase. Solving the isothermal model results in exponentially decaying profiles for both pressure and density. However, because the temperature is fixed—typically at the virial temperature—the model cannot reproduce lower-temperature observables, such as the column densities of ions tracing the cool and warm phases of the CGM.

To account for temperature variations in the CGM, a relation between pressure and gas density is often assumed, either in the polytropic or adiabatic form (Maller & Bullock, 2004; Faerman et al., 2020), or an entropy profile is specified (Voit et al., 2017). These modifications naturally produce radial variations in temperature, along with corresponding pressure and density profiles. Typically, the temperature decreases smoothly from the virial temperature (e.g., $\sim 10^6$ K for the Milky Way) in the inner CGM to $\sim 10^5$ K at the halo boundary, with the temperature being fixed at a given radius. Such models can reproduce observations of the warm and warm-hot phases, for example, the column densities of OVI (warm phase) and OVII (warm-hot phase). However, they still do not capture the full multiphase nature of the CGM, which spans from the cool to the warm-hot phase.

At a given radius, the CGM may exhibit a multiphase structure, with gas temperature varying from the cool ($\sim 10^4$ K) to the hot phase ($\sim 10^7$ K). To capture this multiphase nature, temperature fluctuations can be introduced around a background value, resulting in a range of temperatures at each radial shell. Faerman et al. 2017 modeled the CGM with log-normal temperature fluctuations around a fixed background temperature. In this framework, the pressure is constant (isobaric), so the density distribution is also log-normal ($P \propto nT$). This model could reproduce several observables, but it was limited to isobaric fluctuations and only two phases—the warm and warm-hot components. In

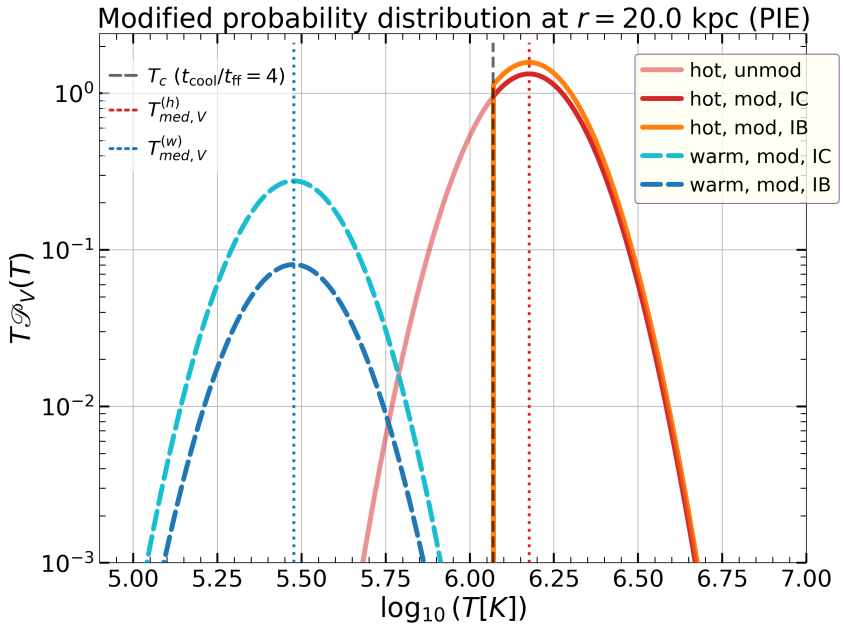



Figure 1.6: Log-normal temperature probability distribution function at a radial distance of 20 kpc from the center of a galaxy (Dutta et al., 2024a). The two peaks correspond to the warm-hot and warm phases. Similarly, multiple peaks can be constructed corresponding to the individual phases of the CGM.

principle, one could extend this approach by considering a multi-peaked log-normal temperature distribution, allowing for pressure fluctuations and different background profiles in pressure, temperature, and density. Dutta et al. 2024a generalized the Faerman et al. 2017 model by incorporating non-isobaric fluctuations and alternative background profiles (e.g., adiabatic models). They also implemented a three-phase log-normal distribution to include the cool phase and applied it to a TNG galaxy, and found that the CGM volume is dominated by warm-hot gas, while luminosity is dominated by the cool and warm-hot phases. In this generalized model, the mean temperature of the log-normal distribution varies with radius, in contrast to the fixed temperature in the original isothermal framework.

This probabilistic approach produces the multiphase nature of the CGM at all radii, providing a more realistic representation of the CGM. A comprehensive comparison of warm-hot gas models of the CGM was carried out by Singh et al. 2024. Beyond hydrostatic models, several alternative models have been developed to interpret CGM observables. These include the beta model (Miller & Bregman, 2013), modified beta model (Miller & Bregman, 2015), and rotating CGM models that account for halo rotation (Sormani et al., 2018). Cooling flow solutions (Stern et al., 2019), which represent steady-state

inflows with radiative cooling, have also been used to model the CGM. To reproduce the X-ray emission from the MW's CGM, disk models (either exponential or empirical) are often introduced (Nakashima et al., 2018; Kaaret et al., 2020), as hydrostatic models alone cannot match the observed X-ray EM. While disk components fit the X-ray EM well, they are sub-dominant in mass and thus cannot reproduce the column densities of ions like OVII and OVIII, which trace the mass-dominant warm-hot CGM. Combining a disk model with an extended halo component provides a better match to all multiphase observables. However, these models are degenerate and must be tested against all observables—such as DM, ion column densities, and X-ray EM—along multiple sightlines. The basic idea is that through such comprehensive comparisons, models that fail to reproduce the full set of observations across different sightlines can be ruled out.

The models described above work well for the volume and mass-dominated warm-hot CGM. However, the cool and warm phases are neither volume nor mass dominant. These cooler phases are expected to be highly clumpy, occupying only a tiny volume fraction ($\lesssim 1\%$) of the CGM. In particular, the cool phase ($\sim 10^4$ K) is typically modeled in the form of clouds. As these clouds move through the hot ambient medium, they are subject to shear instabilities and potential disruption (Lan & Mo, 2019), requiring them to be sufficiently large and dense to survive and produce observable signatures. Several models of the cool CGM exist in the literature (Stern et al., 2016; Faerman & Werk, 2023; Hummels et al., 2024; Yang et al., 2025)

Stern et al. 2016 used a hierarchical model in which larger-density clouds are embedded within smaller-density clouds. Their model was constrained by observed column densities of ions tracing the cool phase. Faerman & Werk 2023 extended the adiabatic CGM model of Faerman et al. 2020 to include cool gas in the CGM of star-forming galaxies, constraining their parameters using the COS-Halos sample (Werk et al., 2013). Hummels et al. 2024 modeled cool clouds from first principles by generating cool cloudlets within each cloud, varying their mass, size, and velocity structure, and computing observables such as column densities, EWs, and covering fractions as a function of impact parameter. They compared their predictions with survey data from MAGG (Dutta et al., 2020) and the M3 Halo project (Huang et al., 2021). Yang et al. 2025 also modeled the cool CGM in the form of clouds, incorporating the observed intrinsic scatter in the particle number density at each radius and using a probabilistic approach. Their model was constrained using the EW distributions of $Ly\alpha$ and MgII from multiple surveys. With

their best-fit parameters, they estimated the mass of cool gas in the CGM of $L^*$ galaxies to be $10.01 \pm 0.06\, M_\odot$ (in $\log_{10}$).

## 1.5 Motivation of the thesis

From the preceding discussions, it is clear that many questions regarding the CGM remain unanswered. In this thesis, we will focus on a few of these questions.

- *What is the origin and spatial distribution of 'super-virial' gas detected in X-ray emission?*

  While the 'virial' or warm–hot component of the MW's CGM ($\sim 10^6$ K) is relatively well studied with theoretical models and simulations, the origin and spatial distribution of a recently detected 'super-virial' or hot X-ray–emitting component ($\sim 10^7$ K) remain unclear. Key questions are: what is the mass content of this hot gas, and how important is it for Galaxy evolution? Does stellar feedback or AGN activity primarily produce this component in the CGM? These questions motivate us to develop a model that can explain and reproduce the observed X-ray properties and predict the mass, energetics, and spatial extent of the 'super-virial' emitting gas.

- *What physical process gives rise to 'super-virial' gas detected in X-ray absorption along the three sightlines?*

  Observations indicate that the emitting and absorbing components of the 'super-virial' gas are distinct, implying that the absorbing hot phase must be modeled separately. This gas exhibits highly ionized species with unusually large column densities of ions such as OVIII, NeX, and SiXIV, and appears to be $\alpha$–enriched with dominant non-thermal line broadening. Along the three sightlines, different sets of ions with varying relative abundances are detected, showing super-solar ionic ratios. These unusual characteristics motivate us to model the absorbing 'super-virial' gas and to explain the observed differences among the three sightlines.

- *How is the cool gas distributed throughout the CGM, and how does this distribution influence the observed properties?*

The cool phase ($\sim 10^4$ K) of the CGM is observed to occupy only a tiny fraction ($\lesssim 1\%$) of its total volume. The covering fraction of cool gas tracer ions such as MgII is relatively high in the inner regions of the CGM but decreases toward larger impact parameters. Observations of the column densities of these ions also show a large scatter (spanning $\sim$1–3 orders of magnitude), with both upper and lower limits measured at similar impact parameters. These observational trends motivate us to model the spatial distribution of the cool gas and to estimate its total mass, which remains uncertain due to the clumpy and patchy nature of this phase.

- *Is the 'super-virial' gas detected in X-ray absorption widespread in the CGM?*

  The detection and characteristics of the 'super-virial' gas in X-ray absorption are particularly intriguing. Unlike the X-ray–emitting hot gas, which is detected along $\approx 80\%$ of the sightlines examined, absorption detections are currently limited to only three sightlines. This scarcity primarily arises from the requirement of bright background quasars, in whose spectra the high-ionization absorption lines tracing the hot gas can be identified. In addition, most existing observations of such quasars are relatively shallow, making these weak absorption features difficult to detect with confidence. A key question, therefore, is whether the absorbing hot gas is as widespread as the emitting hot gas. If it is, what is the mass content of this phase, and how does it influence Galactic evolution? Addressing these questions requires searching for X-ray absorption signatures of the hot gas along multiple sightlines, at least using the currently available archival data. Motivated by this, we investigate the presence of 'super-virial' gas in absorption toward PKS 2155–304, a bright background quasar located in the Southern hemisphere.

## 1.6 Structure of the thesis

This thesis is arranged according to the chapters as follows:

In **Chapter 2**, we focus on the 'super-virial' gas detected in X-ray emission. We propose that this gas originates from a puffed-up, disk-like region surrounding the MW. Using the observed data, we derive a scale radius and scale height of $\approx 5$ and $\approx 1$ kpc, respectively, for this disk-like structure. With these parameters, we successfully reproduce the observed correlation between the EMs of the warm–hot and hot phases.

The total mass of the 'super-virial' emitting phase, estimated from the disk model, is $\sim 4 \times 10^7\,M_\odot$, which is negligible compared to the mass of the warm–hot phase in the MW's CGM. Furthermore, we describe the results of an idealized hydrodynamical simulation of a Milky Way-type galaxy with disk-wide stellar outflows to investigate the possible origin of this hot, X-ray–emitting phase.

In **Chapter 3**, we propose a model that explains the observational signatures of the 'super-virial' gas detected in X-ray absorption. We demonstrate that shock-heated ejecta in core-collapse supernova, with typical blast energy of $\sim 10^{51}$ erg, ejecta mass of $\sim 10\,M_\odot$, and ambient density of $\approx 0.1$ cm$^{-3}$, can produce 'super-virial' temperatures and high column densities of ions such as OVIII, NeX, and SiXIV on timescales of a few $\sim 100$ kyr. The observed $\alpha$-enrichment and super-solar ionic ratios naturally arise from core-collapse supernova nucleosynthesis. Massive runaway stars in the extra-planar regions of the MW are plausible progenitors of such supernovae along the three observed sightlines.

In **Chapter 4**, we present our model for the distribution of cool gas ($\sim 10^4$ K) in the CGM. Based on the observational signatures of cool gas tracer ions such as MgII, we propose that the cool gas resides in clumpy structures, which we refer to as 'cloud complexes' (CCs). Each CC contains numerous small cloudlets, and the CCs themselves are distributed according to a power-law as a function of galactocentric distance. By further assuming a 'mist limit' (unit-area covering fraction) within each CC, we are able to reproduce the observed large scatter in column density, the trends in covering fraction, and the EW distribution of MgII. We also demonstrate that the blending of absorption lines from individual cloudlets intersected along a line of sight, each with a different line-of-sight velocity, naturally produces turbulent broadening at the scale of the CC.

In **Chapter 5**, we present the results of our X-ray absorption analysis toward the blazar PKS 2155–304. We utilized archival grating data of *Chandra* and *XMM–Newton* to search for $z = 0$ absorption lines of H and He like ions of C, N, O, Ne, Mg, and Si. We report, for the first time, the detection of the MgXII line in the MW's CGM, along with the SiXIV line, which are the tell-tale signatures of the 'super-virial' absorbing gas. Based on the detections and non-detections of various ions, we infer the presence of four distinct temperature phases along this sightline: 'super-virial' ($\sim 5 \times 10^7$ K), 'virial' ($\sim 2 \times 10^6$ K), 'sub-virial' ($\sim 2 \times 10^5$ K), and cool phase ($< 1.5 \times 10^5$ K). Since this sightline lies in the southern hemisphere—whereas the previous three detections

were in the north—the detection of hot gas here suggests that the super-virial absorbing component is likely widespread. Moreover, the detection of distinct ions and the large variation in the inferred super-virial temperatures, spanning nearly an order of magnitude across different sightlines, indicate that the absorbing hot gas is highly inhomogeneous in nature.

# Chapter 2

# On the Origin of the $10^7$ K Hot Emitting Gas in the Circumgalactic Medium of the Milky Way

Based on :
Bisht, M. S., Nath, B. B., & Mathur, S. 2024, ApJ, 975, 49B
doi: 10.3847/1538-4357/ad77c0

# Main Results

- A puffed-up, disk-like region around the Milky Way can explain the observed characteristics of the 'super-virial' X-ray–emitting gas.
- Fitting this disk model to the observational data suggests a scale radius of $\approx 5$ kpc and a scale height of $\approx 1$ kpc.
- The disk model successfully reproduces the observed correlation between the emission measures of the virial and super-virial gas components.
- The total mass of this phase, estimated from the disk model, is $\sim 4 \times 10^7\, M_\odot$, significantly smaller than that of the mass-dominant warm–hot phase.
- Disk-wide stellar outflows could plausibly be responsible for the origin of this phase, which is further supported by hydrodynamical simulations using a toy model of stellar outflows.

## 2.1 Introduction

The gas surrounding the stellar disk and the Interstellar medium (ISM) of a galaxy is referred to as the 'Circumgalactic medium' (CGM) (for a review see Tumlinson et al. 2017, Mathur 2022, Faucher-Giguère & Oh 2023). Observations of the CGM of the Milky Way (MW) and other galaxies, as well as numerical simulations, suggest the presence of multiphase gas in the CGM, with a large range in density and temperature. The gas temperature varies from the cold phase ($\sim 10^4$ K) to the virial phase ($\sim 10^6$ K). The 'virial gas' ($\sim 10^6$ K or 0.2 keV), so called because its temperature is comparable to the MW virial temperature, is the volume-filling and the most massive component of the CGM, and is detected in X-rays in both absorption and emission Gupta et al. 2012. Gas in the cold ($10^4$ K) and warm ($10^5$ K) phases is detected in the optical/UV band in absorption using bright background sources (typically a quasar).

Recent observations have, however, indicated the presence of $\sim 10^7$ K (0.8 keV) gas in addition to the gas at lower temperatures. Following Das et al. 2021, we refer to this $\sim 10^7$ K gas as the 'super-virial' gas (instead of 'coronal' or 'hot' gas, to avoid confusion with the $\sim 10^6$ K gas). We will make further distinctions regarding this phase, as follows. We will refer to the 'super-virial' phase that has been detected using SiXIV and NeX absorption lines in the X-ray spectra of background quasars along a few lines of sight (Das et al. 2019b, Das et al. 2021, McClain et al. 2024b, Lara-DI et al. 2023), Lara-DI et al. 2024b, as 'SV absorption'. And by 'SV emission' we will refer to the hot gas that has been detected in the emission studies of the MW CGM in many fields across the sky, in addition to the virial phase. In this paper, we will focus on the 'SV emission' phase, and the case of SV absorption will be dealt with in a separate paper.

Several X-ray observatories (eg, *Chandra* (Weisskopf et al. 2000), *XMM-Newton* (Jansen et al. 2001), *Suzaku* (Mitsuda et al. 2007), *HaloSat* (Kaaret et al. 2019), *eROSITA* (Predehl et al. 2021)) have been put into service for these emission observations. Das et al. 2019a detected the super-virial phase in the MW CGM using XMM-Newton observation towards the Blazar 1ES 1553+113 ($l = 21°.91, b = 43°.96$) in emission. They fitted the total emission from the CGM with a two-temperature thermal plasma model. Assuming solar metallicity, their best-fitted values of two temperatures are $0.15-0.23$ and $0.41-0.72$ keV. Gupta et al. 2021 used *Suzaku* and *Chandra* observations of the MW halo to characterize the emission along four sightlines. Again, for solar metallicity, they found the

two temperatures to be $0.176 \pm 0.008$ keV and 0.65–0.90 keV. Bhattacharyya et al. 2023 used *XMM-Newton* observation towards the Blazar Mrk 421 ($(l = 179°.83, b = 65°.03)$) and 5 other sightlines near the Blazar field to study the emission from MW CGM. Using solar metallicity to analyze their observation, they found the temperature of two phases to be 0.14–0.192 keV and 0.66–1.14 keV. Bluem et al. 2022 used *HaloSat* all-sky survey to study the emission from the MW halo. Assuming 0.3 solar metallicity, they obtained the average temperature of $0.179^{+0.005}_{-0.007}$ and $0.184 \pm 0.009$ keV for northern and southern virial gas, respectively. For the super-virial gas, the average temperature is $0.69^{+0.05}_{-0.06}$ and $0.75 \pm 0.08$ keV, respectively. Ponti et al. 2023 observed the MW halo in the eFEDDS field using *eROSITA*. Their best-fit metallicity was 0.068 $Z_\odot$ for the virial phase, much less than the value of 0.3 $Z_\odot$ that is often used in CGM studies. However, they used 0.7 solar metallicity for the super-virial gas. Sugiyama et al. 2023 studied emission from the MW Halo with *Suzaku* using 130 observations. They used solar metallicity in the super-virial phase for their analysis. Lastly, Gupta et al. 2023 analyzed the X-ray emitting gas in the CGM using 230 *Suzaku* archival observations. Assuming solar metallicity, they found the temperature of virial and super-virial gas to be $\sim 0.2$ and $\sim 0.4 - 1.1$ keV, respectively. All these observations show that the super-virial hot phase of MW CGM, as observed in emission, is ubiquitous across the sky. While a 2-temperature model provided the best fit to all these data, there is clearly some scatter in the temperature of both virial and super-virial phases, suggesting a multiphase nature of the CGM.

Recently Fuller et al. 2023 observed and analyzed the emission from the Orion-Eridanus Superbubble (OES) and found the temperature and EMs of the gas in this region to be similar to the bulk gas in the CGM elsewhere. This result suggests that the super-virial gas is likely associated with core-collapse SNe-driven outflow from the galactic disk. In this paper, we model the super-virial gas ($\sim 10^7$ K) *and* the virial gas ($\sim 10^6$ K) with disk-like profiles, in addition to the extended CGM at the virial temperature. The unique feature of our model is the extraplanar disk-shaped region containing *both* super-virial and virial gas. These two gas phases need not be in hydrostatic equilibrium and are likely to be in a dynamical state. We explain the physical nature of the co-existence of these two phases around the disk, using an idealized numerical simulation of star-formation-driven outflows in an MW-type galaxy. This chapter is organized as follows. Section 2.2 introduces our model, followed by a description of the simulation set-up and results in Sections 2.3 and 2.4. We discuss the implications in Section 5.4 and finally summarise our work in Section 4.7.

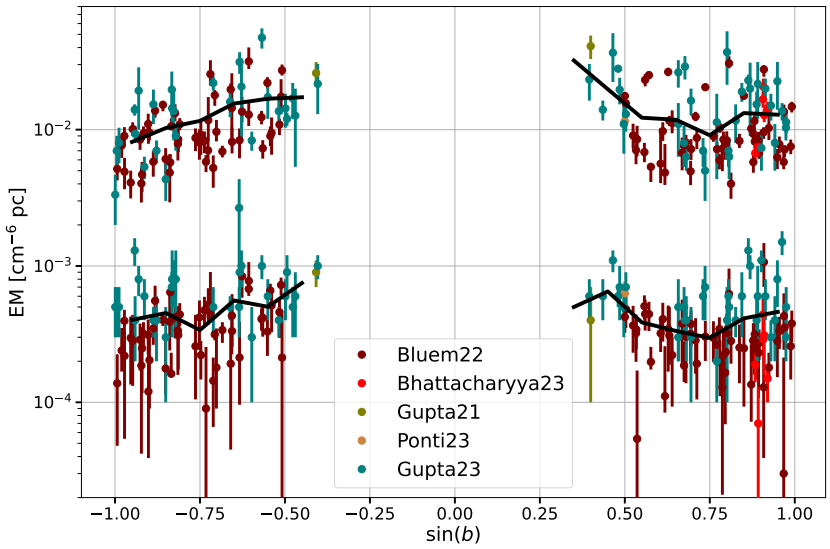



Figure 2.1: The Emission Measure (EM) data from various authors (Bluem et al. 2022,Bhattacharyya et al. 2023, Gupta et al. 2021,Ponti et al. 2023, and Gupta et al. 2023) is plotted as a function of $\sin(b)$, where $b$ is the galactic latitude. The figure contains two sets of data. The top set of points, with EM $\approx 10^{-3} - 10^{-1}$ cm$^{-6}$ pc, corresponds to the virial phase while lower data points with EM $\approx 10^{-5} - 10^{-3}$ cm$^{-6}$ pc correspond to the super-virial phase. The solid black lines show the mean EM calculated in a bin size of $\Delta\sin(b) = 0.1$ for both virial and super-virial datasets. Note the anti-correlation between EM and $\sin(b)$ for both virial and super-virial phases as can be seen by the trend in the black solid lines.

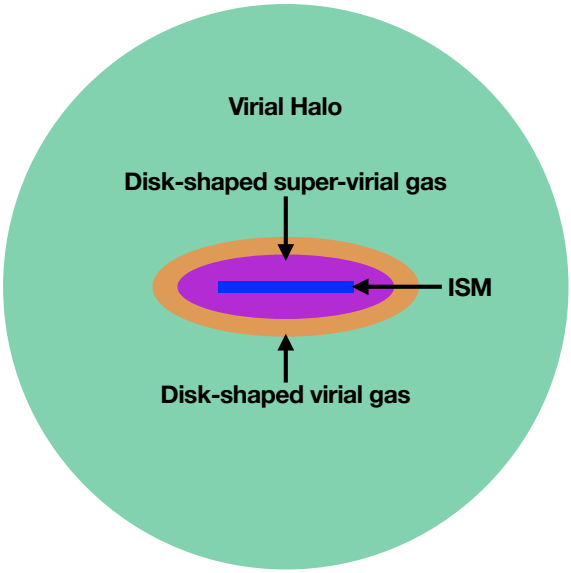



Figure 2.2: The cartoon representation of the structure of the gaseous components of the MW. The blue region in the center shows the Interstellar medium (ISM). The magenta and the yellow regions show the extent of the super-virial and virial temperature-emitting disks, respectively. The extended region in green shows the Galactic virialized Halo. Note that the size of different regions is not to scale; it simply represents the overall structure of the extraplanar gas around the MW.

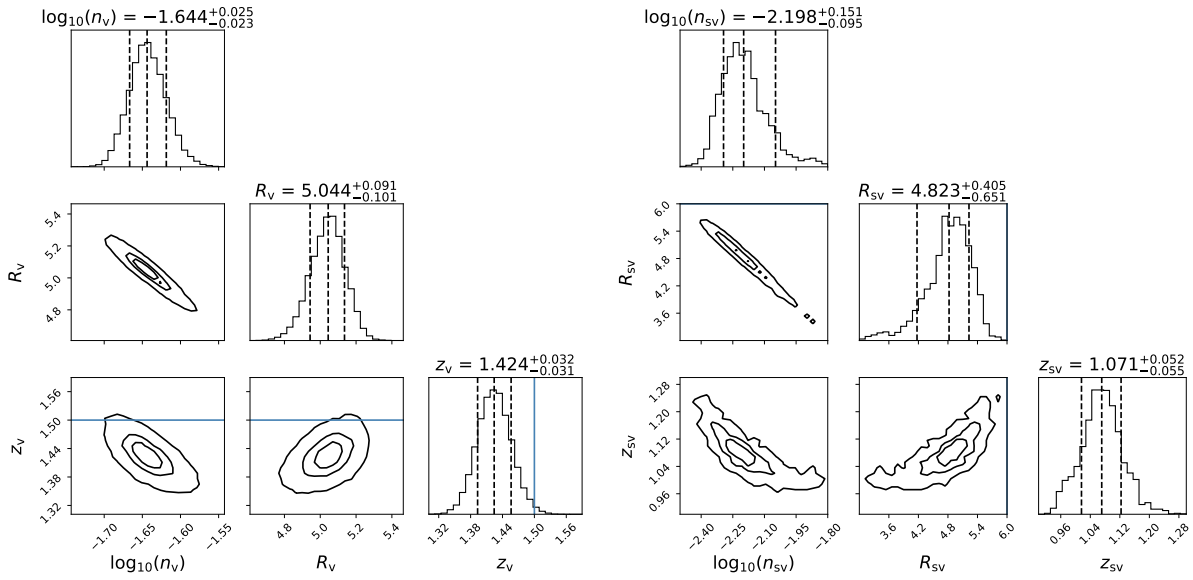



Figure 2.3: This figure shows the results of the MCMC analysis. The *left* and *right* panel shows the corner plot of parameters for virial and super-virial phases, respectively. The three vertical dashed black lines in the 1-D histogram mark the $16^{\text{th}}$, $50^{\text{th}}$, and $84^{\text{th}}$ percentiles of the samples. The three contour levels plotted with black solid lines contain 32, 64, and 96 percent of the samples, respectively. The blue line shows the initial guess value and is visible only in the case of $z_{\rm v}$ as the guess values for other parameters are out of the plot ranges. The values on the top of each 1-D histogram show the $50^{\text{th}}$ percentile value (median) and the error shown corresponds to $16^{\text{th}}$ and $84^{\text{th}}$ percentile which is equal to $1\sigma$ error if the resulting 1-D histogram is Gaussian which is the case for most of the parameters. We performed the analysis using 32 walkers and 50,000 steps with Gaussian priors for all the parameters. We ensured the convergence of samples as the total number of steps is larger than 50 times the autocorrelation time. Note that the width in the Gaussian prior (see Table 2.1) is sufficiently larger than the width in the resulting histogram of the respective parameters. This shows that the resulting values are well-constrained.

## 2.2 Disk-shaped profile of the virial and super-virial gas

To begin with, we seek clues for the possible geometric shape of the region occupied by the 'SV emission' phase. Kaaret et al. 2020; Locatelli et al. 2024; Dutta et al. 2023 and Nakashima et al. 2018 have argued that the CGM emission is best described by a disky extraplanar component. In figure 2.1 we have plotted the observed Emission Measures (EM) of the virial and the super-virial temperature gas as a function of $\sin(b)$, where $b$ is the Galactic latitude for various observations. The black solid lines show the mean EM for both virial and super-virial phases calculated in a bin size of $\Delta\sin(b) = 0.1$. We see an anticorrelation of EM with $\sin(b)$, as expected for a disk-shaped region, for both virial and super-virial phases, as depicted by the trend in black solid lines. We have performed Kendall's tau test to quantify the anticorrelation. For the virial phase, we obtain $\tau = -0.20$ and a p-value $= 10^{-4}$, where $\tau$ is the correlation coefficient and the p-value signifies the probability of the null hypothesis. $\tau$/p-value $= 1/0$ signifies strong correlation while $\tau$/p-value $= 0/1$ signifies no correlation. For the super-virial phase, we obtain $\tau = -0.18$ and p-value$= 5 \times 10^{-4}$. The finite negative $\tau$ values signify the anticorrelation.

Bluem et al. 2022 and Bhattacharyya et al. 2023 have shown that the EMs of the super-virial and virial phases are correlated, suggesting that they are co-spatial. Thus, it appears that both virial and super-virial phase emission may arise in an extra-planar disk around the Galactic disk. A disk-like profile of the super-virial phase is also a natural outcome of the stellar activities in the disk of the MW, as we show in §4. However, in order to understand the virial phase absorption, an extended diffuse component is required (Gupta et al. 2012, 2014).

With this in mind, we set up our geometric model as shown in Figure 2.2. It shows a schematic representation of our model of the extra-planar gas around the MW. The blue slab shows the Galactic ISM. The regions with magenta and yellow colors show the extent of the super-virial and virial disks, respectively. The extended spherical green region shows the virial temperature CGM in the Galactic Halo. Note that the regions in the Figure are not to scale and are only schematic in nature. In what follows, we determine the parameters of these three geometric shapes.

First, let us consider the volume-filling diffuse gas in the Galactic halo at the virial temperature. Consider the halo gas in hydrostatic equilibrium with the dark matter potential of the MW, for which we use the NFW profile (Navarro et al. 1997). We further assume the halo gas to be at a uniform temperature of $3 \times 10^6$ K (isothermal sphere), for simplicity. Although other halo profiles are also possible (Faerman et al. 2020; Voit 2019; Maller & Bullock 2004; Miller & Bregman 2013), we use the simplest model to minimize the number of free parameters.

| **Parameter** | **Virial (V)** | **Super-virial (SV)** |
|---|---|---|
| **Allowed Range** | | |
| $\log_{10}[n\,(\mathrm{cm}^{-3})]$ | $[-5, -0.1]$ | |
| $R$ (kpc) | $[1, 15]$ | |
| $z$ (kpc) | $[0.1, 10]$ | |
| **Initial Guess** | | |
| $\log_{10}[n\,(\mathrm{cm}^{-3})]$ | $-2.0$ | $-3.0$ |
| $R$ (kpc) | 4.5 | 6.0 |
| $z$ (kpc) | 1.5 | 2.0 |
| **Gaussian Prior (Center / Half Width)** | | |
| $\log_{10}[n\,(\mathrm{cm}^{-3})]$ | $-1.5$ / 5 | $-2.5$ / 5 |
| $R$ (kpc) | 5.0 / 10 | 4.0 / 10 |
| $z$ (kpc) | 1.0 / 10 | 1.5 / 10 |
| **MCMC Results** | | |
| $\log_{10}[n\,(\mathrm{cm}^{-3})]$ | $-1.64^{+0.03}_{-0.02}$ | $-2.20^{+0.15}_{-0.10}$ |
| $R$ (kpc) | $5.0^{+0.1}_{-0.1}$ | $4.8^{+0.4}_{-0.7}$ |
| $z$ (kpc) | $1.42^{+0.03}_{-0.03}$ | $1.07^{+0.05}_{-0.06}$ |

Table 2.1: Parameters, allowed ranges, Gaussian priors, and MCMC results for the virial (V) and super-virial (SV) phases. The reported values correspond to the median ($50^{\mathrm{th}}$ percentile) with $1\sigma$ uncertainties given by the $16^{\mathrm{th}}$ and $84^{\mathrm{th}}$ percentiles.

We obtain the following equation for the halo gas density profile

$$n(r) = n_0 \exp\left[-f_0\left\{1 - \frac{\ln(1+x)}{x}\right\}\right], \tag{2.1}$$

where $x = r/r_s$ ($r_s$ is the scale radius in the NFW profile), $n_0$ is the density at the centre and $f_0 = G\mu m_p M_{\rm vir}/[k_B T r_s\{\ln(1+C) - C/(1+C)\}]$ ($C$ being the concentration parameter). We use $M_{\rm vir} = 10^{12}\ M_\odot$, $C = 12$, $r_{\rm vir} = 260$ kpc (Klypin et al. 2002) and $T = 3\times10^6$ K, for which $f_0 = 3$. The central density $n_0$ is obtained from the normalization condition that the total baryonic mass in the CGM ($1.2 \times 10^{11}\ M_\odot$) is 75% of the total baryonic mass in MW (Prochaska & Zheng 2019), assuming a cosmic baryonic fraction of 0.16. This gives $n_0 = 8.8 \times 10^{-4}$ cm$^{-3}$.

With this, we calculate the Emission Measure ($EM = \int n_e n_H dl$) of the virial temperature halo gas. We used $\mu = 0.67$, $\mu_e = 1.18$ and $\mu_H = 1.22$ such that $n\mu = n_e\mu_e = n_{\rm H}\mu_{\rm H}$. We then subtract the halo EM from the total EM of the virial temperature gas to determine the EM from the disk component. We note that the halo contributes only 30% on average to the total EM of the virial phase.

The disk-like model for the extra-planar profile of the virial temperature gas is given by:

$$n_V(R,z) = n_V\ \exp\left(-\frac{|z|}{z_V}\right) \times \begin{cases} 1; & R < R_V \\ \exp\left(-\left[\frac{R-R_V}{2}\right]\right);\ & R \geq R_V\,. \end{cases} \tag{2.2}$$

where $n_V$ is the total number density at the Galactic center for the virial phase, $z_V$ is the scale height, and $R_V$ is the scale radius. Note that the density profile is exponential in the $z$-direction only below $R_V$ while above $R_V$, it is exponential in both $R$ and $z$ directions, where $R$ and $z$ are the cylindrical coordinates.

Similarly, we model the extra-planar super-virial gas profile with a disk-like shape, as follows:

$$\begin{aligned} n_{SV}(R,z) = \quad & n_{SV}\ \exp\left(-\frac{|z|}{z_{SV}}\right) \\ & \times \begin{cases} 1; & R < R_{SV} \\ \exp\left(-\left[\frac{R-R_{SV}}{2}\right]\right);\ & R \geq R_{SV} \end{cases} \end{aligned} \tag{2.3}$$

where $n_{SV}$ is the total number density at the Galactic center for the super-virial phase, $z_{SV}$ is the scale height, and $R_{SV}$ is the scale radius.

To determine the parameters of the disk profiles of both phases, we perform MCMC

analysis using *emcee* (Foreman-Mackey et al. 2013) for the observed EMs reported in the literature (Das et al. 2019a; Gupta et al. 2021; Bluem et al. 2022; Ponti et al. 2023; Gupta et al. 2023 and Bhattacharyya et al. 2023). To obtain the parameters for the extra-planar virial gas, we subtract the EM contribution from the extended halo virial gas profile (see Equation 2.1, isothermal profile) and use the residual EM values as the observed data, as discussed earlier in the section. We assume 0.3 solar metallicity for the virial phase (Toft et al. 2002,Sommer-Larsen 2006, Prochaska et al. 2017) and solar metallicity for the super-virial phase (motivated by the fact that the super-virial phase is likely the result of outflows from core-collapse SNe in the MW disk). We accordingly scale the observed EM values as $\mathrm{EM(Z)} = \mathrm{EM(Z_\odot)} \times (\mathrm{Z/Z_\odot})^{-1}$. We performed MCMC analysis separately for the extra-planar virial and super-virial gas. We use Gaussian priors for all the parameters with 32 walkers and 50,000 steps. We ensured the convergence of the samples as the number of steps (50,000 in this case) is larger than 50 times the autocorrelation time. In Table 2.1, we show the allowed range, initial guess value, line center, and width of the Gaussian priors, and the results of all the parameters in MCMC analysis for both virial and super-virial phases. Figure 2.3 shows the corner plot of MCMC analysis. We find that the parameters of the extra-planar profiles for both SV and virial phases are similar, with comparable values for the scale heights and scale radii, although densities are different. The virial phase emission is significantly brighter (higher EM) compared to the SV phase, resulting in a higher density for the virial phase.

Using the results of the MCMC analysis for the disk-shaped virial and super-virial gas and the extended volume-filling halo virial gas using Equation 2.1, we calculated the EMs for both virial and super-virial phases along the observed lines of sight. Figure 2.4 shows the EM correlation of the two phases. The black open circles show the correlation with the halo virial profile, along with extra-planar super-virial gas. The blue circles correspond to the extra-planar virial and super-virial gas (and no halo gas). The circles in cyan show the correlation in the presence of a halo virial, extra-planar virial, and extra-planar super-virial gas. The observed EM from various authors is plotted with different colors; Bluem et al. 2022 in maroon, Gupta et al. 2023 in green, Bhattacharyya et al. 2023 in red, Gupta et al. 2021 in olive, Ponti et al. 2023 in peru, and Das et al. 2019a in magenta.

It is clear from Figure 2.4 that the model without extra-planar virial gas (black open circles) cannot explain the observed data; a disk-like extraplanar region with virial

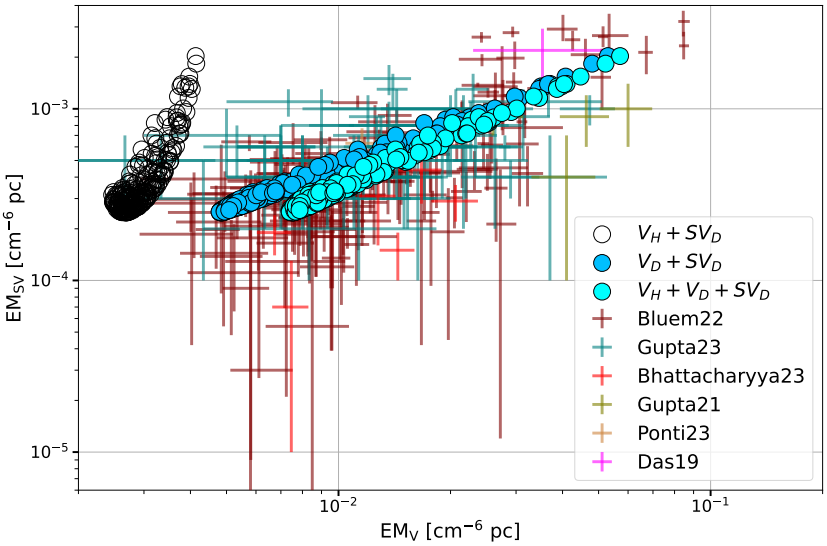



Figure 2.4: The correlation between the Emission Measure (EM) of the virial temperature gas and the EM of the super-virial temperature gas based on our models overplotted on observed EM. The black open circles show the EM correlation for the virial halo profile and super-virial gas in the disk. The blue circles show the EM correlation with the virial and super-virial gas around the disk. The circles in cyan correspond to the virial gas in the halo + the virial gas in the disk and the super-virial gas in the disk. The EM values from our model are plotted for the observed lines of sight. The observational data points from various authors are shown in other colors with error bars. All the observed EM values are rescaled to the metallicity of 0.3 solar for virial gas and solar for super-virial gas. The narrow range in the black points compared to cyan points along the X-axis shows the importance of having a 'disk-shaped' virial phase profile.

temperature gas is required. The observed correlation is well explained by the extra-planar super-virial and virial gas model with an extended virial halo profile (cyan-colored circles). The total mass in the disk-like extra-planar region (Equation 2.3, 2.2) is $M = 10^8 \times n_0 z_0 (8 + 4R_0 + R_0^2)$ $M_\odot$, where $n_0$ is the central density in $cm^{-3}$, $z_0$ and $R_0$ are the scale height and scale radius in kpc respectively. We calculated the mass in the extra-planar virial and the super-virial phase using the best-fit parameters from Table 2.1. We obtain $1.7 \times 10^8$ $M_\odot$ and $3.5 \times 10^7$ $M_\odot$ for the two phases, respectively. Note that this is insignificant compared to the mass of the virial gas in the halo, and, therefore, does not affect the hydrostatic equilibrium that was assumed to obtain Equation 2.1. The baryonic mass of the CGM is dominated by the extended, diffuse gas filling the Galactic halo.

## 2.3 Simulation setup

In §2, we determined the location of the virial and super-virial phases in emission, measured the parameters of the extra-planar disks, measured the density profiles, calculated the EMs, and determined masses in these phases. This answers the question "where is the hot gas?". However, this does not tell us why. A likely answer is the feedback from the stellar disk. To understand the origin of the SV-phase gas, we have built a model of the outflows from the OB associations in the MW disk. We perform a hydrodynamical simulation of outflows from the MW disk and show that the extra-planar super-virial gas may indeed arise from the feedback.

We performed our simulation in 2-D Cylindrical coordinates ($R$ and $z$), using the publicly available hydrodynamical code PLUTO (Mignone et al. 2007). Our initial Galactic setup is similar to Sarkar et al. 2015 with a rotating ISM and non-rotating isothermal CGM, in the gravitational field of a Navarro-Frenk-White halo (Navarro et al. 1997) and Miyamoto-Nagai disk (Miyamoto & Nagai 1975). The temperature, density, and pressure initial conditions are as shown in Figure 2.5. The cold ISM is at $T = 4 \times 10^4$ K and the CGM is at $T = 3 \times 10^6$ K. The temperature gradient, as shown in Figure 2.5 allows for a stable thermal configuration, for the gravitational forces to be supported by gas pressure and rotation, as discussed in Sarkar et al. 2015. We use the HLL Riemann solver and resolve the time using the Runge-Kutta 2nd order scheme.

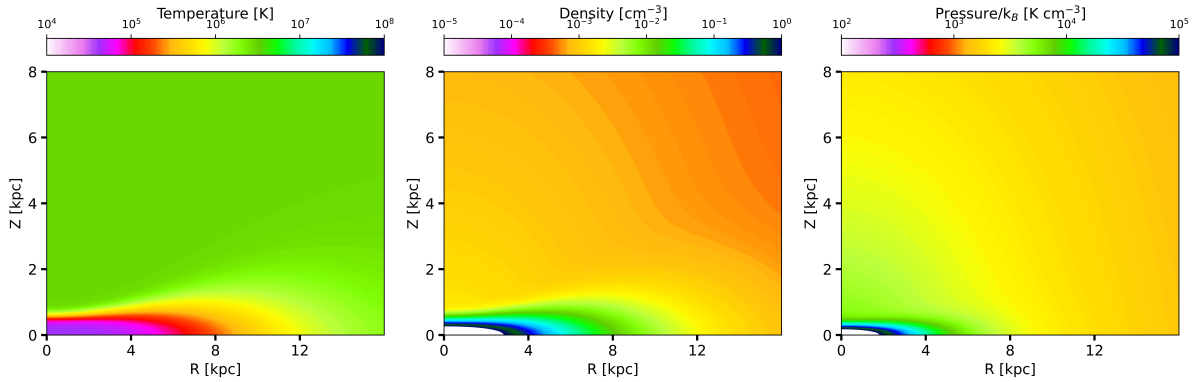



Figure 2.5: The initial temperature, density, and pressure maps. There are temperature and density gradients in both $R$ and $z$ directions, as a result of the hydrostatic equilibrium in which the gravitational force is balanced by gas pressure combined with the rotation of the gas.

*Grid*: We define our simulation box from 10 pc to 30 kpc along the $R$ direction. We take a uniform grid from 10 pc to 10 kpc (450 grid points) and a logarithmic grid from 10 kpc to 30 kpc (62 grid points). In the $z$ direction, we define our computational box from 1 pc to 30 kpc with a uniform grid from 1 pc to 10 pc (20 grid points) and then logarithmic grids from 10 pc to 30 kpc (236 grid points).

*Boundary condition*: We use reflective boundary conditions for inner boundaries in both $R$ and $z$ directions. For the outer boundary in both $R$ and $z$, pressure and density values are set to initial equilibrium values, whereas velocity values are copied from the nearest active zones. We set an 'axisymmetric' boundary condition in the $\phi$ direction.

*Cooling*: We do not allow the Galactic ISM ($R < 15$ kpc and $z < 2$ kpc) to cool. However, we allow the injected and CGM gas to cool, using a radiative cooling function. The metallicity for the injected material and CGM gas is set at $1\,Z_{\odot}$ and $0.3\,Z_{\odot}$ respectively. We set the cooling to be *TABULATED* and use the radiative transfer code *CLOUDY* (Ferland et al., 2017) to obtain the cooling rates.

Various studies have shown that star-forming regions of the MW are not concentrated in the Galactic center but are distributed in rings in the Galactic plane with a peak of star formation around 4–5 kpc (e.g. Elia et al. 2022). Motivated by these observations, we injected mass and energy into the Galactic disk rather than solely in the Galactic center. The star formation rate density has been measured in concentric rings of widths 0.5 kpc

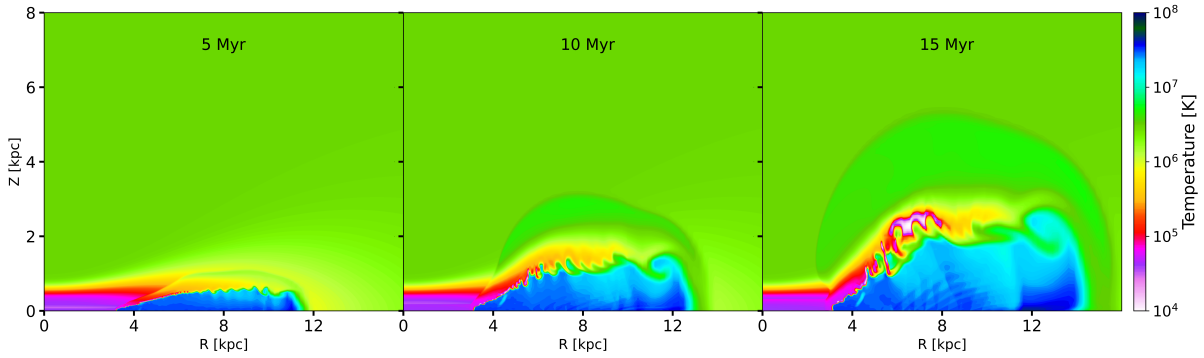



Figure 2.6: Temperature maps at three epochs, at 5, 10 and 15 Myr, from left to right. As the energy is injected in the disk, the hot SV-temperature gas is pushed up, generating an extraplanar region (shown in blue). Above this region, a virial temperature extraplanar region is formed (shown in yellow-green). Shock heating of the halo gas leads to another hot region at higher $z$ (shown in light green).

by Elia et al. 2022 (see their Figure 6). For our calculation, we use these measurements in rings up to 10 kpc. We computed the star formation rate (SFR) in each bin using the observed star formation rate density and the relevant area of the ring. The estimated SFR in the rings, starting from the center, is 0.035, 0.018, 0.011, 0.016, 0.015, 0.038, 0.048, 0.093, 0.174, 0.201, 0.170, 0.158, 0.184, 0.125, 0.079, 0.074, 0.076, 0.068, 0.045 and 0.055 $M_\odot\,yr^{-1}$ respectively.

*Energy and mass injection*: We inject mass and energy in 20 cylindrical rings (of height 10 pc and width 0.5 kpc) up to 10 kpc centered around $0.25, 0.75, ...9.25$ and 9.75 kpc. The amount of mass and energy injected in each bin depends on the SFR of the bin (as mentioned above). Note that this is similar to Vijayan et al. 2018 except that we use the observed SFR in each bin from Elia et al. 2022, whereas Vijayan et al. 2018 used gas density to infer the SFR using the Kennicutt-Schmidt relation (Kennicutt 1998). Assuming that each SN releases $10^{51}$ erg of energy, the relation between mechanical luminosity and SFR is,

$$\mathcal{L} = 10^{51}\,\mathrm{erg} \times n_{\mathrm{SN}} \times \epsilon \times \mathrm{SFR}(M_\odot\,yr^{-1}) \tag{2.4}$$

where $n_{\mathrm{SN}}$ is the number of SNe per unit mass of the stars formed, and $\epsilon$ is the heating efficiency of the gas. Assuming Salpeter IMF (Salpeter 1955) between lower and upper limit on stellar mass of 0.1 and 100 $M_\odot$ respectively, we get $n_{\mathrm{SN}} = 7.6 \times 10^{-3}$. Thus, the

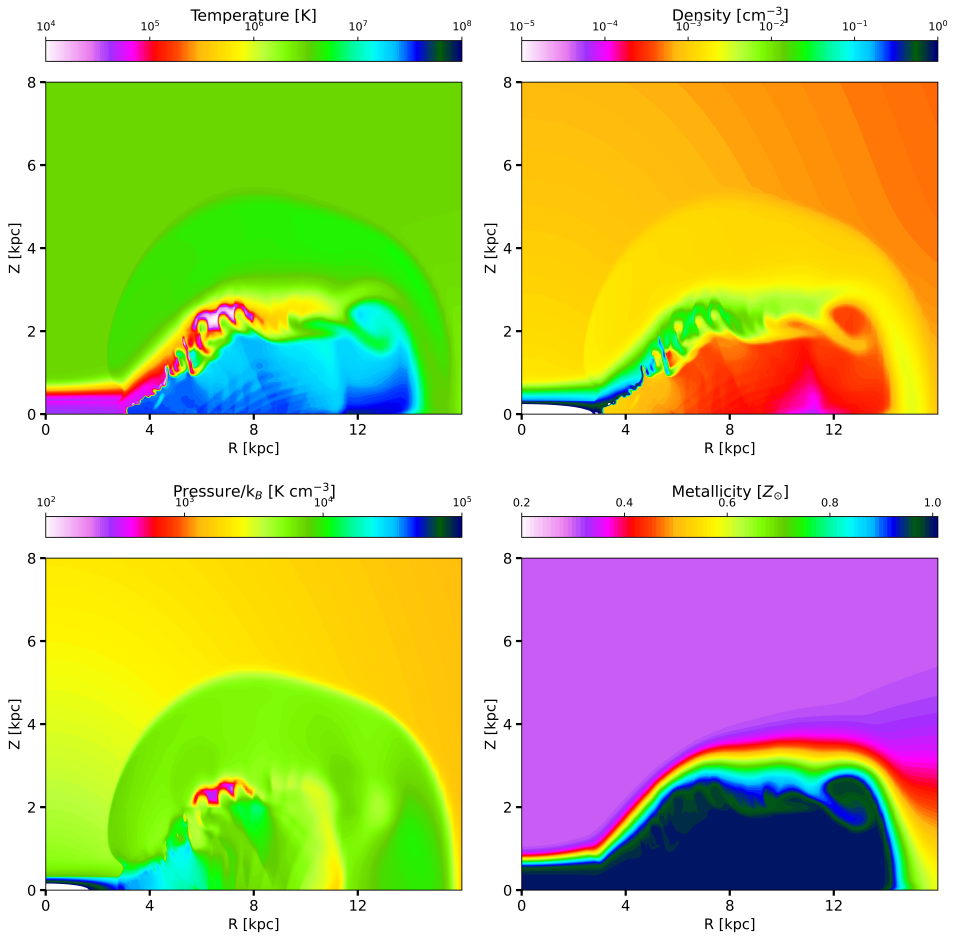



Figure 2.7: This figure shows the simulation results at 15 Myr. The *top left* and *right* panels show the temperature and particle number density maps, respectively. The *bottom left* and *right* panels show the pressure and metallicity maps, respectively.

relation becomes,

$$\mathcal{L} = 2.4 \times 10^{41} \mathrm{erg\,s^{-1}} \times \epsilon \times SFR(M_\odot\, yr^{-1}) \tag{2.5}$$

We assume $\epsilon = 0.3$, which takes into account the radiative loss of energy (Vasiliev et al., 2015; Yadav et al., 2017). This quantifies the amount of energy being injected in each bin. We inject total energy in the thermal form.

The corresponding mass injection rate is quantified by the 'returned fraction' of stellar mass that is returned to the ISM during the stellar evolutionary process. We use a value 0.1 for this returned fraction (Tinsley, 1980) and inject mass in each bin with the rate $\dot{M}_{\rm inj} = 0.1 \times \mathrm{SFR}$. We continuously inject mass and energy for 30 Myr.

## 2.4 Simulation Results

We post-process the simulation data to characterize the extra-planar super-virial and virial gas. In Figure 2.6, we show the temperature evolution at three epochs (5, 10, and 15 Myr). For the Salpeter Initial Mass Function (IMF) (Salpeter 1955), the average mass of supernova progenitors is $\approx 18$ $M_\odot$ (using a threshold of 8 $M_\odot$ for SN progenitors, and stellar masses being distributed from 0.1 to 100 $M_\odot$). The main sequence lifetime of a $18M_\odot$ progenitor star is $\sim 15$ Myr. In other words, the typical time scale for the effects of star-formation-driven perturbations to manifest themselves is $\approx 15$ Myr. This estimate has motivated our choice of epochs to be showcased here.

The blue region in Figure 2.6 shows the hot injected gas with super-virial temperature ($T \geq 5 \times 10^6$ K); as time evolves, the SV gas phase extends to higher $z$ values. The extra-planar region at the SV temperature is thus formed, with a height of about 1 kpc at 10 Myr and about 2 kpc at 15 Myr.

As the injected gas pushes up from the ISM, it heats the gas initially at $T = 10^5$ K (red region in the left panel of Figure 2.5), eventually reaching $T \approx 10^6$ K, in 10 Myr (yellow–green region in Figure 2.6. We identify this extraplanar region with the disk emitting at the virial temperature. At even larger heights, we see a 'light green region' at $T = (4 - 5) \times 10^6$ K. This region is discussed further in §4.1.

Figure 2.7 shows the details of our results at 15 Myr with temperature, particle number density, pressure, and metallicity maps. As in Figure 2.6, we see that the SV hot phase is extended out to about 2 kpc (light blue region in the top left panel). The density in this region is $\approx 10^{-3}$ cm$^{-3}$ (as seen in the top right panel). The region above this SV-phase, identified with an extraplanar region with virial temperature (yellow-green region in the top left panel), has a higher density of $\approx 10^{-2}$ cm$^{-3}$ (green region in the top right panel).

The bottom left panel shows the pressure map. We clearly see the high-pressure regions beyond $R \approx 4$ kpc, showing outflow from the disk. The final pressure is significantly higher than the initial pressure, showing that the virial and super-virial gas in the disk is out of hydrostatic equilibrium and dynamically evolving. Note that we do not see strong outflows from the inner regions ( 0–3 kpc) of the disk as compared to outer regions. The

reason is that the SFR has a Gaussian-like profile along the disk with peak SFR occurring around $\approx$ 4–5 kpc. The other reason is that the ambient density in the inner regions is higher than that in the outer regions (see middle panel of Figure 2.5). The high density in the inner regions provides high resistance to the outflowing gas, whereas the outflow can penetrate the low-density environment in outer regions for approximately the same SFR.

The bottom right panel shows the metallicity map. The enriched and high-metallicity gas in the outflow mixes with the low-metallicity ambient gas, thus contaminating the chemical composition of the injected gas. We have used tracers for the CGM gas and the injected gas to trace the corresponding metallicity. Tracers follow the advection equation for the respective gases. Thus, the tracer tracks the gas and accounts for the amount of mixing of the gases with different tracer values. The tracer value in the mixed gas is the mass-weighted value of the individual gas tracers; thus, it can be used as a proxy for metallicity. Recall that the CGM metallicity is assumed to be $0.3\,Z_{\odot}$ while the injected material has solar metallicity. The map shows that the outflow lifts the high metallicity gas out to the extraplanar region with a height of about 2 kpc; this is the region where we have the SV hot gas. Thus, we see that the hot gas is metal-enriched. Beyond the extraplanar region, we see the mixing of the high metallicity gas from the outflow and the low metallicity CGM gas, with the average metallicity decreasing with $z$. Beyond $z \approx 4$ kpc, we see the low-metallicity of the CGM, without any mixing from the outflow.

### 2.4.1 Hot gas in the extra-planar region

The temperature map presented in Figure 2.7 shows the gas in the extra-planar region to have a range of temperatures. It is also instructive to compare the metallicity map (bottom-right panel of the same Figure) with the top-left panel to understand the origin of gas with various temperatures within this extra-planar region. Recall that the initial gas profile has warm ($\sim 10^5$ K) gas hovering above the disk, joining smoothly into the virial gas in the halo (Figure 2.5). This parcel of gas is seen in red color in the metallicity map. As the collective gaseous disturbances triggered by SNe rise above the disk, this warm gas gets heated to temperatures comparable to that of the virial gas in the halo, as shown by the light-green colored gas in the temperature map. This likely corresponds to the extra-planar virial temperature gas discussed in Section 2.2. A similar temperature

structure of the outflowing gas from a disk-wide star formation process was also seen in Vijayan et al. 2018.

The temperature map (top-left panel of Figure 2.7) also shows an additional hot region at $z \approx 4$–$6$ kpc with $T = (4-5) \times 10^6$ K (shown with light green colour). We see in the bottom right panel of Figure 2.7 that this region has the original metallicity of the CGM, with no mixing from the outflow. Thus, the hot gas in this region is not the hot SN-driven outflowing gas. We find that this phase has been created by mild shock heating, as the outflowing gas hits the virial gas in the halo, with speed $\approx 300$–$400$ km s$^{-1}$ (note the advancement of the outflow in $z$-direction between the snapshots shown in Figure 2.6). Given the virial temperature of the halo gas, the shock has a low Mach number (of order $\approx 2$). The corresponding density jump is $\approx 2$–$3$; this is consistent with the density variations seen in the top-right panel of Figure 2.7. The corresponding temperature jump is also by a factor of $\approx 2$, as seen in the temperature map.

## 2.5 Discussion

For our fiducial model of the halo density profile, we have taken $M_{\rm vir} = 10^{12}\,M_\odot$, $C = 12$ (Klypin et al. 2002) and $T = 3 \times 10^6$ K. However, there is a scatter around these values. In order to determine how these parameters affect our results of the disk parameters (scale height, scale radius, and central density), we varied the halo parameters. We considered the following range in these parameters; $M_{\rm vir} = (0.9-1.2) \times 10^{12}\,M_\odot$, $C = 10-14$ and $T = (2-3) \times 10^6$ K. As a result of these variations, the scale height changes by $+0.4/-0.3$ kpc from the fiducial value of 1.4 kpc. The scale radius changes by $+0.1/-0.9$ kpc from the fiducial value of 5.0 kpc. The central density changes by $+0.8/-0.5\,(\times 10^{-2}$ cm$^{-3})$ from the fiducial value of $2.3 \times 10^{-2}\,$cm$^{-3}$. As such, the variation in the halo parameters does not change the results of the disk parameters significantly.

To test the convergence of our simulation, we performed a higher-resolution run. We doubled the resolution compared to the resolution of $(R \times z)$ $512 \times 256$ in our fiducial run. We found that the main results show essentially no difference, signifying convergence; they were similar to the fiducial runs shown in Figure 2.7.

With our model, we have demonstrated the presence of extra-planar super-virial and virial temperature gas around the Galactic disk. The model also has higher density in

the virial temperature disk than in the SV disk, as observed (§2), and the likely high metallicity of the super-virial gas. In the initial discovery papers, the CGM was modeled as a two-temperature plasma in both absorption and emission studies (§1). Over the years, it was realized that the CGM actually has a range of temperature even in the X-ray band (Bhattacharyya et al., 2023; McClain et al., 2024b). The model we present here naturally explains this range of temperature. We have shown that the CGM in the vicinity of the disk has these characteristics for $\sim$ 5–15 Myr, which is the timescale of manifestations of SNe-triggered outflows after the onset of star formation. It then follows that such is likely to be the case even in the case of self-sustained star formation in the disk for a much longer time.

In this paper, we have provided a possible explanation for the super-virial phase that has been detected in emission studies. As noted in the Introduction, a few lines of sight have also detected the hot gas in absorption. The observed Oxygen column densities, are $(0.8 - 5.7) \times 10^{17}$, $(4.9 - 12.9) \times 10^{17}$, and $(2.2 - 6.8) \times 10^{16}$ cm$^{-2}$ along IES 1553+113 (Das et al. 2019b), Mrk 421 (Das et al. 2021), and NGC 3783 (McClain et al. 2024b) respectively. Note that we calculated the Oxygen column density from the observed column density of OVII and OVIII, assuming Collisional Ionization Equilibrium (CIE) at the observed temperatures along the respective lines of sight. Can we explain the column density of the absorbing hot gas with our model? To answer this question, we estimated the Oxygen column density along three observed lines of sight using our disk-like model for the super-virial phase. The model predicted total column densities of $1.1 \times 10^{19}$, $3.8 \times 10^{18}$ and $1.2 \times 10^{19}$ cm$^{-2}$ along IES 1553+113, Mrk 421 and NGC 3783 respectively.

Therefore, to match the predicted and observed column densities, we need the Oxygen mass fraction ($f_O$) of at least 0.2, and 0.05, along IES 1553+113 and NGC 3783, respectively. This is much higher than the Solar Oxygen abundance of $4 \times 10^{-4}$ (Asplund et al. 2009). Incidentally, the Oxygen mass fraction in the typical supernova ejecta is $\sim 0.1$ (Nomoto et al. 2006), which is comparable to that required to explain the observations along two sightlines. However, the Oxygen mass fraction is likely to be lower due to the mixing of the gas from supernovae ejecta ($\alpha$-enriched) and the gas in the CGM with sub-solar metallicity. The Oxygen column density along Mrk 421 is so high that it requires exceptional explanation, and our disk model cannot explain such a high column density. To conclude, it is difficult to explain the absorption observations with our model, and therefore, the origin of the 'SV emission' phase is likely to be different than that of

the 'SV absorption' phase, and they should be treated separately.

## 2.6 Summary

In this work, we have proposed a new model for the origin and extent of the gas emitting at the super-virial temperature ($\sim 10^7$ K) in the CGM of the Milky Way. We suggest that the origin of the super-virial gas observed in emission is connected to outflows from star-forming regions in the MW disk. A disk-like profile is thus naturally expected from the extended outflows in the disk. Moreover, we posit that this super-virial disk profile co-exists with a disk-shaped profile of virial gas. Together they can explain the Emission Measure (EM) correlation of the virial ($\sim 10^6$ K) and the super-virial phase ($\sim 10^7$ K) (see Figure 2.4).

To support our model, we have performed a hydrodynamical numerical simulation of an MW-type disk in which star-forming regions are located. Our simulation results show that the extra-planar super-virial gas has roughly a 'puffed-up' disk-like feature, along with a similarly shaped region for the virial gas. Moreover, the composition of the super-virial gas is shown to be unmixed with the halo CGM gas and is thus likely to retain its high metallicity signature of SNe-enriched gas, which are at the root of this super-virial phase.

# Chapter 3

# Can Supernovae from Runaway Stars Mimic the Signs of Absorbing "Supervirial" Gas?

Based on :
Bisht, M. S., Banerjee, P., Nath, B. B., & Shchekinov, Y. 2024, ApJ, 975, 26B
doi: 10.3847/1538-4357/ad77be

# Main Results

- Shock-heated ejecta from core-collapse supernovae can account for the high 'super-virial' temperatures and unusually high ionic column densities observed in X-ray absorption along three sightlines.
- The ejecta from core-collapse supernovae can naturally explain the observed characteristics of the absorbing 'super-virial' gas, namely $\alpha-$ enrichment and super-solar ionic abundance ratios.
- Supernova explosions with typical blast energy $\sim 10^{51}$ erg, ejecta mass $\sim 10\,M_{\odot}$, and ambient density $\approx 0.1$ cm$^{-3}$ can reproduce these characteristics within a timescale of a few $\sim 100$ Kyr.
- Massive runaway stars could serve as plausible progenitors of such supernovae occurring in the extra-planar regions of the MW along these three sightlines.

## 3.1 Introduction

Circumgalactic medium (CGM) is the gaseous component surrounding the stellar disk and the interstellar medium (ISM) of the Galaxy (Tumlinson et al. 2017; Faucher-Giguère & Oh 2023). The gas in the CGM is multiphase, as suggested by observations and numerical simulations, and the gas temperature varies from $\sim 10^4$ K (cold phase), $\sim 10^5$ K (warm phase) to $\sim 10^6$ K (virial phase or hot phase). However, a few recent observations have reported the existence of an additional phase called the 'super-virial' phase ($\sim 10^7$ K) in the CGM of MW. This has been detected by using absorption lines of Hydrogen and Helium-like ions of Si, Ne, and Mg in the X-ray spectra of bright quasars along various sight lines. Das et al. 2019b used *XMM-Newton* observations towards the Blazar IES 1553+113 ($l = 21.91°$, $b = 43.96°$) to discover this phase through NeIX and NeX ions in a rather high S/N spectra. They also detected other ions (see their Table 1) and found the super-virial phase to be $\alpha$-enhanced, with super-solar values of the ratios of ions (see their Table 2) indicating enrichment by core-collapse supernovae (CCSNe).

Further observation by Das et al. 2021 towards Mrk 421 ($l = 179.83°$, $b = 65.03°$) also detected the super-virial phase using Si and Mg ions. They detected a variety of other ions in the virial and lower temperature phases as well (see their Table 1). The super-virial phase was again found to be $\alpha$-enhanced, with super-solar values of the abundance ratio of ions (see their Table 2). In addition, they inferred the dominance of non-thermal broadening in this phase. More recently, McClain et al. 2024b used *Chandra* observations towards the quasar NGC 3783 ($l = 287.46°$, $b = 22.95°$) to study the gas in absorption. They detected the super-virial phase with Ne ions (see their Table 1). Stacking *Chandra* observations along 46 lines of sight Lara-DI et al. 2023 has also detected SiXIV and SXVI absorption lines with an average column density $8.7 \times 10^{15}$ and $1.5 \times 10^{16}\,\mathrm{cm}^{-2}$, respectively, with super-virial temperatures (Lara-DI et al., 2024b).

Table 3.1 summarizes the absorption data for the SV absorbing phase from these observations for various ions. Observers had also modeled the absorption systems as consisting of gas at multiple temperatures, then used collisional ionization equilibrium (CIE) to deduce the temperature and ionic column densities of the multiple phases using the PHASE model (Krongold et al. 2003). These quantities are modeled, and the derived inferences depend on various assumptions. In the following, we work with the column densities mentioned in Table 3.1, which are directly observed, and compare our model

predictions with them. This is particularly important because in our proposed scenario that will be discussed later, CIE is not applicable, and the super-viral nature of gas is implied due to high observed column densities of H-like ions such as OVIII, NeX, and SiXIV. We will refer to gas at $T \gg 10^6$ K as the super-virial phase below. Note that He-like ions from these elements may have contributions from lower temperatures as well, which is why we focus on the H-like ions in this paper.

The signature of a $\sim 10^7$ K gas phase has also been seen in X-ray emission over the entire sky and has been modeled as an additional component along with the virial phase (Das et al., 2019a; Gupta et al., 2021; Bluem et al., 2022; Bhattacharyya et al., 2023; Ponti et al., 2023; Sugiyama et al., 2023). The typical emission measure (EM) of this phase is of order $\approx 10^{-3}$ cm$^{-6}$ pc. The corresponding (equivalent Hydrogen) column density of this gas can be estimated as $N \approx (L \times EM)^{1/2}$, where $L$ is the size of the region occupied by hot gas. If this hot gas that is seen in emission *also* causes the absorption signatures, then the typical length scale would be $L \approx N^2/EM$. Using the reported column densities (of order $10^{21}$ cm$^{-2}$ (e.g., Das et al. 2021) in absorption studies, the length scale turns out to be exceedingly large ($\gg$ Mpc). This implies that the $\sim 10^7$ K gas that is seen in emission *cannot* explain the absorption observations. It is therefore reasonable to assume that the hot gas seen in emission and absorption has different origins. In this paper, we focus on an explanation of $T \gg 10^6$ K gas seen in absorption studies, and refer to it as the 'SV absorbing' phase.

We propose a novel explanation for the absorption line from the SV absorbing phase, and argue that it could be due to a supernova remnant (SNR) above the Galactic disk. Several observations have detected stars in the 'extra-planar' region of the MW that is occupied by the CGM. These stars are ejected from the Galactic disk through various processes. Stars can get a kick velocity if one of the stars in a binary system explodes as a supernova (Blaauw, 1961) or through dynamical interaction in large open clusters (Poveda et al., 1967). These processes can launch a star into the CGM with speeds of $\lesssim 400\,\mathrm{km\,s^{-1}}$ which is less than the escape velocity. They are called runaway stars (Silva & Napiwotzki, 2011). The massive stars among these runaway stars can explode as CCSNe above the Galactic disk, in the extra-planar region.

We demonstrate that the column density along observed lines of sight can be produced by extra-planar supernovae if the lines of sight pass through them. The reverse shock can heat up gas (shocked ejecta) to the super-virial temperatures ($\sim 10^7$ K). This reverse-

shocked ejecta can explain the observed chemical properties of the super-virial phase, since it is $\alpha$-enriched and has a super-solar abundance ratio of ions (Nomoto et al., 2006; Woosley & Heger, 2007). Our proposal, therefore, unburdens one from trying to explain the absorption lines in the context of MW-wide phenomena, the difficulty of which is illustrated by the estimates mentioned above. While the proposal is admittedly offbeat, our guiding principle is the old adage that after exhausting other possibilities, even an unusual idea, if deemed plausible, is worth pursuing. Our goal in this paper is to show the plausibility of the proposed scenario, along with offering a testable prediction.

This chapter is organized as follows. Section 3.2 describes the details of modeling of massive stars and core-collapse supernova and the associated evolution of the non-radiative supernova remnant, followed by results in Section 5.3. We discuss our results and their implications in Section 5.4 and end with a summary in Section 4.7.

## 3.2 Simulation of Core-Collapse Supernova and Evolution of the Remnant

We first give a brief description of the simulation of the evolution of massive stars and the associated nucleosynthesis leading up to and including the CCSNe.

### 3.2.1 Modelling Massive Star Evolution and Nucleosynthesis in CCSNe

We use the 1D hydrodynamic code KEPLER (Weaver et al., 1978; Rauscher et al., 2003) to simulate the detailed evolution of non-rotating massive stars with an initial solar composition adopted from Asplund et al. 2009. We adopt the default procedures as the ones described in detail in Woosley & Heger 2007 with the detailed stellar physics described in Woosley et al. 2002. Briefly, we follow the evolution starting from the star's birth just before the zero-age main sequence to the eventual endpoint of its life where the star explodes via CCSN. At all stages of evolution, the detailed nucleosynthesis is followed by a large adaptive co-processing network. Convective mixing is modelled using the mixing length theory with the Ledoux criteria for stability, along with semiconvection

| Reference | $N_{\rm OVIII}$ | $N_{\rm NeX}$ | $N_{\rm SiXIV}$ |
|---|---|---|---|
| | ($\times 10^{15}$ cm$^{-2}$) | | |
| Das et al. (2019b) (IES1553+113) | $3.4 \pm 1.4$ | $15.8 \pm 4.6$ | – |
| Das et al. (2021) (Mrk421) | $2.24 \pm 0.44$ | $2.12^{+0.70}_{-0.66}$ | $7.48 \pm 2.08$ |
| McClain et al. (2024b) (NGC3783) | $9.66^{+3.90}_{-3.93}$ | $15.28 \pm 3.37$ | $< 35.26$ |

Table 3.1: This table shows the observed column density of OVIII, NeX, and SiXIV from Das et al. 2019b, Das et al. 2021, and McClain et al. 2024b towards IES1553+113, Mrk421, and NGC3783, respectively.

and overshoot for convective boundaries (Woosley & Weaver, 1988). Mass loss via wind, which has a large impact on massive star evolution, is included with mass loss rates adapted from Nieuwenhuijzen & de Jager 1990 for the main sequence and red giant phase. The explosion due to core-collapse supernova is modelled by driving a piston from the base of the mass shell where the entropy per baryon exceeds $4\,k_{\rm B}$, which roughly coincides with the base of the Oxygen shell (Woosley & Heger, 2007; Heger & Woosley, 2010). The acceleration of the piston is adjusted so that the final kinetic energy matches the desired explosion energy. We consider models of mass ranging from 11–30 $M_\odot$ with a fiducial explosion energy of $1.2 \times 10^{51}$ erg. The amount of mass ejected during CCSN, $M_{\rm ej}$, depends on the mass left over following the mass lost in the wind. Since mass loss is stronger in more massive progenitors, lower mass models have very little mass loss, whereas more massive models lose a substantial part of their mass. For example, the $11\,M_\odot$ models loses only $\sim 0.35\,M_\odot$ whereas a $25\,M_\odot$ model loses $\sim 10\,M_\odot$. The final values of $M_{\rm ej}$ varies between $\sim$ 9–13 $M_\odot$. On the other hand, the mass of the core $M_{\rm c}$, defined as the part excluding the envelope where almost all the metals synthesized in the star are contained, also increases with the progenitor, which varies between 1.25–8 $M_\odot$.

### 3.2.2 Modelling the Supernova Remnant

We simulate the evolution of nonradiative SNR starting from the early ejecta-dominated (ED) phase to the Sedov-Taylor (ST) phase by using a simple 1D hydrodynamics code following the exact prescription of Truelove & McKee 1999. The code solves the Euler equations of hydrodynamics in Lagrangian form, assuming spherical symmetry, using a

finite difference method for an equation of state of an ideal monoatomic gas ($\gamma = 5/3$). The ambient medium is assumed to be cold (zero thermal pressure) and of uniform density $\rho_0$. The ejecta, following free expansion for a few years after the explosion, is also assumed to be cold, which is a very good approximation as indicated by KEPLER models. Instead of using an exact density profile from a freely expanding ejecta from the CCCN simulation discussed above, following Truelove & McKee 1999, we consider density profiles that do not introduce any length scales and allow us to write the Euler equations in terms of characteristic length, mass, and time scales such that the solution is dimensionless in characteristic units. The solution of the Euler equations in such cases is referred to as unified solutions by (Truelove & McKee, 1999). The characteristic units depend on the total ejecta mass $M_{\rm ej}$, ambient density $\rho_0$, and the explosion energy $E$. Thus, for a given ejecta density profile, the solution for different values of $M_{\rm ej}$, $\rho_0$, and $E$ can be found from a single unique solution in terms of the characteristic units which are given by (Truelove & McKee, 1999);

$$
\begin{aligned}
R_{\rm ch} &\equiv M_{\rm ej}^{1/3}\rho_0^{-1/3} \\
&= 14.73 \left(\frac{M_{\rm ej}}{10\,M_\odot}\right)^{1/3} \left(\frac{0.1\,{\rm cm}^{-3}}{n_0}\right)^{1/3} \ {\rm pc}, \qquad (3.1)\\
t_{\rm ch} &\equiv E^{-1/2} M_{\rm ej}^{5/6} \rho_0^{-1/3} \\
&= 6.43 \left(\frac{10^{51}\,{\rm erg}}{E}\right)^{1/2} \left(\frac{M_{\rm ej}}{10\,M_\odot}\right)^{5/6} \left(\frac{0.1\,{\rm cm}^{-3}}{n_0}\right)^{1/3} \ {\rm kyr}, \qquad (3.2)\\
M_{\rm ch} &\equiv M_{\rm ej} \\
&= 1.99 \times 10^{34} \left(\frac{M_{\rm ej}}{10\,M_\odot}\right) \ {\rm g}, \qquad (3.3)
\end{aligned}
$$

where $n_0$ is the ambient atomic number density. We adopt a mean atomic number $\bar{A} = 1.276$ for the ambient medium corresponding to a gas of solar composition from Asplund et al. 2009 such that $n_0 = \rho_0/(\bar{A} m_{\rm H})$, where $m_{\rm H}$ is the mass of a hydrogen atom. Based on the above characteristic quantities, we can also define the characteristic velocity

$v_{\rm ch}$, density $\rho_{\rm ch}$, and pressure $P_{\rm ch}$ as

$$v_{\rm ch} \equiv \frac{R_{\rm ch}}{t_{\rm ch}} = E^{1/2} M_{\rm ej}^{-1/2}$$
$$= 2.24 \times 10^{8} \left(\frac{E}{10^{51}\,{\rm erg}}\right)^{1/2} \left(\frac{10\,M_\odot}{M_{\rm ej}}\right)^{1/2} \ {\rm cm\,s^{-1}} \tag{3.4}$$
$$\rho_{\rm ch} \equiv \frac{M_{\rm ch}}{R_{\rm ch}^3} = \rho_0$$
$$= 2.12 \times 10^{-25} \left(\frac{n_0}{0.1\,{\rm cm^{-3}}}\right) \ {\rm g\,cm^{-3}} \tag{3.5}$$
$$P_{\rm ch} \equiv \frac{M_{\rm ch}}{R_{\rm ch} t_{\rm ch}^2} = E M_{\rm ej}^{-1} \rho_0$$
$$= 1.07 \times 10^{-8} \left(\frac{E}{10^{51}\,{\rm erg}}\right) \left(\frac{10\,M_\odot}{M_{\rm ej}}\right) \left(\frac{n_0}{0.1\,{\rm cm^{-3}}}\right) \ {\rm dyne\,cm^{-2}} \tag{3.6}$$

### Initial velocity profiles

The initial velocity profile is adopted assuming a freely expanding ejecta given by (Truelove & McKee, 1999)

$$v(r) = \ \frac{r}{t_{\rm ini}}, \quad r \le R_{\rm ej} \tag{3.7}$$
$$= \ 0, \quad r > R_{\rm ej}. \tag{3.8}$$

where $R_{\rm ej}$ is the radius of the expanding ejecta at the initial starting time $t_{\rm ini}$. This agrees very well with the simulated velocity profile from CCSN models from KEPLER.

### Density profile without a core

For the density profile, we first consider an idealized ejecta with a constant density $\rho$ without any core, corresponding to the $n = 0$ power-law density profile discussed in Truelove & McKee 1999 given by

$$\rho(r) = \ \frac{3}{4\pi} \frac{M_{\rm ej}}{R_{\rm ej}^3}, \quad r \le R_{\rm ej} \tag{3.9}$$
$$= \ \rho_0, \quad r > R_{\rm ej}. \tag{3.10}$$

The value of $R_{\rm ej}$ for a given $t_{\rm ini}$ depends only on $M_{\rm ej}$ and $E$. In order to find this dependence, it is useful to define $v_{\rm ej}$, which is the maximum velocity of the ejecta corresponding to the outermost surface of the ejecta, i.e., $v(r = R_{\rm ej}) = R_{\rm ej}/t_{\rm ini}$. Using the fact that

$E = 0.5 \int_0^{R_{\rm ej}} 4\pi\rho r^2 v^2 dr$ we find

$$v_{\rm ej} = \left(\frac{10}{3}\right)^{1/2} E^{1/2} M_{\rm ej}^{-1/2}$$
$$= 4.09 \times 10^8 \left(\frac{E}{10^{51}\ {\rm erg}}\right)^{1/2} \left(\frac{10\,M_\odot}{M_{\rm ej}}\right)^{1/2} {\rm cm\,s^{-1}} \quad (3.11)$$

Thus, for a given $t_{\rm ini}$, the velocity and density profile are uniquely determined by $M_{\rm ej}$ and $E$. Similar to Truelove & McKee 1999, we use the $*$ symbol to denote quantities in characteristic units such that $t^* = t/t_{\rm ch}$, $\rho^* = \rho/\rho_{\rm ch}$, etc. We adopt $t^*_{\rm ini} = 0.01$ as the default value. In characteristic units, however, the velocity and density profiles are independent of $M_{\rm ej}$, $E$, and $n_0$ and only depend on $t^*_{\rm ini}$. For the adopted density profile, we have a constant $v^*_{\rm ej} = 1.8259$ and $R^*_{\rm ej} = 1.8259 t^*_{\rm ini}$. The velocity and density profiles in characteristic units are given by

$$v^*(r^*) = \frac{r^*}{t^*_{\rm ini}}, \quad r^* \le R^*_{\rm ej} \quad (3.12)$$
$$= 0, \quad r^* > R^*_{\rm ej}, \quad (3.13)$$

and

$$\rho^*(r^*) = \frac{0.0392}{t^{*3}_{\rm ini}}, \quad r^* \le R^*_{\rm ej} \quad (3.14)$$
$$= 1, \quad r^* > R^*_{\rm ej}. \quad (3.15)$$

### Density profiles with a core

We next consider more realistic density profiles that have a core. We adopt cores of constant density $\rho_{\rm c}$ of mass $M_{\rm c}$ surrounded by a lower density envelope of constant density $\rho_{\rm env}$. The ratio $\beta = M_{\rm c}/M_{\rm ej}$ and $\eta = \rho_{\rm c}/\rho_{\rm env}$ are parameters that are varied depending on the progenitor profile. The profile without any core discussed above corresponds to $\beta = 0$ and $\eta = 1$. This parametrization of the density profile is roughly consistent with detailed density profiles from the CCSN ejecta from KEPLER following free expansion. The values of $\beta$ and $\eta$ from the CCSN models range from $\sim$ 0.14–0.6 and $\sim$ 10–20, respectively. Although this parametrization of the density profile introduces two new parameters, because it does not introduce any new length scales, it can still be written in characteristic units to yield unified solutions for fixed values of $\beta$ and $\eta$. The density

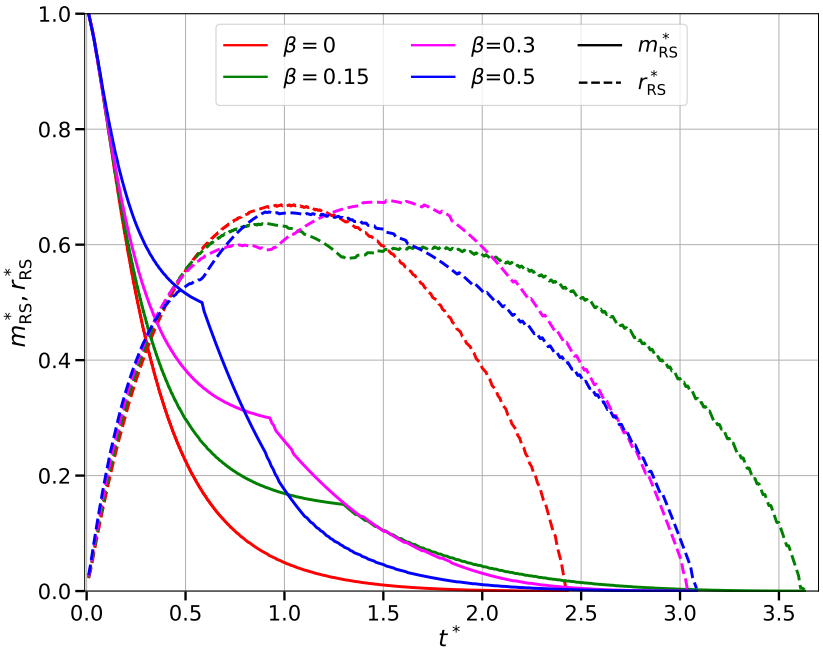



Figure 3.1: Temporal evolution of the position of the reverse shock front in Eulerian coordinate $r_{\rm RS}$ (dashed lines) and Lagrangian coordinate $m_{\rm RS}$ (solid lines) for the different density profiles in characteristic coordinates. The red, green, magenta, and blue lines show the variation for $\beta = 0, 0.15, 0.3$ and $0.5$ respectively.

profile is given by

$$\rho(r) = \frac{3\kappa_1}{4\pi}\frac{M_{\rm ej}}{R_{\rm ej}^3}, \quad r \leq R_{\rm c} \tag{3.16}$$

$$= \frac{3\kappa_1}{4\pi\eta}\frac{M_{\rm ej}}{R_{\rm ej}^3}, \quad R_{\rm c} < r \leq R_{\rm ej} \tag{3.17}$$

$$= \rho_0, \quad r > R_{\rm ej}, \tag{3.18}$$

where $\kappa_1 = \eta(1-\beta)+\beta$. The radius of the core $R_c$ is related to $R_{\rm ej}$ by

$$R_{\rm c} = \left(\frac{\beta}{\kappa_1}\right)^{1/3} R_{\rm ej} \equiv \kappa_2 R_{\rm ej} \tag{3.19}$$

The above expression for density is very similar to the expression for a profile without a core in Eq. 3.10, but with the additional factors of $\kappa_1$, $\eta$, and $\kappa_2$. In this case, $R_{\rm ej}$ for a given $t_{\rm ini}$ depends on $\beta$ and $\eta$ in addition to $M_{\rm ej}$ and $E$. As before, $R_{\rm ej}$ can be calculated for a given value of $t_{\rm ini}$ from $v_{\rm ej}$ which is given by

$$v_{\rm ej} = \left(\frac{10}{3}\right)^{1/2} \kappa_3 E^{1/2} M_{\rm ej}^{-1/2}, \tag{3.20}$$

where

$$\kappa_3 = \left(\frac{\eta}{\kappa_1}\frac{1}{(\eta-1)\kappa_2^5+1}\right)^{1/2}. \tag{3.21}$$

The expression for $v_{\rm ej}$ above is almost identical to the expression for the profile with no core given in Eq. 3.11 but with the additional factor of $\kappa_3$ which depends on $\beta$ and $\eta$. The density profile for a fixed $\beta$ and $\eta$ can again be written in characteristic coordinates with the solution being independent of $E$ and $M_{\rm ej}$. As before, we adopt $t^*_{\rm ini} = 0.01$. We explore values of $\beta = 0.15, 0.30$, and $0.50$ that cover the range of mass models. We adopt a value of $\eta = 15$ that is roughly consistent with all the models.

## 3.3 Results

### 3.3.1 Overall Evolution of the Ejecta

As described in (Truelove & McKee, 1999), because the freely expanding ejecta has a velocity that is orders of magnitude larger than the sound speed of the ambient medium, a forward blast wave is launched into the ambient medium that leads to compression and heating. This, in turn, exerts pressure back on the freely expanding ejecta that compresses the ejecta and launches a reverse shock. The shocked ejecta (due to reverse shock) is always separated from the less dense shocked ambient medium by the contact discontinuity at $M = M_{\rm ej}$. The reverse shock continues to travel inwards (in mass coordinates) and results in the heating up of the shocked ejecta due to compression. Because the velocity of the initial freely expanding ejecta decreases with radius, the reverse shock progressively encounters slower ejecta velocities as it moves inward. The reverse shock eventually reverses the direction of the expanding ejecta, leading to an implosion at $t^* \gtrsim 1$. This can be seen clearly from Fig. 3.1, where the dashed and solid red lines show the evolution of the position of the reverse shock in Eulerian coordinates ($r_{\rm RS}$) and Lagrangian coordinates ($m_{\rm RS}$), respectively, for the density profile without a core. We note here that the location of the reverse shock front is defined as the coordinate where the pressure jumps from zero (corresponding to unshocked ejecta) to a non-zero value (corresponding to shocked ejecta). By this time, the forward blast wave in the ambient medium transitions to the ST phase. Eventually, the reverse shock reaches the center at $t^* \gtrsim 2$, leading to an outward-going secondary blast-wave shock referred to as the bounce. As mentioned in Truelove & McKee 1999, the secondary blast-wave shock reverses the direction of the infalling material that was previously shocked by the reverse shock.

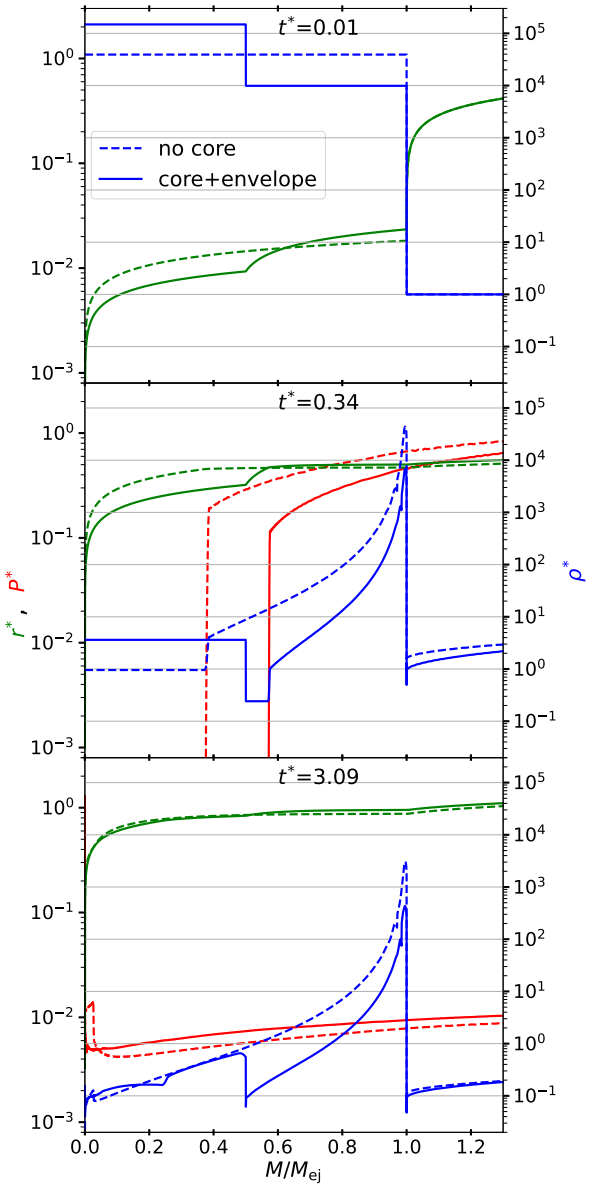



Figure 3.2: Pressure, mass density, and radius profile as a function of $M/M_{\rm ej}$ at three epochs in the characteristic unit. The solid and dashed line shows the case with *core+envelope* ($\beta = 0.5$) and *no core*, respectively. The blue color shows the mass density profile (right y-axis). The red and green color shows the pressure and radius profile (left y-axis), respectively. The *top panel* shows the initial setup at $t^* = 0.01$. The *middle panel* shows the profiles at $t^* = 0.34$ when the reverse shock is about to hit the core for *core+envelope* case. The *bottom panel* shows the profiles when the reverse shock has hit the center of the ejecta at $t^* = 3.09$ for *core+envelope* case. For *no core* case, the reverse shock has already hit the center by $t^* = 3.09$ and the secondary shock wave has started traveling outwards, as can be seen by the jump in pressure (dashed red line) and density profile (dashed blue line).

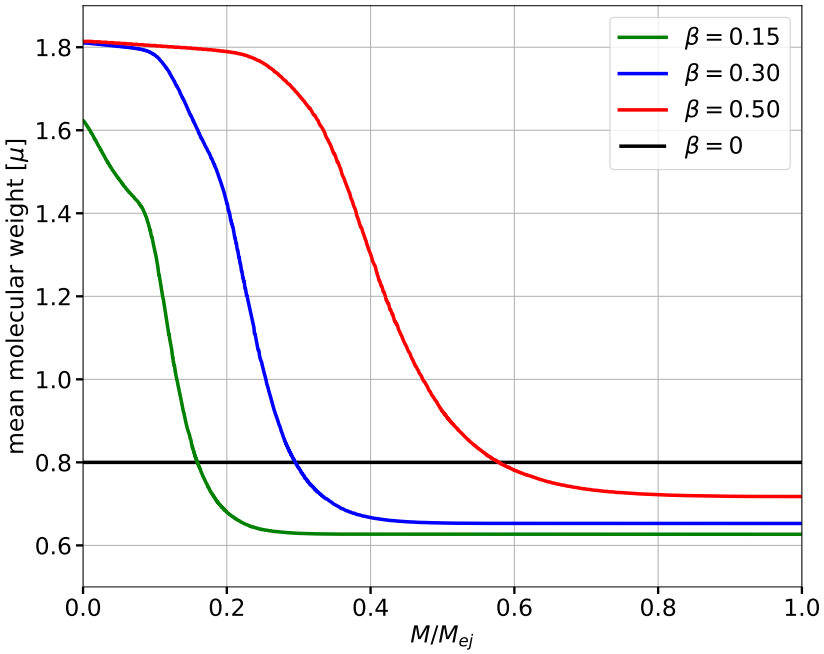



Figure 3.3: Mean molecular weight profile as a function of $M/M_{\rm ej}$ calculated using KEPLER. The black, green, blue, and red lines show the mean molecular weight profile for $\beta = 0, 0.15, 0.30$, and $0.50$, respectively.

The propagation of the reverse shock discussed above applies only to density profiles without a core. In the case of the density profiles with a core, when the reverse shock reaches the core–envelope boundary, the large density gradient causes a bounce and launches a forward secondary blast-wave shock wave that travels outwards. The corresponding position of the reverse shock for the various values of $\beta$ is shown in Fig. 3.1. As can be seen from the figure, the reverse shock is heavily slowed down by the bounce at the core–envelope boundary, and starts to move out again in Eulerian coordinates (dashed green, magenta, and blue lines) even though it continues to move inwards in Lagrangian coordinates (solid green, magenta, and blue lines). In the case of density profiles with cores, the reverse takes longer to reach the center, with profiles with the smallest core taking the longest (see Fig. 3.1). When the secondary blast-wave shock reaches the contact discontinuity, another secondary reverse shock is launched, and the process repeats itself. During this, the original reverse shock in the core eventually reaches the center, leading to a bounce, and is helped along by subsequent arrivals of secondary reverse shocks.

In all cases, we end our simulation at $t^* = 10$, well after the reverse shock has reached the center. Following bounce when reverse shock reaches the center, 3D effects such as inhomogeneities and turbulent mixing due to Raleigh-Taylor instabilities become

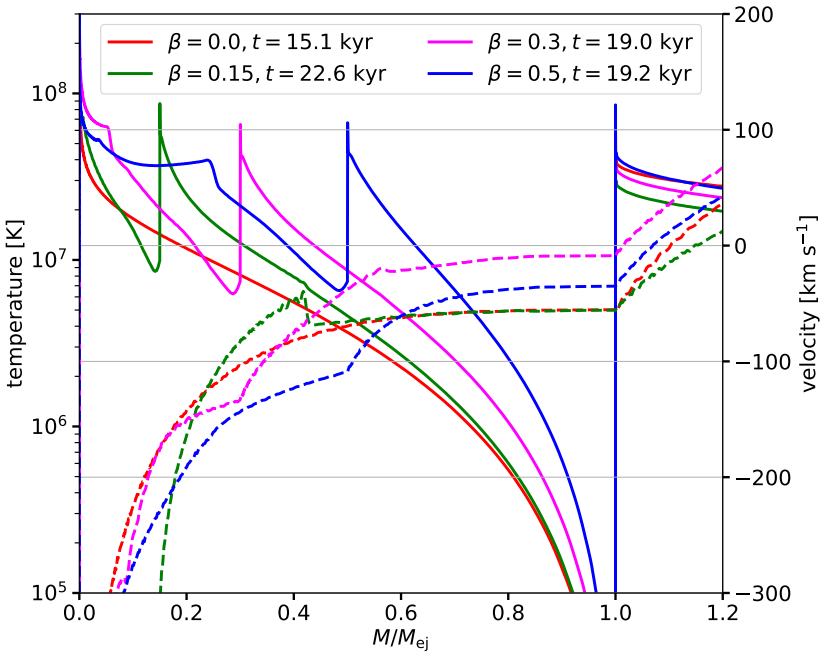



Figure 3.4: Temperature (solid lines) and velocity profiles (dashed lines) for different values of $\beta$ when the reverse shock hits the center of the ejecta in the respective cases. Red, green, magenta, and blue colors show the cases with $\beta = 0, 0.15, 0.3$, and 0.5, respectively. The profiles are plotted for the fiducial case with $E = 10^{51}\,\mathrm{erg}$, $M_{\rm ej} = 10\,M_\odot$ and $n_0 = 0.1\,\mathrm{cm}^{-3}$.

increasingly important at the contact discontinuity with multiple cycles of secondary shock waves resulting in the contact discontinuity being erased and the flow subsequently evolves as an ST solution throughout the remnant (Truelove & McKee, 1999).

### 3.3.2 Evolution of Pressure, Density, and Temperature of Shocked Ejecta

In order to illustrate the evolution of the structure of the ejecta, we consider the density profiles with $\beta$ of 0 and 0.5. Figure 3.2 shows the pressure and density profiles in characteristic coordinates as a function of the mass coordinate at various instants of the evolution, ranging from the initial to the final stage when the reverse shock reaches the center. The radial (Eulerian) coordinate $r$ is also plotted as a function of the mass coordinate. The evolution of pressure and density for both profiles is largely similar, where the compression due to the reverse shock leads to a pressurized ejecta with a relatively flat pressure profile in terms of the mass coordinate. The density of the shocked ejecta is highest at the contact discontinuity at $m^* = 1$ and decreases with decreasing $m^*$ as the reverse shock moves inwards.

By the time the reverse shock has reached the center, the central density is lower by $\sim$ four orders of magnitude compared to the highest density at the contact discontinuity. By this time, all the matter in the ejecta is compressed into a thin shell in Eulerian coordinates, and almost all of the ejecta is confined to a narrow range of radial coordinates. In profiles with a core, the jump in density due to the core and the associated slowdown of the reverse shock discussed earlier leads to a shallower density gradient in the core by the time the reverse shock has reached the center.

The temperature $T$ can be calculated from the pressure and density, assuming an ideal gas law given by

$$T = \frac{\mu m_u}{k_{\rm B}} \frac{P^* P_{\rm ch}}{\rho^* \rho_{\rm ch}}, \tag{3.22}$$

where $\mu$ is the mean molecular weight of the ejecta, $m_u$ is the atomic mass unit, and $k_{\rm B}$ is the Boltzmann constant. Because of the metallicity gradient with an increasing amount of metals in the core, for a given progenitor, $\mu$ increases with decreasing mass. Figure 3.3 shows the variation of $\mu$ with mass coordinate for a $11, 18$, and $25\,M_\odot$ models corresponding to $\beta$ of $0.15, 0.3$, and $0.5$, respectively, assuming a fully ionised ejecta. For

the profile without a core, i.e., $\beta = 0$, we adopt a constant $\mu = 0.8$ which corresponds to the mass-averaged value for a typical CCSN progenitor over the ejecta mass. Because the unified solution in characteristic coordinates for a given density and $\mu$ profile remains unchanged, $T \propto P_{\rm ch}/\rho_{\rm ch} = EM_{\rm ej}^{-1}$. Figure 3.4 shows the temperature and velocity for $E = 10^{51}\,{\rm erg}$, $M_{\rm ej} = 10\,M_\odot$, and $n_0 = 0.1\,{\rm cm}^{-1}$ when the reverse shock has reached the center for the various density profiles. As can be seen from the figure, for density profiles with a core, the temperature (solid green, magenta, and blue lines) of the shocked ejecta in the core is $\gtrsim 6 \times 10^6\,{\rm K}$ in all cases. For the density profile without a core (solid red line), the inner $\sim 40\%$ of the inner ejecta lies above this temperature. The maximum temperature occurs at the center due to a combination of lowest density and highest $\mu$ with a maximum temperature of $\sim 6 \times 10^7\,{\rm K}$. Because $T \propto E$, for a given density profile, increasing $E$ by some factor will lead to an overall increase in $T$ by the same factor. For example, for $E = 10^{52}\,{\rm erg}$, $T$ will increase by a factor of 10 compared to what is plotted in Fig. 3.4. The corresponding velocity profiles for the various values of $\beta$ are also shown in Fig. 3.4 (dashed lines). As mentioned earlier, by the time the reverse shock reaches the center, the explosion turns into an implosion and the velocity of the entire ejecta is negative with values of $\lesssim 0$ and $\lesssim -300\,{\rm km\,s^{-1}}$ at the contact discontinuity and the center, respectively.

### 3.3.3 Comparing Timescales

Before we discuss column densities, it is important to consider the ionization, recombination, and cooling timescales of the shocked heated ejecta relative to the dynamical time. The radiative cooling time for the gas in the ejecta is $t_{\rm c} = 3k_BT/(2n_{\rm ion}\Lambda)$, where $\Lambda$ (erg cm$^3$ s$^{-1}$) is the cooling function and $n_{\rm ion}$ is the total number density of ions. The recombination timescale for an ion is $t_{\rm re} = 1/(n_e\alpha_{\rm ion}(T))$, where $\alpha_{\rm ion}(T)$ is the recombination coefficient of the ion at temperature T (Verner & Ferland 1996) and $n_e$ is the number density of electrons. The ionization timescale for an ion due to thermal electrons is $t_{\rm ion} = 1/(n_e q_i(T))$ where $q_i$ is the ionization coefficient of the ion (Voronov 1997). Figure 3.5 shows the minimum ionization and recombination timescales for OVI/OVII and OVII/OVIII, along with the cooling timescale relative to the dynamical timescale of the material in the inner core of the ejecta with $\beta = 0.3$ that contains almost all of the metals. As can be seen from the figure, the fastest cooling time is an order of magnitude longer than the dynamical time, implying that cooling is essentially negligible on dynamical

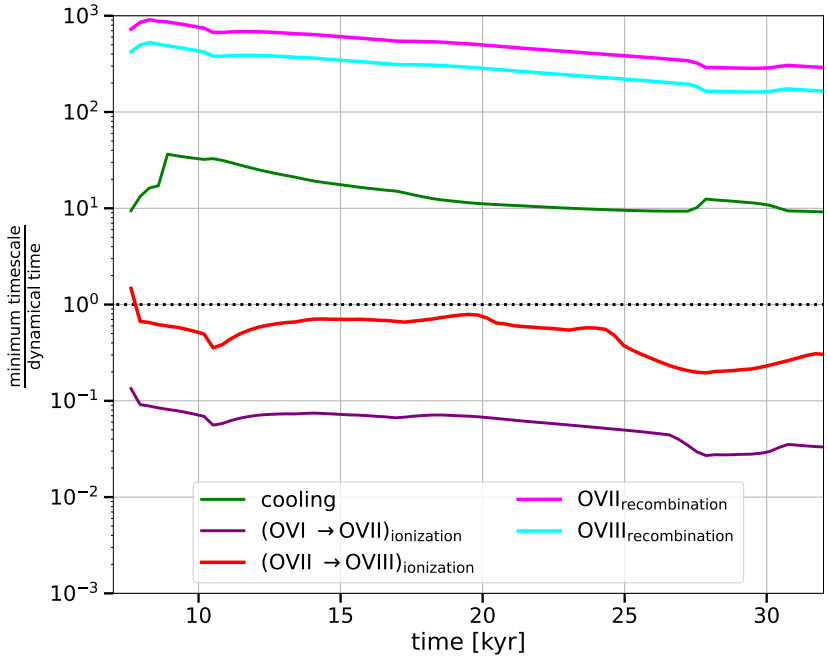



Figure 3.5: This figure shows the ratio of "minimum" radiative cooling, recombination, and ionization timescale to the dynamical time as a function of time. The "minimum" timescale corresponds to the mass shell which has minimum radiative cooling/ionization/recombination time within $M/M_{\rm ej} \leq 0.2$ and $T \geq 4 \times 10^6$ K. The green line shows the ratio of radiative cooling to dynamical time calculated using the cooling function for core composition with CLOUDY (Ferland et al. 2017). The magenta and cyan lines show the ratio of the recombination timescale (Verner & Ferland 1996) to the dynamical timescale for OVII and OVIII, respectively. The purple and red lines show the ratio of the ionization timescale (Voronov 1997) to the dynamical time for OVI and OVII, respectively. The above timescales are plotted for $E = 10^{51}$ erg, $M_{\rm ej} = 10\ M_\odot$, $n_0 = 0.1{\rm cm}^{-3}$ and $\beta = 0.3$.

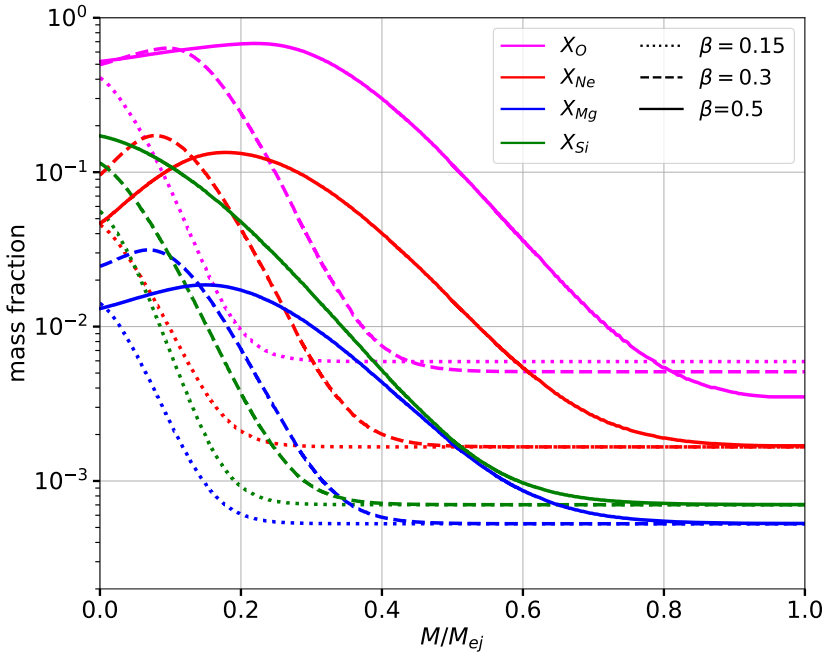



Figure 3.6: Mass fraction of different elements as a function of $M/M_{\rm ej}$ obtained using KEPLER. The magenta, red, blue, and green lines show Oxygen, Neon, Magnesium, and Silicon mass fraction profiles, respectively. The solid, dashed, and dotted lines refer to the case with $\beta = 0.5, 0.3$ and 0.15 corresponding to 25, 18, and 11 $M_\odot$ mass models, respectively.

timescales. This justifies our assumption of neglecting the cooling of the shocked ejecta.

The ionization timescale, on the other hand, is shorter than the dynamical timescale, whereas the recombination timescales are more than two orders of magnitude longer. Thus, even though ionization can occur as the reverse shock heats up the ejecta, recombination is essentially negligible. Consequently, CIE does not apply to the reverse shock-heated ejecta and cannot be applied for estimating the abundance of ions. On the other hand, because recombination is negligible, the time evolution of the ionization of the ejecta can be easily calculated, which can then be used to calculate the column density of different ionization states for an element and compared directly with the observed values (Table 3.1). However, in order to calculate the column densities of different ionization states, we need to first calculate the total column density of the corresponding element. We discuss this in detail in the following section.

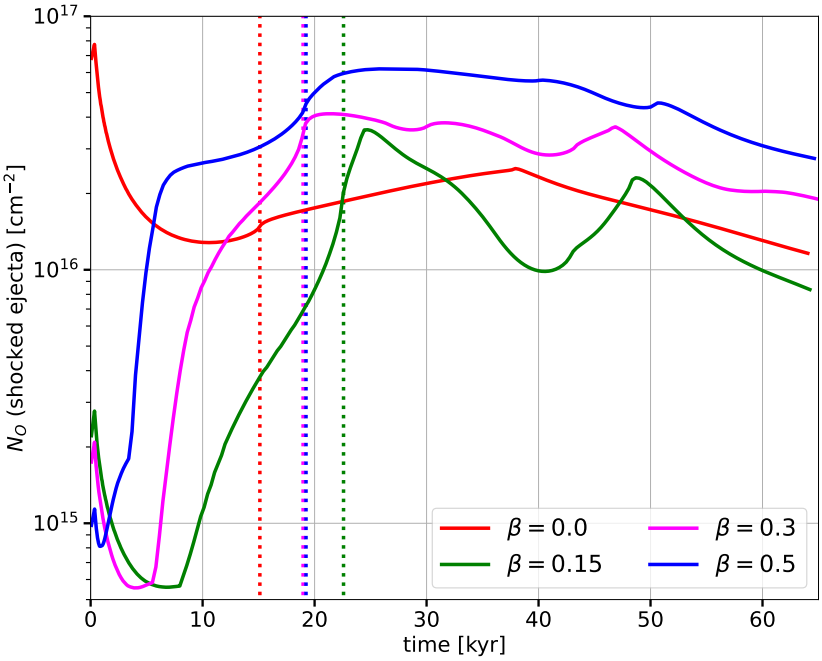



Figure 3.7: Evolution of Oxygen column density of the shocked ejecta with time for density profiles with different core sizes of $\beta = 0, 0.15, 0.3$, and 0.5 shown in red, green, magenta, and blue, respectively. For *no core* case ($\beta = 0$), we use a constant Oxygen mass fraction of 0.15 throughout the ejecta. The dotted vertical lines in the respective color show the time when the reverse shock hits the center of the ejecta. The curves correspond to the adopted fiducial values of $E = 10^{51}$ erg, $M_{\rm ej} = 10\,M_\odot$, and $n_0 = 0.1\,{\rm cm}^{-3}$.

### 3.3.4 Evolution of Column Density

We calculate the time evolution of the total elemental column densities across all ionization states for Oxygen, Neon, and Silicon in the shock-heated ejecta. The column density $N$ at time $t$ for any element in the shocked ejecta is given by

$$N(t) = 2\int_0^{R_{\rm ej}(t)} \frac{X\rho(t)}{m_u A} dr, \tag{3.23}$$

where $X$ is the mass fraction of the element and $A$ is the mass number. The factor of 2 is to account for the fact that light from a background source traverses the material in the shell formed by the SNR twice before reaching Earth. We note here that for realistic density profiles, i.e., with cores, almost the entire contribution to column density for a metal is from the shocked core with negligible contribution from the envelope. We note here that because the shocked core has temperatures $\gg 10^6$ K for all the density profiles as discussed in the previous section, the contribution to the column density is essentially from the SV phase.

Since the characteristic solution remains unchanged for a given density profile and $N$ has the dimensions of number density multiplied by distance, the scaling relation for $N \propto \rho_{\rm ch} R_{\rm ch} = \rho_0^{2/3} M_{\rm ej}^{1/3}$. Because $M_{\rm ej}$ varies only slightly from 9–13 $M_\odot$ across all progenitors with a dependence of $N \propto M_{\rm ej}^{1/3}$, column density is effectively independent of the ejecta mass. The ambient density $\rho_0$ is the only parameter that can potentially have an appreciable effect on $N$ for a given density profile. The nature of the progenitor also affects the column density, primarily due to the size of the core and the slightly different metal fractions in the core. Figure 3.6 shows the elemental mass fraction profile for the progenitors with different core sizes corresponding to different progenitor masses. The mass fraction of metals is slightly higher in more massive models that have larger cores. This leads to an overall enhancement of the column density of metal as it directly scales with the mass fraction (see Eq. 3.23 above).

To illustrate the evolution of column density with time for various progenitors, we adopt the fiducial $E = 10^{51}$ erg, $M_{\rm ej} = 10\,M_\odot$, and $n_0 = 0.1\,{\rm cm}^{-3}$ corresponding to $t_{\rm ch} = 6.2$ kyr. Figure 3.7 shows the evolution of the Oxygen column density of the shocked ejecta for density profiles with different core sizes. As can be seen from the figure, the column density starts with a relatively high value due to the high initial density near the contact discontinuity, but starts to decrease as the shocked ejecta keeps expanding. The

column density eventually increases with time as the reverse shock moves inward and more metal is heated up. The increase is particularly dramatic for density profiles with cores, where the column density starts to rise rapidly when the reverse shock reaches the core, which takes longer for profiles with smaller cores. The instant when the reverse shock hits the center is shown using dotted vertical color lines in figure 3.7 for various values of $\beta$. As mentioned earlier, by this time the ejecta to temperatures of $\gtrsim 6\times10^6$ K corresponding to 'super-virial' temperatures. Even after the shock reaches the center, the column density increases slightly due to the increased density due to implosion. Following the bounce at the center, the column density effectively plateaus out and remains roughly constant until the end of the simulation. This is primarily because almost all of the ejecta is confined to a narrow range of radius by the time the shock reaches the center. Consequently, to zeroth order, all the material in the ejecta is roughly at the same radius $R_c$. This implies that

$$N \propto \int_0^{R_{ej}} \rho dr = \int_0^{R_{ej}} \frac{dm}{4\pi r^2} \approx \frac{M_c}{4\pi R_c^2}. \tag{3.24}$$

Following the bounce at the center, the implosion is gradually turned into an explosion after multiple secondary blast waves are generated, as described earlier. The average velocity of the shocked ejecta $\bar{v}_{ej}$, however, remains very low, including being negative during some intervals during a series of implosions and explosions. As a result, $R_c$ and consequently $N$ change slowly on timescales of $\gg t_{ch}$. For example, compared to the peak value after the bounce $t^* \sim 3$, the value of $N$ decreases by a factor of 2.7, 4.4, 2.2, and 2.2, for density profiles with $\beta$ of 0, 0.15, 0.3, and 0.5, respectively, by $t^* = 10$. It is important to note that after bounce, due to repeated cycles of implosions and explosions, the column density does not decrease monotonically with time, as can be seen from Fig. 3.7. So, the effective timescale during which the column density changes is even longer than what is estimated above ($t^* = 10$).

### 3.3.5 Comparison with Observations

We now compare the theoretical column densities for Oxygen, Silicon, and Neon ions with the observed range of values. Because $N$ is not very sensitive to $E$ and $M_{ej}$, we consider the fiducial values of $10^{51}$ erg and $10\,M_\odot$, respectively. We consider an ambient density of $n_0 = 0.1\,\mathrm{cm}^{-3}$ for the three profiles with cores. Here, we do not consider the profile without a core as it does not correspond to any physical model.

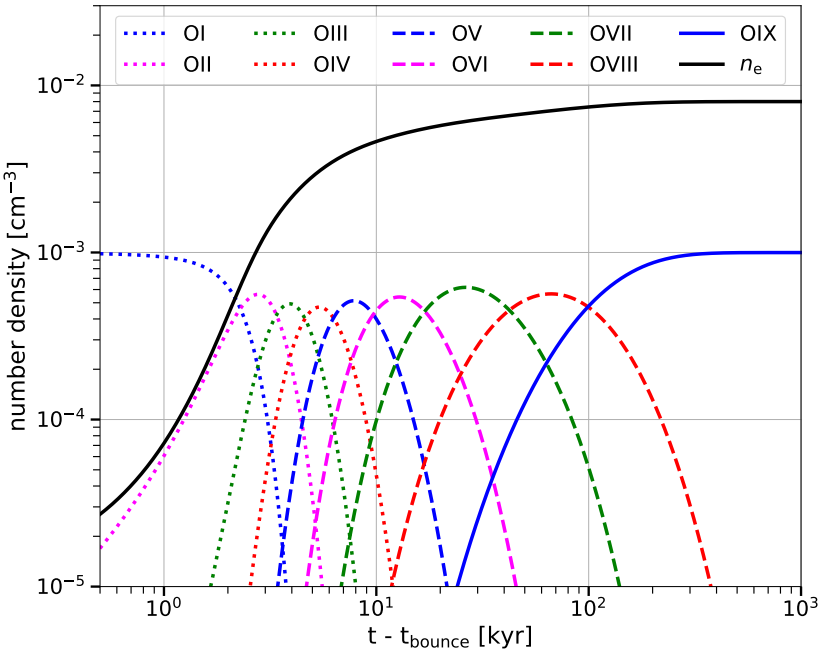



Figure 3.8: Ionization of a Oxygen gas at $T = 5$ keV with initial OI abundance of $0.001\,\mathrm{cm}^{-3}$ and initial $n_e = 10^{-5}\,\mathrm{cm}^{-3}$.

In order to compare our results with the observed column density of ions, the ion fraction of OVIII, NeX, and SiXIV is required, for which we use the following procedure. Since the recombination timescale is much larger than the dynamical time (cyan and magenta lines in figure 3.5), the recombination of ions is neglected in our calculation. We solve the system of coupled linear differential equations governing the ionization equation to find the abundance of various ionization states of various elements as a function of time, starting from the neutral to the fully ionized state. The rate of change of the abundance of the $i^{\mathrm{th}}$ state of ionization of an atom depends on the rate of ionization of the $i^{\mathrm{th}}$ to $(i+1)^{\mathrm{th}}$ state. This is counteracted by the production of the $i^{\mathrm{th}}$ state by the ionization of the $(i-1)^{\mathrm{th}}$ state. We adopt the ionization rates from Voronov 1997 and consider ionization due to thermal electrons. The ionization parameter $q$, depends only on the temperature of the electrons.

The ionization essentially occurs after the reverse shock heats up all the metal in the ejecta, i.e., after bounce. As discussed earlier, the mass density of the shocked ejecta varies very slowly after bounce. Moreover, the cooling timescale is an order of magnitude longer than the dynamical timescale (green line in figure 3.5). For this reason, for simplicity, we assume that the temperature and mass density remain constant while solving for the ionization. We adopt $n_{\mathrm{ion}} \approx 0.001$–$0.002\,\mathrm{cm}^{-3}$, which is taken from the density profile of

the ejecta after the reverse shock has hit the center ($t \sim 20$ kyr). Since the temperature of the shocked core varies somewhat with the density profile, we take a range of 3–10 keV for Oxygen, Magnesium, and Neon and 10–18 keV for Silicon. These numbers are adopted directly from the range of temperatures found in the inner part of the ejecta ($M/M_{\rm ej} < 0.2$) as can be seen in Fig. 3.4.

For illustration, we show the evolution of the ionization for a gas composed of Oxygen with an initial OI abundance of $0.001{\rm cm}^{-3}$ and initial $n_e = 10^{-5}$ corresponding to an initial ionization fraction of $\sim 0.1\%$. Figure 3.8 shows the evolution of OI–OIX along with $n_e$, for an electron temperature of 5 keV. As can be seen from the figure, $n_e$ increases rapidly on timescales of $\sim$ kyr and reaches an ionization fraction of $\sim 80\%$ within 40 kyr as Oxygen gets progressively more ionized. Beyond this epoch, the gas is primarily composed of OVII–OIX, and full ionization is reached by $\sim 200\,$kyr.

Since we are interested in H-like, i.e., almost fully ionized ions, we fix the value of $n_e$ of the gas assuming it is almost fully ionized. This does not affect the evolution of highly ionized atoms but allows us to readily calculate the fractional abundance of any ion for different atoms, independent of the composition. We adopt $n_e = 0.01$ cm$^{-3}$ for Oxygen, Neon, and $n_e = 0.005$ cm$^{-3}$ for Silicon, corresponding to almost fully ionized gas for the estimated values of $n_{\rm ion}$ from simulations. The resulting values of ion fractions of an element are computed for the range of temperatures mentioned above, yielding a range of ion fractions for each ion. This range of ion fractions for each ion of an element, when folded with the range of total elemental column densities found in various density profiles, results in a band of ion column density as a function of time. We consider total column densities of $(1-6)\times10^{16}$, $(2-8)\times10^{15}$, and $(1-5)\times10^{15}\,{\rm cm}^{-2}$ for Oxygen, Neon, and Silicon, respectively, corresponding to the range of values found in all the density profiles. Figure 3.9 shows the calculated band of column density of OVIII, NeX, and SiXIV, superposed with the observed column densities of respective ions towards Mrk421, IES1553+113, and NGC3783 (see Table 3.1). The dashed lines in the respective colors show the observed upper and lower limits. The curved bands show the ionic column densities from our model.

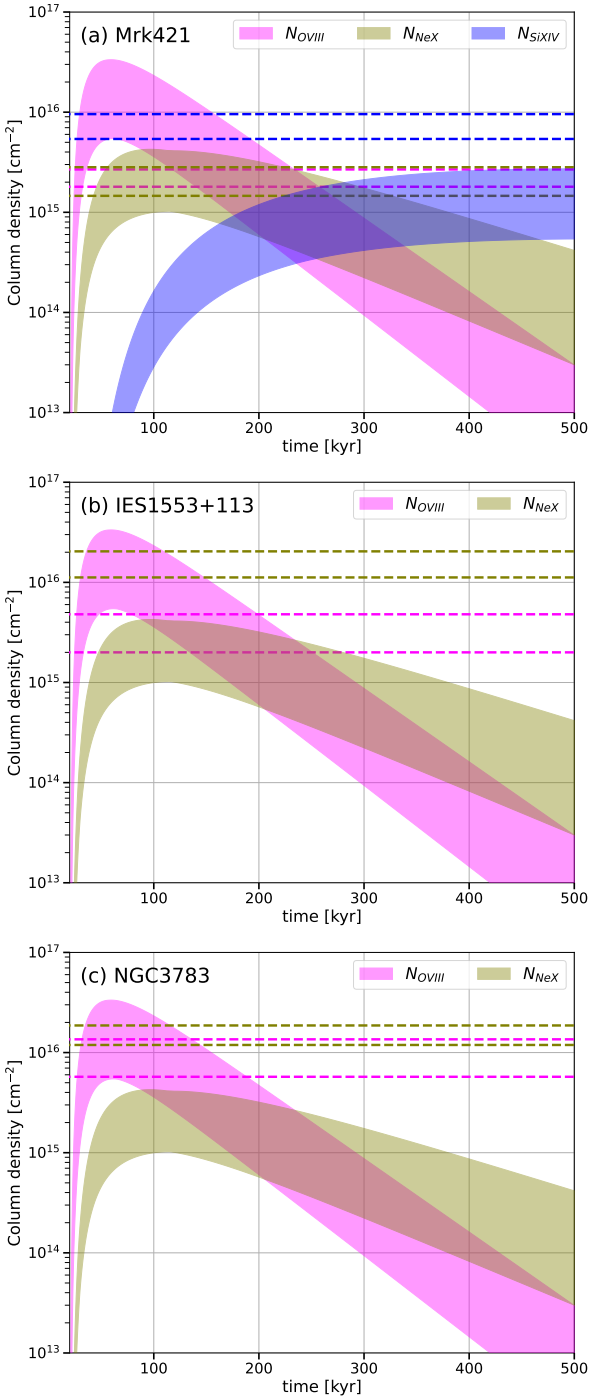



Figure 3.9: Column density of ions as a function of time for three lines of sight. The *top (a), middle (b)* and *bottom (c)* panel shows the column density towards Mrk421 (Das et al. 2021), IES1553+13 (Das et al. 2019b), and NGC3783 (McClain et al. 2024b) respectively. The magenta, green, and blue bands show the column density range of OVIII, NeX, and SiXIV, respectively, calculated from our model. The dashed lines in the same color show the upper and lower limits of the observed column density of respective ions.

#### Mrk 421

The top panel of Figure 3.9 compares the results for our fiducial case with the observations towards Mrk 421 Das et al. 2021. Interestingly, the colored bands of our model prediction for all three ions (OVIII, NeX, and SiXIV) show an overlap at $\sim$ 200–300 kyr, which also approximately matches the observed bands for OVIII and NeX. There is a slight shortfall in the SiXIV column density, by a factor of $\approx 2$, which can be potentially explained by variations in supernova yields.

#### IES1553+113

The middle panel of Figure 3.9 shows the comparison with observed column densities of OVIII and NeX towards IES1553+113 Das et al. 2019b. We again find an overlapping region for OVIII and NeX column densities, around $t \sim$ 100–400 kyr, and it matches the observed column density of OVIII to a large extent. The predicted NeX column density falls short of the observed values, again by a factor $\approx 2$, which can be due to uncertainties in SN yield.

#### NGC 3783

We show the comparison of our results with the observations towards NGC 3783 McClain et al. 2024b in the bottom panel of Figure 3.9. Again, there is an overlap between the column densities of OVIII and NeX for similar timescales as in the previous case. In this case, the OVIII column densities can explain the observed values, and for NeX as well, if the yield is increased by a factor of $\approx 2$ or the ambient density is increased to $\approx 0.3$ cm$^{-3}$.

## 3.4 Discussion

We have shown that the observed column density of OVIII, NeX, and SiXIV can be naturally explained if the line of sight passes through the reverse shocked gas in a non-radiative SNR in the extra-planar region of MW within $\sim$ 100–400 kyr from the time of the explosion. We have explored the variation of column density and temperature with

reasonable values of ejecta mass, blast energy, and ambient density. As mentioned in the introduction, such supernova explosions far from the Galactic plane can naturally be explained by massive runaway stars. However, to evaluate the feasibility of runaway massive stars exploding as supernovae above the Galactic plane as the primary source for the observed events, it is important to compare the frequency of such events with the observed frequency. In the solar neighbourhood, among massive stars that end their life as CCSNe, i.e., O stars and some B stars, $\sim 30\%$ of O stars and $\sim 10\%$ of B stars are found to be runaway stars (Gies & Bolton, 1986; Stone, 1991). On the other hand, the frequency of Galactic CCSN within the last $\lesssim 1$ Myr is constrained to be $1.9 \pm 1.1$ per century from the observed $\gamma$-ray emission from $^{26}$Al (Diehl et al., 2006). Based on the results presented in Section 3.3.5, the observed column densities of OVIII, NeX, and SiXIV can be explained if the explosion occurred $\sim$ 100–400 kyr ago. Assuming $\sim 20\%$ of all CCSNe are due to runaway OB stars with a total rate of $\sim 2$ per century, the number of such progenitors that were born during an interval of $\Delta \sim 250$ kyr is $N_{\rm runaway}(\Delta) \sim 1000$.

In order to estimate the final location of the supernova from runaway stars, the motion of the star after it is ejected from the Galactic disk needs to be simulated. We use GALPY (Bovy, 2015) to simulate the motion of runaway stars within the Galactic potential. Runaway OB stars can have large ejection velocities of up to $\sim 400\,{\rm km\,s^{-1}}$ from the disc that can be modelled by a Maxwellian distribution as found in Silva & Napiwotzki 2011. Following their result, we adopt a Maxwellian velocity distribution with a mean velocity of $150\,{\rm km\,s^{-1}}$ for the ejection velocity from the Galactic disk whose direction is assumed to be isotropic. Each runaway star is considered to have travelled a period of $\tau$ before it explodes as a supernova. The runaway star can be ejected either during the early phase of its life via the dynamical ejection mechanism from young open clusters (Poveda et al., 1967) or during the later phase via the binary ejection mechanism when one of the stars in a binary explodes as a supernova (Blaauw, 1961). We choose the value of $\tau$ from a uniform distribution ranging from 1–10 Myr to account for both early and late ejection. The initial radial coordinate of birth location is assumed to follow the stellar mass distribution from McMillan 2017. We use `MWPotential2014` in GALPY as the model for the MW potential with the circular velocity $v_{\rm c}(R_\odot = 8.21\,{\rm kpc}) = 233.1\,{\rm km\,s^{-1}}$ adapted from the best-fit values for the MW from McMillan 2017.

Figure 3.10a-b shows the final location of supernova explosion for a given realization of 1000 runaway stars in terms of their latitude $b$ and height $z$ above the Galactic plane as

a function of their distance $d$ from the Sun. Fig. 3.10c shows the corresponding locations in the $z$-$b$ plane. As can be seen from Fig. 3.10b, a majority ($\sim 93\%$) of the supernovae from runaway stars are confined to $|z| \leq 1\,\mathrm{kpc}$ and almost all of them at $|z| \lesssim 2\,\mathrm{kpc}$ with $d \lesssim 25\,\mathrm{kpc}$. Because of the low value of $z$, the overwhelming majority of $\sim 98.5\%$ of the sources have $|b| \lesssim 15^\circ$ where the sources with lower values of $d$ tend to have higher $b$. However, there are still $\sim 15$ events that occur at high latitudes of $> 15^\circ$ with values of up to $\sim 60^\circ$, out of which $\sim 9$ and $\sim 5$ occur at low heights of $|z| \lesssim 1\,\mathrm{kpc}$ and $|z| \lesssim 0.5\,\mathrm{kpc}$, respectively. These low $z$ and high $b$ sources are ideally suited to be the ones that correspond to observed sources that can satisfy the observed high values of $b$ along with high ambient densities. The cold neutral medium (CNM) and warm neutral medium (WNM) have mid-plane densities of $\approx 0.3$ and $0.1\,\mathrm{cm}^{-3}$, with a scale height of $\approx 0.15$ and $0.40\,\mathrm{kpc}$, respectively (Kalberla & Kerp, 2009). Thus, WNM in particular can provide the assumed fiducial ambient density of $0.1\,\mathrm{cm}^{-3}$. As a consequence of low $|z| \lesssim 1\,\mathrm{kpc}$, sources with high latitudes are also constrained to be confined to relatively low values of $d$ ranging from $\sim 0.75$–$1.5\,\mathrm{kpc}$. In particular, sources at highest latitudes of $\sim 60^\circ$ are also the closest sources at $d \sim 0.75$–$0.83\,\mathrm{kpc}$.

We note that recently, Lara-DI et al. 2023 have reported very high average column density of SiXIV of $(8.7 \pm 1.6) \times 10^{15}\,\mathrm{cm}^{-2}$, implying supervirial gas with $T \gtrsim 10^7\,\mathrm{K}$, using stacked spectra from *Chandra* along 46 different Quasar sightlines. We note here that the 'average' column density of SiXIV reported by Lara-DI et al. 2023 is that obtained from the stacked 'line', and is not the total column density divided by the number of sightlines used in stacking. A follow-up work found three distinct phases similar to Das et al. 2019b, including a very hot phase with $T \sim 3.2 \times 10^7\,\mathrm{K}$ from the same stacked sources (Lara-DI et al., 2024b). Even though these results do provide hints that supervirial gas with high column densities for H-like ions like SiXIV is possibly widespread in the CGM, currently, there is no robust observational constraint on the covering fraction of the absorbing hot gas. Future detections of high column density along a large number of individual sightlines are required to determine the covering fraction. In this regard, it is important to note here that $10^7$ K gas seen in emission needs to be differentiated from that seen in absorption, and although the covering fraction of emitting 'super-virial' gas is large, the case of the gas seen in absorption is likely different.

With regard to the scenario presented here, assuming the size of shocked gas from each SNR to be $\sim 30\,\mathrm{pc}$, the covering fraction for high latitude ($b > 15^\circ$) sources ranges

from $\sim 0.015$–$0.030$ steradian corresponding to $\lesssim 0.25\%$ of the sky whereas the covering fraction for low latitude ($b < 15^\circ$) sources ranges from 0.05–0.07 steradian corresponding $\lesssim 0.7\%$ of the sky. Thus, although the current scenario of CCSN from runaway stars can explain the high column density of highly ionized H-like ions like SiXIV along individual sightlines, they cannot account for a widespread CGM-wide distribution. It is important to note that regardless of whether superviral gas is present along particular sightlines or spread throughout the Galaxy, SNR from massive runaway stars will be present along multiple sightlines, including high altitudes that would have a high column density of highly ionized H-like ions. In this regard, it is interesting to note that at least 7 and 17 sources out of the total 46 sources in Lara-DI et al. 2023 have $|b|< 20^\circ$ and $|b|< 30^\circ$, respectively. Some of these sources could be due to CCSN from runaway massive stars.

Besides runaway stars, there are also other types of stars above the Galactic disk, although their numbers are relatively much smaller. Binary stars through dynamical interaction with a super-massive black hole (SMBH) in the center of MW can also eject one of the stars with a speed more than the escape velocity of the MW, thus producing hyper-velocity stars (Brown 2015). Some of the hypervelocity stars in the extra-planar region might have an external origin as well (Gülzow et al. 2023). Apart from being launched into the extra-planar region, stars are also formed *in situ* above the disk (Tüllmann et al., 2003; Martínez-Delgado et al., 2021; Howk et al., 2018). We do not consider these categories of stars important for our discussion because of their small numbers.

We should also like to mention the possibility of the ambient density being comparable to or even larger than the fiducial value of 0.1 cm$^{-3}$ at a height $\geq 0.5$ kpc above the disk. It is known that there are HI clouds above the disk, up to a height of $\sim 1.5$ kpc, and with average densities $\approx 0.3$ cm$^{-3}$ and diameters of $\approx$ 20–30 pc Lockman 2002. The current understanding is that these clouds originate in the disk and have moved up owing to their large vertical velocities. They also appear to have large turbulent speed, of order $\approx 75$ km s$^{-1}$ Kalberla & Dedes 2008, which is estimated from fitting the emission spectrum. According to Lockman 2002, as much as half the mass of the HI halo of the MW could be contained in such 'halo clumps'. These clouds are likely to be supported against the gravitational potential by random turbulent speeds, with which they can reach a height up to a few kpc Kalberla & Kerp 2009. It is difficult to estimate the volume filling factor of such clouds from their observed incidence rate (on average, one cloud per two square degrees) because of projection effects. However, the observed gas densities and the typical

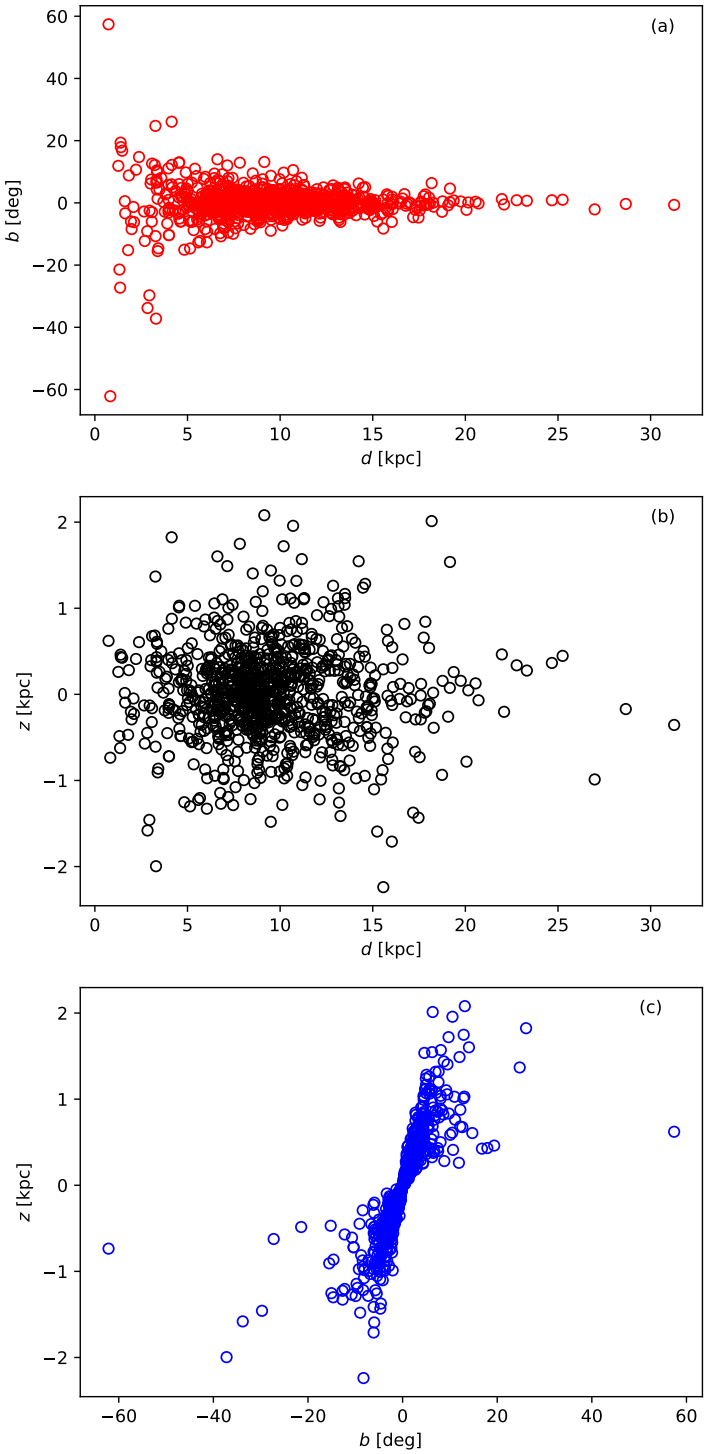



Figure 3.10: The final position of 1000 runaway massive stars where they explode as core-collapse supernovae: (a) latitude $b$ versus distance $d$ from the Sun, (b) Height $z$ from the Galactic plane versus $d$, and (c) $z$ versus $b$.

heights of these clouds are within the ranges required in our scenario. It is possible that the SNe discussed here could go off inside one such clump above the disk, in which case our assumption of ambient density would be quite reasonable.

Can these SNe be detected by other means, or do they leave any other signature? SNe produce radioactive $^{26}$Al which $\beta$-decays to excited states of $^{26}$Mg that subsequently emits the well known 1.809 MeV $\gamma$-ray (Diehl et al., 2006). The yield of $^{26}$Al in massive stars of 10–30 $M_\odot$ range from $\sim (0.3\text{–}1.5) \times 10^{-4}\, M_\odot$ (Tur et al., 2010). This corresponds to a photon flux of $F_\gamma \lesssim 1.8 \times 10^{-6}\, \gamma\, \mathrm{cm^{-2}\, s^{-1}}$ for a source at a distance of 1 kpc. This is more than an order of magnitude less than the line sensitivity of INTEGRAL at 1 MeV of $2.4 \times 10^{-5}\, \gamma\, \mathrm{cm^{-2}\, s^{-1}}$. This implies that even for the highest latitude sources that are also the nearest at $d \sim 1$ kpc, INTEGRAL cannot detect $\gamma$-rays from $^{26}$Al. However, future proposed $\gamma$-ray detectors such as GRAMS (Aramaki et al., 2020), that has a proposed line sensitivity of $(1.3\text{–}7.2) \times 10^{-7}\, \gamma\, \mathrm{cm^{-2}\, s^{-1}}$ for the 1.809 MeV $\gamma$-ray, would have a very good chance of detecting such sources.

The radio luminosity of SNRs at, say, 1.4 GHz can be estimated, using Equation 2 of Leahy et al. 2022, as,

$$\begin{aligned} L_{1.4} \quad &\approx 1.7 \times 10^{22}\, \mathrm{erg\, s^{-1}\, Hz^{-1}} \\ &\times \left(\frac{\eta}{5 \times 10^{-3}}\right) \left(\frac{R_b}{20\, \mathrm{pc}}\right)^3 \left(\frac{v_b}{300\, \mathrm{km/s}}\right)^{3.2} \end{aligned} \tag{3.25}$$

where $R_b, v_b$ are forward shock distance and velocity, and $\eta$ is a parameter that encodes various physical processes, such as the fraction of supernovae energy going into relativistic electrons, the efficiency of magnetic field amplification, etc. For our fiducial case, the forward shock has a speed of $\approx 300$ km s$^{-1}$ when the forward shock reaches $\sim 20$ pc. Leahy et al. 2022 have found, after comparison with observations, the value of $\eta$ to lie between $10^{-5}$–$10^{-1}$. Its value is likely to be on the lower side, given the weak magnetic field expected above the Galactic disc. If we require the radio flux at 1.4 GHz from an SNR at a distance of 1 kpc to be comparable to the observed flux of, say, Mrk 421 Błażejowski et al. 2005 ($\nu F_\nu \approx 5 \times 10^{-14}$ erg cm$^{-2}$), then the value of $\eta \approx 2 \times 10^{-5}$, which is the acceptable range, as mentioned above. In other words, the radio signature of the proposed SNR would be indistinguishable from or swamped by the background source, provided the supernova goes off at a distance of a kpc. However, at lower frequencies, while the synchrotron emission from SNR is expected to have a spectral index of $\sim -0.5$, that of the background blazar typically has a flatter index (with an average radio spectral index of 0.03, see Fig. 25 of Abdo et al. 2010) , that extends down to $\sim 300$ MHz Nori

et al. 2014, below which the index becomes positive due to self-absorption (Mooney et al., 2019). Therefore, a low-frequency observation of these blazars may be able to pick up the emission from the foreground SNR, which is brighter than the blazar at these frequencies. However, the radio spectral indices of blazars vary, and so do those of SNRs, from $\sim -0.85$ (shell-type) to $\sim 0$ (filled-center type) (Ranasinghe & Leahy 2023, their Fig. 7), and such variations may make it difficult to detect a foreground SNR in radio.

Finally, we note that a key difference between the scenario proposed in this work from the analysis used to infer super-virial gas in studies such as Das et al. 2019a, 2021; Lara-DI et al. 2024b, is the assumption of CIE. As mentioned in Section 3.3.3, the usual assumption of CIE is not at all applicable for the ejecta heated by the reverse shock described in this work. The abundance of ions is not in equilibrium but changes with time due to ionization, and eventually, all atoms become fully ionized. However, the timescale for ionization is different for each element, with longer timescales for heavier atoms. In our scenario, although a temperature cannot be assigned from an observed absorption line due to a lack of CIE, the super-viral nature of the gas is directly implied from large column densities observed for highly ionized H-like ions such as OVIII, NeX, and SiXIV.

## 3.5 Summary

Observations of the CGM of the MW in absorption along three lines of sight indicate rather large values of the column density of highly ionized H-like ions (Table 3.1) with temperatures larger than the virial temperature of the MW. In this paper, we argue that the observed column density of H-like ions such as OVIII, NeX, and SiXIV, implying super-virial temperatures exceeding a few million degrees K, can be naturally produced by supernovae remnants redfrom runaway stars above the Galactic disk, because of heating of metal-enriched ejecta by reverse shock. We show that observed column density is achievable with reasonable values of ejecta mass of $10\,M_{\odot}$, blast energy of $10^{51}$ erg, and the ambient density of $\sim 0.1$ cm$^{-3}$. We would like to propose that if the 'super-virial' phase with high column density of H-like ions is found to be limited to a few lines of sight rather than being widespread throughout the CGM, it is likely caused by the chance coincidence of supernovae remnants of runaway stars in the lines of sight to background sources.

# Chapter 4

# Misty, patchy, and turbulent: constraining the cool circumgalactic medium with mCC

Based on :
Bisht, M. S., Sharma, P., Dutta, A., & Nath, B. B. 2025, MNRAS, 542, 1573B
doi: 10.1093/mnras/staf1319

## Main Results

- The patchy, clumpy distribution of cool CGM gas distributed in the form of cloud complexes (CCs) naturally reproduces the observed scatter in the column densities of tracer ions such as MgII at similar impact parameters.
- A population of $\sim 10^3$ CCs, each with a size of $\sim 10$ kpc and following a power-law radial distribution ($dN_{\rm CC}/dR \propto R^{-1}$), can reproduce the COS-Halos observations (Werk et al., 2013) with a total cool gas mass of $\sim 10^{10}\,M_{\odot}$.
- The blending of absorption lines from multiple cool cloudlets intersected along a single line of sight, each with distinct line-of-sight velocities within a CC, gives rise to turbulent broadening on the CC scale.
- Assuming the mist limit (i.e., a unit area covering fraction) within a CC simplifies the computation of observables such as column density and equivalent width.

## 4.1 Introduction

The circumgalactic medium (CGM) is the vast reservoir of gas surrounding the stellar disk and the interstellar medium (ISM) of galaxies (Tumlinson et al., 2017; Faucher-Giguère & Oh, 2023). Various observations and numerical simulations suggest CGM to be multiphase with gas temperature varying by $\sim$ 2-3 orders of magnitude ($\sim 10^4$-$10^7$ K for Milky Way-like galaxies). Unlike the intracluster medium (ICM) of massive clusters of galaxies, which has been mapped extensively in X-ray emission (a recent review is Donahue & Voit 2022), the hot CGM in Milky Way-like galaxies (like X-ray emitting ICM, also likely to be the mass/volume dominant phase) is too dilute and compact to be mapped in emission. The cool/warm gas ($\sim 10^{4-5}$ K) in the CGM of foreground external galaxies is detected in absorption lines of low/intermediate ionization metal ions like MgII, CaII, SiII, CII, CIV, OVI in the spectra of bright background sources (typically quasars; Srianand & Khare 1993; Charlton et al. 2003; Chen et al. 2010; Bordoloi et al. 2011). Cool gas has recently been observed even in emission (MgII emission; Burchett et al. 2021; Zabl et al. 2021; Guo et al. 2023; Pessa et al. 2024), but emission is most sensitive to the densest cool gas.

A fundamental but unconstrained physical property of the CGM (unless qualified, we refer to the CGM of Milky Way-like galaxies) is its mass fraction in the cool phase. Although the cool ion (e.g., Mg II) column density (inferred from absorption lines) directly counts the number of ions along the sightline, the cool CGM mass is highly uncertain because of the limited number of quasars behind most intervening galaxies. Additionally, a significant variation in the inferred column density at similar impact parameters introduces uncertainty in estimating the cool gas mass. A key result of this paper is that the combination of the average column density and the area covering fraction (both observationally available quantities) provides a robust estimate of the cool gas mass in the CGM ($\sim 10^{10} M_\odot$ for Milky Way-like galaxies). Metal ion absorption is also affected by the elemental abundances, the photoionizing background, non-equilibrium effects, and dust depletion. Since the dispersion measure provides column density of free electrons, which is not affected by these complications, fast radio bursts (FRBs) are promising probes of the total CGM mass (Prochaska & Zheng 2019; Cook et al. 2023). However, we cannot distinguish the various thermal phases of the CGM from FRB dispersion measures.

The cool gas in the CGM likely has various formation channels (Decataldo et al. 2024),

including, e.g, cooling from hot gas in the CGM due to thermal instabilities (McCourt et al. 2012; Voit et al. 2017), cosmological accretion onto the galaxy (Rahmani et al. 2018; Afruni et al. 2019), stellar and AGN outflows (Augustin et al. 2021; Burchett et al. 2021), and stripping from satellite galaxies (Rubin et al. 2012; Roy et al. 2024). Cool gas clouds are also disrupted by shear instabilities, potentially leading to their evaporation in the presence of a surrounding hot medium (Lan & Mo 2019). Several theoretical and semi-analytical studies have attempted to investigate the structure and distribution of cool gas within the CGM (Stern et al. 2016; Hummels et al. 2024; Faerman & Werk 2023; Yang et al. 2025). The models presented in this paper are agnostic to the specific cool gas formation and disruption mechanisms but provide a tool for building phenomenological models of the mass and radial distribution of the cool gas in the CGM.

The cool gas is observed to have an area covering fraction of order unity (Dutta et al. 2020; Huang et al. 2021), while the volume fraction is expected to be $\lesssim 1\%$ (Faerman & Werk 2023; Dutta et al. 2024a). This suggests that the cool gas is not uniformly distributed in the CGM, unlike the hot gas, but rather distributed in clumpy structures dispersed in the hot CGM.

Recently, Dutta et al. 2024a (hereafter D24) modeled the cool gas with a three-phase, one-zone CGM model. This model fills all the cool CGM gas uniformly as a mist of numerous cloudlets, with a small volume filling fraction but a unity area covering fraction, in the entire CGM. We refer to this as the *mCGM* (misty CGM) model. They modeled the cool gas in one of the TNG50-1 halos and predicted the baseline column density of MgII to be $\sim 10^{13}\,\mathrm{cm}^{-2}$ (the solid cyan line in their Fig. 11). This is smaller than the typical observed column density, despite the large scatter in observed values and several stringent upper limits, suggesting that the cool gas does not block all sightlines uniformly. In the *mCGM* model, the cool gas is distributed throughout the CGM volume, resulting in a low number density and therefore a low column density. To explain the empty sightlines and the observed scatter in the column density, the cool gas ought to be distributed in a smaller volume than the entire CGM. This will result in a higher particle number density and a larger column density for sightlines passing through cool clouds and non-detection along the empty sightlines. One can distribute the cool gas in several cloud complexes (CCs) rather than uniformly throughout the entire CGM and better explain the observations. In this paper, we extend the work of D24, moving beyond a completely misty CGM to a more realistic CGM filled with misty cloud complexes. We

refer to our model based on CCs as *mCC* model, which stands for misty cloud complex.

Another closely related work to ours is the *CloudFlex* model (Hummels et al. 2024; hereafter HR24). They generated numerous ($\gtrsim 10^6$) cloudlets within a CC, modeled absorption profiles, and based on their analytic halo scale model for cool gas mass distribution, predicted the equivalent width (EW) distribution of the MgII line. The CCs in the CGM are analogous to terrestrial clouds that are made up of an astronomical number of tiny water droplets. The CGM observations of individual absorption components at high-velocity resolution suggest the cloudlets to be $\lesssim 1$ pc (e.g., Fig. 17 of Sameer et al. 2024 and Fig. 3 of Chen et al. 2023). It is impossible to computationally model such an enormous number of cloudlets within a CC from first principles[1]. Instead, in this work (section 4.3) we present a computationally tractable approach complementary to HR24, treating the cloudlets within a CC analytically in the mist limit and generating Monte Carlo realizations of a manageable number ($10^{3-4}$) of CCs throughout the CGM.

We put our *mCC* model in the context of *mCGM* (D24) and *CloudFlex* (HR24) models. Following HR24, we create Monte Carlo realizations of cloudlets within a single CC in section 4.4, with an increasing number of smaller cloudlets to show that the misty CC approximation provides a satisfactory description of the otherwise computationally intractable realization of an enormous number of cloudlets within a CC. Later in section 4.5, we generate Monte Carlo realizations of not only individual cloudlets within a single CC but also the distribution of CCs across the CGM. In this computationally prohibitive model, we cannot reach the mist limit, but we compare the distribution of EWs and obtain the best model parameters. To conclude, our *mCC* model not only acts as a tractable bridge between the simple misty CGM model of D24 and the realistic but computationally expensive *CloudFlex* model (HR24), but also provides an intuitive understanding of the complex distribution of cool gas in the CGM.

The MgII doublet metal transition $\lambda\lambda\,2796, 2803$ is well observed and studied in the absorption of quasar light from the intervening CGM of external galaxies. In this work, we focus on MgII $\lambda$2796, but our model can also be used to analyze other cool ions like SiII, CaII, and CII, and with simple extension, also intermediate ions such as CIV and OVI (c.f. section 4.6.2). Starting with MgII observational data in section 4.2, we present our misty cloud complex (mCC) model in section 4.3. In section 4.4, we zoom in on a single

[1]If 1 pc is the typical cloudlet size, we would need $\sim 10^{13}$ cloudlets to make up $10^{10} M_\odot$ in the cool CGM.

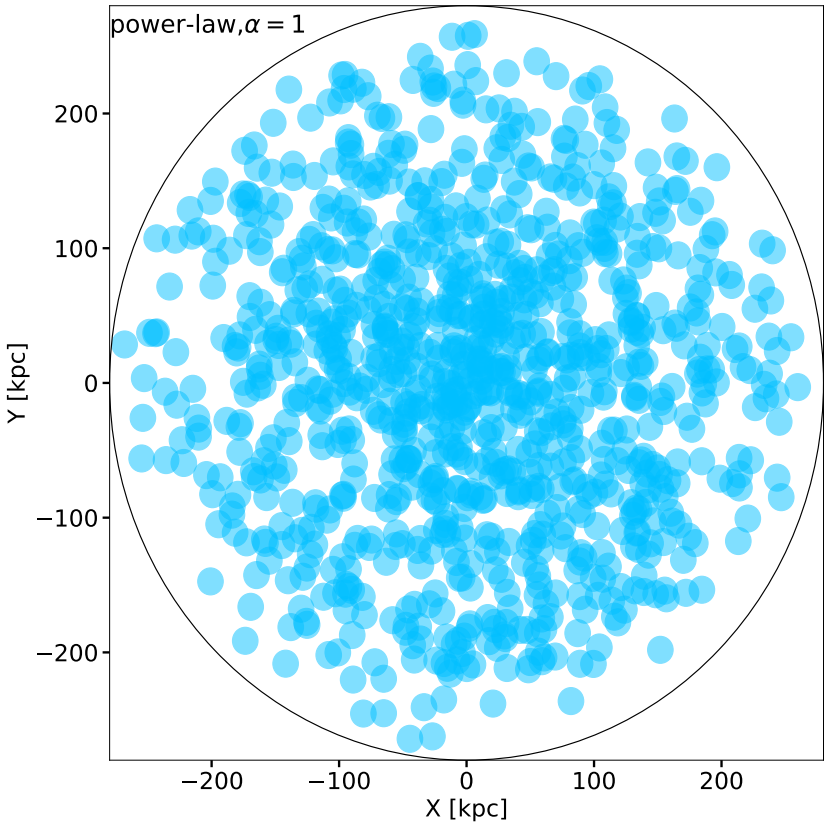



Figure 4.1: The line of sight (LOS) projected distribution of $10^3$ CCs each of radius 10 kpc in the CGM of radius 280 kpc with a power-law CC distribution of index $\alpha = 1$ (Eq. 4.7). Notice that there are numerous empty regions towards the outer regions of CGM and comparatively fewer empty regions in the center. The LOSs passing through CGM outskirts will, therefore, not produce strong ion absorption in contrast with the central sightlines intersecting multiple CCs.

CC to verify the mist limit, particularly in velocity space. In section 4.5 we consider the distribution of cloudlets within CCs (rather than assuming the mist limit), distributed non-uniformly in the CGM. We end with a discussion and summary in sections 5.4 and 4.7, respectively.

## 4.2 Observational Data

Several surveys have been conducted to study cool gas in the CGM in the last $\sim$ 2-3 decades over several redshift and stellar mass ranges, eg, MAGiiCAT (Nielsen et al. 2013), MAGG (Dutta et al. 2020), SDSS DR16 (Anand et al. 2021), CUBS (Qu et al. 2023), and

MEGAFLOW (Cherrey et al. 2025), etc. For uniformity in redshift and stellar masses, in our work, we compare our model results with the COS-Halos (Werk et al. 2012) survey and the Magellan MagE Mg II (M3) Halo project (Huang et al. 2021). The COS-Halos survey comprises 44 $\sim L^*$ galaxies with stellar mass in the range $10^{9.5}$-$10^{11.5}\,M_\odot$ with a median of $10^{10.5}\,M_\odot$ at the impact parameter of 15-160 kpc. The redshift range of these galaxies is 0.1-0.4 with a median redshift of 0.22. We obtained the MgII column density and equivalent width data from Werk et al. 2013 and the corresponding normalized impact parameter values from Werk et al. 2014. The M3 Halo project comprises 211 isolated galaxies with an impact parameter of $9-497$ kpc, with a median of 94 kpc. The redshift range is $0.1-0.48$ with a median of 0.21. These galaxies span a wide range in stellar mass of $2\times10^8-4\times10^{11}\,M_\odot$ with a median stellar mass of $4\times10^{10}\,M_\odot$. They obtained the best-fit log-log relation between the MgII equivalent width $W_{2796}$ and the impact parameter ($R_\perp$) for the isolated galaxy sample as,

$$\begin{aligned}\log W_{2796}(\text{Å}) &= (1.35\pm0.25)-(1.05\pm0.17)\log R_\perp \\ &\quad +(0.21\pm0.08)\times(\log \mathrm{M}^*_\odot-10.3).\end{aligned} \tag{4.1}$$

They have also estimated the covering fraction at various impact parameter ranges with various equivalent width thresholds, which we will compare with our model prediction later.

Note that the two surveys have similar median stellar mass and redshift. Therefore, we use the observational data from both surveys to compare the MgII column density, EW, and covering fraction with our model predictions. Since the median redshift of these surveys is $\sim 0.2$, we compute the MgII ion fraction at the redshift of 0.2 for our model. Our model can also be compared with observations from other surveys with different redshift ranges, provided that the ion fraction is computed at that redshift.

## 4.3 Misty cloud complexes in the CGM

Motivated by observations and simulations (area covering fraction and volume fraction), we assume that the cool gas resides in cloudy structures rather than filling the entire CGM volume (D24). We refer to these structures as 'cloud complexes' (CCs) following HR24. These CCs are filled with tiny cool gas cloudlets. One of the caveats of the misty CGM model of D24 is that it predicts cool gas along all LOSs, which is inconsistent with

observations. If, instead, the cool gas is spread non-uniformly in these CCs, there will be sightlines not covered by cool gas. For illustration, in Figure 4.1, we show the line of sight (LOS) projected distribution of CCs in the CGM where the number density of CCs as a function of distance from the center follows a power-law profile with a power-law index of 1. There are $10^3$ CCs in total, each of radius 10 kpc, distributed in the CGM of radius 280 kpc. There are numerous empty regions without any CCs. The LOSs passing through these regions will result in no detection of cool gas (corresponding to the upper limits on the MgII column). These empty regions are everywhere in the CGM (fewer in the central region than in the outskirts). The LOSs passing through multiple CCs will result in a higher column density of cool ions. Therefore, an intrinsic scatter in the column density at a similar impact parameter is a natural outcome of the distribution of cool gas in CCs rather than uniformly in the entire CGM.

We consider the CCs to be misty (the mist limit is attained for numerous enough tiny cloudlets; see Appendix A), with the area covering fraction of cloudlets within a CC equal to unity ($f_A^{\rm cl} = 1$). The area covering fraction of CCs ($f_A^{\rm CC}$ different from $f_A^{\rm cl}$) is the fraction of the CGM area occupied by CCs. This cannot exceed unity if we do not separately count the areas of overlapping CCs; otherwise, it may exceed unity. Assuming the mist limit within each CC, we distribute the CCs in the CGM, compute the observables (column density, equivalent width distributions, covering fraction), and compare them with observations. For concreteness, we compare average quantities for a uniform and a power-law distribution of CCs.

If $M_{\rm cool}$ and $N_{\rm CC}$ are the total cool gas mass and the total number of CCs in the CGM, respectively, then the mass of each CC is $M_{\rm CC} = M_{\rm cool}/N_{\rm CC}$, assuming (for simplicity) that all the CCs have the same mass. The average number density of cool gas in each CC (distinct from the physical density of the cool gas) is then $\langle n_{\rm gas}\rangle = 3M_{\rm CC}/(4\,\pi R_{\rm CC}^3\,\mu m_{\rm p})$, where $R_{\rm CC}$ is the radius of CC and $\mu m_p$ is the mean molecular weight which we assume to be $0.6m_p$ ($m_p$ is proton mass) since hydrogen is mostly ionized even in cool CGM. We fix the mass and radius of CCs and refer to this model as the 'basic' model. Later, in Sec. 4.3.8, we consider the size and mass distribution of CCs in the CGM and refer to it as the 'advanced' model.

### 4.3.1 Analytical estimates

Before examining the Monte Carlo realization of CCs distributed across the CGM, it is helpful to provide analytic estimates of the average number of CCs and the mean ion column density along a LOS to facilitate a better understanding of the model.

#### Uniform distribution of cloud complexes

We begin with a uniform distribution of CCs in the CGM. So, the average number density of CCs is $\langle n_{\rm CC}\rangle = 3N_{\rm CC}/(4\ \pi R^3_{\rm CGM})$,[2] where $R_{\rm CGM}$ is the CGM radius. The average number of CCs intersected along a given LOS (see Table 4.1 for a list of commonly used symbols) at an impact parameter $R_\perp$ is

$$\langle N_{\rm CC,LOS}\rangle(R_\perp) = 2\int_0^{s_{\rm max}} \langle n_{\rm CC}\rangle \pi R^2_{\rm CC} ds, \tag{4.2}$$

where $ds$ is the line element along the LOS and $s_{\rm max} = \sqrt{R^2_{\rm CGM} - R^2_\perp}$. This trivial integral gives the average number of CCs encountered along a LOS,

$$\langle N_{\rm CC,LOS}\rangle(R_\perp) = \frac{3N_{\rm CC}R^2_{\rm CC}}{2R^3_{\rm CGM}}\sqrt{R^2_{\rm CGM} - R^2_\perp}. \tag{4.3}$$

The area covering fraction of CCs in a CGM starts to approach unity when the average number of CCs along a LOS exceeds unity, i.e., $\langle N_{\rm CC,LOS}\rangle \gtrsim 1$. For fiducial parameters ($R_{\rm CC} = 10$ kpc, $R_{\rm CGM} = 280$ kpc), this happens when $N_{\rm CC} \gtrsim 500$. The average column density of an ion is

$$\langle N_{\rm ion}\rangle(R_\perp) = 2\int_0^{s_{\rm max}} (\langle n_{\rm CC}\rangle \pi R^2_{\rm CC} ds)(\langle n_{\rm ion}\rangle(R)\langle L\rangle), \tag{4.4}$$

where the terms in the first bracket count the average number of CCs intersected along $ds$ and the terms in the second bracket represent the average column density of an ion from a single CC. Here $\langle n_{\rm ion}\rangle(R)$ is the average number density of an ion in a CC at a distance $R$ from the center, which equals $\langle n_{\rm gas}\rangle \times f_{\rm ion}(R)$, where $f_{\rm ion}(R)$ is the ion fraction that depends on the physical number density of the cool gas for a given redshift and metallicity and $\langle n_{\rm gas}\rangle$ is the average number density of cool gas in a CC (distinct

[2]Note that we do not consider the inner 10 kpc region of the galaxy. The average number density of CCs ($\langle n_{\rm CC}\rangle$) does not vary significantly if we consider only the CGM volume excluding the ISM, since $R^3_{\rm CGM} \gg (10\ {\rm kpc})^3$.

| Symbol | Meaning |
|---|---|
| $R_{\rm CGM}$ | Radius of CGM |
| $R_{\rm CC}$ | Radius of a cloud complex |
| $R_{\perp}$ | Impact parameter |
| $M_{\rm cool}$ | Total cool gas mass in the CGM |
| $M_{\rm CC}$ | Mass of a cloud complex |
| $N_{\rm CC}$ | Number of cloud complexes in the CGM |
| $\alpha$ | Power-law index of CC radial distribution |
| $N_{\rm cl}$ | Number of cloudlets in a CC |
| $r_{\rm cl}$ | Radius of a cloudlet |
| $f_A^{\rm CC}$ | Area covering fraction of CCs in CGM |
| $f_A^{\rm cl}$ | Area covering fraction of cloudlets in a CC |
| $\langle N_{\rm CC,LOS}\rangle$ | Average number of CCs intersected along a sightline |
| $\langle N_{\rm ion}\rangle$ | Average column density of an ion along a sightline |
| $f_{\rm V}$ | Volume filling fraction of cool gas in a CC |
| $f_{\rm V}^{\rm CC}$ | Volume filling fraction of CCs in CGM |
| $n_{\rm cool}$ | Physical number density of cool gas |
| $\langle n_{\rm gas}\rangle$ | Average density of gas in a misty CC |
| $\langle n_{\rm CC}\rangle$ | Average number density of CCs |
| $\langle n_{\rm ion}\rangle$ | Average number density of an ion |
| $f_{\rm ion}$ | Ion fraction |
| $b_{\rm thermal}$ | Thermal broadening |
| $b_{\rm turb,CC}$ | Turbulent broadening across a CC |
| $b_{\rm tot}$ | Total broadening |
| $W_{2796}$ | Equivalent Width of MgII |
| $v_{\rm LOS}$ | LOS velocity |

Table 4.1: Symbols used in this paper and their description. Our *fiducial parameters* are $R_{\rm CGM} = 280$ kpc, $R_{\rm CC} = 10$ kpc, $M_{\rm cool} = 10^{10} M_{\odot}$, $N_{\rm CC} = 10^3$, and $\alpha = 1$.

from physical density of cool gas)[3], $\langle L \rangle$ is the area-averaged path length across a CC, which is equal to,

$$\langle L \rangle = \frac{\int_0^{R_{\rm CC}} 2\pi b db \, 2\sqrt{R_{\rm CC}^2 - b^2}}{\int_0^{R_{\rm CC}} 2\pi b db} = \frac{4}{3} R_{\rm CC}. \tag{4.5}$$

Therefore, we get the following expression for the average column density of an ion along the LOS at an impact parameter of $R_\perp$,

$$\langle N_{\rm ion} \rangle (R_\perp) = 2 N_{\rm CC} \left( \frac{R_{\rm CC}}{R_{\rm CGM}} \right)^3 \langle n_{\rm gas} \rangle \int_{R_\perp}^{R_{\rm CGM}} f_{\rm ion}(R) \frac{R dR}{\sqrt{R^2 - R_\perp^2}}. \tag{4.6}$$

### Power-law distribution of cloud complexes

Next, we use a power-law distribution of the number of CCs as a function of $r$ of the form

$$\langle n_{\rm CC} \rangle (R) = n_0 \left( \frac{R}{R_{\rm CGM}} \right)^{-\alpha}, \tag{4.7}$$

where $\alpha$ is the power-law index and $n_0$ is obtained using the normalization condition $N_{\rm CC} = \int \langle n_{\rm CC} \rangle (R) 4\pi R^2 dR$. We get the following expressions for the average number of CCs intersected and the column density of an ion along a LOS at an impact parameter $R_\perp$,

$$\langle N_{\rm CC,LOS} \rangle (R_\perp) = 2 n_0 \pi R_{\rm CC}^2 R_{\rm CGM}^\alpha \int_{R_\perp}^{R_{\rm CGM}} \frac{R^{-\alpha+1}}{\sqrt{R^2 - R_\perp^2}} \, dR, \tag{4.8}$$

and

$$\langle N_{\rm ion} \rangle (R_\perp) = \frac{8}{3} n_0 \pi R_{\rm CC}^3 R_{\rm CGM}^\alpha \langle n_{\rm gas} \rangle \int_{R_\perp}^{R_{\rm CGM}} f_{\rm ion}(R) \frac{R^{-\alpha+1}}{\sqrt{R^2 - R_\perp^2}} \, dR. \tag{4.9}$$

In addition to the average column density, we also calculate the standard deviation using estimates derived in Appendix A.2.

### Volume & mass fraction of cool gas in CCs

The mass fraction of CGM in the cool ($\sim 10^4$ K) phase is subdominant compared to the volume-filling hot phase (e.g., D24, Faerman & Werk 2023). The volume fraction is even smaller since cool gas is denser. Table 3 in D24 quotes a cool mass fraction of 11.9% and a volume fraction of 0.16% for a Milky Way-like TNG50 halo. Since in our CC model,

[3]Physical density is the true or the local density of the cool gas whereas the average density is the global average density taking into account the full available volume (see Figure 2 of D24).

cool gas is confined only within CCs, we expect the volume and mass fraction of cool gas within a CC to be higher than the whole CGM.

The volume fraction of cool gas within a CC is

$$f_V = \frac{M_{\rm cool}}{N_{\rm CC}\mu m_p n_{\rm cool}(4\pi R_{\rm CC}^3/3)} = 0.016 \left(\frac{M_{\rm cool}}{10^{10}\ M_\odot}\right) \times \left(\frac{N_{\rm CC}}{10^3}\right)^{-1} \left(\frac{n_{\rm cool}}{10^{-2}\,{\rm cm}^{-3}}\right)^{-1} \left(\frac{R_{\rm CC}}{10\,{\rm kpc}}\right)^{-3}, \tag{4.10}$$

and the mass fraction is,

$$f_M = \frac{M_{\rm CC}}{M_{\rm CC} + (1-f_V)\mu m_p n_{\rm hot}(4\pi R_{\rm CC}^3/3)}, \tag{4.11}$$

which equals 0.62 for our fiducial parameters (assuming $n_{\rm hot} = 10^{-4}$ cm$^{-3}$ for hot gas in pressure equilibrium with cool clouds). As expected, the volume and mass fraction of cool gas within CCs are higher than in the full CGM. The volume fraction of CCs within the CGM is

$$f_V^{\rm CC} = N_{\rm CC}\left(\frac{R_{\rm CC}}{R_{\rm CGM}}\right)^3 = 0.05 \left(\frac{N_{\rm CC}}{10^3}\right)\left(\frac{R_{\rm CC}}{10\,{\rm kpc}}\right)^3 \left(\frac{R_{\rm CGM}}{280\,{\rm kpc}}\right)^{-3}. \tag{4.12}$$

However, the volume fraction of cool gas in the CGM as a whole would be tiny, $f_V^{\rm CC} \times f_V \approx 0.08$ %, consistent with Table 3 of D24 based on a Milky Way-like TNG50 halo. The volume fraction of CCs is typically small, yet the area covering fraction can be substantial because of projection along the LOS (e.g., see Figure 4.1). This also means that the probability for the overlap of two CCs is small ($\sim 5\%$), implying that such overlapping CCs do not affect our statistics. Therefore, we do not bother about ensuring that CCs do not overlap.

### 4.3.2 Physical number density profile of cool gas

The pressure of the cool gas is expected to be higher in the central regions than in the outskirts. This pressure variation will result in density variation across the CGM, with higher density in the center and lower density in the outskirts. Motivated by Stern et al. 2016, who modeled the cool photoionized CGM gas and found that the mean cool gas density scales as $R^{-1\pm0.3}$ (see also, Faerman et al. 2025), we assume the following cool gas density profile,

$$n_{\rm cool}(R) = 10^{-3} \times \left(\frac{R}{R_{\rm CGM}}\right)^{-1} {\rm cm}^{-3}. \tag{4.13}$$

A similar density scaling with radius is also found by Werk et al. 2014 for the COS-Halos sample. The CGM is expected to have a shallower density profile compared to the dark matter density because of feedback (e.g., see Fig. 2 in Sharma et al. 2012 for the hot gas density profiles inferred in groups and clusters), and we try this specific form to test the impact of varying $n_{\rm cool}$ with radius. The variation in the physical density of cool gas only changes the ion fraction ($f_{\rm ion}$; see Appendix A.1) as a function of radius at a given redshift and for a given metallicity.

### 4.3.3 Understanding analytical results

Using the analytical estimates and the physical density of cool gas, we calculate and compare the mean MgII column density for various parameters. We adopt $M_{\rm cool} = 10^{10}\,M_{\odot}$, $R_{\rm CC} = 10$ kpc, $N_{\rm CC} = 10^3$, and $R_{\rm CGM} = 280$ kpc as our fiducial values. There are several observational studies of the coherence length of the metal-bearing cool gas in the CGM. Afruni et al. 2023 and Shaban et al. 2025 found the coherence length of MgII to be $\sim 5$ and 2.7 kpc respectively while Dutta et al. 2024b estimated it to be $\approx 10$ kpc. Therefore, we choose 10 kpc as our fiducial value for the radius of CC. To obtain the MgII ion fraction, we consider Eq. 4.13 for the cool gas density profile. We compute the MgII ion fraction using CLOUDY (Ferland et al. 2017) at a redshift of 0.2 and a temperature of $10^4$ K. We choose KS18 (Khaire & Srianand 2019) as the background radiation field (see Figure A.2). We also consider a constant metallicity of 0.3 solar (Prochaska et al. 2017) to compute the MgII column density.

In the *top panel* of Figure 4.2, we show the average MgII column density as a function of the normalized impact parameter for various models. The black line shows the baseline MgII column density from the misty CGM model of D24. We choose the parameters similar to (but not identical to; in particular, our CGM extent of 280 kpc is smaller than their choice of 333 kpc) what D24 found for one of the Milky Way-like TNG50 halos. The blue line shows the average MgII column density for uniform distribution (Eq. 4.6) while magenta and orange lines show the column density for power-law distribution with power-law index of $\alpha = 1$ and 2 respectively (Eq. 4.9). The column density profile from D24 shows no trend with impact parameter,[4] while uniform and power-law distributions of

[4]This is due to constant ion fraction values assumed at all radii. In Fig. 11 of D24, they assume a constant $f_{\rm MgII} = n_{\rm MgII}/n_{\rm Mg}$, which gives a flatter MgII column density compared to a self-consistent model that allows $f_{\rm MgII}$ to vary with pressure (e.g., see Fig. 6 of Faerman & Werk 2023).

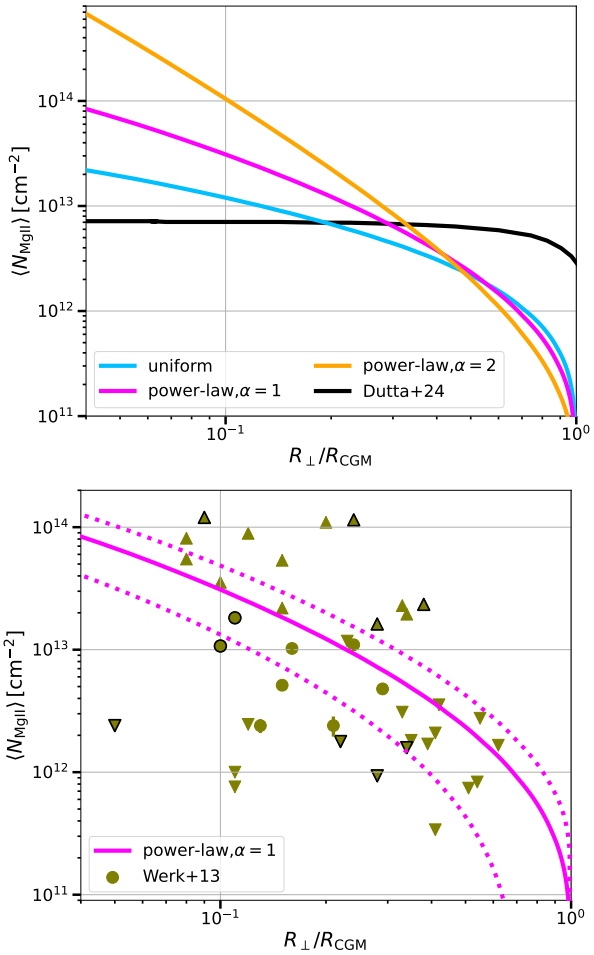



Figure 4.2: The *top panel* shows the mean MgII column density as a function of normalized impact parameter. The black line shows the baseline column density from D24. The blue line shows the mean MgII column density for uniform distribution, while magenta and orange lines show the same for power-law distribution of CCs in the CGM with power-law index of 1 and 2 respectively (Eqs. 4.6, 4.9). The baseline column density predicted by D24 shows no trend with the impact parameter, while the uniform and power-law distributions show a declining trend, which is observationally observed. However, the column density values for the power-law index of $\alpha = 1$ (magenta line) better match the typical values from observations. So we choose a power-law distribution with index $\alpha = 1$ as our fiducial parameter. The solid magenta line in the *bottom panel* shows the mean MgII column density for the fiducial value of $\alpha = 1$. The dotted magenta lines show the expected standard deviation (see Appendix A.2) from the average. The data points are from the COS-Halos survey (Werk et al. 2013). Even the data with smaller redshift $(0.15 - 0.25)$ and stellar mass bins $(10.5 - 11$ in $\log_{10}$; encircled with black color) show intrinsic scatter in the column density data.

CCs in CGM show a declining trend with the impact parameter, which is what is observed. This declining trend has contributions from both the power-law distribution of CCs and the variable ion fraction with radius. Clearly, uniform and power-law distributions with $\alpha = 2$, respectively, under- and over-predict the typical MgII column density values. Therefore, we choose a power-law distribution with index $\alpha = 1$ as our fiducial model.

In the *bottom panel*, the solid magenta line shows the mean MgII column density for our fiducial model ($\alpha = 1$). The dotted magenta lines show the expected spread (standard deviation) in column density (see Eq. A.4), which is computed by taking care of the variation in the number of CCs along a LOS and the deviation in the intersected length of a CC. To estimate the standard deviation, we choose the MgII ion fraction value at the smallest 3D distance (equal to the impact parameter) at a given impact parameter. Also plotted are the observations from the COS-Halos (Werk et al. 2013) survey. The circles show detections, while the upper and lower triangles show the lower and upper limits, respectively. The data points encircled with black color are the sub-samples with a narrower redshift range of $0.15 - 0.25$ and stellar mass range of $10.5 - 11.0$ (in log10). The observationally inferred column densities are typically the total column density along a LOS, summing over the individually detected components.

Notice a larger scatter in the observed MgII column density values at similar impact parameters. The large scatter can arise due to various possibilities like a broad range in the halo/stellar masses of galaxies, a range in redshifts, different galaxy types (quiescent/star-forming), and orientation. However, the sub-samples (points encircled with black color) with a narrow range in stellar mass and redshift also show significant scatter. Therefore, there must be an intrinsic or true scatter in the column densities of ions tracing the cool CGM. The true scatter most likely arises due to the clumpy nature of the cool gas, projection effects, and intrinsic scatter in the cool gas number density at similar impact parameters (Yang et al. 2025). Using absorption line measurements in the spectra of multiple background quasars at different impact parameters, Rao et al. 2013 and Lehner et al. 2020 mapped the CGM of M31 and found a clear scatter in the column densities of ions tracing its cool gas. By combining the observed column densities of SiII, SiIII, and SiIV, Lehner et al. 2020 showed that the total silicon column density also exhibits scatter (see their Fig. 10), indicating the clumpy nature of the cool gas. The true scatter would be clearer from future observations/surveys (e.g., Ng et al. 2025) with a larger sample of galaxies having similar stellar mass, redshift, and types. Our

analytical expressions (Eqs. 4.6, 4.9) pass through the general scatter of the observations. The average column density does not provide stringent constraints on the nature and distribution of CCs because of a large spread and scattered upper/lower limits in the observationally inferred MgII column density. These observations motivate our Misty CC model.

### 4.3.4 Monte Carlo realizations of CCs in the CGM

The analytical estimates of the mean column density and its deviation provide an excellent framework to compare the trends in observed column density. However, to compare the possible intrinsic spread in observed MgII column densities and EW with the model prediction, we need to create a Monte Carlo realization of CCs in the CGM. The intrinsic scatter in the observed column density values at similar impact parameters can be reproduced by limiting the cool gas to misty CCs rather than filling the entire CGM by cool mist (as in D24).

To generate a Monte Carlo realization of CCs in the CGM, we populate $N_{\rm CC}$ number of CCs each of radius $R_{\rm CC}$ in the CGM for power-law distributions with index $\alpha = 1$. We first sample the radial distance $r$ of the center of CC from the power-law distribution (see Eq. 4.7). We then draw a uniform deviate in $\phi$ ranging from 0 to $2\pi$ and in $\cos\theta$ from $-1$ to 1. Using these $r, \phi$ and $\theta$, we compute the $x, y, z$ coordinates. We ensure that the CCs are not populated beyond the CGM boundary ($R_{\rm CGM}$) by recomputing the CC coordinates in case they are.

After generating the centers of CCs, we shoot $10^4$ LOSs (spaced uniformly in $\log_{10} R_\perp$) through the CGM in the $z$ direction. We then compute the $x, y$ coordinates of the LOS by drawing a random value of $\phi$ uniformly between 0 and $2\pi$ and calculate the number of CCs intersected and the corresponding intersected lengths along each LOS. We calculate the total column density for each intersected CC using the intersected length, the average cool gas density in the CC ($\langle n_{\rm gas} \rangle$), and the MgII ion fraction. To calculate the MgII column density, we calculate the MgII ion fraction using the physical cool gas density (Eq. 4.13) and the ion fraction at a redshift of 0.2, assuming a cool gas temperature of $10^4$ K, metallicity of 0.3, and KS18 as background radiation field (see Appendix A.1). Recall that our CCs are assumed to be uniform and in the mist limit. In the observations, column density is typically derived from the Equivalent Width (EW) based on Voigt

profile modeling of various absorption components in the background quasar continuum produced by the intervening CGM. In our model, we first calculate the column density and then the corresponding EW, assuming a velocity field in the CGM and turbulent broadening across a CC, which we discuss below in detail.

### Computing Equivalent Width

We can compute the EW using the column density estimated above using the curve of growth and assuming a reasonable $b$-parameter (that characterizes the thermal and turbulent broadening of the absorption line; Draine 2011). For a MgII column density $\gtrsim 10^{13}$ cm$^{-2}$, the EW will be lower than the linear extrapolation of the flat portion of the curve of growth (see Figure 4.3). For example, if we have 10 CCs (coinciding in LOS and turbulent velocities so that they produce a single absorption feature) along a LOS, each with a MgII column density $\sim 10^{13}\,\mathrm{cm}^{-2}$, then the EW computed using the total column density will be lower than the sum of EWs computed for each CC individually. However, summing the EWs is appropriate when the LOS CCs are kinematically non-overlapping. The correct EW along a LOS lies between these two extremes and depends on the details of the LOS and the turbulent velocities of cloud complexes.

### Ansatz for turbulent broadening across a CC

To compute EW, we consider both thermal and turbulent broadening across a CC. We assume the temperature of the cool gas to be $10^4$ K, which gives thermal broadening of $b_{\rm thermal} = \sqrt{2k_BT/(Am_p)} = 2.6\,\mathrm{km\,s^{-1}}$ for MgII. We also consider the contribution of turbulent broadening ($b_{\rm turb,CC}$; across a CC) for each CC. We compute $b_{\rm turb,CC}$ in as follows. Assuming that turbulence is driven at CGM global scales with velocity dispersion $\sigma_{\rm turb,CGM}$ that cascades down to CC scale without loss,[5] the velocity dispersion at CC scale is given by $\sigma_{\rm turb,CC} = \sigma_{\rm turb,CGM} \times (R_{\rm CC}/R_{\rm CGM})^{1/3}$. Therefore, the total broadening is $b_{\rm tot} = \sqrt{b^2_{\rm thermal} + b^2_{\rm turb,CC}}$ (in the micro-turbulent limit; Mihalas 1978), where $b_{\rm turb,CC} = \sqrt{2}\sigma_{\rm turb,CC}$. To estimate $\sigma_{\rm turb,CGM}$, we assume the turbulent Mach number of the hot ($\sim 2 \times 10^6$ K), volume-filling CGM to be $\sim 0.5$ (e.g., Schmidt et al. 2021; Mohapatra

[5]In Kolmogorov-like turbulence, kinetic energy cascades without loss across inertial scales with the turbulent velocity at scales $l$ and $L$ related as $v_l = v_L(l/L)^{1/3}$, down to the small viscous scale at which it dissipates (Kolmogorov 1991).

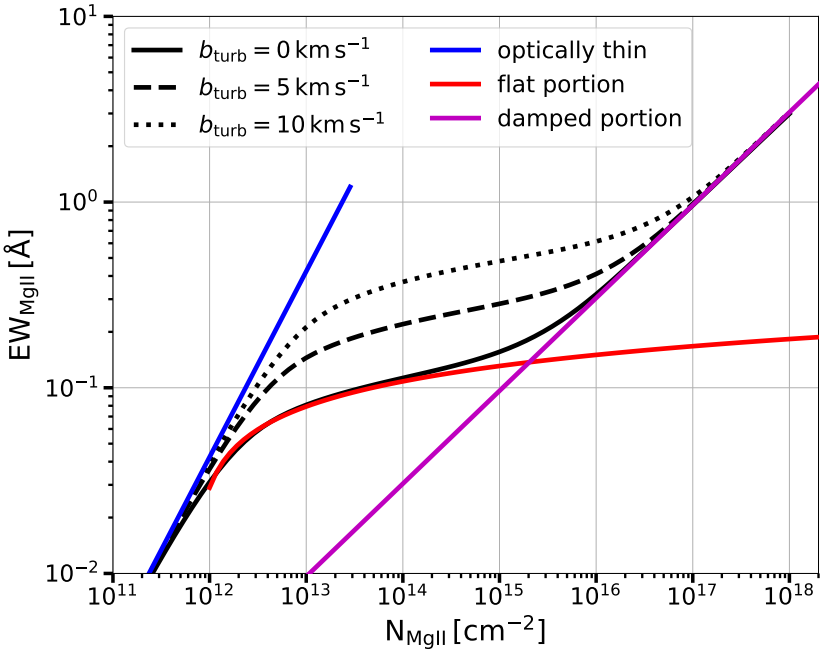



Figure 4.3: Variation in MgII EW with MgII column density. The black lines show the EW for various $b_{\rm turb}$ values. The solid blue, red, and magenta lines show the analytical relation between EW and column density in the optically thin limit, and in the flat and damped portions of the curve of growth. These analytic relations are from Draine 2011 (see Chapter 9). We assume thermal broadening at $T = 10^4$ K for MgII, which gives $b_{\rm thermal} = 2.6\,{\rm km\,s^{-1}}$. In the flat portion (applicable to most of our CCs, see Fig. 4.2), the EW increases with increasing turbulent broadening.

et al. 2022a).[6] These assumptions give $\sigma_{\rm 3Dturb,CGM} \approx 107\,{\rm km\,s^{-1}}$. For $R_{\rm CC} = 10$ kpc and $R_{\rm CGM} = 280$ kpc, we get $\sigma_{\rm 3Dturb,CC} = 35\,{\rm km\,s^{-1}}$. Thus, the 1D turbulent dispersion is $\sigma_{\rm turb,CC} = \sigma_{\rm 3Dturb,CC}/\sqrt{3} = 20\,{\rm km\,s^{-1}}$. For simplicity, we choose the turbulent broadening parameter to be the same for all intersected lengths across the CC.

Figure 4.4 shows the contour plot of the maximum MgII column density (black lines indicate $\log_{10} N_{\rm MgII}$; corresponding to the LOS passing through the center of a CC) and equivalent width (in Å; magenta lines) for a single CC in the $N_{\rm CC} - R_{\rm CC}$ parameter space for a fixed total cool gas mass $M_{\rm cool} = 10^{10}\,{\rm M_\odot}$. The MgII column density for a LOS passing through the center of a CC is $\langle n_{\rm MgII} \rangle \times 2R_{\rm cc}$, which simplifies to

$$N_{\rm MgII,max} = 9.2 \times 10^{12}\ {\rm cm^{-2}} \left(\frac{M_{\rm cool}}{10^{10}\ M_\odot}\right) \left(\frac{N_{\rm CC}}{10^3}\right)^{-1} \left(\frac{R_{\rm CC}}{10\,{\rm kpc}}\right)^{-2}. \tag{4.14}$$

To compute the MgII column density above, for simplicity, we assume the MgII ion fraction to be 0.2. Note that MgII fraction of 0.2 correspond to the gas density of $\sim 10^{-2}\,{\rm cm^{-3}}$ at redshift of $\sim 0.2$ (see Fig. A.2). We first generate the normalized absorption profile ($I_\nu = \exp[-\tau_\nu]$, where $\tau_\nu \propto N_{\rm MgII}$ is the frequency-dependent optical depth; see Eq. 9.5 in Draine 2011) and then compute the area under the normalized absorption profile as the definition of EW. In the linear regime of the curve of growth ($N_{\rm MgII} \lesssim 10^{12}\,{\rm cm^{-2}}$; see Fig. 4.4), the EW and column density contours run parallel to each other, which suggests a single value of EW for a given value of column density (Eq. 4.14). At higher column densities, $N_{\rm MgII} \gtrsim 10^{12}\,{\rm cm^{-2}}$, for a fixed column density the EW increases with an increase in $R_{\rm CC}$ as $b_{\rm turb,CC}$ is larger for a larger CC according to our ansatz for CGM turbulence (see Figure 4.3). This regime lies in the flat part of the curve of growth. Therefore, to obtain a higher column density and EW per CC, one needs larger and fewer CCs. Thus, the observed column density and EW distributions can constrain the cool CGM mass and the CC numbers and sizes.

### Ansatz for LOS velocity of CCs

To compute the absorption spectrum along a LOS, we require the LOS velocities of the intersected CCs. We assign a 3D velocity field with a Gaussian distribution and a

[6] Direct observations of turbulence in the hot CGM are not available for Milky Way mass halos. The CGM is expected to have a larger turbulent Mach number than the intracluster medium, for which the hot phase turbulence is subsonic with a turbulent Mach number $\sim 0.2$ (Hitomi Collaboration et al. 2016).

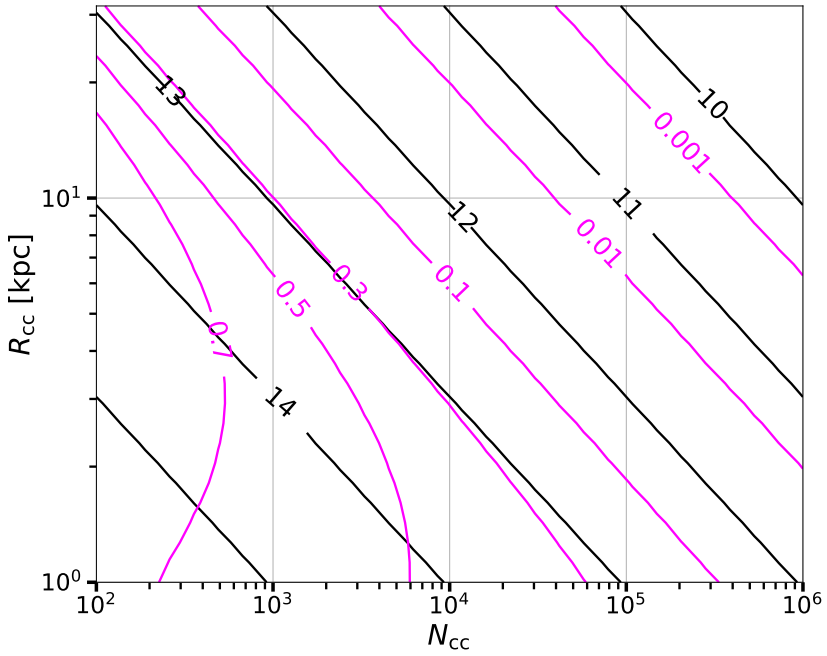



Figure 4.4: Contours of equal (in $\log_{10}$) maximum MgII column density (corresponding to LOS passing through the center of a CC; black lines) and equivalent width (magenta lines, in units of Å) in the parameter space of $N_{CC}$ and $R_{CC}$ for a single cloud complex with $M_{cool} = 10^{10} M_{\odot}$. For MgII column densities $\gtrsim 10^{13}$ cm$^{-2}$, the EW saturates in the flat part of the curve of growth (see Figure 4.3) and the curves of constant EW are no longer parallel to the constant column density contours. The EW increases with $R_{CC}$ for a fixed MgII column density because of a larger $b_{turb,CC}$ (see Fig. 4.3).

Kolmogorov power spectrum[7]. ($v_l \propto l^{1/3}$) on a $1800^3$ grid across the entire CGM. Every CC is assigned the velocity from the closest grid cell. The turbulent velocity field has zero mean and standard deviation $\sigma_{\rm 3Dturb,CGM} = 107\,{\rm km\,s^{-1}}$ (assuming our ansatz for global CGM turbulence). In addition to this bulk velocity, each CC also has a Gaussian spread in its internal velocities ($\sigma_{\rm turb,CC}$), as mentioned earlier. To generate the absorption profile along each LOS, we consider the blending of absorption profiles from all intersected CCs. The optical depth along a LOS is computed as the sum of the optical depths from each intersected CC, $\tau(\nu) = \sum_i \tau_i(\nu)$, where the summation goes over all the intersected CCs. Thus, the normalized absorption profile is given as $I(\nu) = \exp[-\tau(\nu)]$ and the area under it gives the total EW along a LOS.

### 4.3.5 Comparing MgII column density with observations

The top panels of Figure 4.5 show the column density distribution along $10^4$ sightlines (empty sightlines are not shown) across the CGM with $10^3$ CCs and a CC radius $R_{\rm CC} = 10$ kpc, but with the cool gas mass of $10^9$, $10^{10}$ and $10^{11} M_\odot$; we choose the power-law index $\alpha = 1$. The data points shown in green color are from the COS-Halos survey (Werk et al. 2013). The average MgII column density varies linearly with the cool gas mass, which suggests that the column density distribution of cool gas tracers (like MgII) is a quantitative indicator of the cool gas mass in the CGM. The trend and average MgII column density are most consistent with a cool CGM mass $\sim 10^{10} M_\odot$. The distribution of MgII column density from our Monte Carlo-generated LOSs is too small (large) for $10^9 (10^{11}) M_\odot$ in the cool CGM.

The bottom $3 \times 3$ panels of Figure 4.5 show the variation in MgII column density for cool CGM mass of $10^{10} M_\odot$ with a variation of the number of CCs ($N_{\rm CC}$ across rows) and the CC radius ($R_{\rm CC}$ across columns). For small $R_{\rm CC}$ and $N_{\rm CC}$, the detected column densities are much larger, but the covering fraction is small since most sightlines do not encounter cool gas. Since we only show detections, the cases with a small covering fraction will have a smaller number of grey circles. For larger $R_{\rm CC}$, the covering fraction increases, and the individual LOS column densities are smaller. With an increasing number of CCs and CC sizes (bottom right panels), the scatter in MgII column density

[7] Chen et al. 2023 found that the Kolmogorov scaling is consistent with the observations for clouds with sizes $\lesssim 1$ kpc. The same scaling holds at a much larger scale in extended QSO nubulae (Chen et al., 2024)

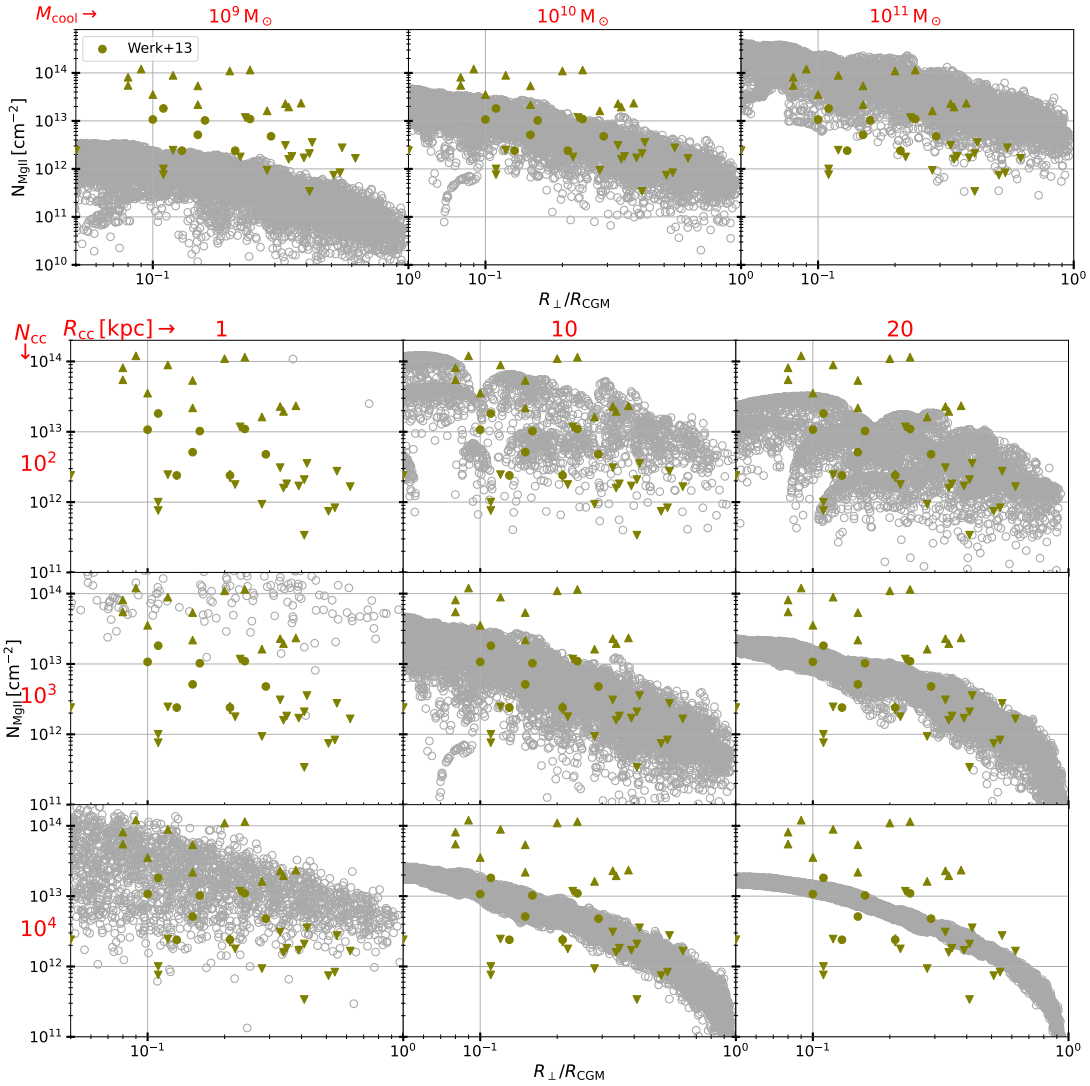



Figure 4.5: Variation in the MgII column density along $10^4$ sightlines with the cool gas mass (top panels), and number and radius of CCs (bottom $3 \times 3$ panels) for a power-law ($\alpha = 1$) distribution of CCs in the CGM. Only non-zero values are shown with circles, resulting in a smaller number of them when the covering fraction is small. The data points shown in green color are from the COS-Halos survey (Werk et al. 2013). It is evident from the top panels that cool CGM mass of $\sim 10^{10}\,M_\odot$ best matches the observed data. The bottom panels show the variation in MgII column density with $R_{\rm CC}$ and $N_{\rm CC}$ for a fixed cool gas mass of $10^{10}\,M_\odot$. Notice that the increase in the size of CC results in less scatter in the column density because with larger CCs, the volume fraction of CCs is larger, and a similar number of CCs is intersected along different sightlines. A similar trend is observed for a larger number of CCs in the CGM. For the range of parameters we explored, $N_{\rm CC} = 10^3$ CCs with $R_{\rm CC} = 10$ kpc and $M_{\rm cool} = 10^{10} M_\odot$ best explain the observed MgII column density distribution.

decreases. The observed spread in the inferred column densities of cool/warm gas can thus help us constrain cool/warm CGM parameters such as $M_{\rm cool}$, $N_{\rm CC}$, and $R_{\rm CC}$. The observed column density distribution is most consistent with the simulated distribution for $N_{\rm CC} = 10^3$, $R_{\rm CC} = 10$ kpc, $M_{\rm cool} = 10^{10} M_{\odot}$, and with the power-law index of $\alpha = 1$ (see Fig. 4.2), so we adopt these as our fiducial values.

### 4.3.6 Comparing MgII Equivalent Width and covering fraction with observations

For each LOS, we quote a single EW, corresponding to the area under the absorption spectrum across velocities, and do not separate different absorption components. Most of the observational works quote a single EW along a LOS, adding EWs of multiple absorption components if present, implicitly assuming a single absorption component in the curve of growth modeling. The advancement of high-resolution spectrographs and precise modeling will make it possible to model the total absorption on a component-by-component basis, a method currently being applied in a few limited studies (Sameer et al. 2024).

The *top panel* of figure 4.6 shows the MgII EW for our fiducial *mCC* model. The grey scatter points show the EW distribution from Monte Carlo realizations of CCs along various LOSs; empty sightlines are not shown, and the black line shows the mean EW. The observed relation of EW with impact parameter ($R_{\perp}$) from Huang et al. 2021 is shown using an orange line, with the dotted lines showing the $1\sigma$ uncertainty. The green data points are from the COS-Halos survey (Werk et al. 2013). The EW distribution from our model matches the COS-Halos samples (though there is a large scatter in the observed EWs). Even though our model predicts EW values slightly less than the fits from Huang et al. 2021, the values are consistent within the $1\sigma$ limit. Moreover, observational distribution is likely to be biased toward higher values because of the difficulty in detecting weak absorption features. The log-log EW-impact parameter relation from Huang et al. 2021 predicts larger EW, especially at lower and higher impact parameters. However, adopting a log-linear relation between the EW and impact parameter will result in the mean EW distribution shape, which resembles our model (see figure 12 of Dutta et al. 2020). In the *bottom panel*, the solid and dashed black lines show the MgII covering fraction as a function of the normalized impact parameter from our model for the EW

thresholds of 0.3 Å and 0.1 Å, respectively. The orange data points are from Huang et al. 2021 with an EW threshold of 0.3 Å. Our misty CC model with fiducial parameters effectively reproduces the covering fraction and equivalent width (EW) distributions.

### 4.3.7 Estimating cool gas mass in the CGM

One of the fundamental physical properties of the CGM is its mass distribution across different temperature phases. While the volume-filling hot phase is difficult to observe, quasar absorption lines from cool and warm CGM ions are commonly observed. However, there are large variations in the inferred column densities and several upper and lower limits (e.g., see Fig. 4.2). Because of these wild variations, it is hard to estimate the cool and warm gas masses. The large variations and scatter in the column density carry important information that can help us infer the physical properties of the cool/warm CGM.

#### Relation between average column density & covering fraction

For the same cool CGM mass, the CCs can be arranged in different physical configurations – compact CCs with smaller $R_{\rm CC}$ or fewer CCs. With compact CCs and fewer of them, we expect to encounter several empty sightlines, resulting in a small covering fraction. But whenever a LOS encounters a CC, in this case, it is with a large column density (e.g., compare the second-left column of Figure 4.5 with the bottom-left column). One can easily verify that the product of the average column density (averaged over detections) and the covering fraction is roughly the same for the same cool CGM mass. Figure 4.7 shows the correlation between the average MgII column density and the covering fraction of CCs in the CGM for various combinations of $R_{\rm CC}$, $N_{\rm CC}$, and $M_{\rm cool}$. We chose 100 random samples (with selection probability proportional to the projected area from a total of $10^4$ (see Figure 4.5) to be statistically consistent with observations and compute the average MgII column density and covering fraction (defined as the ratio of non-empty sightlines and the total number of sightlines [100]) for these.[8] The colored points with solid, dashed, and dotted black lines on their borders correspond to the cool gas mass

[8]We bin the projected CGM into 10 radial annuli of equal areas and then select 10 LOSs randomly from each annulus, resulting in a total of 100 LOSs. This ensures that the probability of the selection of a LOS is proportional to the area of the annulus to which it belongs.

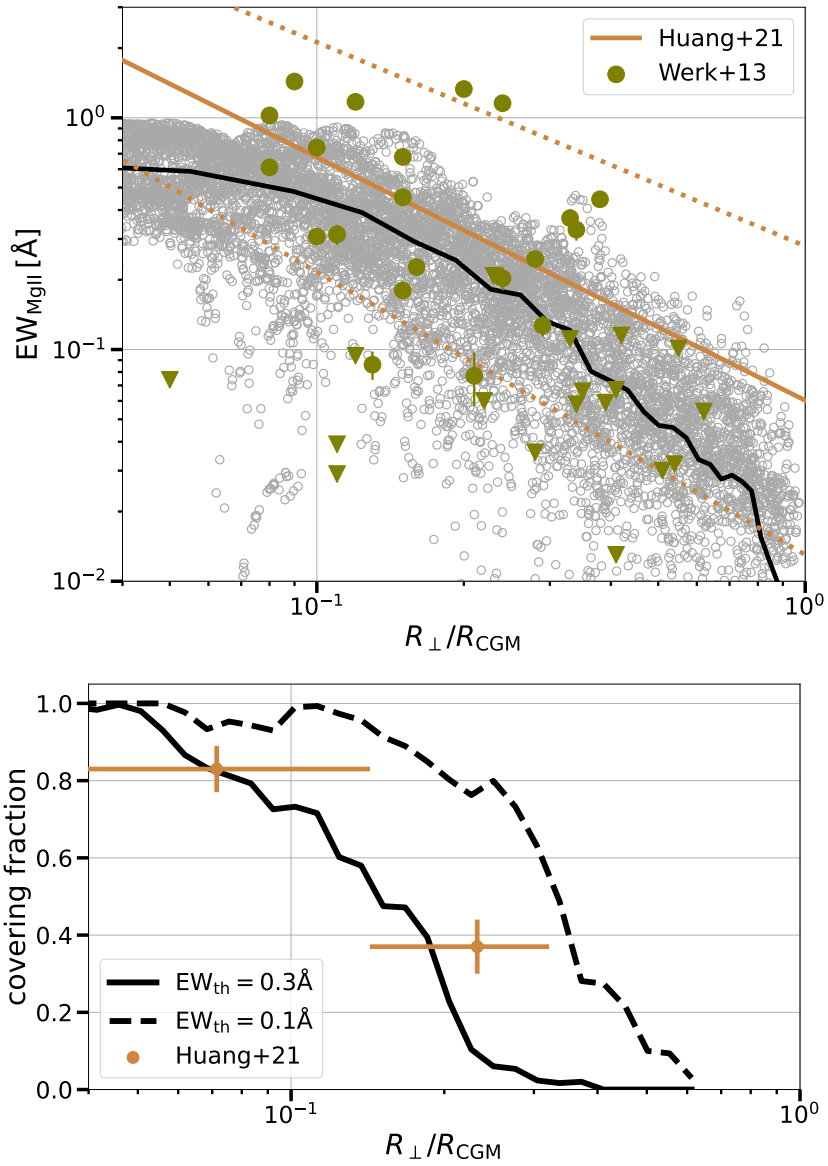



Figure 4.6: The *top panel* shows the MgII EW distribution as a function of the normalized impact parameter for our fiducial *mCC* model. The grey points (note that empty sightlines are not shown) show the total MgII EW as a function of the impact parameter for $10^4$ sightlines. The black solid line shows the mean EW. The solid and dotted orange lines show the best-fit relation and $1\sigma$ spread based on observations from Huang et al. 2021. The green points are the EW data points from the COS-Halos survey (Werk et al. 2013). The *bottom panel* shows the covering fraction as a function of the normalized impact parameter: the solid black line for an EW threshold of 0.3 Å and the dashed black line for 0.1 Å. The orange points show the covering fraction values from Huang et al. 2021 for the EW threshold of 0.3 Å. Our mCC model with the fiducial parameters reproduces the EW distribution and covering fractions.

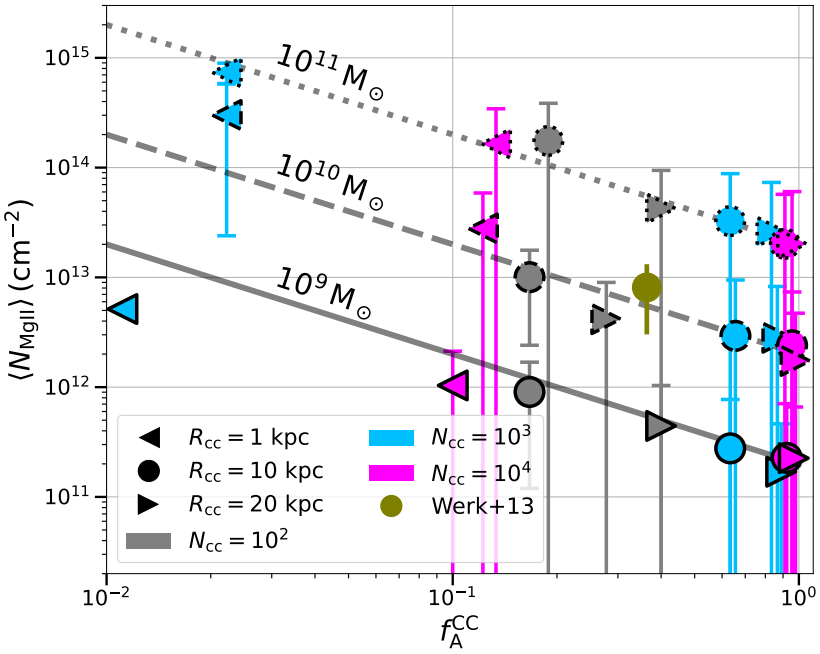



Figure 4.7: The average MgII column density as a function of the area covering fraction of CCs for various combinations of the cool gas mass, $N_{CC}$ and $R_{CC}$ (see Figure 4.5). The colored points with solid, dashed, and dotted black lines on their borders are for a cool gas mass of $10^9$, $10^{10}$, and $10^{11}\,M_\odot$ respectively. The error bars on each point show the standard deviation on the column densities. The dotted, dashed, and solid black lines show the contours of constant average MgII column density times the covering fraction for three different values $\langle N_{\rm mgII} \rangle \times f_{\rm A}^{\rm CC} = 10^{11.3}, 10^{12.3}$, and $10^{13.3}$ cm$^{-2}$, respectively. The product of these two quantities closely tracks the cool CGM mass and hence can be used as an observable proxy for the cool CGM mass. To compute the above quantities, we selected 100 random sightlines (so that the probability of selection is proportional to the projected CGM area) out of $10^4$ to be statistically consistent with the typical size of observational samples. The green point represents the result from the COS-Halos (Werk et al. 2013) survey, the position of which indicates a cool gas mass of $\sim 10^{10}\,{\rm M}_\odot$ for the COS-Halos galaxies.

of $10^9, 10^{10}$, and $10^{11}\,\mathrm{M}_\odot$, respectively. The error bar shows the standard deviation in the column densities. The dotted, dashed, and solid black lines show the contours of a constant average column density times the covering fraction for the three cases with $\langle N_{\mathrm{mgII}} \rangle \times f_{\mathrm{A}}^{\mathrm{CC}} = 10^{11.3}, 10^{12.3}$, and $10^{13.3}$ cm$^2$. The points corresponding to the same cool CGM mass have a similar value of $\langle N_{\mathrm{mgII}} \rangle \times f_{\mathrm{A}}^{\mathrm{CC}}$, regardless of $R_{\mathrm{CC}}$ and $N_{\mathrm{CC}}$. The green point shows the result from the COS-Halos (Werk et al. 2013) survey. The positions of the data point indicate a cool gas mass of approximately $\sim 10^{10}\,\mathrm{M}_\odot$ for COS-Halos galaxies. We calculate the covering fraction from COS-Halos data by dividing the number of detected LOSs by the total number of observed sightlines, excluding lower limits. A more accurate statistical analysis of the data is beyond the scope of our paper. Thus, we have shown that the combination of the covering fraction and average column density can constrain the mass of the cool CGM. Moreover, the intrinsic spread in column density distribution constrains the number of CCs and their sizes.

### 4.3.8 'Advanced' Model: varying size and mass of CCs

So far, we have considered the 'basic' model, where we consider a fixed radius and cool gas mass of cloud complexes. However, cool clouds in the CGM are observed to have a range of sizes and masses, from $\sim$ pc size (Hsu et al. 2011) to $\sim$ kpc size (Dutta et al. 2024b) and mass varying from $\sim 10^4$ to $\sim 10^8\,M_\odot$. A large variation in size and mass of cool clouds is also seen in cosmological simulations (Nelson et al. 2020; Ramesh & Nelson 2024; Ramesh et al. 2025) and idealized simulations (Gronke et al. 2022; Das & Gronke 2024; Tan & Fielding 2024). Galactic feedback processes also affect the distribution of clouds in the inner CGM, making the radial distribution profiles shallower in the inner region of the CGM, and even a turnover in the index can occur at lower radii (Nelson et al. 2020; Augustin et al. 2025). Therefore, in this subsection, we move beyond our 'basic' model with fixed size and mass of CCs in the CGM, and introduce a size and mass distribution of CCs, examining the impact of these modifications on the observables. Along with these modifications, we also incorporate a realistic radial distribution of CCs in the CGM to mimic the effect of galactic feedback processes. We refer to this modified model as the 'advanced' model.

Motivated by the observations and simulations mentioned above, we adopt a power-

law distribution of the radius of spherical CCs in the CGM as.

$$\frac{dN_{\rm CC}}{dR_{\rm CC}} \propto R_{\rm CC}^{-\eta} \tag{4.15}$$

Gronke et al. 2022; Das & Gronke 2024; Tan & Fielding 2024 in their idealized simulation consistently found that the volume distribution of cool clouds follows a power-law behaviour $V^{-1}$, where $V$ is the volume of cool clouds. Therefore the size distribution, assuming $r \propto V^{1/3}$, also follows a power-law distribution with $r^{-1}$. The power-law behaviour of the size distribution of cool clouds is also found in cosmological simulations with index $\sim 1.5$ (as can be inferred from Figs. 10 and 3 of Ramesh & Nelson 2024 and Ramesh et al. 2025 respectively). Therefore, we choose the fiducial value of the power-law index $\eta$ as 1. Apart from the power-law behavior, simulations show a turnover at smaller sizes (Figs. 10 and 3 of Ramesh & Nelson 2024 and Ramesh et al. 2025 respectively, and Fig. 12 of Gronke et al. 2022), likely due to the resolution limit. Therefore, we choose the lower and higher cutoffs of 100 pc and 10 kpc on the size distribution of CCs. Similarly, we consider a power-law mass distribution of the CCs.

$$\frac{dN_{\rm CC}}{dM_{\rm CC}} \propto M_{\rm CC}^{-\zeta} \tag{4.16}$$

Like the size distribution, the idealized simulations (Gronke et al., 2022; Das & Gronke, 2024; Tan & Fielding, 2024) show a power-law mass distribution of cool clouds with index 2, while the cosmological simulations show a power-law with index $\sim 1$ (Fig. 9 of Ramesh & Nelson 2024). Therefore, we adopt the fiducial value of the power-law index $\zeta$ as 2 and lower and upper cutoffs of $10^5$ and $10^7\,M_\odot$. For the radial distribution of CCs in the CGM, we adopt a broken power-law profile to mimic the effect of galactic feedback processes on the distribution of clouds in the following form.

$$\begin{aligned} \frac{dN_{\rm CC}}{dR} &\propto R^{-\alpha_1}; R \leq R_0 \\ &\propto R^{-\alpha_2}; R > R_0 \end{aligned} \tag{4.17}$$

The broken power-law distribution is seen in simulations (Fig. 9 in Nelson et al. 2020 and Fig. 11 in Ramesh & Nelson 2024). We adopt the shallower (inner regions) and steeper (outer regions) indices to be $\alpha_1 = 0.1$ and $\alpha_2 = 1$, respectively. Morgan & Bailin 2025 analyzed the isolated galaxies in the TNG100 simulation and found a characteristic scale of 0.2 times the virial radius, corresponding to the size of outflows. Motivated by this result, we choose the break point of the broken power-law to be $R_0 = 50$ kpc.

With these modifications, we generate CCs in the CGM so that the total CC mass reaches the total cool gas mass in the CGM, which we have taken to be $10^{10}\,M_\odot$. Note

that in this 'advanced' model with the fiducial parameters, we generate a larger number of CCs $(21,622)$ than $10^3$, our fiducial value in the 'basic' model. We also ensure that the average number density of cool gas in each CC is less than the physical density (see Eq. 4.13) at the radial location of the CC by regenerating the mass of the CC, where the average/global density is $3M_{\rm CC}/(4\pi R_{\rm CC}^3 \mu m_{\rm p})$. The above condition also ensures that the cool gas volume fraction within each CC is less than unity. After generating the CCs of variable size and mass, we follow similar steps as in our 'basic' model to compute the observables.

In Fig. 4.8, we show the MgII column density as a function of normalized impact parameter for both 'basic' (grey points) and 'advanced' (blue points) models for $10^4$ sightlines (empty sightlines are not shown). The green data points are from the COS-Halos survey (Werk et al. 2013). The solid grey and blue lines show the average MgII column density for the 'basic' and 'advanced' models, respectively. The average column density shows a similar declining trend in both the 'basic' and 'advanced' models. The 'advanced' model shows a larger scatter in column density values compared to the 'basic' model due to variation in size and mass of CCs, which effectively generates a larger number of CCs. The overall covering fraction is also higher in the case of the 'advanced' model due to a smaller size (larger number) of CCs, the overall average column density is lower, such that the product of average column density and covering fraction is constant for the fixed cool gas mass in the CGM as compared to the 'basic' model.

The highest column density is also larger for the 'advanced' model due to these variations. Varying the upper/lower limits and slope of the CCs' size, mass, and radial distribution has a similar impact on the column density distribution as in the case of the 'basic' model (see Fig. 4.5). The parameter variation that produces a larger number of CCs (larger index and smaller lower/upper cutoff on size and mass distribution), results in the larger covering fraction, and smaller scatter in the column density and smaller average column density value, since the area covering fraction times the average column density is constant for the fixed cool gas mass in the CGM. For example, changing the power-law index of mass distribution to 3/1 from the fiducial value of 2 results in a total of $50,789/4,165$ CCs, which results in a smaller/larger scatter and smaller/larger average MgII column density. Similarly, increasing the broken power-law index to 2 (outer regions) from 1 results in a larger number of CCs in the central region and fewer in the outskirts. This results in a smaller scatter and covering fraction at inner regions

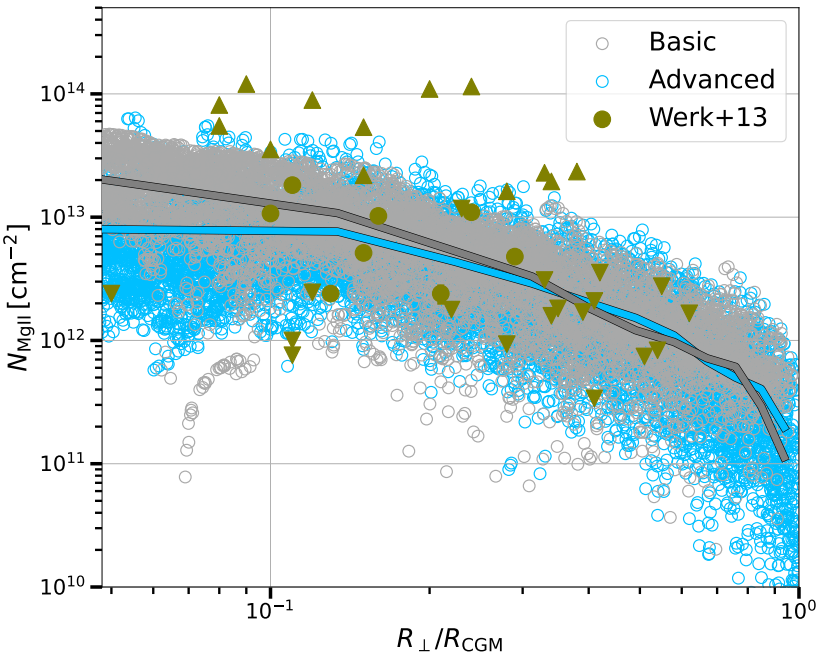



Figure 4.8: The grey and blue points show the MgII column density for the 'basic' and 'advanced' (considering the size, mass, and realistic radial distribution of CCs in the CGM) models, respectively, along a total of $10^4$ sightlines (empty sightlines are not shown). The solid lines in the respective colors show the average MgII column density. The green data points are from the COS-Halos survey (Werk et al. 2013). Notice a slight decrement in the average column density for the 'advanced' model and therefore a larger covering fraction, since the product of average column density and covering fraction is fixed for the fixed total cool gas mass in the CGM. The scatter is larger in the case of the 'advanced' model due to the size and mass variation of the CCs.

and thereby a larger average column density. Changing the break point from 50 kpc to 100 kpc does not affect the distribution significantly. Although the above results are generally valid, noticeable variation in column density occurs only when there is a substantial change in these parameters.

## 4.4 Line blending with smaller cloudlets

In the last section, we analyzed the distribution of misty CCs in the CGM. Mist limit refers to a unit area covering fraction within a CC with an enormous number ($N_{\rm cl} \to \infty$) of tiny ($r_{\rm cl} \to 0$) cloudlets. In this section, we investigate the mist limit kinematically

using the MgII absorption profile by generating a large number of cloudlets (of small size) within a CC. Therefore, we look for the convergence of the MgII absorption profile from tiny cloudlets within a CC and compare it with the misty CC model in the previous section. To do so, following HR24, we zoom in on a single CC, generate spherical cloudlets within it, and assign velocity to each cloudlet. We assume turbulent broadening across a cloudlet (in a similar manner as done in the previous section) along with thermal broadening, even though turbulent broadening across a $\sim$ parsec size cloudlet is smaller than thermal broadening and the LOS velocity spread of cloudlets across the CC. We show that turbulent broadening across a CC emerges due to the blending of absorption profiles of individual cloudlets intersected along a LOS, which are typically closely spaced in the LOS velocity space.

Instead of generating cloudlets throughout the entire CC ($M_{\rm CC} = 10^7\,M_\odot$, $R_{\rm CC} = 10$ kpc), which would yield an excessively large number of cloudlets ($\sim 10^{10}$ for $r_{\rm cl} = 1$ pc), we focus on a smaller cylindrical region along the LOS to keep the total cloudlet count computationally manageable. We select a cylinder with a radius of 40 pc and a height of 20 kpc, positioning it at the center of the CC. This allows us to generate and analyze fewer cloudlets in a reduced volume. We uniformly populate cloudlets in the cylindrical volume and ensure that the cloudlets are within the cylinder by regenerating the coordinates of the cloudlets that lie outside it. We vary the size of spherical cloudlets with $r_{\rm cl} = 10, 1$, and 0.1 pc and a fixed $n_{\rm cool} = 10^{-2}\,{\rm cm}^{-3}$. Once we generate the coordinates of all cloudlets, we create a 3D realization of the velocity field following the Kolmogorov spectrum at the CC scale over a grid of $200^3$. Each cloudlet is assigned this background velocity field based on the nearest grid to the cloudlet. The velocity field has zero mean and standard deviation $\sigma_{\rm 3Dturb,CC} = \sigma_{\rm 3Dturb,CGM} \times (R_{\rm CC}/R_{\rm CGM})^{1/3} = 35\,{\rm km\,s^{-1}}$ for $R_{\rm CC} = 10$ kpc and $R_{\rm CGM} = 280$ kpc with $\sigma_{\rm 3Dturb,CGM} = 107\,{\rm km\,s^{-1}}$ estimated in the previous section. We then shoot a LOS through the center of the cylinder/CC and compute the number of intersected cloudlets, the respective column densities, the LOS velocities ($z$ component of velocity), and the absorption profile.

Note that we also consider turbulent broadening across a cloudlet following Section 4.3.4, which further broadens the absorption profile compared to purely thermal broadening. Though for smaller size cloudlets ($\lesssim$ pc), this effect is negligible, and thermal broadening dominates over turbulent broadening. We assume the temperature of the cool gas to be $10^4$ K, which corresponds to $b_{\rm thermal} = 2.6\,{\rm km\,s^{-1}}$ for MgII. To obtain the

column density of MgII from the total column density (calculated using the intercepted cloudlet length) of the individual intersected cloudlets, we adopt $f_{\rm MgII}$ of 0.2 assuming a 0.3 solar metallicity (see Appendix A.1 and figure A.2).

Figure 4.9 shows the impact of smaller cloudlets and, therefore, a larger number of cloudlets in a CC on the overall absorption profile along a LOS. Using total broadening (thermal and turbulent), MgII column density and LOS velocity ($z$ component of velocity) of the individual intersected cloudlets, we generate the absorption profiles of intersected cloudlets as shown with dashed grey lines in Figure 4.9. The orange line shows the total absorption profile from all the intersected cloudlets, calculated similarly as done in the previous section for misty CCs across the whole CGM. The blue line shows the overall absorption profile smoothed with a velocity resolution of 6 km s$^{-1}$. The magenta line shows the absorption profile from our fiducial misty CC model with $M_{\rm CC} = 10^7\,M_\odot$, $R_{\rm CC} = 10$ kpc, and $n_{\rm cool} = 10^{-2}\,{\rm cm}^{-3}$ along a LOS passing through the center of CC smoothed with a velocity resolution of 6 km s$^{-1}$.

As the cloudlet size decreases, more cloudlets are generated to maintain the same cool gas mass in a CC. This results in more intersected cloudlets along a LOS (25, 260, and 2411 cloudlets for $r_{\rm cl} = 10, 1$, and 0.1 pc). The larger number of intersected cloudlets results in an overall broad absorption profile. The overall absorption profiles for $\lesssim 0.1$ pc size cloudlets (bottom panel of Fig. 4.9) roughly match the absorption profile predicted by our misty CC model (magenta line). Decreasing the radius of cloudlets further will result in lesser and fewer components in the blue absorption line and a closer match with the mist-limit. This signifies that the turbulent velocity of individual tiny cloudlets results in the turbulent broadening across a CC, well modeled by our misty CC ansatz.

Figure 4.10 shows the impact of position and LOS velocity distribution of the cloudlets on the blending of the absorption profiles along a LOS. The lines in the top panel with different colors show the individual MgII absorption profiles along a LOS similar to the top panel of Fig. 4.9. Note that we only show 16 cloudlets out of 25 intersected cloudlets for clarity. The solid orange line shows the overall absorption profile from all the intersected cloudlets. Depending on the LOS velocity of the intersected cloudlets, the absorption profiles may be blended. In the bottom panel, we show the $z$ coordinate of the intersected cloudlets on the y-axis and the LOS velocity on the x-axis (same as in the top panel). The color of the points in the bottom panel is consistent with the absorption profile of the cloudlets in the top panel. The cloudlet at the leftmost side on the LOS velocity

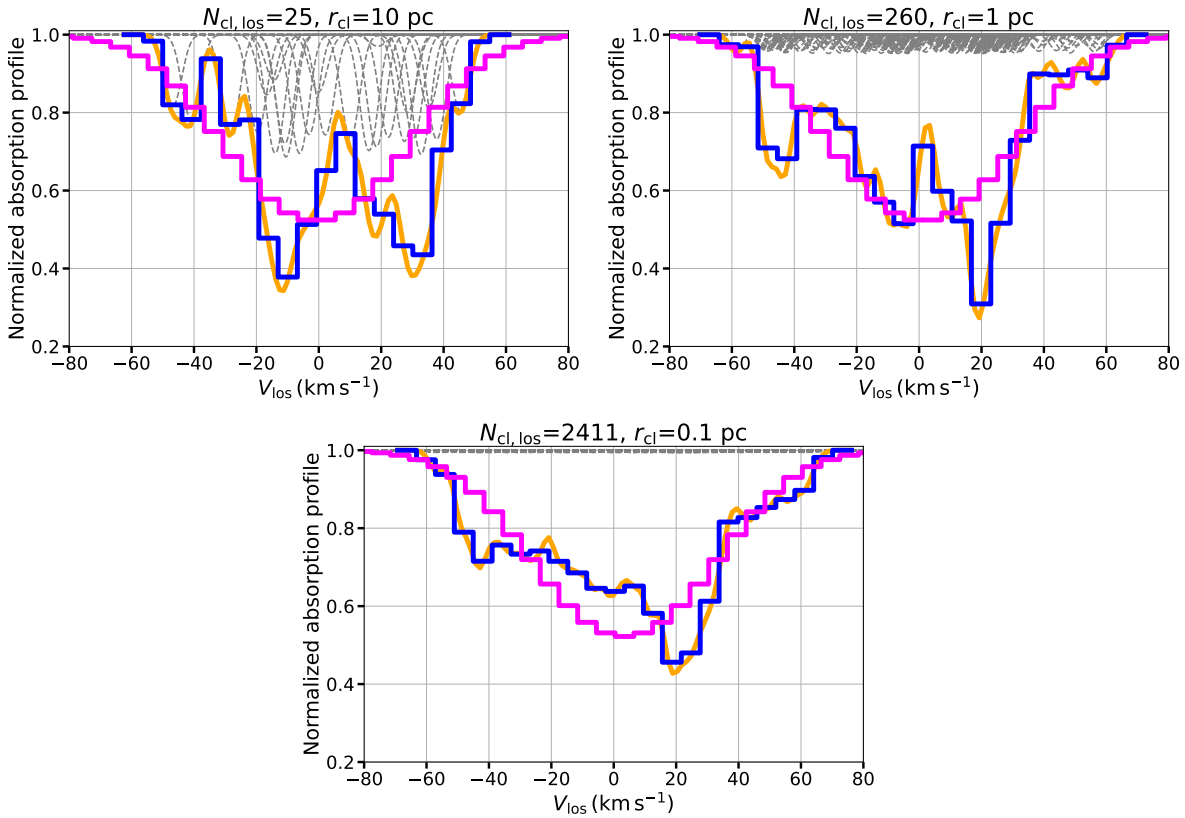



Figure 4.9: Normalized MgII absorption profile for increasing (decreasing) number (size) of cloudlets in a CC along a LOS. The dashed grey lines show the absorption profile from individual intersected cloudlets. The orange lines show the overall absorption profiles from the intersected cloudlets along the LOS. The blue lines show the overall absorption profile smoothed with a velocity resolution of 6 km s$^{-1}$. The magenta lines show the absorption profile for the misty CC model along the sightline passing through the CC center smoothed with a velocity resolution of 6 km s$^{-1}$ (see section 4.3.4 on how to calculate the CC absorption profile in the mist limit). As the size of cloudlets decreases from 10 to 0.1 pc (top to bottom panels), more and more cloudlets are intersected along the LOS. With an increase in the intersected cloudlets, the overall absorption profiles become broader with fewer absorbing components. For cloudlet size $\lesssim$ 0.1 pc, our misty CC model (magenta line, smoothed to a resolution of 6 km s$^{-1}$) is roughly matching the total absorption profile.

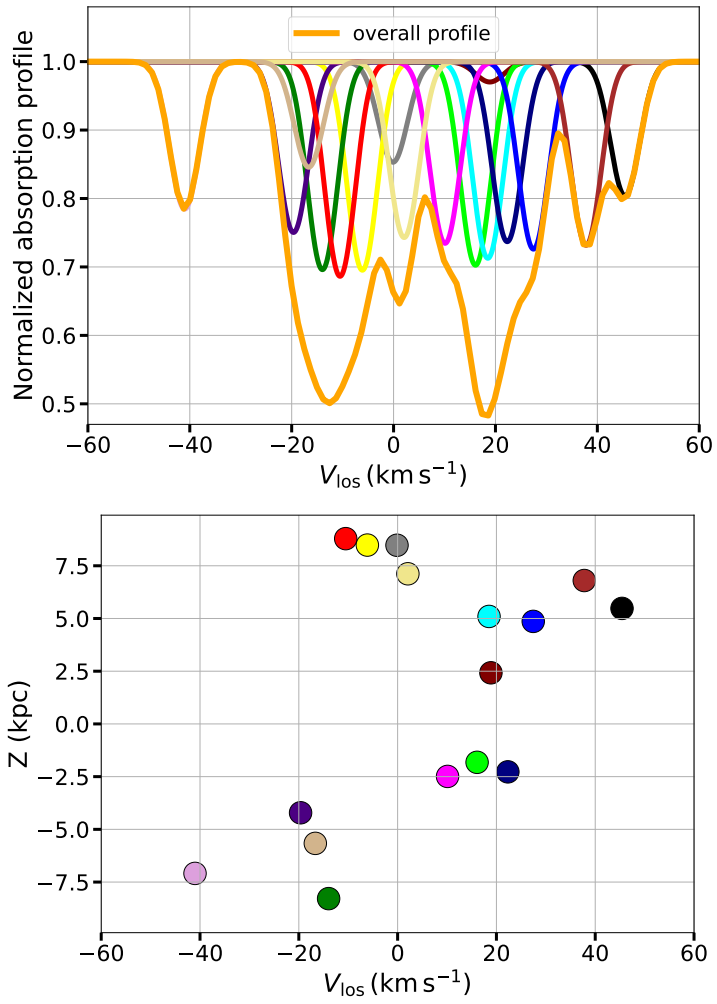



Figure 4.10: In the *top panel*, the lines in different colors (total 16) show the MgII absorption profile from individual cloudlets intersected along a LOS through a CC (same as top panel of Fig 4.9 except that we only consider 16 out of 25 cloudlets for clarity). The solid orange line shows the overall/total absorption profile from all the intersected cloudlets. Due to the blending of absorption profiles, only 8 absorbing components are seen in the overall absorption profile. In the *bottom panel*, we show the $z$ coordinate and the LOS velocity of the intersected cloudlets. The color of the points corresponding to individual cloudlets is consistent with the top panel. Based on the position and velocity distribution, the cloudlets will be blended in the absorption spectrum. This illustration shows that cloudlets that are far apart in physical space may be blended due to similar LOS velocity, whereas cloudlets that are very close in physical space may have disparate LOS velocities, which makes it very difficult to infer 3D information from the 2D observations.

space with $z \approx$ -7.5 kpc and $v_{\rm LOS} \approx$ -40 $\rm km\,s^{-1}$ is not blended with other cloudlets as can be seen with the absorption profile in the top panel. The two cloudlets around $v_{\rm LOS} \approx -15\,\rm km\,s^{-1}$ (green and red points in the bottom panel) are blended, as can be seen with the overlapping absorption profiles in the top panel, but are separated by $\approx 16$ kpc in physical space. This signifies that *the cloudlets far away in physical space can be blended due to similar LOS velocity.* This makes it extremely challenging to extract the 3D information of the cool cloud components from 2D observational information. In contrast, the two cloudlets, which are around $v_{\rm LOS} \approx$ -10 km $\rm s^{-1}$ (red and yellow points in the bottom panel) are close in both velocity and physical space and are also blended as seen in the absorption profile in the top panel.

## 4.5 Direct modeling of cloudlets & CCs across CGM

In Section 4.3, we assumed that CCs are misty and focused on the distribution of CCs in the CGM. In this section, rather than assuming the mist limit, we extend the work further and distribute the cool cloudlets explicitly within all the CCs across the entire CGM. We analyze the distribution of cloudlets within CCs and CCs across the CGM and check for the parameters that best match the observations within computational limitations. The exercise in section 4.4 allowed us to investigate the impact of minuscule cloudlets on the observed absorption spectrum. Because of the computational cost, such small cloudlets cannot be populated across the entire CGM. This section takes an approach similar to *CloudFlex* (HR24) and similarly cannot easily reach the mist limit because of computational limitations. In fact, our approach in this section is even more expensive because the distribution functions of various observables from a single CC were combined analytically in HR24, but here we also treat the distribution of CCs from first principles. The range of investigations in this work allows us to understand the relations between these various related approaches, namely, *mCGM*, *mCC*, and *CloudFlex*.

*Generation of CCs across the CGM:* We first generate the centers of $N_{\rm CC}$ number of CCs with a power-law distribution in $R$ with an index $\alpha$, as done in Section 4.3 (see Eq. 4.7). To determine the 3D coordinates of the centers of each CC, we follow the procedure described in section 4.3.4. The lower and upper limits of radial (galactocentric) distances of the centers of these CCs are $R_{\rm min} = 10$ kpc and $R_{\rm max} = 280$ kpc, respectively. For the fiducial case, we adopt $N_{\rm CC} = 10^3$ and $\alpha = 1$ (as in our fiducial mCC model), but also

| Parameter | Fiducial Value | Tested Range | Description |
|---|---|---|---|
| **CGM** | | | |
| $R_{\rm CGM}$ [kpc] | 280 | – | Radius of the CGM |
| $M_{\rm cool}$ [$M_\odot$] | $10^{10}$ | $10^9$–$10^{11}$ | Total cool gas mass in the CGM |
| **Cloud Complex** | | | |
| $N_{\rm CC}$ | $10^3$ | $10^2$–$10^4$ | Number of cloud complexes (CCs) |
| $R_{\rm min}$ [kpc] | 10 | – | Minimum distance of CC center from galactic center |
| $R_{\rm max}$ [kpc] | 280 | – | Maximum distance of CC center from galactic center |
| $\alpha$ | 1 | 0–2 | Power-law index of CC radial distribution |
| **Cloudlet** | | | |
| $r_{\rm min}$ [kpc] | 0.1 | – | Minimum distance of cloudlet center from CC center |
| $r_{\rm max}$ [kpc] | 10 | 1–20 | Maximum distance of cloudlet center from CC center |
| $\beta$ | 0 | 0–2 | Power-law index of cloudlet radial distribution |
| $a_{\rm min}$ [kpc] | 0.01 | 0.001–0.1 | Minimum semi-axis length of a cloudlet |
| $a_{\rm max}$ [kpc] | 0.5 | 0.1–1 | Maximum semi-axis length of a cloudlet |
| $\gamma$ | 1 | 0–2 | Power-law index of cloudlet size distribution |

Table 4.2: Model parameters, fiducial values, tested ranges, and brief descriptions for direct modeling of cloudlets within cloud complexes distributed throughout the CGM.

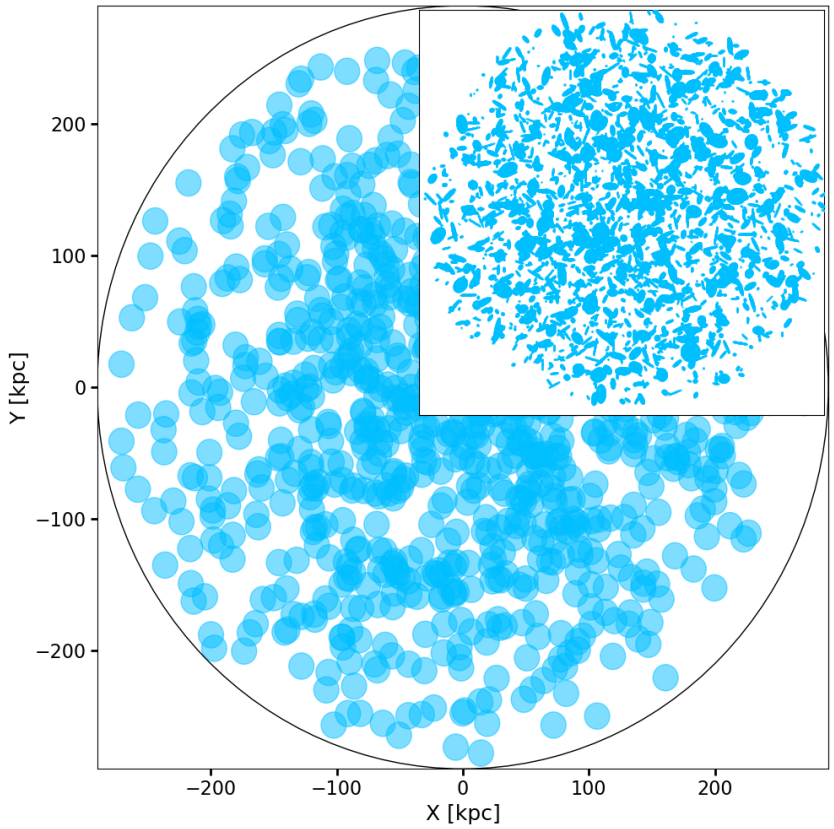



Figure 4.11: LOS projected distribution of CCs and cloudlets in the CGM for $M_{\rm cool} = 10^{10}\,{\rm M}_{\odot}$, $N_{\rm cc} = 10^3$, and $\alpha = 1$. Due to the power-law nature of the distribution of CCs and the projection effect, more CCs are found in the central region than in the outskirts. The inset shows the cloudlets within one of a CC for $\beta = 0$ and $\gamma = 1$ (fiducial parameters; see Table 4.2). In this fiducial case, $\approx 5 \times 10^8$ total cloudlets are generated, with $\approx 5 \times 10^5$ cloudlets per CC. Note that we only show $2 \times 10^3$ cloudlets in the inset to better highlight the variety of cloudlets with different sizes and orientations. Also, we do not explicitly show the distribution of cloudlets within all the CCs. The distribution of these cloudlets shows qualitative similarity to Figure 7 of Ramesh & Nelson 2024 that shows a snapshot from a high-resolution simulation of a Milky Way-like CGM.

check the variation with $N_{\rm CC} = 10^{2,4}$ and $\alpha = 0, 2$ (see Table 4.2).

*Location of Cloudlets:* After generating all the CCs, we populate cool cloudlets in each of them until the total cloudlet mass reaches the total cool gas mass $M_{\rm cool}$ (our fiducial value is $10^{10} M_{\odot}$). As in our *mCC* model, we follow the same cool gas number density profile (see section 4.3.2)[9] To obtain the mass of each cloudlet and the column density. We use a power-law distribution of index $\beta$ for the distribution of cloudlets within a CC as a function of radial distance from the center of each CC. This is similar to what we did for distributing CCs across the CGM. The lower and upper limits of distances of the centers of cloudlets from a CC center are $r_{\rm min}$ and $r_{\rm max}$, respectively. To determine the 3D location of the centers of each cloudlet, we follow the same procedure as adopted for determining the centers of CCs in the CGM. For the fiducial case, we adopt $M_{\rm cool} = 10^{10}\,{\rm M}_{\odot}$, $\beta = 0$, $r_{\rm max} = 10$ kpc, $r_{\rm min} = 0.1$ kpc. We also check the variation in observables due to variation in these parameters (see Table 4.2).

*Shape and size of cloudlets:* We assume the cloudlets to be ellipsoidal since they are expected to be non-spherical in general. The ellipsoidal cloudlets have three semi-axes and three rotation angles as parameters. We generate the semi-axes from a power-law distribution with index $\gamma$. The lower and upper limits of the semi-axes are $a_{\rm min}$ and $a_{\rm max}$ respectively. The three rotation angles are generated from a uniform distribution between 0 and $2\pi$. For our fiducial case, we adopt $\gamma = 1$, $a_{\rm min} = 0.01$ kpc, and $a_{\rm max} = 0.5$ kpc. We vary these parameters to check their impact on the observables.

We assign 3D velocity to each cloudlet following the same method as done for misty CCs in section 4.3. The velocity fields are generated on a $600^3$ grid across the entire CGM. Table 4.2 lists all the parameters, their fiducial values, and the variations that we tried. We allow cloudlets to overlap as ensuring non-overlapping cloudlets is very expensive, and it has a minimal impact on the results (see section 2.2.1 in HR24). The total number of cloudlets generated will depend on various parameters. Decreasing $a_{\rm min}$, $a_{\rm max}$, and increasing $\gamma$, $M_{\rm cool}$, while holding other parameters fixed, will result in more cloudlets.

Once we generate all the CCs and cloudlets, we shoot $10^4$ sightlines (uniformly spaced in $\log_{10} R_{\perp}$) into the CGM. Fig. 4.11 shows the LOS projected distribution of cool gas

[9]We use the physical or the local density in this section. The average or the global density concept does not apply here due to the non-mist limit.

cloudlets in the CGM for the fiducial parameters. The circular regions show the CCs within which ellipsoidal cloudlets are distributed. There are more CCs in the central region than in the outskirts due to the power-law distribution in $r$ ($\alpha = 1$) and the projection effect. The inset shows the LOS projected distribution of cloudlets in one of the CCs. We only show $2 \times 10^3$ cloudlets (total $\approx 5 \times 10^5$ cloudlets per CC) to better highlight the range in sizes and orientations of the ellipsoidal cloudlets.

Next, we calculate the number of cloudlets intersected and the intersected lengths along all the $10^4$ LOSs. We then calculate MgII column density using the length intersected through individual cloudlets along a sightline. To determine the total MgII EW along a sightline, we first generate the total absorption profile due to all the intersected cloudlets along a LOS. We then calculate the area under the total absorption profile as the total EW along a LOS (as done in section 4.3 for misty CC). Note that simply adding EWs from individual intersected cloudlets results in a higher total EW. We assume the temperature of the cool gas to be $10^4$ K, corresponding to the Doppler $b$ parameter of 2.6 km s$^{-1}$ for MgII. In this section, we do not consider turbulent broadening across a cloudlet. The turbulent broadening across the $\sim$ pc scale cloudlet is typically less than or equal to thermal broadening, so it does not significantly affect our EW and covering fraction results.

### 4.5.1 Comparing with observations

Figure 4.12 shows the various observable statistics with the variation in $\gamma$, the power-law index of cloudlets' semi-axis length distribution (size distribution). We fix the other parameters to the fiducial values (see Table 4.2). In the *top panel*, we show the normalized histogram of the number of intersected cloudlets, $\log_{10} N_{\rm MgII}$, and $\rm EW_{MgII}$ along $10^4$ LOSs (empty sightlines are not shown for number of intersected cloudlets and column density although they are considered in normalization). Note that we quote total column density and EW along a LOS. The blue, magenta, and grey lines show the variation with $\gamma = 0, 1, 2$, respectively. As $\gamma$ increases, the size distribution becomes steeper and therefore a larger number of cloudlets (smaller in size) are generated to keep the same cool gas mass. The total number of cloudlets generated for $\gamma = 0, 1, 2$ is $\sim 5 \times 10^6, 5 \times 10^7, 10^9$ respectively. Due to the larger number of cloudlets, the number of intersected cloudlets is also high (top left panel), which results in a higher column density and thereby a higher

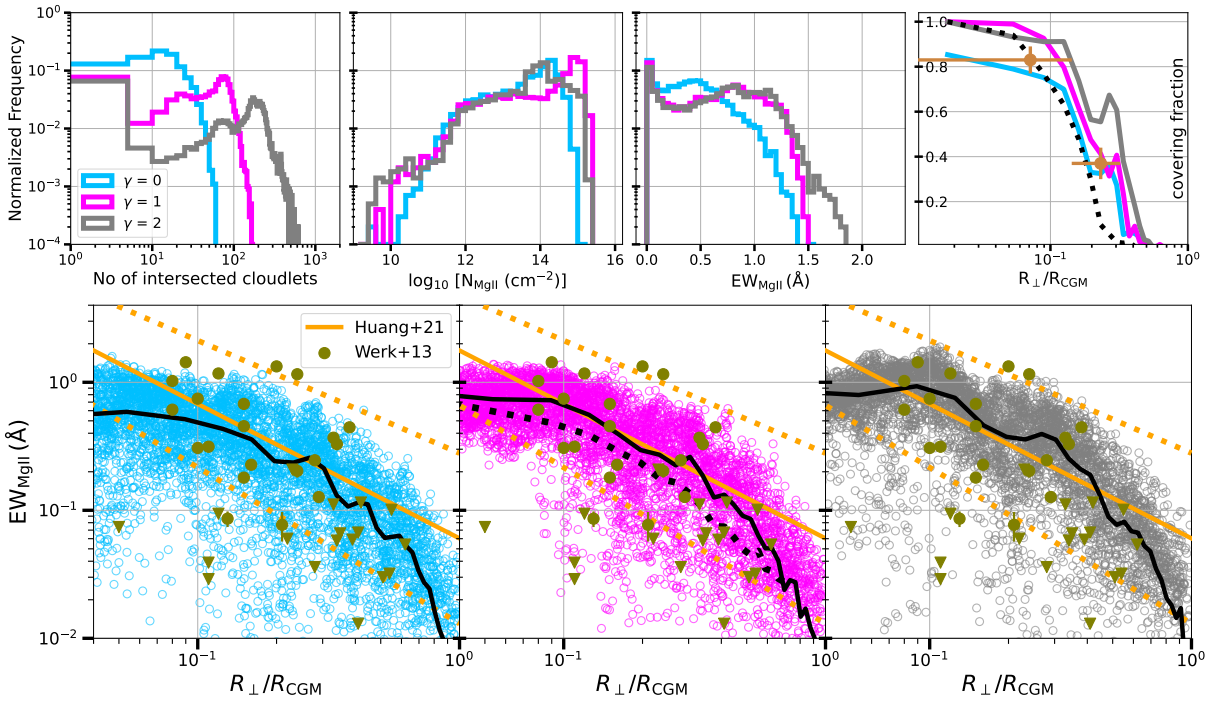



Figure 4.12: The *top panel* shows the normalized histogram of the number of intersected cloudlets, $\log_{10} N_{\rm MgII}$, and MgII EW along $10^4$ LOSs (empty sightlines are not shown for number of intersected cloudlets and column density although they are taken into account for normalization). The blue, magenta, and grey colors correspond to $\gamma = 0, 1, 2$, the power-law index of the semi-axes distribution of ellipsoidal cloudlets. Note that the larger the $\gamma$, the larger the number of cloudlets, keeping other parameters fixed. The total number of cloudlets generated for $\gamma = 0, 1, 2$ is $\sim 5 \times 10^6, 5 \times 10^7, 10^9$ respectively. The rightmost panel shows the MgII covering fraction as a function of normalized impact parameter for an EW threshold of 0.3 Å. The data points are from Huang et al. 2021 while the dotted black line is from our misty CC model (see Fig. 4.6) with fiducial parameters. In the *bottom panel*, the colored scatter points show the total EW along all the LOSs as a function of the normalized impact parameter for the different values of $\gamma$, respectively. The color of the points is consistent with the top panel. The solid black lines show the mean EW, while the dotted black line in the middle panel shows the mean EW for our fiducial misty CC model (see top panel of Fig. 4.6). The solid orange and dashed lines show the best-fit relation and $1\sigma$ uncertainty from Huang et al. 2021 while data points in green are from the COS-Halos survey (Werk et al. 2013). The observed EW trend and covering fraction match better for the $\gamma = 1$ case.

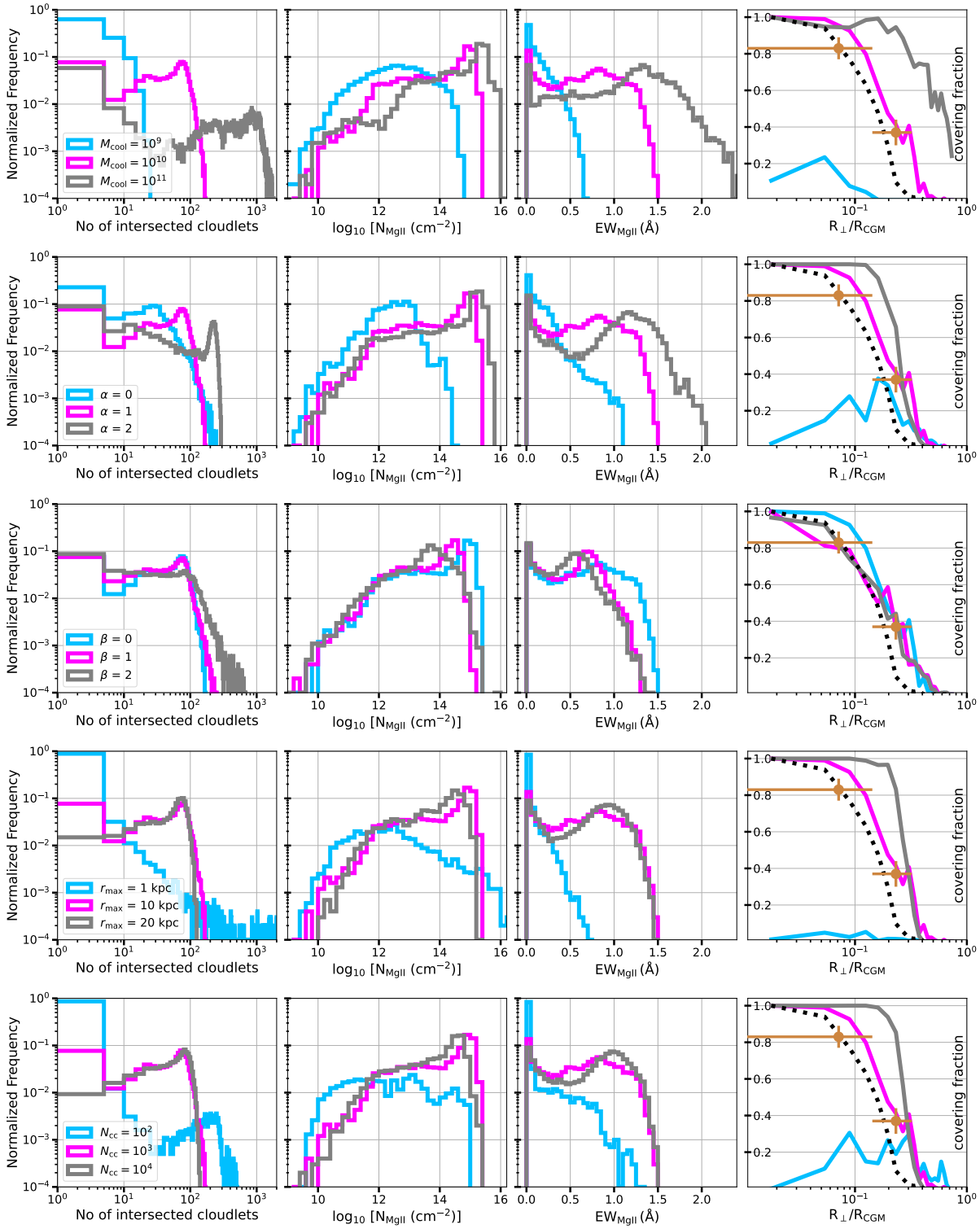



Figure 4.13: This figure shows the histograms of the number of intersected cloudlets, MgII column density, MgII EW, and MgII covering fraction (same as the top left panels in Figure 4.12) to show variation with different parameters. We vary a single set of parameters for each row and hold the other parameters fixed to their fiducial values.

equivalent width. The maximum EW is higher for higher values of $\gamma$, because adding EWs of a larger number of kinematic components results in larger EW along a LOS due to the flat part of the curve of growth (Fig. 4.3). The rightmost top panel shows the MgII covering fraction as a function of the normalized impact parameter for an EW threshold of 0.3 Å. The data points are from Huang et al. 2021. The dotted black line shows the covering fraction from the misty CC model (section 4.3; see Fig. 4.6). The covering fraction increases with increasing $\gamma$ (larger number of cloudlets) as EW is larger for larger values of $\gamma$ (see EW distribution).

In the *bottom panels* of Fig. 4.12, we show the MgII EW distribution as a function of the normalized impact parameter for $10^4$ LOSs. The scatter points are the total EW values along each LOS (empty sightlines are not shown). The blue (left panel), magenta (middle panel), and grey (right panel) colors show the EW values for $\gamma = 0, 1, 2$, respectively. The green data points are from the COS-Halos survey (Werk et al. 2013). The solid and dotted orange lines show the best-fit EW-impact parameter relation and $1\sigma$ scatter of the observed data from Huang et al. 2021. The solid black line shows the mean EW profile in each panel, while the dotted black line in the middle panel shows the average EW value from the fiducial misty CC model. As we see from left to right, the mean EW increases with increasing $\gamma$ (larger number of cloudlets). It shows that $\gamma = 1$ with other parameters set to their fiducial values matches the observed range. Note that the $\gamma = 1$ model with other parameters fixed to their fiducial value generates $\approx 5 \times 10^7$ cloudlets while the $\gamma = 2$ case generates $\sim 10^9$ cloudlets, which is computationally expensive, and therefore we choose $\gamma = 1$ as our fiducial value even though $\gamma = 2$ also closely matches the observations. The fiducial number of CCs is $10^3$, which means that each CC has $\approx 5 \times 10^4$ cloudlets. This is less than the number of cloudlets $\sim 10^7$ generated in a single CC for achieving the mist limit (especially in velocity space; see Fig. 4.9) in section 4.4. Therefore, the cloudlets are not completely in the mist limit within a CC for these fiducial parameters. To attain the mist limit within each $10^3$ CC, one needs to generate a total of $\sim 10^{10}$ cloudlets in the CGM, which is computationally prohibitive. Therefore, we are limited to generating and analyzing $\approx 10^8$ cloudlets in the entire CGM, which corresponds to $\sim 10^5$ cloudlets in each CC. Although our CCs are not entirely in the mist limit in this section for most parameter combinations in Table 4.2, some of the key observables like the distribution and the covering fraction appear reasonably converged (see Fig. 4.12).

In Figure 4.13, we show the results similar to the top panels of Figure 4.12 by varying cool gas mass ($M_{\rm cool}$), power-law index of radial distribution of CCs ($\alpha$), power-law index of distribution of cloudlets within CC ($\beta$), the size of CC ($r_{\rm max}$), and number of CCs ($N_{\rm CC}$). While showing the variation with a parameter, we fix the other parameters to their fiducial values.

The first row in Fig. 4.13 shows the variation with $M_{\rm cool} = 10^9$ – $10^{11}\,M_\odot$. As the cool gas mass increases, the number of cloudlets increases, leading to more intersected cloudlets along LOSs, which in turn raises the MgII column density, EW, and covering fraction. The dotted black line shows the covering fraction from the misty CC model. The covering fraction values are better matched with the $10^{10} M_\odot$ model. The second row shows the variation with $\alpha$, the power-law index of the radial distribution of CCs. The number of cloudlets is the same for all the values of $\alpha$. As $\alpha$ increases, the CCs become more concentrated toward the inner regions of the CGM. This leads to a higher number of intersected cloudlets along the sightlines in the center, resulting in a larger column density, EW, and covering fraction. Our fiducial case with $\alpha = 1$ (magenta line) matches the covering fraction better than other values of $\alpha$.

The third row in Fig. 4.13 shows the variation with $\beta$, the power-law index for the radial distribution of cloudlets within a CC. Even in this case, the number of cloudlets is the same. A larger value of $\beta$ suggests that the cloudlets are more concentrated towards the center of a CC. This results in more intersected cloudlets along a LOS passing close to the center of the CC. The column density does not show significant variation with $\beta$, while EW decreases with increasing $\beta$ due to the close packing of cloudlets in velocity space. The blending of absorption lines from cloudlets results in fewer kinematic components (see section 4.4), which results in a lower EW than having more kinematic components. The covering fraction values predicted from all values of $\beta$ are nearly the same. The fourth row shows the variation with $r_{\rm max}$, the CC size. For larger CC, the cloudlets are more dispersed, while for smaller $r_{\rm max}$, the cloudlets are tightly packed in a CC. The smaller CC results in a higher number of intersected cloudlets and a larger column density. The EW shows an opposite trend with the size of CC, as cloudlets are closely packed in velocity space for a much smaller size CC, which results in smaller EW values due to fewer kinematic components along a LOS, as discussed previously. The column density and EW values are very similar for 10 and 20 kpc CCs, whereas the covering fraction better matches the 10 kpc CC model.

The fifth row shows the variation with the number of CCs ($N_{\rm CC}$). The total number of cloudlets is roughly the same for all three cases, with a larger number of cloudlets per CC in the case of a smaller number of CCs and vice versa. The number of cloudlets intersected is larger for a smaller number of CCs, while the column density and EW are larger for a larger number of CCs due to the higher probability of intersection of more CCs along LOSs. However, the covering fraction is well matched by $10^3$ CCs in the CGM. Encouragingly, on comparing with observations, the fiducial parameters from the mCC model and first principles modeling of cloudlets and CCs are the same (namely, $R_{\rm CC} = 10$ kpc, $N_{\rm CC} = 10^3$, $\alpha = 1$, $M_{\rm cool} = 10^{10} M_{\odot}$).

## 4.6 Discussion

Now we discuss the various implications of our models in modeling and understanding the multiphase CGM revealed by multi-wavelength observations. Our models and other similar approaches (e.g., D24; HR24, Yang et al. 2025) for the cool CGM go beyond the traditional hydrostatic models describing the hot CGM. The primary aim of these models is to provide robust physical insights rather than precisely matching the quasar absorption data (which are still biased by spectra quality and analysis methods).

### 4.6.1 Utility of CC-like approaches to model multiphase CGM

While an extreme idealization, CCs are useful building blocks of a multiphase CGM. Unlike the complete mist limit, CCs can give a non-unity covering fraction of cool and warm gas as probed by quasar sightlines. Moreover, the statistics of column densities and their covering fractions can constrain the mass of the cool gas, typical sizes of CCs, their numbers, and their occurrence with the distance from the center.

Most importantly, since the number of cloudlets in a CC is expected to be much larger than the number of CCs filling the CGM, it is computationally efficient to model CCs analytically in the mist limit and then populate their Monte Carlo realization to compare the post-processed column density and equivalent width statistics with observational inferences.

Our work demonstrates that the observationally inferred distribution of MgII column

density and equivalent width can be reproduced by the misty CC model with several cloudlets along each LOS across a single CC. This translates into a cloudlet size of $\lesssim$ pc, which is beyond the reach of even the highest resolution galaxy formation simulations (e.g., see Ramesh & Nelson 2024). A small cloudlet size is also required for the cool CGM gas, in the form of cloudlets, to be suspended in long-lived CCs (see section A.0.1); large enough cloudlets will simply precipitate towards the galactic center.

### Comparison with D24

A large variation in EW and column density at the same distance from the galactic center implies that the misty cool gas does not fill the entire CGM uniformly, as assumed by D24. A more accurate description is in terms of misty CCs that fill the CGM sporadically. Such a model can naturally explain the large variation in column density along different sightlines (see Fig. 4.5). Unlike D24, here we explore the distribution of direct observables such as EWs. With different levels of modeling of CCs and cloudlets within them, we explore the connections between the *misty CGM* model and the more computationally intensive models like *CloudFlex*.

### Comparison with HR24

HR24 computes the statistical properties of CCs from first principles by populating them with cloudlets with a range of masses (assuming a power-law distribution in the cloudlet mass, $dN/dm_{\rm cl} \propto m_{\rm cl}^{-\delta}$). For a constant density cloudlet, this corresponds to a size distribution of $dN/dr_{\rm cl} \propto r_{\rm cl}^{-3\delta+2}$ ($r_{\rm cl}^{-4}$ for their fiducial $\delta = 2$; corresponds to many more small cloudlets compared to the big ones). The mass/volume distribution of cloudlets $dV/dr_{\rm cl} \propto r_{\rm cl}^3 dN/dr_{\rm cl} \propto r_{\rm cl}^{5-3\delta}$; the area distribution $dA/dr_{\rm cl} \propto r_{\rm cl}^2 dN/dr_{\rm cl} \propto r_{\rm cl}^{4-3\delta}$. Similarly, the column density distribution $dN_{\rm cool}/dr_{\rm cl} \propto r_{\rm cl} dN/dr_{\rm cl}$. For HR24's fiducial value of $\delta = 2$, the mass/volume, area, and column densities (even more so than mass) are all dominated by the smallest cloudlets. For power-law distributions, the average properties are typically dominated by either the higher or the lower (as in the present case) cutoff. This justifies our misty-CC model in which CCs are made up of infinitesimal cloudlets (section 4.3) that provide a computationally inexpensive way to produce observables from just thousands of CCs that can be compared efficiently with observations.

HR24 carried out a comprehensive study of the variation of various parameters of their model of cloudlets within CCs. However, they were limited by computational cost in generating an enormous number of small cloudlets for their models approaching the mist limit. They found that the cool gas mass, the smallest cloudlet mass, the cool gas density, and the CC size most affected the column density and EW distributions. The variation of other parameters within a reasonable range, such as the cloudlet size distribution, their radial distribution within CC, and turbulent velocity parameters, had a relatively minor impact. Their comprehensive exploration allows us to focus on the complementary aspects in our work. In addition to the misty CC model (section 4.3), we study the observational properties of CCs populated with tiny (up to 0.1 pc) cloudlets and their implications for the realistic modeling of the multiphase CGM. In particular, we study how the cloudlets within a CC start to overlap increasingly in velocity space with a decreasing cloudlet size (section 4.4). This further motivates our misty CC model, in which we approximate the spread in LOS velocity of numerous cloudlets with a single turbulent broadening parameter (see Fig. 4.9). Further, we model ellipsoidal (as opposed to spherical in *CloudFlex*) cloudlets from first principles and populate the entire CGM with these. This approach is even more expensive than HR24's approach but produces results largely consistent with them.

### 4.6.2 Modeling intermediate temperature gas

The primary focus of this paper is on modeling the cool gas. In principle, the same setup can also be applied to the intermediate temperature (warm) gas with few modifications. The warm gas is also expected to reside in clumpy structures like CCs, but with a larger volume fraction as compared to cool gas because of its lower (physical) density. To model the warm gas, we consider the misty cool CCs in the CGM. Each cool CC is assumed to have not only cool cloudlets but also warm and hot gas inside it. The warm gas is expected to envelop the cloudlets within a CC (see Fig. 8 in Armillotta et al. 2017). The cool cloudlet volume fraction within a CC is small ($\sim 0.016$; see Eq. 4.10). Being 10-30 times lower in density, the warm gas (traced by OVI) will occupy a larger volume by a similar factor, assuming a similar mass in warm and cool gas (a similar cool and warm gas mass is suggested by Table 3 in D24). This implies a volume fraction of the warm phase in a CC $\sim 20-50\%$; the majority of volume, even within a CC, is in the hot phase. We assume our CCs to be misty even in the warm phase with the same size as cool CCs

and the same total cool and warm gas masses, shoot lines of sight through the CGM, and compute the column density of OVI using the photo (PIE) + collisional (CIE) ionization equilibrium OVI fraction at $10^{5.5}$ K and redshift of 0.2 (the fraction of OVI is roughly constant $\approx 0.24$ over wide a density range). Note that OVI is a good tracer of $\sim 10^{5.5}$ K warm gas in the CGM under CIE. There can, however, be a significant amount of OVI produced by the lower temperature gas ($\lesssim 10^5$ K) under PIE depending on the strength of the radiation field (Werk et al. 2016).

Figure 4.14 shows the column density distribution of OVI tracing the warm ($10^{5.5}$ K) gas along $10^4$ sightlines (empty sightlines are not shown). The observational data points in green color are from the COS-Halos (Werk et al. 2013) survey. Predictions from our simple Misty CC model agree well with the observed distribution of OVI column density, including the upper and lower limits. This simple exercise shows the predictive power, flexibility, and computational efficiency of our Misty CC model for studying the multiphase CGM. Just as the combination of the covering fraction and the average column density provides an unbiased estimate of the cool CGM mass, the same observables for OVI can be applied easily to estimate the warm CGM mass. However, warm gas may not always be associated with cool clouds, and there can be extended structures possibly due to the various formation channels like cosmological accretion (McQuinn & Werk 2018), and galactic processes (Shapiro & Field 1976), etc. Therefore, this simple modeling of warm gas in the form of spherical cloud complexes does not reflect the expected diverse morphology of warm gas in the CGM.

### 4.6.3 Astrophysical Implications

The majority of the baryonic mass in the universe is in the diffuse intergalactic and circumgalactic medium. While the IGM dominates the global baryonic mass budget of the local Universe, even within galactic halos, the majority of baryons reside in the diffuse CGM and not in the dense interstellar medium and stars. Being major matter reservoirs, the CGM controls star formation in galaxies across cosmological timescales.

Fundamental questions in CGM research are regarding the fraction of baryons in the CGM as a function of halo mass, its spatial extent, and the distribution of the CGM mass across different temperature phases. While direct observations of the volume-filling hot CGM are rare (being volume-filling and close to hydrostatic, the hot CGM is easier to

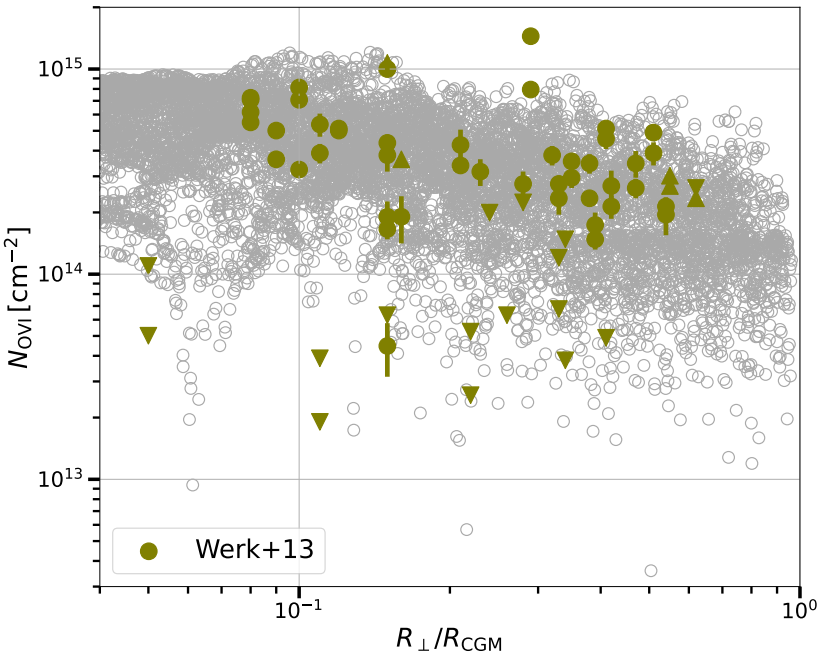



Figure 4.14: Column density distribution of OVI along $10^4$ sightlines, as predicted by our fiducial CC model with a simple prescription for warm gas (see section 4.6.2). Moreover, we assume the OVI ion fraction from photo+collisional ionization equilibrium at $10^{5.5}$ K, and assume similar cool and warm gas masses. The observed data points are from the COS-Halos (Werk et al. 2013) survey. The spread of OVI columns from our Monte Carlo model matches well with the observed spread.

model), the cool and warm phases are routinely probed through quasar absorption lines. However, since cool and warm CGM phases are not volume-filling and occur in the form of clouds, the inferred column densities show a large scatter even in a uniform galaxy sample, which prevents us from drawing robust conclusions about their mass budget.

We show that a large variation in the column density of the cool/warm ions is natural in a CGM in which these phases are not spread uniformly throughout the CGM, but are instead confined to thousands of $\sim 10$ kpc CCs spread sporadically throughout the CGM (see Figs. 4.5, & 4.14). Moreover, the average column density and the area covering fraction in a uniform galaxy+quasar sample can constrain the mass of the cool and warm phases of the CGM, as illustrated in Fig. 4.7.

### Inferring cool CGM mass from quasar absorption

One of the ultimate goals of our (and similar) models is to obtain a robust estimate of the cool/warm CGM mass from observations. Fig. 4.7 shows that a combination of the area-averaged MgII column density and the area covering fraction provides a robust proxy for the mass in cool CGM. Both ion column density and covering fraction can be inferred from observational samples of galaxies probed by quasar sightlines. However, the primary observable in these studies is the transmitted flux spectrum, which at high resolution can have many components separated by small centroid velocity shifts for the same sightline. Each of these resolved components (depending on the spectral resolution of the spectrograph) can be modeled as a misty and turbulent CC along the LOS, each composed of numerous cloudlets. Physically distinct CCs may coincide in velocity space, and similarly, cloudlets within a CC may be distinct in velocity (e.g., Fig. 4.10). Since the column density essentially counts all the ions along the LOS, this complication does not affect the cool CGM mass estimate.

There are different approaches to analyzing absorption spectra. The most reliable technique with high spectral resolution ($\lesssim 10$ km s$^{-1}$) is to fit the absorption profile with a number of absorption components with Voigt profiles. The best fit Voigt profile can give us the turbulent broadening parameter $b_{\rm turb}$ (particularly in the presence of multiple ions tracing the same phase that coincide kinematically) and column density for each component. We can add the column densities of all components along the LOS to obtain the total column density along it. For low-resolution spectra, the Voigt profile

fitting of components fails, and most studies employ the AOD (apparent optical depth) method (Savage & Sembach 1991). Under this, we obtain the optical depth spectrum and convert it into a column density spectrum (assuming that the absorption lines are not saturated). The column density spectrum is integrated to give the total ion column along the LOS. This popular method may underestimate the column density because of saturation and unresolved substructure. Section 4.4 essentially shows that both Voigt profile fitting and even fitting a single turbulent broadened misty CC model (implying that AOD method will also work well; large cloudlets without much internal turbulence can become saturated, reducing the accuracy of the AOD/mCC method) give a good estimate of the true column density of cloudlets along a LOS even with extreme blending in velocity due to thousands of cloudlets along the LOS.

Fig. 4.7, which plots the covering fraction versus the average column density, shows that a combination of these two observables provides a good estimate of the cool CGM mass. The column density along different sightlines can give us the average column density that should be plotted on the y-axis of Fig. 4.7. All spectrographs have a finite sensitivity and will inevitably miss out on weak absorption components, giving us a lower limit on the LOS column density. Similarly, saturated lines can give us a lower limit on the column density (e.g., see COS-Halos markers in Fig. 4.2). We calculate the covering fraction on the x-axis of Fig. 4.7 as the fraction of LOSs with EW larger than a small enough value (say 0.3 Å) so that the bulk of the EW distribution is sampled by observations. If these conditions are satisfied, Fig. 4.7 provides a robust way to estimate the cool gas mass in the diffuse CGM.

### Quasar absorption lines versus other CGM probes

Emission is weighted toward the highest density in the CGM, so it cannot typically probe the diffuse outer CGM (except through stacking; e.g., Zhang et al. 2019), which holds most of the CGM mass (e.g., Nielsen et al. 2024). Thus, emission gives a biased estimate of the CGM mass. FRBs are sensitive to the total number of electrons along the LOS, including the contribution of IGM, FRB host galaxy, and the Milky Way (e.g., Macquart et al. 2020; Connor et al. 2025), and the CGM contribution is typically subdominant. Moreover, while FRBs may be an unbiased probe of total CGM mass, one cannot separate the contribution from different temperature phases.

Similarly, the thermal Sunyaev-Zeldovich (tSZ) effect probes the integrated pressure along the LOS and, like FRBs, cannot distinguish between different CGM phases. Moreover, the signal is too small to be detected in individual galaxies and requires stacking of similar mass galaxies (e.g., Singh et al. 2015; Bregman et al. 2022; Das et al. 2023). The kinetic SZ signal is proportional to the product of the LOS velocity of the galaxy halo (determining which requires large galaxy surveys) and the electron column density, but stacking is necessary to detect the signal averaged over the whole CGM (e.g., see Schaan et al. 2021).

Therefore, quasar absorption line studies are the only means to study the various phases of the CGM. With an increasingly large number of background quasar-galaxy pairs, improving spatial and spectral resolution, and availability of a range of ions tracing a range of temperatures, quasar absorption lines have a unique position as the probe of the multiphase CGM. However, the modeling of the cool/warm phase is nontrivial, and more accurate models, going beyond the models presented in this work, are necessary to derive unbiased physical properties from observations.

Carefully combining the results from different observational probes from the CGM while being mindful of biases inherent in different techniques is the best way of obtaining robust physical constraints on the physical properties of the CGM. For this, we need robust phenomenological models of the multiphase CGM that can make testable predictions. While simulations of the CGM are steadily increasing in resolution and the included physics (Ramesh & Nelson 2024), we are still some way off from getting robust predictions from them because of insufficient spatial/mass resolution (we need a resolution better than a few pc in the cool phase to obtain converged results for MgII EW distribution; e.g., see section 4.4 & Figs. 4.9 & 4.12) and because of ambiguities related to feedback and sub-grid physics. The gap between expensive cosmological simulations and high-resolution observations can be filled by novel phenomenological models such as ours.

### 4.6.4 Caveats & future directions

The observational distribution of EWs and column densities of cool ion tracers in the CGM suggests a patchy distribution of cool gas in cloud complexes rather than uniformly throughout the CGM, as assumed in D24. But our assumption of spherical CCs

with a constant cloudlet size, a uniform distribution of cloudlets within a CC, a fixed turbulent broadening across a CC across all sightlines, etc., are extreme idealization. In our 'advanced' model, we have varied the size, mass, and radial distribution of CCs and shown that the trends are the same for both models. We have also considered the ellipsoidal cloudlets to roughly mimic the true shape of cloudlets in the CGM in Sec. 4.5. The distribution of cloudlets within a CC does not affect the results significantly (third row in Fig. 4.13). Consideration of the broadening based on the intersected length across a CC also does not significantly impact the EW distribution and covering fraction, since broadening is proportional to the cube root of the length scale. However, the column density and EW distribution with a range of CC models (e.g., see Fig. 4.5,4.6) follow observations, highlighting the utility and computational tractability of the misty CC model. We assumed spherical CCs, but they are likely to have a head-tail structure. Moreover, with a range of cloudlets, the large ones may not be dragged enough (e.g., see Eq. A.1) to remain in a turbulent CC but can instead precipitate towards the center replenishing the ISM, as required by the star formation histories over cosmological timescales (e.g., see Bera et al. 2023).

Our misty CC model can easily include an intrinsic scatter (Yang et al. 2025) within a CC as well for different phases. Moreover, similar to D24, which populates the whole CGM with a log-normal temperature (or 2-D density temperature) distribution, we can easily extend our misty CCs to have a range of temperatures and densities (which can also be adjusted according to the ambient pressure profile). These temperature and density distributions and the multiphase turbulence properties of CCs can be calibrated with detailed simulations of multiphase CGM patches (e.g., Mohapatra et al. 2022b). These models can also accommodate warm/cool gas within CCs that is mainly supported by nonthermal pressure of cosmic rays or magnetic fields, as suggested by some simulations (e.g., Sharma et al. 2010; Nelson et al. 2020; Butsky et al. 2020). The biggest advantages of the mCC model presented in section 4.3 are their flexibility and much lower computational cost relative to models that model the cloudlets from first principles (e.g., HR24, our models in section 4.5).

Misty CCs may also provide a useful recipe for modeling unresolved multiphase gas phenomenologically in galaxy simulations that typically lack sufficient resolution to resolve realistic CGM cloudlets (e.g., see Weinberger & Hernquist 2023; Butsky et al. 2024 for recent works along these lines). We can populate CCs aware of their origins in differ-

ent parts of the CGM, such as the high-pressure galactic outflows, low-metallicity IGM filaments, galactic fountains, and high-velocity clouds, etc., and produce observables to match more sophisticated observational samples that test anisotropies of CGM absorbers relative to the galaxy's minor axis and distance from the galactic center. The low computational cost, realism, and flexibility of our mCC model allow us to adapt it to produce observable distributions for a range of model variations.

## 4.7 Summary

Here we provide a summary of the salient aspects of this paper.

1. We present the misty cloud-complex (*mCC*) model to understand and match the observed distribution of column densities, equivalent widths (EWs), and covering fractions of cool ions such as MgII (Fig. 4.5, 4.6) and warm ions like OVI (Fig. 4.14). This model further expands and explores the connections between the misty CGM models of Dutta et al. 2024a and the *CloudFlex* model presented by Hummels et al. 2024. The former model assumes that the cool/warm gas is uniformly spread throughout the CGM, producing a smooth variation of cool gas column density. The *CloudFlex* model assumes the CGM cool gas to be spread across cloud complexes (CCs) and quantifies the distribution of column densities and equivalent widths across sightlines through these CCs, which are populated by $\sim 10^6$ cloudlets (it is computationally difficult to increase the number of cloudlets per CC much beyond this). Like *CloudFlex*, our misty CC model also assumes the cool gas to be spread over CCs but models the cool cloudlets analytically in the mist limit (analogous to D24). This makes our model analytically tractable and computationally inexpensive compared to *CloudFlex* (which has a hard time reaching the mist limit due to computational limitations). With only $\sim 10^3$ CCs spread over the CGM, our *mCC* model can satisfactorily reproduce the observational spread of MgII EWs and other observables (e.g., see Figs. 4.5 & 4.6).

2. Beyond our 'basic' misty CC model, where we assume fixed CC size and mass, we consider more realistic mass, size, and radial distribution of CCs in the CGM in our 'advanced' model, motivated by observations and simulations. Both models show similar qualitative features, but the scatter in the column density is larger for the

'advanced' model due to size and mass variation of CCs, which results in a larger number of CCs than in the 'basic' model.

3. We demonstrate that the combination of the average CGM column density and covering fraction provides a robust estimate of the cool CGM mass (see Fig. 4.7). The observed distribution of the inferred MgII column density and EW from the COS-Halos survey (Werk et al. 2013; Milky Way-like galaxies) suggests a cool CGM mass $\sim 10^{10} M_{\odot}$ (see Fig. 4.5, 4.6). Further, about $\sim 10^3$ CCs each of $\sim 10$ kpc seems to match the observed distribution of MgII column density and equivalent width well. Encouragingly, these parameters are consistent with our mCC model and with the first principles modeling of cloudlets across the CGM.

4. We quantify the mist limit within a CC for the parameters quantifying a CC (see Appendix A): the volume fraction of cool gas within CC ($f_V$) and the number of cloudlets ($N_{\rm cl}$). We find that the mist limit, for which a typical sightline encounters at least one cloudlet, starts to be approached for $N_{\rm cl} \gtrsim f_V^{-2}$. Further, we show that $\sim$ pc scale cloudlets within CCs produce extreme blending in absorption spectra, but the total absorption spectrum requires only a few components that can be well fit by the *mCC* ansatz for the scaling of turbulent broadening with the CC size (see Fig. 4.9) We also show that it is impossible to unambiguously infer the 3D information of cool cloud components from absorption spectra (see Fig. 4.10).

5. In section 4.5, we directly generate cloudlets in all CCs spread throughout the CGM. We confirm that it is computationally challenging to approach the mist limit for a small number ($\lesssim 10^6$) of cloudlets within a CC. The observed MgII EW distribution and covering fraction (COS-Halos sample; Werk et al. 2013) match with our direct modeling of cloudlets for $\sim 10^3$ CCs with a total cool CGM mass of $\sim 10^{10} M_{\odot}$ and a typical size $\sim 10$ kpc, distributed radially with a power-law with index $\alpha = 1$ (see Fig. 4.12 and 4.13).

To conclude, this paper bridges the gap between quasar absorption studies, simpler phenomenological modeling of cool CGM, and the first-principles cosmological galaxy formation simulations that typically severely lack the resolution to resolve cool cloudlets. The flexibility and ease in creating various observables from our simple, robust, but realistic model will help improve the modeling of the cool CGM.

## 4.8 Data Availability

We have made all the codes and data used in this work public in the *GitHub* repo `mCC`[10]. Any other data associated with this article is available upon reasonable request to the corresponding author.

[10] https://github.com/mukeshrri/mCC

# Chapter 5

# Detection of 'super-virial' gas in the Circumgalactic medium of the Milky Way towards PKS 2155-304

Based on :
Bisht, M.S., Das, S., Mathur, S., Roy, M., Krongold, Y., Gupta, A. 2025, submitted to ApJ [under review]
doi: 10.48550/arXiv.2509.02019

# Main Results

- We detected $z = 0$ CGM absorption lines of various ions in the X-ray spectra of PKS 2155-304 using *Chandra* and *XMM-Newton* grating data.
- For the first time, we detected Mg XII K$\alpha$ line in the CGM of the MW along with Si XIV K$\alpha$, which are the tell-tale signatures of the 'super-virial' gas ($\sim 10^7$ K) in X-ray absorption.
- Using model-independent analysis and hybrid-ionization modeling, we inferred four distinct temperature phases along this direction, namely 'super-virial' or hot phase ($\approx 5 \times 10^7$ K), 'virial' or warm-hot phase ($\approx 2 \times 10^6$ K), 'sub-virial' or warm phase ($\approx 2 \times 10^5$ K), and cool phase ($< 1.7 \times 10^5$ K).
- We found that the hot phase has a super-solar composition of [Mg/O] and [Si/O], and is $\alpha$-enriched, consistent with previous such studies along different sightlines.
- This study marks the first investigation of its kind at southern Galactic latitude and provides clear evidence that the super-virial absorbing phase is likely widespread.

## 5.1 Introduction

Galaxy disks are surrounded by the vast reservoir of gas known as the Circumgalactic medium (CGM; Tumlinson et al. 2017). The circumgalactic gas plays a vital role in galactic evolution, as it includes both inflowing material from the intergalactic medium (IGM), which serves as fuel for star formation, and outflowing gas expelled by stellar feedback and active galactic nucleus (AGN) activity. Depending on the physical processes at play in the CGM (Donahue & Voit 2022; Faucher-Giguère & Oh 2023), the gas may either remain in the halo for extended periods due to long cooling times or cool and condense, eventually falling back onto the galactic disk to fuel future star formation.

The CGM of the Milky Way (MW) is diffuse and multiphase with temperatures ranging from the cool ($\sim 10^4$ K), warm ($\sim 10^5$ K), to the warm-hot phase at the virial temperature ($\sim 10^6$ K) and number density varying by $2-3$ orders of magnitude $\sim 10^{-4} - 10^{-1}\,\mathrm{cm}^{-3}$. The most massive and the most volume-filling phase is the warm-hot phase (Mathur 2022). The cool and warm gas in the CGM is typically detected as UV/optical absorption in the spectra of the bright background sources like quasars using tracers like Mg II , C II , Ca II , Si II , Si IV , C IV , O VI , etc. The warm-hot virial phase is detected in both X-ray absorption (Nicastro et al. 2002; Williams et al. 2005; Gupta et al. 2012, 2014; Nicastro et al. 2016; Gupta et al. 2017; Gatuzz & Churazov 2018) and X-ray emission (Kuntz & Snowden 2000; Yoshino et al. 2009; Henley & Shelton 2010, 2013; Henley et al. 2015; Nakashima et al. 2018; Kaaret et al. 2020).

Recently, even hotter ($\sim 10^7$ K) 'super-virial' gas has been detected in the CGM of the MW coexisting with the virial phase. This hot gas has been found in X-ray absorption (Das et al. 2019b, 2021; Lara-DI et al. 2023; McClain et al. 2024b; Lara-DI et al. 2024a) and X-ray emission (Das et al. 2019a; Gupta et al. 2021; Bluem et al. 2022; Bhattacharyya et al. 2023; Ponti et al. 2023; Sugiyama et al. 2023; Gupta et al. 2023). By studying and analyzing the X-ray data toward the Galactic X-ray Binaries (XRBs), Lara-DI et al. 2024c and Roy et al. 2025 concluded that indeed the hot gas or the 'super-virial' gas detected in absorption has an origin beyond the Galactic disk, from the extra-planar region or the extended medium. Using 'shadow observations' with *Suzaku*, Gupta et al. 2025 conclusively showed that the hot gas in emission is also from regions beyond the Galactic disk. However, the temperature and chemical composition in emission differ from those in absorption; thus, the super-virial temperature gas detected in absorption

and emission is not the same phase, even though both phases may exist in the extra-planar region of the Galaxy.

In X-ray absorption, the super-virial gas is detected along three individual sightlines with high quality grating spectra, 1ES 1553+113 (Das et al. 2019b; $l = 21.21°, b = 43.96°$), Mrk 421 (Das et al. 2021; $l = 179.83°, b = 65.03°$), and NGC 3783 (McClain et al. 2024b; $l = 287.46°, b = 22.95°$) using the absorption lines of Hydrogen-like and Helium-like ions of Carbon, Nitrogen, Oxygen, Neon, Magnesium, and Silicon in the continuum of the background quasar. These three sightlines probed the 'super-virial' gas in the Northern hemisphere. Lara-DI et al. 2023, 2024a stacked 47 sightlines across the sky and detected this super-virial phase using Si XIV and S XVI absorption lines. In this work, we have extended the search for the hot gas in X-ray absorption towards another sightline with high-quality grating spectra, PKS 2155-304 that lies in the Southern latitudes.

PKS 2155-304 is well observed by *Chandra* (Weisskopf et al. 2000) and *XMM-Newton* (Jansen et al. 2001) for calibration purposes and studying the blazar itself. The deep archival data obtained from these sensitive instruments across multiple sightlines offer a valuable opportunity to study the Milky Way CGM using X-ray absorption line spectroscopy (Mathur 2022), allowing tighter constraints on its physical properties. We utilize archival data for our study and searched for absorption lines of Hydrogen and Helium-like ions of Carbon, Nitrogen, Oxygen, Neon, Magnesium, and Silicon.

In Section 5.2, we discuss our data reduction and analysis method, followed by results in Section 5.3. Finally, we discuss and conclude this work in Sections 5.4 and 5.5.

## 5.2 Data Reduction and Analysis

PKS 2155-304 is a well-studied Blazar ($l = 17.7°$, $b = -52.2°$) at $z = 0.116$ (Falomo et al. 1993). There are several archival *Chandra*[1] and *XMM-Newton*[2] observations available towards this sightline. We use the grating data of these observatories to look for $z = 0$ absorption lines of H-like and He-like metal ions. We analyze ACIS-MEG, ACIS-LETG, and HRC-LETG data of *Chandra* and RGS1 and RGS2 data of *XMM-Newton*.

[1] https://cda.harvard.edu/chaser/

[2] https://heasarc.gsfc.nasa.gov/docs/archive.html

Table 5.1: Detected/non-detected ions and their EW for various instruments.

| Ion | Transition | $\lambda_0$ (Å) | EW (mÅ) | | | | |
|---|---|---|---|---|---|---|---|
| | | | HRC-LETG | ACIS-LETG | ACIS-MEG | RGS1 | RGS2 |
| (1) | (2) | (3) | (4) | (5) | (6) | (7) | (8) |
| C V | K$\alpha$ | 40.267 | $7.3 \pm 3.3$ | – | – | – | – |
| C VI | K$\alpha$ | 33.736 | $< 9.8$ | $6.3 \pm 3.1$ | – | $6.2^{+2.0}_{-1.7}$ | $5.9 \pm 1.6$ |
| N VI | K$\alpha$ | 28.787 | $5.2 \pm 2.0$ | $< 10.5$ | – | cool pixel | $< 6.6$ |
| N VII | K$\alpha$ | 24.781 | $< 5.3$ | $3.2 \pm 1.4$ | – | chip gap | $< 4.3$ |
| O IV | K$\alpha$ | 22.741 | $5.8^{+2.1}_{-2.0}$ | $4.9 \pm 1.6$ | – | node gap | dead CCD |
| O V | K$\alpha$ | 22.370 | $< 9.0$ | $< 4.2$ | $< 15.4$ | $< 5.6$ | dead CCD |
| O VII | K$\alpha$ | 21.601 | $10.6 \pm 1.9$ | $9.5^{+1.0}_{-1.9}$ | $13.5^{+3.4}_{-2.1}$ | $15.4^{+1.2}_{-1.1}$ | dead CCD |
| | K$\beta$ | 18.627 | $< 7.5$ | $2.1^{+1.2}_{-1.0}$ | $< 9.0$ | $4.7^{+1.0}_{-1.3}$ | $< 1.8$ |
| O VIII | K$\alpha$ | 18.969 | $5.1^{+1.4}_{-1.8}$ | $3.6 \pm 1.1$ | $6.6 \pm 2.0$ | cool pixel | $7.6 \pm 1.1$ |
| Ne IX | K$\alpha$ | 13.447 | $6.6^{+1.7}_{-1.6}$ | $< 4.0$ | $3.4^{+1.1}_{-1.3}$ | dead CCD | $7.0^{+1.2}_{-1.1}$ |
| Ne X | K$\alpha$ | 12.134 | $< 7.9$ | $< 3.3$ | $< 3.4$ | dead CCD | $< 4.0$ |
| Mg XI | K$\alpha$ | 9.169 | $< 7.2$ | $< 1.6$ | $< 0.7$ | $< 4.3$ | $5.7 \pm 1.7$ |
| Mg XII | K$\alpha$ | 8.421 | $< 8.2$ | $< 2.6$ | $1.5 \pm 0.6$ | $< 5.9$ | $< 9.1$ |
| Si XIII | K$\alpha$ | 6.648 | $< 3.1$ | $< 2.4$ | $< 2.5$ | $< 6.3$ | $< 8.5$ |
| Si XIV | K$\alpha$ | 6.182 | $3.7 \pm 1.8$ | $< 2.5$ | $< 2.6$ | $< 18.8$ | $< 24.9$ |

### 5.2.1 Data Reduction

We extract all the archival data of ACIS-LETG[3], HRC-LETG[4], ACIS-MEG[5] and RGS1/RGS2[6] for our analysis.

For *Chandra* data, we process and reduce the data for each observation with the latest calibration database of `CIAO` v4.16 using the `Chandra_repro` command. We combine the positive 1$^{st}$ order spectra for all the observations and similarly, the negative 1$^{st}$ order spectra for all the observations. We then combine the co-added positive and negative order spectra individually for ACIS-LETG, HRC-LETG, and ACIS-MEG using the `combine_grating_spectra` command. In HRC-LETG, the spectrum is the combination of all the orders (1$^{st}$ to 8$^{th}$), as HRC cannot resolve the individual diffracted orders. To account for the contribution of all the orders, we add the positive and negative order RMF and ARF files of all the observations for each order (1 to 8) using `addresp` command. We load the response files corresponding to all the orders for our HRC-LETG analysis.

For *XMM-Newton* RGS1/RGS2 data, we use the latest calibration data `CALDB` v4.11.2 and reduce the data using the `rgsproc` command. We then determine the Good Time Interval (GTI) using the `tabgtigen` command by removing time intervals where the background count rate exceeds $0.1\,\mathrm{cnt\,s^{-1}}$. After obtaining GTI, we combine the first-order spectra of all the observations using the `rgscombine` command separately for RGS1 and RGS2. We only consider the 1$^{st}$- order spectra for all the instruments (except HRC-LETG), as the effective area is lower for higher-order spectra.

After obtaining all the spectra (3 from *Chandra* and 2 from *XMM-Newton*), background spectra, response matrix file (RMF), and ancillary response file (ARF), we load them in `XSPEC` v12.13.0 for further analysis. The total exposure times for ACIS-LETG, HRC-LETG, ACIS-MEG, RGS1/RGS2 are 718.1, 319.5, 289.4, and 1981 Ks, respectively.

[3]ObsID: 1015, 1703, 1790, 1795, 1796, 1797, 2323, 2324, 2335, 3168, 3667, 3668, 3669, 3707, 4416, 6090, 6091, 6874, 6924, 6927, 7293, 8388, 9704, 9706, 9708, 9710, 9713, 10662, 11965, 13096, 15475, and 16423.

[4]ObsID: 331, 1013, 1704, 3166, 3709, 4406, 5172, 6922, 6923, 7294, 7295, 8379, 9707, 9709, and 9711.

[5]ObsID: 337, 1014, 1705, 3167, 3706, 3708, 5173, 6926, 7291, 8380, 8436, 9705, and 9712.

[6]ObsID: 0080940101, 0080940301, 0080940401, 0124930101, 0124930201, 0124930301, 0124930501, 0124930601, 0158960101, 0158960901, 0158961001, 0158961101, 0158961301, 0158961401, 0411780101, 0411780201, 0411780301, 0411780401, 0411780501, 0411780601, 0411780701, 0411780801, 0411781301, 0411781701, 0411782101, 0727770101, 0727770501, 0727770901, and 0727771301.

Table 5.2: Parameters of the absorption lines used for our analysis. Fourth column: detected EW; fifth, sixth, and seventh columns: column density contribution from the three distinct temperature phases calculated using hybrid-ionization modeling; eighth column: total column density across three phases; ninth column: column density from detected EW using the linear part of the curve of growth.

| (1) Ion | (2) Transition | (3) Instrument | (4) EW (mÅ) | (5) $N_{T_1}$ ($cm^{-2}$) | (6) $N_{T_2}$ ($cm^{-2}$) | (7) $N_{T_3}$ ($cm^{-2}$) | (8) $N_{tot}$ ($cm^{-2}$) | (9) $N_{EW}$ ($\times 10^{15}$ $cm^{-2}$) |
|---|---|---|---|---|---|---|---|---|
| C V | K$\alpha$ | HRC-LETG | $7.27 \pm 3.31$ | $1.3 \pm 0.5 \times 10^{15}$ | $9.8^{+12.2}_{-1.7} \times 10^{13}$ | – | $1.4^{+0.62}_{-0.52} \times 10^{15}$ | $0.78 \pm 0.36$ |
| C VI | K$\alpha$ | RGS2 | $5.94 \pm 1.60$ | $4.3^{+0.8}_{-1.2} \times 10^{12}$ | $8.3^{+7.1}_{-2.6} \times 10^{14}$ | $4.4^{+3.6}_{-1.0} \times 10^{14}$ | $1.3^{+1.1}_{-0.4} \times 10^{15}$ | $1.42 \pm 0.38$ |
| N VI | K$\alpha$ | HRC-LETG | $5.18 \pm 1.96$ | $2.7^{+2.7}_{-0.5} \times 10^{14}$ | $3.8^{+3.8}_{-1.0} \times 10^{14}$ | – | $6.5^{+6.5}_{-1.5} \times 10^{14}$ | $1.05 \pm 0.40$ |
| N VII | K$\alpha$ | HRC-LETG | $< 5.26$ | $3.2^{+4.2}_{-0.2} \times 10^{11}$ | $7.7^{+3.1}_{-0.4} \times 10^{14}$ | $3.8^{+3.1}_{-0.9} \times 10^{14}$ | $1.2^{+0.6}_{-0.1} \times 10^{15}$ | $< 2.33$ |
| O VII | | | | $5.0^{+16.9}_{-4.9} \times 10^{13}$ | $4.4^{+2.2}_{-0.5} \times 10^{15}$ | – | $4.5^{+2.4}_{-0.5} \times 10^{15}$ | ~~9.32~~$^{+1.81}_{-0.76}$ [a] |
| | K$\alpha$ | ACIS-LETG | $9.50^{+0.96}_{-1.88}$ | | | | | $3.31^{+0.34}_{-0.65}$ |
| | K$\beta$ | ACIS-LETG | $2.06^{+1.22}_{-1.00}$ | | | | | $4.59^{+2.72}_{-2.22}$ |
| O VIII | K$\alpha$ | ACIS-LETG | $3.60 \pm 1.11$ | – | $1.9^{+1.3}_{-0.4} \times 10^{15}$ | $3.1^{+2.8}_{-0.7} \times 10^{15}$ | $5.0^{+4.1}_{-1.1} \times 10^{15}$ | $2.72 \pm 0.84$ |
| Ne IX | K$\alpha$ | HRC-LETG | $6.62^{+1.67}_{-1.64}$ | – | $1.1^{+0.2}_{-0.6} \times 10^{16}$ | – | $1.1^{+0.2}_{-0.6} \times 10^{16}$ | $5.71^{+1.44}_{-1.42}$ |
| Ne X | K$\alpha$ | HRC-LETG | $< 7.91$ | – | $1.3 \pm 0.7 \times 10^{14}$ | $5.2^{+5.9}_{-0.7} \times 10^{15}$ | $5.3^{+6.0}_{-0.8} \times 10^{15}$ | $< 14.59$ |
| Mg XI | K$\alpha$ | ACIS-MEG | $< 0.66$ | – | $4.7^{+0.9}_{-2.5} \times 10^{14}$ | – | $4.7^{+0.9}_{-2.5} \times 10^{14}$ | $< 1.19$ |
| Mg XII | K$\alpha$ | ACIS-MEG | $1.47 \pm 0.59$ | – | – | $6.1^{+8.0}_{-0.5} \times 10^{15}$ | $6.1^{+8.0}_{-0.5} \times 10^{15}$ | $5.44 \pm 2.27$ |
| Si XIII | K$\alpha$ | HRC-LETG | $< 3.07$ | – | $4.69^{+5.05}_{-1.11} \times 10^{14}$ | – | $4.69^{+0.99}_{-0.26} \times 10^{14}$ | $< 10.35$ |
| Si XIV | K$\alpha$ | HRC-LETG | $3.73^{+1.75}_{-1.78}$ | – | – | $5.5^{+7.0}_{-0.5} \times 10^{16}$ | $5.5^{+7.0}_{-0.5} \times 10^{16}$ | $26.54^{+12.44}_{-12.63}$ |

[a] Saturation corrected column density. It cannot be used in analysis, as O VII has a significant contribution from various temperature phases.

We use $\chi^2$ statistics for our analysis throughout the work. We quote $1\sigma$ error for detections and $3\sigma$ upper limit for non-detections.

### 5.2.2 Data Analysis

After obtaining the spectra, we model the continuum with a power-law absorbed by our Galactic disk using Tuebingen-Boulder ISM absorption model `tbabs`×`powerlaw`. `tbabs` calculates the cross section for X-ray absorption by the ISM as the sum of the cross sections for X-ray absorption due to the gas-phase ISM, the grain-phase ISM, and the molecules in the ISM. We fix the equivalent Hydrogen column density for `tbabs` model to $N_{\rm H} = 1.3 \times 10^{20}\,{\rm cm}^{-2}$ (HI4PI Collaboration et al., 2016). We let the index and normalization of the power-law vary. Next, we search for the H/He-like ions of Carbon, Nitrogen, Oxygen, Neon, Magnesium, and Silicon. To do so, we select $\approx \pm 2$ Å wavelength range around the $z = 0$ values of strong lines of these metals. To account for the metal absorption line, we add an absorbing Gaussian model (`agauss`). Therefore, our overall model is `tbabs*(po+agauss)`. For the line center of the Gaussian, we start with the $z = 0$ value of the absorption line and allow it to vary within the resolution element[7] of the respective grating. We fix the width of the Gaussian to $10^{-5}$ Å as the absorption lines are not expected to be resolved. We allow the normalization of the Gaussian to vary. We calculate the equivalent width (EW) of the absorption line using the `eqw` command. To calculate the $1\sigma$ uncertainty in EW, we first calculate $1\sigma$ error in normalization of the Gaussian using the `error` command. We then fix the normalization of the Gaussian to the $1\sigma$ upper and lower values and calculate the EW corresponding to these values, which is the $1\sigma$ uncertainty in EW. We call it a detection if the significance of EW is more than $2\sigma$,[8]; otherwise, we quote a $3\sigma$ upper limit on the EW. We repeat the above analysis for strong lines of each ion and each instrument and list our results in Table 5.1.

We show the EW of detected and non-detected ions in Table 5.1 for all the instruments. We detect (significance $\geq 2\sigma$) several absorption lines in different instruments. There is no wavelength coverage in MEG for C and N lines. C V K$\alpha$ is detected only in HRC-LETG, as there is no wavelength coverage in other instruments. C VI K$\alpha$ detection in ACIS-LETG, RGS1, and RGS2 are consistent with each other within $1\sigma$ uncertainty, while the $3\sigma$ upper limit from HRC-LETG is also consistent with different

[7]Resolution element ($\Delta\lambda$, FWHM) of 23, 50, and 70 mÅ for MEG, LETG, and RGS, respectively.
[8]Significance is defined as the ratio of best-fit EW to the $1\sigma$ error on the lower side

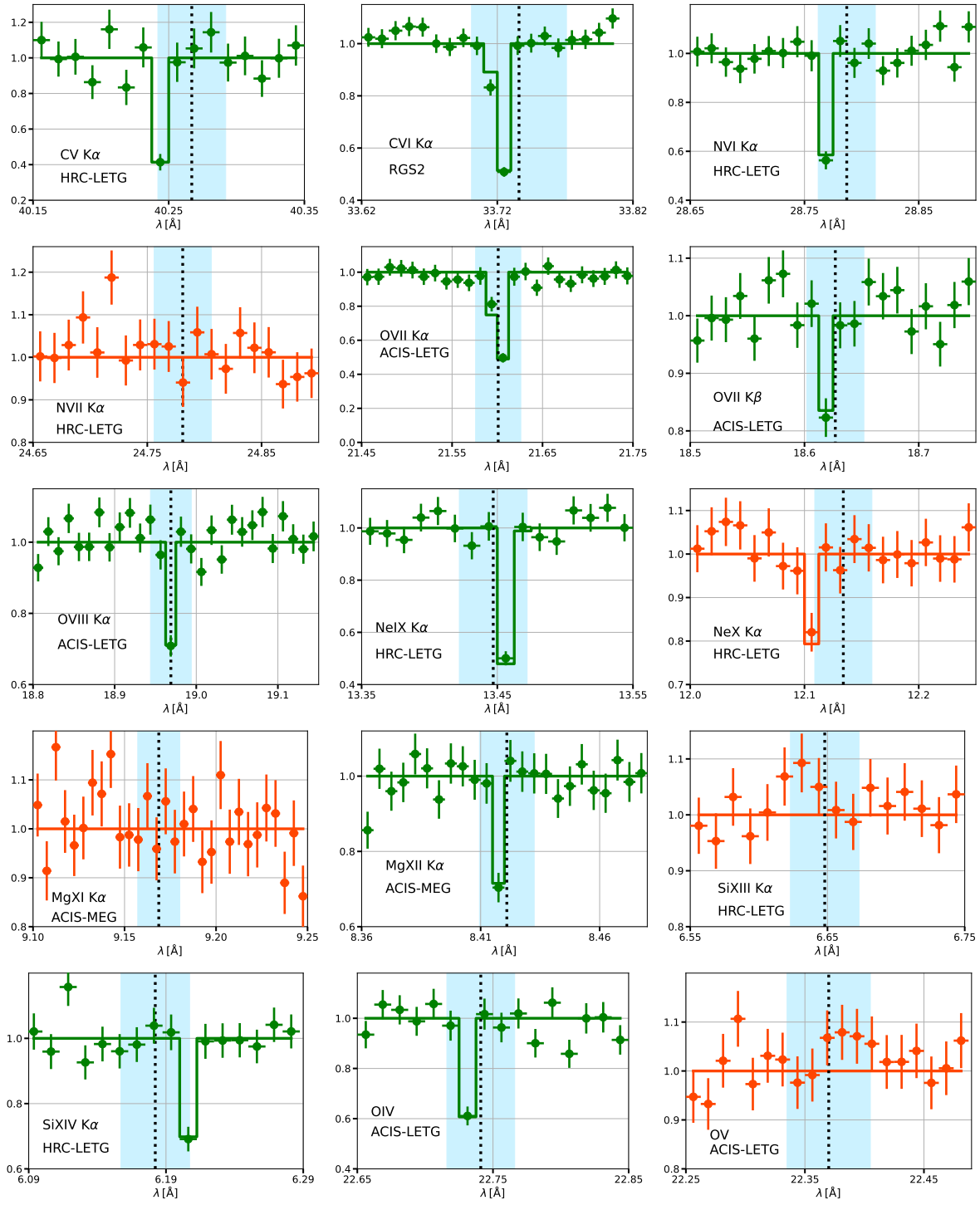



Figure 5.1: Normalized absorption profile of the detected (green) and non-detected (red) ions. The dotted black vertical line in each panel shows the $z = 0$ value of the line center of the respective ions. The shaded blue region in each panel indicates the resolution element of the respective instrument relative to the $z = 0$ value of the line center of the ion.

instruments. N VI K$\alpha$ is detected only in HRC-LETG, while ACIS-LETG and RGS2 show non-detection. For RGS1, there is a cool pixel at the corresponding wavelength. Detection and non-detections are consistent with each other. We detect N VII K$\alpha$ only in ACIS-LETG, while HRC-LETG and RGS2 show non-detection, and in RGS1, there is a chip gap at this wavelength. Again, detections and non-detections are consistent across instruments. O IV K$\alpha$ is detected in HRC-LETG and ACIS-LETG, and they are consistent with each other. We do not detect O V in any of the instruments. O VII K$\alpha$ is detected in all the instruments except for RGS2 due to a dead CCD ($\approx$ 20–24 Å). The EW value in ACIS-LETG is the lowest among all the instruments and is consistent only with HRC-LETG within 1$\sigma$ uncertainty. The EW values in RGS1 and MEG are high and are consistent with each other, but not with other instruments together. O VII K$\beta$ is detected in ACIS-LETG and RGS1, while there is no detection in other instruments, which are consistent with each other within error bars except for RGS1. O VIII K$\alpha$ shows a similar trend as O VII K$\alpha$, whereas there is cool pixel at this wavelength for RGS1.

Ne IX K$\alpha$ is detected in HRC-LETG, MEG, and RGS2, while ACIS-LETG shows non-detection. The values are not consistent across instruments. Neon lines cannot be detected in RGS1 due to a dead CCD at $\approx$ 10–14 Å. Ne X K$\alpha$ is not detected in any of the instruments. Mg XI K$\alpha$ is not detected in any of the instruments except in RGS2. MEG, which is most sensitive at these wavelengths, shows a non-detection with a 3$\sigma$ upper limit of 0.7 mÅ, while the EW obtained using RGS2 is very high. This could be due to the effect of a nearby cool pixel. Mg XII K$\alpha$ is detected in the CGM of the MW for the first time. It is detected in MEG, and the upper limits from other instruments are consistent with detection. Si XIII K$\alpha$ is not detected in any instruments. However, Si XIV K$\alpha$ is detected in HRC-LETG, with non-detection in other instruments, which are consistent with detection within 1$\sigma$ uncertainty.

Thus, we see that for most lines the measured EWs, either detections/non-detections, are consistent across instruments within 1$\sigma$ uncertainties. The only exceptions are the O VII K$\alpha$ and K$\beta$, O VIII K$\alpha$, Ne IX K$\alpha$, and Mg XI K$\alpha$. The inconsistencies in the EW values across instruments may be attributed to the impact of cool pixels in the surrounding wavelength regions, most notably in RGS1 and RGS2.

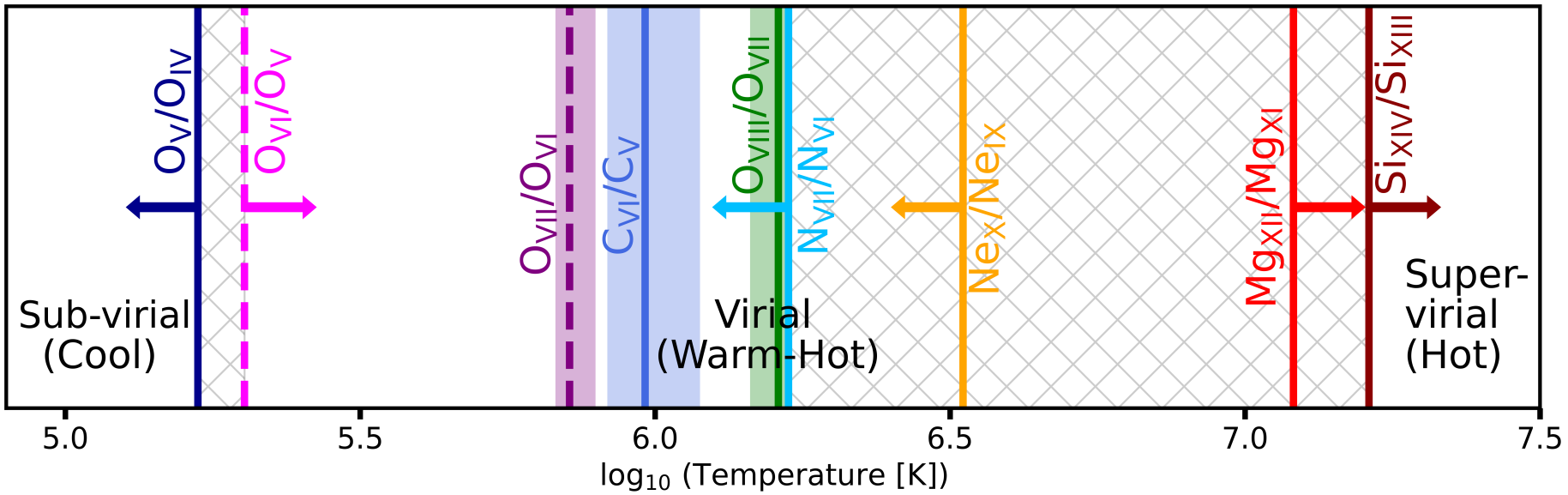



Figure 5.2: Temperature ranges estimated from the column density ratio of two adjacent ions of the same metal probed in X-ray absorption. It clearly shows the multiphase nature of the CGM with *temperature valleys* (hatched region) in between. The dashed magenta and purple lines show the temperature estimated from the column density ratios of O VI (detected in UV absorptions by Collins et al. 2004), O V (non-detection in this work), and O VII (this work), O VI (Collins et al., 2004) respectively.

### 5.2.3 Model-independent Analysis

In Table 5.2, we show the detected line details in the selected instrument for each ion based on the sensitivity at the respective wavelength value and significance of detection. We use these wavelength ranges for the specific instruments in our further analysis. The detections in the respective mentioned instruments are: C V K$\alpha$ (2.2$\sigma$), C VI K$\alpha$ (3.7$\sigma$), N VI K$\alpha$ (2.6$\sigma$), O IV K$\alpha$ (3.1$\sigma$) O VII K$\alpha$ (5.1$\sigma$), O VII K$\beta$ (2.1$\sigma$), O VIII K$\alpha$ (3.2$\sigma$), Ne IX K$\alpha$ (4.0$\sigma$), Mg XII K$\alpha$ (2.4$\sigma$), and Si XIV K$\alpha$ (2.1$\sigma$). We use the detected/non-detected ions in the mentioned instruments for our further analysis. In Figure 5.1, we show the normalized absorption profile (uncolvolved spectra with continuum normalized to unity) of the detected and non-detected ions in green and red colors, respectively. The black dotted line in each panel shows the $z = 0$ wavelength value, and the blue band shows the resolution element of the instrument. The best-fit wavelength within the resolution element for all the ions is shifted from the $z = 0$ value.

By fitting the metal absorption line using the Gaussian profile, we obtain the Equivalent Width (EW), which we then convert into column density using the linear part of the curve of growth (Draine 2011). We also detect the K$\beta$ line of O VII along with the K$\alpha$ line. Therefore, we obtain the Doppler $b$ parameter and the saturation corrected column density for O VII by combining the EW from K$\alpha$ and K$\beta$ lines using the flat part of the curve of growth.

The Doppler $b$ parameter and the column density ratio of detected H to He-like ions of the same element can be used to estimate the temperature of the gas bearing these ions under Collisional Ionization Equilibrium (CIE), assuming the ions exist in the same phase. The upper limit (non-detection) on the column density also provides useful constraints on the physical conditions of the gas bearing these ions, assuming CIE.

The temperature estimated from the column density ratio of C VI to C V is $9.6^{+2.3}_{-1.3} \times 10^5$ K, N VII to N VI is $< 1.7^{+0.3}_{-0.1} \times 10^6$ K, O IV to O V is $< 1.7 \times 10^5$ K, O V to O VII is $> 3.3 \times 10^5$ K, O VIII to O VII is $1.6^{+0.1}_{-0.2} \times 10^6$ K, Ne X to Ne IX is $< 3.3 \pm 0.5 \times 10^6$ K, Mg XII to Mg XI is $> 1.2 \pm 0.2 \times 10^7$ K, and Si XIV to Si XIII is $> 1.6^{+0.2}_{-0.3} \times 10^7$ K under CIE. These model-independent temperature estimates suggest the presence of the 'super-virial' or hot gas along with expected virial or warm-hot and 'sub-virial' or warm gas as shown in Figure 5.2. A further lower temperature cool gas is also indicated by the

column density ratios of O V and O IV . This cool phase is observed for the first time in X-ray studies. The dashed magenta and purple lines show the temperature estimated from the column density ratios of O VI (detected by Collins et al. 2004 in UV), O V (X-ray non-detection in this work), and O VII (X-ray detection in this work), O VI (Collins et al., 2004) respectively. The limits on the estimated temperature also demonstrate the presence of a *temperature valley* (hatched region in Figure 5.2) between the virial gas ($\sim 10^6$ K) and the super-virial gas ($\sim 10^7$ K). A *temperature valley* is also present between the sub-virial (warm) and cool phase.

These model-independent results show the multiphase nature of the CGM with *temperature valleys* in between, which roughly mimics the 'multi-peaked' log-normal distribution in temperature in the CGM (Dutta et al., 2024a). A 'Multi-peaked' log-normal distribution is obtained by adding multiple log-normal distributions with different peaks, heights, and widths. The multiple peaks may correspond to our model-independent temperature estimates, suggesting different temperature phases in the CGM. These estimated temperatures, along with the column density of the ions, can be used to estimate the abundance ratios of the elements. This abundance ratio can then be used to compare with the solar abundance ratio of the respective elements to check the solar/non-solar mixture of the abundance ratios of the elements. Since we have only upper limits on temperature using Ne and N ions, we assume that $N_{\rm Ne} \geq N_{\rm Ne\,IX}$ and $N_{\rm N} \geq N_{\rm N\,VI}$ . Therefore, we get a lower limit on [N/O] and [Ne/O] abundance ratios. The abundance ratio for [N/O] is $\geq -0.29^{+0.17}_{-0.19}$, [Ne/O] is $\geq 0.37^{+0.14}_{-0.20}$. These values clearly show that Neon is super-solar relative to Oxygen, while N is in solar mixture with O, assuming they exist in the same phase. These estimates clearly show the complex metal mixing and different temperature phases of the CGM of the Milky Way.

The $b$ parameter obtained for O VII is $48.8^{+4.6}_{-12.5}$ km s$^{-1}$ that correspond to a temperature of $2.3^{+0.4}_{-1.0} \times 10^6$ K assuming no non-thermal broadening. This temperature estimate is consistent with the temperature obtained from the column density ratios of O VIII and O VII within $1\sigma$ error.

### 5.2.4 `PHASE` model

To model all the detected and non-detected absorption lines self-consistently using the Voigt profiles, we fit the observed spectra with the `PHASE` model (Krongold et al. 2003;

Nicastro et al. 2018; Das et al. 2019b, 2021). PHASE model is a hybrid-ionization model based on collisional ionization and photo-ionization. The parameters of the PHASE model are temperature, equivalent hydrogen column density, the relative abundance of elements, non-thermal broadening, photo-ionization parameter ($U$), and redshift (equivalent to the line of sight velocity that shifts the line center). The abundance of elements is set to a solar value by default, but can be varied independently for He, C, N, O, Ne, Mg, Al, Si, S, Ar, Ca, Fe, and Ni. Therefore, the PHASE model can be used to disentangle various temperature phases and chemical composition of the CGM based on the observed absorption lines.

To fit with the PHASE model, we adopt the same wavelength range and continuum for each ion as used to detect it in a model-independent way in Sec. 5.2.2 and Table 5.2 for the respective instruments. We freeze the photo-ionization parameter $U$ to its lowest value of $10^{-3.9}$, assuming photo-ionization is negligible. Since the detected absorption line centers are consistent with the resolution element of the respective instruments, we fix the redshift parameter $z$ to 0 initially. We assume purely thermal broadening of the absorption lines, as shown by Das & Gronke 2024, that the non-thermal broadening along this sightline is insignificant.

We use the power-law continuum with the same index and normalization over the specified wavelength range for each ion, as discussed previously, and freeze these parameters for further analysis. The continuum model results in $\chi^2$/dof of 5354.35/5620. We then add a single temperature PHASE model with solar composition, which improves the fit ($\chi^2$/dof of 5202.63/5618) but cannot reproduce all the detected ions.

To check the importance of the non-solar composition of various elements relative to O, we allow the composition of C, N, Ne, Mg, and Fe to vary in a single temperature PHASE model, which results in a significant improvement in the fit with $\chi^2$/dof of 5179.24/5612 with null-hypothesis probability of 0.03%. It suggests the importance of the non-solar chemical composition. We refer to this virial warm-hot phase as PHASE_A or $T_2$.

However, this single temperature phase model with non-solar composition could not reproduce the column density of high ionization species like Mg XII and Si XIV , and under-predicts the O VIII column density. It indicates the presence of an additional, higher-temperature phase. Therefore, we add another temperature PHASE model to fit the data. We do not force any parameters of the two-temperature PHASE model to be the

same, except that we tie the relative abundance of [C/O] and [N/O] to be the same in both phases, as the observed ions of C and N are not expected to contribute significantly in the hot phase.

For the higher temperature phase, we vary the relative abundance of Ne, Si, Mg, and Fe. The two-temperature non-solar `PHASE` model results in $\chi^2$/dof of 5166.68/5606 with null-hypothesis probability of 3.4%, which is an improvement over the single-temperature non-solar phase model and successfully produces the Mg XII , Si XIV , and total O VIII column density. We refer to this 'super-virial' hot phase as `PHASE_B` or $T_3$.

The primary motivation of this work is to detect the hot super-virial phase along with the virial phase, which is successfully recovered using our `PHASE_A` and `PHASE_B` models discussed above. But these two-temperature phases under-predict the column density of C V K$\alpha$ and N VI K$\alpha$ lines. To account for the observed excess column density of C V and N VI lines, we add another `PHASE` model. We refer to this phase as `PHASE_C` or $T_1$ or sub-virial phase. We allow the temperature and equivalent H column density to vary, and we tie the C and N abundances in this phase to the virial phase. We fix the other metal abundances to the default solar value in this phase, which resulted in $\chi^2$/dof of 5162.39/5604 with null-hypothesis probability of 9.8%. However, the ions tracing the sub-virial phase (C V and N VI ) are blue-shifted; therefore, we vary the redshift parameter (equivalent to line-of-sight velocity) in the `PHASE_C`. This improved the fit-statistics further with $\chi^2$/dof of 5156.53/5603 with null-hypothesis probability of 1.2%. This additional phase successfully reproduces the excess C V K$\alpha$ and N VI K$\alpha$ column density. Therefore, all the observed column density values are well reproduced by our final best-fit `PHASE` model: `PHASE_A*PHASE_B*PHASE_C`. We show the results of our best-fit `PHASE` model in Table 5.3 with $1\sigma$ uncertainties.

Since we did not detect Mg XI , which traces the warm-hot gas, and Ne X , which traces the hot gas, do we require a non-solar composition of Mg in the warm-hot phase and Ne in the hot phase? To check the significance of non-solar composition of [Mg/O] in warm-hot phase, we freeze all the parameters in our best-fit `PHASE` model except T, $N_H$, and Mg composition in warm-hot phase, with $\chi^2$/dof of 5156.53/5617. We then freeze the [Mg/O] composition to solar value, which resulted in $\chi^2$/dof of 5156.55/5618. We calculated F-test statistics and found the null hypothesis probability of 88%. Similarly, we carried out the above analysis for Ne in the hot phase, which resulted in a null hypothesis probability of 38%. These results indicate that the non-solar compositions of Mg in the

| Parameter | PHASE_C ($T_1$) | PHASE_A ($T_2$) | PHASE_B ($T_3$) |
|---|---|---|---|
| T [K] | $2.2 \pm 0.5 \times 10^5$ | $1.8^{+0.3}_{-0.2} \times 10^6$ | $5.4^{+1.9}_{-0.8} \times 10^7$ |
| $N_{\rm H}$ [cm$^{-2}$] | $1.9^{+0.9}_{-0.8} \times 10^{18}$ | $8.8^{+2.2}_{-4.8} \times 10^{18}$ | $2.5^{+0.7}_{-1.0} \times 10^{21}$ |
| $v_{\rm los}$ [km s$^{-1}$] | $-95^{+23}_{-9}$ | – | – |
| [C/O] | tied to PHASE_A | $0.23^{+0.24}_{-0.16}$ | tied to PHASE_A |
| [N/O] | tied to PHASE_A | $0.35^{+0.30}_{-0.42}$ | tied to PHASE_A |
| [Ne/O] | – | $1.02^{+0.28}_{-0.27}$ | – |
| [Mg/O] | – | – | $0.43^{+0.21}_{-0.29}$ |
| [Si/O] | – | – | $0.93^{+0.22}_{-0.40}$ |
| [O/Fe] | – | $> -0.30$ | $> 1.0$ |
| [Ne/Fe] | – | $> 0.72$ | – |
| [Mg/Fe] | – | – | $> 1.43$ |
| [Si/Fe] | – | – | $> 1.93$ |

Table 5.3: Best fit PHASE model parameters.

warm-hot phase and Ne in the hot phase are statistically not required.

Further, we carry out statistical tests to verify if the line of sight velocity is consistent with 0 km s$^{-1}$ in both the hot and warm-hot phases. To do so, we freeze all the parameters except $T$ and $N_{\rm H}$ in the respective test phase. We then vary the redshift parameter (equivalent to line of sight velocity) in the respective phase and calculate the significance of non-zero line of sight velocity. For the hot phase, we obtain $\chi^2$/dof of 5155.77/5617 with null-hypothesis probability of 36%. Similarly, for the warm-hot phase, we obtain $\chi^2$/dof of 5154.82/5617, with null-hypothesis probability of 17%. Therefore, the line-of-sight velocity is consistent with zero in both warm-hot and hot phases.

## 5.3 Results

Using the PHASE model analysis, we infer three temperature phases of the CGM using the X-ray absorption lines towards PKS 2155-304. As expected from the model-independent temperature results, we detect virial, super-virial, and sub-virial phases from the PHASE model. In Table 5.3, we show the results of our best-fit PHASE model with $1\sigma$ error. In Table 5.2, the first column shows the ion, the second column shows the transition, the third column shows the instrument used to detect it, the fourth column shows the

equivalent width in mÅ, the ninth column shows the column density computed assuming linear part of the curve of growth, the fifth, sixth, seventh, and eighth columns show the column density predicted from `PHASE_C` ($N_{T_1}$), `PHASE_A` ($N_{T_2}$), `PHASE_B` ($N_{T_3}$) and total from all the three phases respectively. Therefore, the eighth and ninth columns can be compared with each other. The total column density predicted from the `PHASE` model is consistent with detection within $1\sigma$ error bars and $3\sigma$ upper limits for non-detections. For O VII , we detected both the K$\alpha$ and K$\beta$ lines. The ninth column for O VII in Table 5.2 shows the saturation corrected column density for O VII (line through the column density value). The saturation corrected column density cannot be used for analysis as both the warm-hot and warm phases contribute to the column density of O VII .

In Figure 5.3, we show the contribution of different phases for all the detected ions from our best-fit `PHASE` model. The blue dotted, green dashed, and red dashed-dotted lines show the contribution of warm ($T_1$), warm-hot ($T_2$), and hot ($T_3$) phases, respectively. Our analysis indicates that Mg XII and Si XIV originate exclusively from the hot phase, whereas Ne IX comes from the warm-hot phase. O VIII has a significant contribution from both warm-hot and hot gas, while O VII has contributions from warm-hot and warm phases. This suggests that the observed O VII and O VIII column density ratios cannot be used exclusively to estimate the temperature of the gas in the CGM, as they contribute significantly to different temperature phases. C VI comes from the warm-hot phase with a contribution from the hot phase, and N VI comes from both the warm and warm-hot phase. C V has a predominant contribution from the warm phase (see Table 5.2). Therefore, a similar conclusion holds for estimating temperature using the column density ratios of C VI and C V .

### 5.3.1 Temperature

For the virial, super-virial, and sub-virial phases, we obtain the best-fit temperature of $1.8^{+0.3}_{-0.2} \times 10^6$ K, $5.4^{+1.9}_{-0.8} \times 10^7$,K, and $2.2 \pm 0.5 \times 10^5$ K, respectively. The best-fit virial temperature along 1ES 1553+113 (Das et al., 2019b), Mrk 421 (Das et al., 2021), and NGC 3783 (McClain et al., 2024b) is $1.29^{+0.16}_{-0.27} \times 10^6$ K, $1.5 \pm 0.06 \times 10^6$ K, $6.76^{+2.79}_{-1.01} \times 10^5$ K, while the super-virial temperature is $1.15 \pm 0.26 \times 10^7$ K, $3.2^{+0.94}_{-0.31} \times 10^7$ K, and $4.07^{+1.3}_{-0.52} \times 10^6$ K respectively. The sub-virial temperature along Mrk 421 is $3.0 \pm 0.25 \times 10^5$ K. The best-fit virial, super-virial, and sub-virial temperatures for the stacked sightlines (Lara-DI

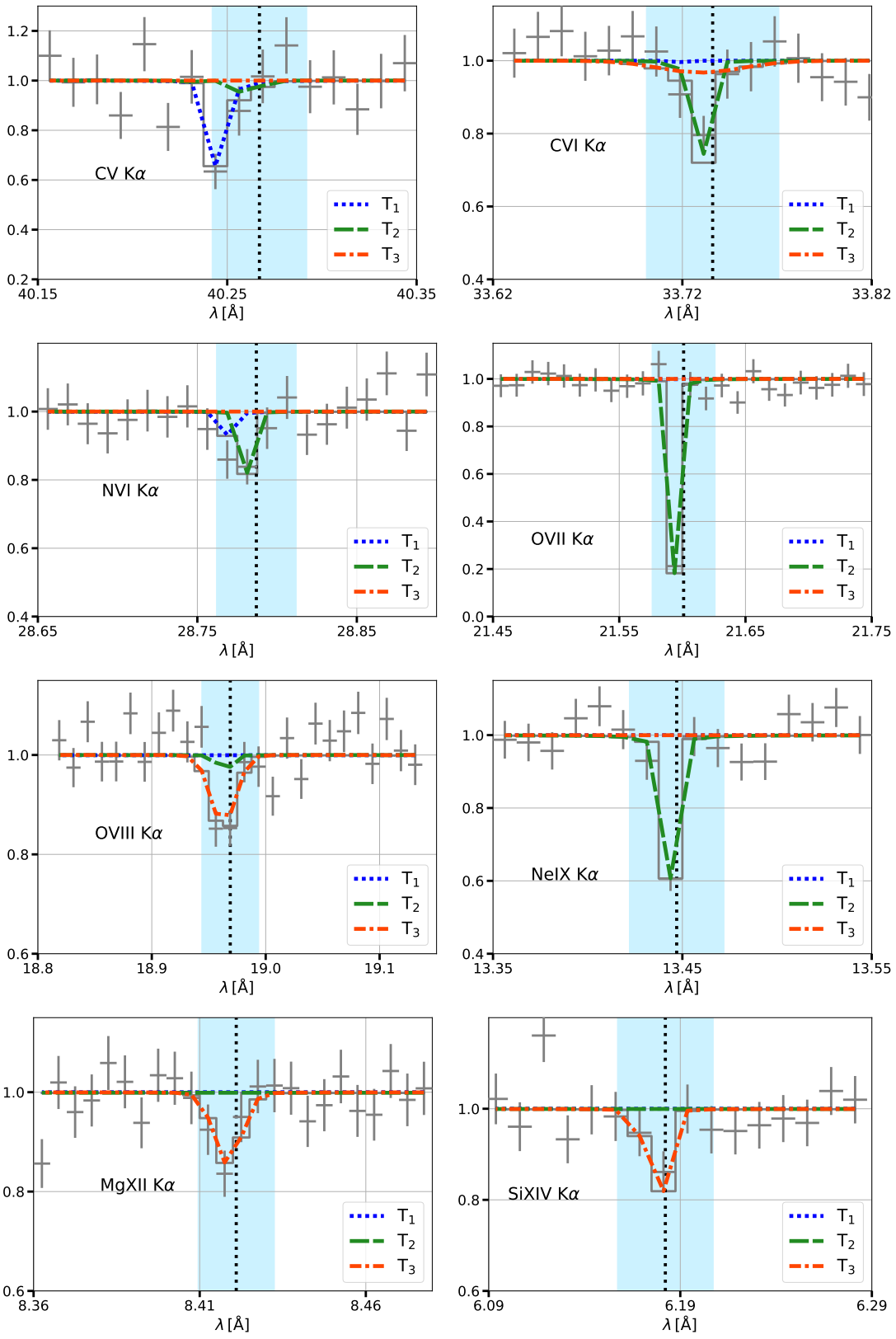



Figure 5.3: Individual contribution of different temperature phases for detected ions. The grey color shows the best-fit `PHASE` model, while blue, green, and red colors show the contribution of sub-virial ($T_1$), virial ($T_2$), and super-virial ($T_3$) phases, respectively.

et al., 2024a) are $1.55^{+0.23}_{-0.26} \times 10^6$, $3.16^{+0.23}_{-0.21} \times 10^7$, and $2.45^{+0.86}_{-0.36} \times 10^5$ K, respectively.

Figure 5.4 shows the best-fit temperature and $1\sigma$ uncertainties from previous studies along various lines of sight (Mrk 421, green; stacked, grey; 1ES 1553+113, yellow; NGC 3783, red). The temperature ranges from this work (along PKS 2155-304) are plotted in blue. The left arrow shows the cool phase temperature estimated using O V (non-detection) and O IV (detection) line ratios. This marks the first time that cool gas has been detected via X-ray absorption lines in such studies. The three points in each row (same color) show the temperature for the sub-virial, virial, and super-virial phases along PKS 2155-304, Mrk 421, and stacked sightlines, while along 1ES 1553+113 and NGC 3783, the two points show virial and super-virial phases. For a given sightline, the temperatures of different phases show no overlap, considering the $1\sigma$ variation, which points to the robust detection of these distinct phases and a temperature valley in between. There is no overlap between the hot and warm-hot temperatures from all the observations within $1\sigma$ uncertainties. This shows the clear demarcation between virial and super-virial phases. Similarly, the sub-virial and virial phases are distinct, as there is no overlap between the temperatures of these two phases within $1\sigma$ error. The temperature values in the sub-virial phase are consistent with each other within $1\sigma$ uncertainty. This temperature comparison plot indicates the multiphase nature of CGM along all directions.

We detected four distinct temperature phases along PKS 2155-304 for the first time. Along Mrk 421, Das et al. 2021 found three temperature phases. Since Das et al. 2021 did not look for O IV and O V X-ray absorption lines, a cooler temperature gas may also be present along Mrk 421. Similarly, a cooler temperature gas may also exist in stacked sightlines (Lara-DI et al., 2024a). Along 1ES 1553+113, Das et al. 2019b detected warm-hot and hot gas using RGS1/RGS2 in *XMM-Newton*. However, they could not detect a lower temperature gas because of the limited wavelength coverage of RGS1/RGS2. Their hot gas temperature is also lower than the hot gas temperature among other sightlines (except NGC 3783). This is again because of the limited wavelength coverage of RGS1/RGS2 at lower wavelengths. They detected Ne X as a tracer of hot gas. Other hot gas tracer ions like Mg XII and Si XIV , which fall at lower wavelengths, might be present along this sightline, which can further modify the hot gas temperature to higher values, but could not be detected.

The warm-hot gas temperature along NGC 3783 is the lowest among other sightlines. This could be the weighted average temperature of warm-hot and warm gas. McClain

et al. 2024b only used MEG for their study and did not look for ions tracing the lower temperature gas due to the limited wavelength coverage of MEG. As a hot gas tracer, they only detected Ne X and could not detect other ions. The limited number of detected ions for warm-hot and hot gas may not reflect the true temperature distribution along a given sightline, which can result in average temperatures between two temperature phases. This could be the case along NGC 3783. A large range in the inferred temperature along various sightlines also points towards the temperature inhomogeneities in the CGM. The inhomogeneity is larger for the hot phase, which could be the result of scattered stellar outflows from the Galactic disk.

### 5.3.2 Equivalent H column density

Virial, super-virial, and sub-virial phases have an equivalent H column density (relative to solar abundance of Oxygen in that phase) of $8.8^{+2.2}_{-4.8} \times 10^{18}$, $2.5^{+0.7}_{-1.0} \times 10^{21}$, and $1.9^{+0.9}_{-0.8} \times 10^{18}$ cm$^{-2}$ respectively. Equivalent H column density towards 1ES 1553+113, Mrk 421, and NGC 3783 for virial phase is $13.3^{+5.0}_{-4.5} \times 10^{18}$, $8.4 \pm 0.8 \times 10^{18}$, $1.26^{+0.83}_{-0.64} \times 10^{20}$, while for super-virial phase is $2.9^{+2.4}_{-2.0} \times 10^{20}$, $9.1^{+2.7}_{-2.9} \times 10^{20}$, and $4.47^{+2.94}_{-2.28} \times 10^{19}$ cm$^{-2}$. The equivalent H column density for the sub-virial phase towards Mrk 421 is $1.1^{+0.2}_{-0.3} \times 10^{18}$ cm$^{-2}$. Note that the uncertainties along Mrk 421 and 1ES 1553+113 are with 90% and 99.73% confidence levels, respectively, while others are with $1\sigma$. The temperature and equivalent H column density for the super-virial phase predicted by our best-fit `PHASE` model are maximum along this line of sight compared to the other three lines of sight (Das et al. 2019b, 2021; McClain et al. 2024b) and stacked sightlines (Lara-DI et al., 2024a). A large variation in inferred temperature and equivalent H column density for the hot phase across different sightlines suggests the inhomogeneous nature of this phase.

### 5.3.3 Abundance Ratios

We find that the abundance ratios of the ions in the warm-hot and hot phases are non-solar. C and Ne are super-solar relative to Oxygen in the virial phase. Mg and Si are super-solar relative to Oxygen in the super-virial phase. In Fig. 5.5, we show the importance of non-solar composition of the abundance ratio of ions. The dotted colored line in subplots shows the normalized absorption profile of various ions for solar abundance

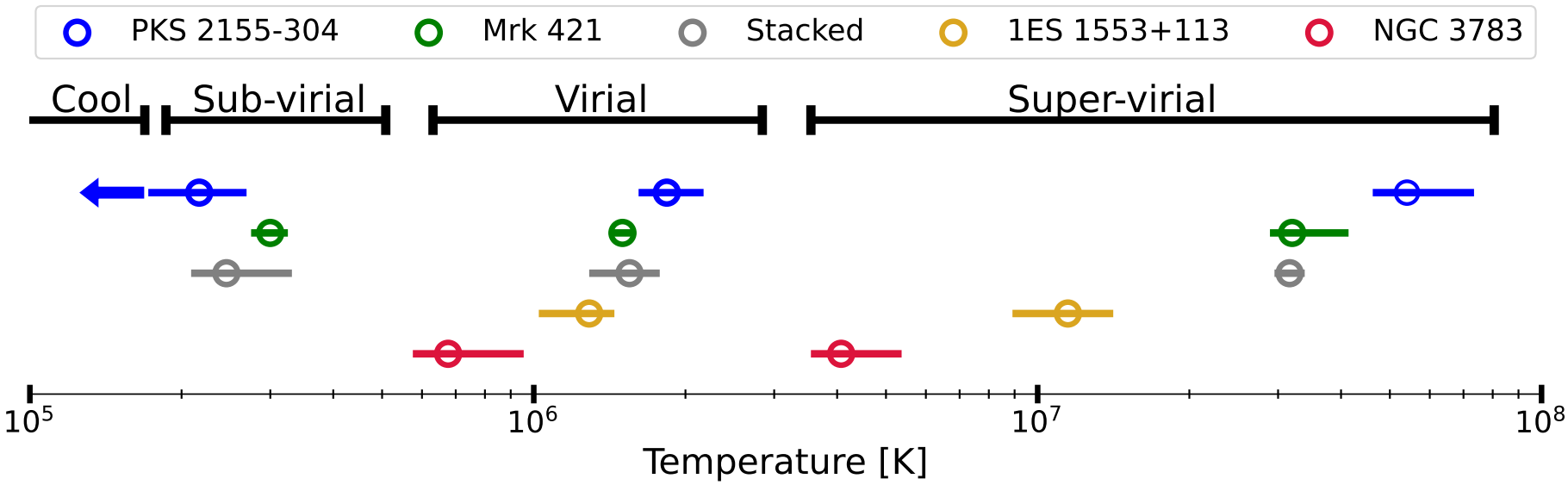



Figure 5.4: Comparison of best-fit temperatures and associated $1\sigma$ uncertainties from previous studies along various lines of sight (Mrk 421, green, Das et al. 2021; stacked, grey, Lara-DI et al. 2024a; 1ES 1553+113, yellow, Das et al. 2019b; NGC 3783, red, McClain et al. 2024b). The temperature ranges from our study (PKS 2155-304) are plotted in blue. The left arrow shows the cool gas temperature estimated from the column density ratios of O V (non-detections) and O IV (detections) in our study. Therefore, we detect four temperature phases along PKS 2155-304. This is the first time that 4 temperature phases are inferred in such studies using X-ray absorption lines. This plot shows the multiphase nature of CGM along various lines of sight and within specific phases as well.

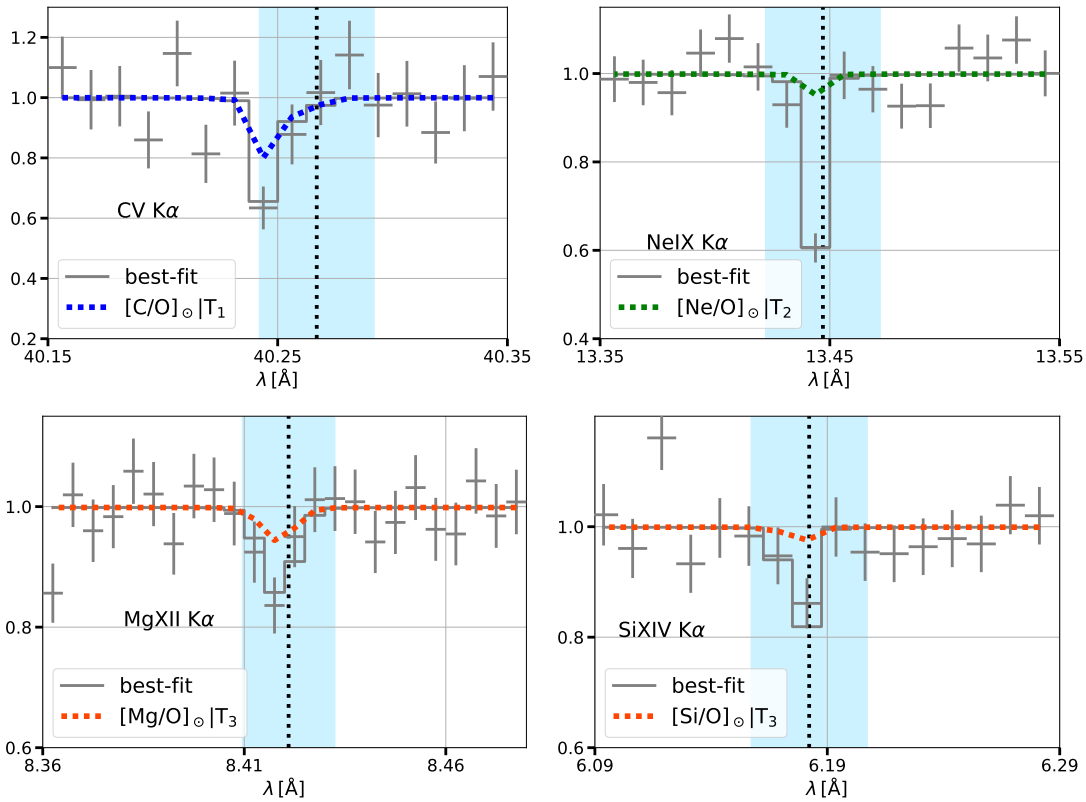



Figure 5.5: Non-solar abundance ratios of C, Ne, Mg, and Si relative to O in the respective phases.

ratios of the respective element relative to O in various phases.

Along with these elements, we have also varied the composition of Iron in both virial and super-virial phases. We find $\alpha$-enhancement in both the virial and super-virial phases, which is in line with all the previous studies along different sightlines. In the top panel of Fig. 5.6, the green line shows the normalized spectrum for $[\mathrm{Ne/Fe}]_\odot$ in the virial phase. In the bottom panel, the dotted, dashed, and dashed-dotted red lines show the normalized spectrum for $[\mathrm{O/Fe}]_\odot$, $[\mathrm{Mg/Fe}]_\odot$, and $[\mathrm{Si/Fe}]_\odot$, respectively, in the hot phase. The virial and super-virial phases are $\alpha$-enhanced as evident from this plot.

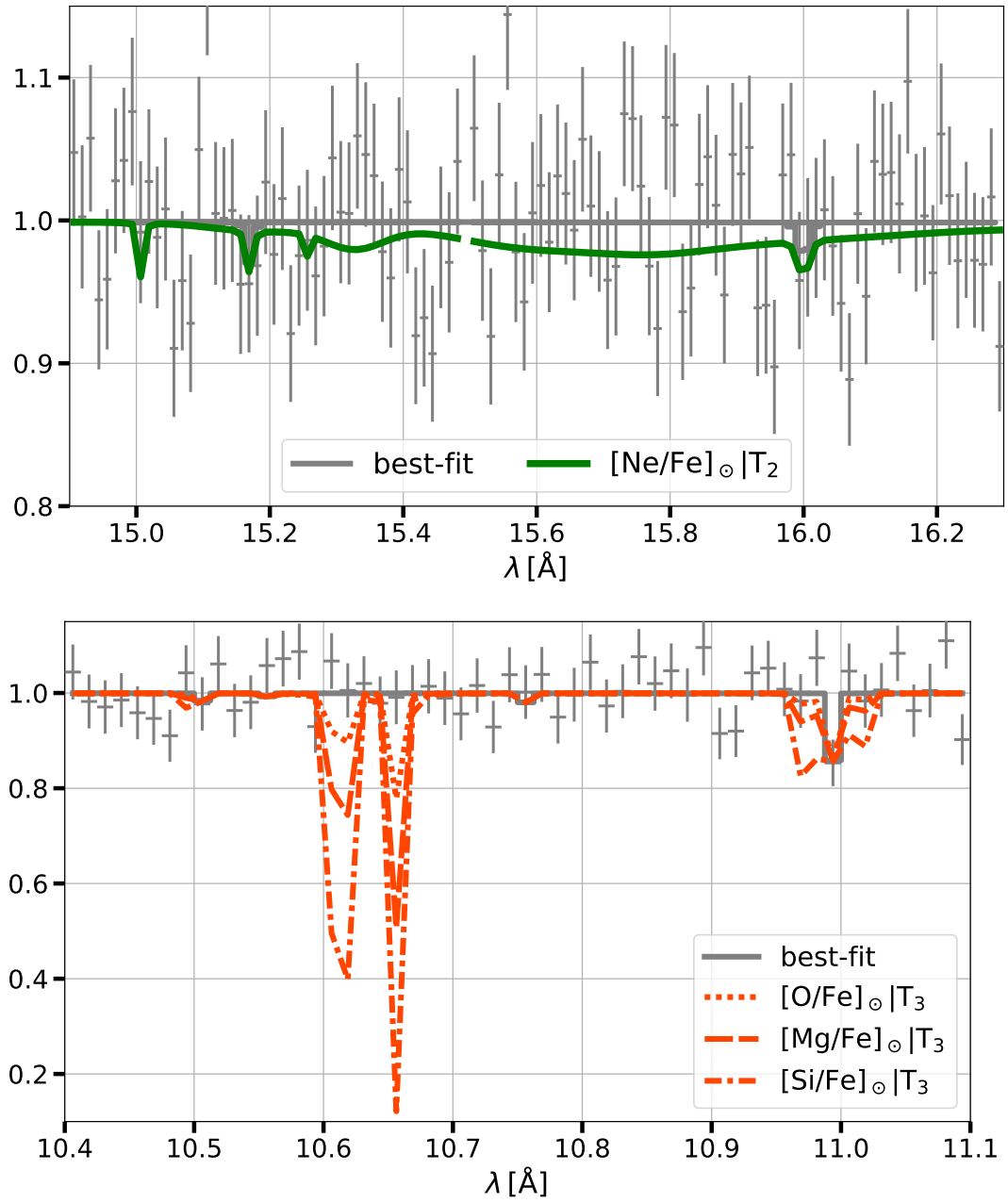



Figure 5.6: *Top panel*: The green line shows the normalized spectrum for the Solar abundance ratio of Ne to Fe in the warm-hot phase. *Bottom panel*: The dotted, dashed, and dashed-dotted red lines show the normalized spectrum for solar abundance ratios of O to Fe, Mg to Fe, and Si to Fe in the hot phase. This shows the $\alpha-$enhancement in virial and super-virial phases.

## 5.4 Discussion

### 5.4.1 Comparison with previous studies

#### X-ray

Nevalainen et al. 2017 studied and analyzed the $z = 0$ absorption lines in the spectra of PKS 2155-304. They detected various ions individually in the spectra of RGS1, RGS2, LETG/HRC, and LETG/ACIS (see their Figure 2). Since their motivation was to study the X-ray counterpart of the far-ultraviolet observations, which revealed a transition temperature along this sightline, they did not look for the ions tracing very hot gas in the CGM. Therefore, they did not analyze the MEG/ACIS data, which is sensitive to detecting such ionic transitions. They have reported a detection of the O V line in RGS1 and LETG/HRC; however, we did not detect it (see Figure 5.1) in any of the instruments. The $3\sigma$ and $2\sigma$ upper limits on the EW from our analysis are 5.6 and 4.3 mÅ respectively, which is consistent with their detection of $3.0 \pm 1.5$ mÅ for RGS1. However, the number of observations used in our analysis is larger than that analyzed in Nevalainen et al. 2017. Our analysis has a total exposure time of 1.98 Ms, compared to 1.7 Ms in Nevalainen et al. 2017 for RGS1.

A similar study is carried out along various other lines of sight, including 1ES 1553+113 (Das et al. 2019a), Mrk 421 (Das et al. 2021), and NGC 3783 (McClain et al. 2024b). This is the first study that is conducted in the southern latitude ($b = -52.2°$), which indicates the presence of super-virial in the southern Galactic latitude as well. Mrk 421 ($l = 179.83°$) lies in the Galactic anti-center direction, while PKS 2155-304 is towards the Galactic center ($l = 17.7°$). Das et al. 2021 inferred three temperature phases along Mrk 421, which is similar to three temperature phases (hot/warm-hot/warm) along this sightline. The temperature, equivalent H column density, and abundance pattern are similar along both lines of sight, even though they lie completely in opposite directions. This suggests that the super-virial gas detected in X-ray absorption studies is likely widespread. Further observations with high signal-to-noise grating data across a broader array of sightlines are necessary to clarify and characterize the properties of the hot gas observed in X-ray absorption studies.

### UV

There is observational evidence of highly ionized High Velocity Clouds (HVC) towards PKS 2155-304. Collins et al. 2004 used the Hubble Space Telescope (HST) and the Far Ultraviolet Spectroscopic Explorer (FUSE) to study the UV absorption towards PKS 2155-304. They detected two absorbing components at $V_{LSR}$ of $-140$ and $-270$ km s$^{-1}$ in O VI and C IV . These negative LSR velocities are also consistent with our blue-shifted detection of ions like C V , C VI , and N VI (see Figure 5.1 and 5.7), which possibly have a significant contribution from the HVCs.

In Figure 5.7, we show the line of sight velocity for each ion calculated from the best fit and theoretically predicted $z = 0$ wavelength value. The blue and red colors show blueshift and redshift, respectively, and the error bars in the respective colors show the resolution element around the best-fit values. The error bars in black color show the measured $1\sigma$ error about the best fit value. The two black points on the left side of the Figure 5.7 correspond to the two velocity components of the UV High Velocity Clouds (HVCs) (Collins et al., 2004). C V and N VI lines, which are the tracers of the warm/cool phase, are blue-shifted. O VII and O VIII lines are roughly consistent with zero velocity as these ions trace the virial gas, which is expected to be in hydrostatic equilibrium with the dark matter Halo. The Si XIV line, which traces hot gas, is red-shifted. It shows that the hot gas is probably outflowing due to feedback from the Galactic disk and Galactic center. The Mg XII line is also expected to be red-shifted as a tracer of the hot gas, but is rather blue-shifted. This shows the complex and inhomogeneous mixing of inflowing and outflowing gas in the CGM. McClain et al. 2024b also detected the blueshifted and redshifted absorption lines in their analysis towards NGC 3783. They found O VII K$\alpha$, O VII K$\beta$, and Ne IX K$\alpha$ lines to be redshifted, while O VIII K$\alpha$ and Ne X K$\alpha$ lines were blueshifted (see their Figure 1 and Table 1). However, they did not claim detections of inflow/outflow because the available evidence was scarce and based on a limited set of tracer ions.

Along with various other lines, Collins et al. 2004 detected the O VI line (1031.93 Å) with column densities of $13.80 \pm 0.03$ and $13.56 \pm 0.06$ (in $\log_{10}$) in the two absorbing components. Since X-ray instruments cannot resolve these two components, we add the two column densities to compare with our analysis. The total O VI column density is therefore $9.94^{+0.99}_{-0.89} \times 10^{13}$ cm$^{-2}$. Since the O VI K$\alpha$ (22.02 Å) line is highly blended with

the O II K$\beta$ line in X-ray (Mathur et al. 2017), we cannot independently compute the O VI column density from X-ray. However, the O VI column density predicted from our best-fit `PHASE` model is $1.06^{+0.57}_{-0.34} \times 10^{14}$ cm$^{-2}$, which is consistent with the UV measurements within $1\sigma$ uncertainties.

The O VI column density predicted from X-ray along Mrk 421 was $1.82^{+0.14}_{-0.27} \times 10^{14}$ cm$^{-2}$ which was smaller by a factor of $\approx 2$ than the observed UV value of $(2.66 - 3.15) \times 10^{14}$ cm$^{-2}$ along that direction. Even photo-ionization in the warm phase could not account for the excess O VI observed along this sightline in UV, which suggests the effect of other processes like radiative cooling or non-thermal sources (Das et al., 2021) deviating from CIE. However, along PKS 2155-304, the consistency in O VI column density between X-ray and UV suggests that the warm phase is in CIE. Thus, the ionization conditions along the two sightlines are different for the warm gas traced by O VI .

The total C IV (1548.20 Å) column density from the UV observation is $7.22^{+0.62}_{-0.55} \times 10^{13}$ cm$^{-2}$. The C IV column density predicted by the `PHASE` model is $2.85^{+2.68}_{-1.26} \times 10^{13}$ cm$^{-2}$, which is less than the UV measurements. The excess C IV is therefore, $N(\text{C IV})_{UV} - N(\text{C IV})_X = 4.37^{+2.06}_{-0.71} \times 10^{13}$ cm$^{-2}$. This 'missing' C IV in X-rays might come from a further lower temperature gas, as suggested by the temperature estimated from the column density ratios of O V and O IV (see Figure 5.2). The observed UV and inferred X-ray C IV column density along Mrk 421 were consistent with each other within $2\sigma$, but the X-ray C IV column density was larger than what was observed in UV. The excess column density in that case would come from low/intermediate velocity clouds (LVC/IVC) in the disk/halo. However, along PKS 2155-304, the C IV UV column density is larger than what is predicted from our X-ray analysis. Therefore, the two lines of sight are also different in C IV properties.

### 5.4.2 Origin of the super-virial gas

The X-ray emitting and absorbing super-virial gas is believed to have distinct origins. Bhattacharyya et al. 2023 showed that the emitting super-virial gas has a dominant contribution from Fe line emission, whereas the absorbing super-virial gas is found to be $\alpha$-enhanced. Bisht et al. 2024b also showed that the absorbing and emitting super-

[10]Estimated from the best-fit wavelength and the $z = 0$ rest wavelength using $v/c = (\lambda - \lambda_0)/\lambda_0$, as shown in Figure 5.1.

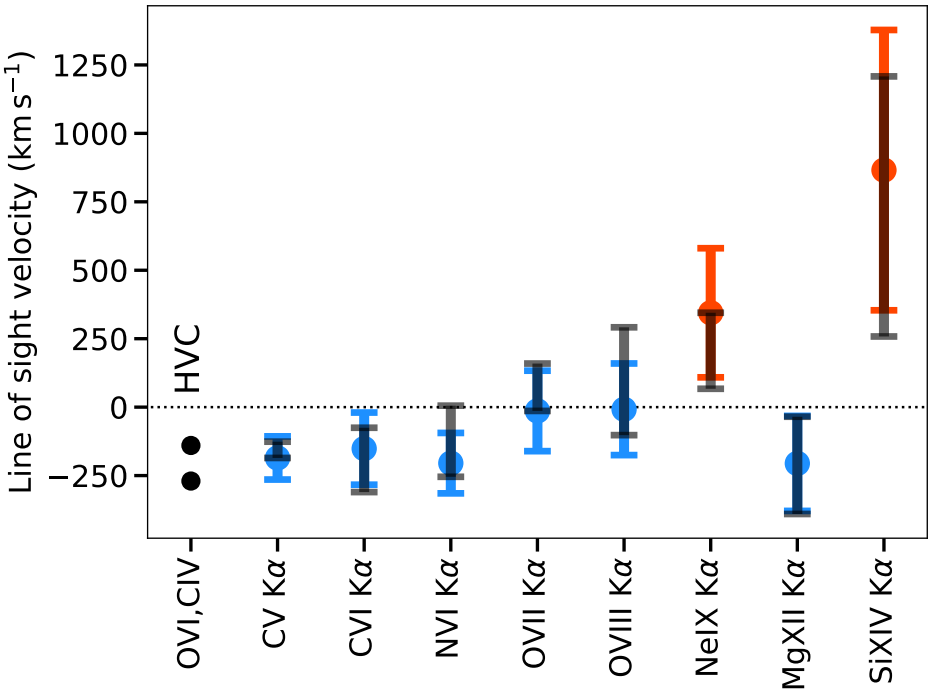



Figure 5.7: The line of sight velocity[10] of the detected transitions. The blue and red colors show blueshift and redshift, respectively. The error bars in the respective color indicate the resolution element of the instruments used to detect these ions relative to the best-fit velocity. The error bars in black show the $1\sigma$ error about the best-fit value. Two black points on the left side of the plot correspond to the two velocity components (-140 and -270 km s$^{-1}$) detected in UV (O VI and C IV ) along this sightline for HVC (Collins et al., 2004).

virial gas has to be treated separately, based on the typical value of Emission Measure (EM) and column density. The emitting super-virial gas is ubiquitous across the CGM, and Bisht et al. 2024b showed that a puffed up disk-like geometry with a typical scale radius and scale height of $\approx 5$, and 1, respectively, can match the characteristics of this gas. Bisht et al. 2024b further showed that the disk-wide stellar outflows from the MW central disk can give rise to such a puffed-up disk with super-virial temperatures using hydrodynamical simulations of stellar outflows. However, this puffed-up disk-shaped gas cannot account for the extremely high column density of ions detected in absorption.

Vijayan & Li 2022 in their hydrodynamical simulations of star-forming galaxies also found hot gas ($\sim 10^7$ K; see their Figure 7). But the star formation rate (SFR) they considered, $10\,M_\odot\,\mathrm{yr}^{-1}$ is higher than the SFR of MW (Elia et al., 2025). The signatures of super-virial gas are also found by Roy et al. 2024 as a result of compressive heating of infalling gas into a galaxy in their simulation. However, their temperature values are significantly lower than those inferred from X-ray absorption studies, and they have not quantified the characteristics of super-virial gas (super-solar abundance ratios, $\alpha$-enrichment) beyond temperature.

Based on the properties of the absorbing super-virial gas (high temperature, super-solar abundances, and $\alpha-$enrichment), Bisht et al. 2024a showed that the core collapse supernovae from runaway stars in the extra-planar regions along these specific sightlines can give rise to these characteristics around $\sim$ 100 kyr timescale. They showed that the reverse shock in the supernova remnant (SNR) can heat the ejecta to super-virial temperatures, and the extremely high column density detected along these sightlines can be matched with a typical blast energy of $10^{51}$ erg, ejecta mass of $\sim 10\,M_\odot$, and ambient density of $\sim 0.1$ cm$^{-3}$. The ejecta of a core-collapse supernova is $\alpha$-enhanced and has super-solar composition, which naturally explains these findings. However, the covering fraction of such objects in the sky is $\lesssim 1\%$ and therefore cannot account for super-virial gas along all the detected lines of sight.

We further investigate whether the newly detected Mg XII K$\alpha$ line could arise from the ISM of the Galaxy, instead of the extended region. Following Lara-DI et al. 2024c; Roy et al. 2025, we looked for the Mg XII K$\alpha$ line in the XRB sightlines. Out of 27 XRBs, 4 sources exhibit a statistically significant ($> 3\sigma$) detection of the Mg XII absorption line. The absorption lines in two of the four sightlines are broad, suggesting an origin in the immediate environment of the source XRB. Thus, only in 2 out of 27 sightlines,

corresponding to a fraction of $\sim 7.5\%$, the Mg XII K$\alpha$ may arise in the ISM. This small fraction, together with the Lara-DI et al. (2024c); Roy et al. (2025) results on other lines related to the hot gas, suggests that the super-virial phase likely resides in the extra-planar region.

## 5.5 Conclusion

In this work, we have investigated the highly ionized metal absorption lines at $z = 0$ in the Galactic halo using the X-ray grating data of *Chandra* and *XMM-Newton* toward the Blazar PKS 2155-304 and obtained the following results:

1. We detect Hydrogen-like and Helium-like ions of various elements, and for the first time, detect the Mg XII K$\alpha$ absorption line in the MW CGM (see Fig. 5.1 and Table 5.1 and 5.2).

2. For the first time, we identify four thermal phases using X-ray absorption lines (see Figs. 5.2 and 5.4). Our detection of highly ionized metals like Mg XII and Si XIV confirms the existence of super-virial hot gas ($\approx 5 \times 10^7$ K) along this sightline (see Table 5.3). The temperatures of the warm-hot (virial) and warm (sub-virial) phases are $\approx 2 \times 10^6$ and $\approx 2 \times 10^5$ K, respectively. The 4$^{\rm th}$ phase (cool phase; $T < 1.7 \times 10^5$ K) is detected using the column density ratios of O V (non-detection) and O IV (detection). This extends the previous detections of two (Das et al., 2019b; McClain et al., 2024b) and three (Das et al., 2021; Lara-DI et al., 2023) thermal phases.

3. The hot gas has a super-solar composition of [Mg/O] and [Si/O] and is $\alpha$-enhanced, which is in line with the previous studies along other lines of sight. [C/O] and [Ne/O] are super-solar in the sub-virial and virial phases, respectively (see Fig. 5.5 and 5.6).

4. For the first time, we have also gained kinematic insights in the highly ionized phases of the CGM. Tracers of the sub-virial phase are blue-shifted ($v_{\rm los} \approx -100$ km s$^{-1}$), while tracers of the super-virial phase may be red-shifted, indicating a scenario with cool inflowing and hot outflowing gas embedded in the quasi-static warm-hot gas along this sightline (see Fig. 5.7).

5. This is the fourth *individual* sightline along which the super-virial hot phase has been looked for and been detected. It suggests that this phase is likely widespread in the Galactic halo. A statistically large number of sightlines is required to determine its *true* covering fraction and subsequently, mass.

6. We find the presence of a *temperature valley* between the warm-hot and hot phases, and another *temperature valley* between the sub-virial and cool phases (see Fig. 5.2). This indicates the multi-peaked temperature distribution in the highly ionized CGM of the MW. A large variation (an order of magnitude) in the temperature and equivalent Hydrogen column density of the hot gas across different sightlines suggests it is thermally and chemically inhomogeneous.

# Chapter 6

# Conclusion & Future Directions

This thesis presents a comprehensive investigation of the multiphase circumgalactic medium, with an emphasis on understanding the origin, thermal/chemical structure, and spatial distribution of the recently discovered hot or 'super-virial' phase ($\sim 10^7$ K) in the circumgalactic medium of the Milky Way. Through a combination of analytical modeling, hydrodynamical simulations, Monte Carlo realizations, and X-ray absorption-line observations, the work captures the CGM's complexity across its full temperature spectrum—from cool phase ($\sim 10^4$ K) to highly ionized X-ray gas ($\sim 10^7$ K). A key outcome is the identification and characterization of the 'super-virial' phase, including its first observed detection in the southern Galactic hemisphere.

## 6.1 Origin of X-ray Emitting Super-Virial Gas

We demonstrated that the X-ray *emitting* and the X-ray *absorbing* hot phases cannot have the same origin, due to inconsistent length scales implied by emission measure and column density measurements. Using an analytical model, we showed that a puffed-up disk-like region with a scale radius of $\approx 5$ kpc and a scale height of $\approx 1$ kpc can explain the observed characteristics of the 'super-virial' emitting gas. Using an idealized 2D hydrodynamical simulation, we showed that the disk-like region naturally arises from disk-wide stellar feedback, which could be the possible origin of this phase. This model successfully matches the observed sky variation of the emission measure and provides a physically plausible explanation for the widespread hot X-ray emission. The inferred

mass of this component ($4 \times 10^7\,M_\odot$) is $\approx$ 4 orders of magnitude less than the mass-dominated warm-hot or 'virial' phase.

## 6.2 Supernovae From Runaway Stars as Sources of X-ray Absorbing Super-Virial Gas

The X-ray absorbing 'super-virial' gas detected along three northern-hemisphere sightlines in the CGM of the MW shows high column density of highly ionized species such as OVIII, NeX, and SiXIV, high temperatures, $\alpha$-enhanced, and dominant non-thermal broadening. We demonstrated that these characteristics can be explained by shock-heated ejecta from core-collapse supernovae occurring in the extra-planar regions of the MW. In particular, reverse-shocked supernova ejecta with explosion energy $E \sim 10^{51}$ erg and ejecta mass $M_{\rm ej} \sim 10\,M_\odot$, expanding into a medium with number density of $n \sim 10^{-3}\,{\rm cm}^{-3}$ reproduce the observed ion column densities on timescales of $\sim 10^5$ years. However, the scarcity of massive runaway progenitors implies an intrinsically low sky covering fraction ($\lesssim 1\%$), suggesting that this mechanism alone cannot account for 'super-virial' absorbing gas, if detected along a large number of sightlines in the future.

## 6.3 Structure of the Cool CGM: Misty Cloud Complexes (mCC)

We developed a physically motivated model for the cool ($\sim 10^4$ K) CGM composed of clumpy cloud complexes (CCs) filled with tiny cloudlets in the "mist limit" (unit area covering fraction within a cloud complex). Using Monte Carlo realizations of CCs in the CGM, we demonstrated that the large scatter in observed MgII column densities at similar impact parameters arises naturally in our model. We showed that the COS-Halos MgII column density (Werk et al., 2013) can be explained with a total cool gas mass of $\sim 10^{10}\,M_\odot$, $\sim 10^3$ CCs each with a radius of $\sim$ 10 kpc. We further showed that the combination of area covering fraction and average MgII column density, both of which are observationally available, can be used to constrain the mass of the cool phase in the CGM. Using a simple exercise, we demonstrated that the blending of absorption lines of

individual intersected cloudlets with distinct line of sight velocities within a CC gives rise to turbulent broadening at the CC scale.

## 6.4 Detection of Super-Virial Gas Toward PKS 2155-304

Using *Chandra* and *XMM-Newton* archival gratings, we detected Mg XII K$\alpha$ and Si XIV K$\alpha$ in the CGM of the MW towards PKS 2155-304—the first such detection in the southern Galactic hemisphere. Our model-independent analysis and hybrid-ionization modeling revealed four distinct temperature phases along this sightline, namely 'super-virial' ($\approx 5\times10^7$ K), 'virial' ($\approx 2\times10^6$ K), 'sub-virial' ($\approx 2\times10^5$ K), and cool phase ($< 1.7\times10^5$ K). This work demonstrated that the 'super-virial' absorbing phase is not confined to the northern hemisphere and is likely widespread and thermally/chemically inhomogeneous.

## 6.5 Future Directions

The detection of 'super-virial' absorption in only a handful of directions limits our ability to assess its global properties and origin. Expanding the number of high-S/N sightlines with *Chandra* and *XMM-Newton* is crucial to determine its covering fraction, its relation to Galactic structures (Fermi Bubbles, superbubbles), extra-planar SN, and its connection to accretion or feedback events. Upcoming missions like NewAthena, Arcus, and Lynx will be transformative.

Idealized 3D simulations with outflows incorporating chemical enrichment will help understand the origin of 'super-virial' emitting and absorbing gas. This will refine the baryon census estimates and test metal-transport models.

# Bibliography


Abdo, A. A., Ackermann, M., Agudo, I., et al. 2010, , 716, 30, doi: 10.1088/0004-637X/716/1/30

Afruni, A., Fraternali, F., & Pezzulli, G. 2019, , 625, A11, doi: 10.1051/0004-6361/201835002

Afruni, A., Lopez, S., Anshul, P., et al. 2023, , 680, A112, doi: 10.1051/0004-6361/202347867

Anand, A., Nelson, D., & Kauffmann, G. 2021, , 504, 65, doi: 10.1093/mnras/stab871

Aramaki, T., Adrian, P. O. H., Karagiorgi, G., & Odaka, H. 2020, Astroparticle Physics, 114, 107, doi: 10.1016/j.astropartphys.2019.07.002

Armillotta, L., Fraternali, F., Werk, J. K., Prochaska, J. X., & Marinacci, F. 2017, , 470, 114, doi: 10.1093/mnras/stx1239

Arnaud, K., Dorman, B., & Gordon, C. 1999, XSPEC: An X-ray spectral fitting package, Astrophysics Source Code Library, record ascl:9910.005. http://ascl.net/9910.005

Asplund, M., Grevesse, N., Sauval, A. J., & Scott, P. 2009, , 47, 481, doi: 10.1146/annurev.astro.46.060407.145222

Augustin, R., Péroux, C., Hamanowicz, A., et al. 2021, , 505, 6195, doi: 10.1093/mnras/stab1673

Augustin, R., Tumlinson, J., Peeples, M. S., et al. 2025, arXiv e-prints, arXiv:2501.06551, doi: 10.48550/arXiv.2501.06551

Ayromlou, M., Nelson, D., & Pillepich, A. 2023, , 524, 5391, doi: 10.1093/mnras/stad2046

Bera, A., Kanekar, N., Chengalur, J. N., & Bagla, J. S. 2023, , 956, L15, doi: 10.3847/2041-8213/acf71a

Bhattacharyya, J., Das, S., Gupta, A., Mathur, S., & Krongold, Y. 2023, , 952, 41, doi: 10.3847/1538-4357/acd337

Binney, J. 1977, , 215, 483, doi: 10.1086/155378

Bisht, M. S., Banerjee, P., Nath, B. B., & Shchekinov, Y. 2024a, , 975, 26, doi: 10.3847/1538-4357/ad77be

Bisht, M. S., Nath, B. B., & Mathur, S. 2024b, , 975, 49, doi: 10.3847/1538-4357/ad77c0

Bisht, M. S., Sharma, P., Dutta, A., & Nath, B. B. 2025, , 542, 1573, doi: 10.1093/mnras/staf1319

Blaauw, A. 1961, , 15, 265

Bland-Hawthorn, J., & Gerhard, O. 2016, , 54, 529, doi: 10.1146/annurev-astro-081915-023441

Błażejowski, M., Blaylock, G., Bond, I. H., et al. 2005, , 630, 130, doi: 10.1086/431925

Bluem, J., Kaaret, P., Kuntz, K. D., et al. 2022, , 936, 72, doi: 10.3847/1538-4357/ac8662

Bordoloi, R., Lilly, S. J., Knobel, C., et al. 2011, , 743, 10, doi: 10.1088/0004-637X/743/1/10

Bovy, J. 2015, , 216, 29, doi: 10.1088/0067-0049/216/2/29

Bregman, J., Cen, R., Chen, Y., et al. 2023, Science China Physics, Mechanics, and Astronomy, 66, 299513, doi: 10.1007/s11433-023-2149-y

Bregman, J. N., Hodges-Kluck, E., Qu, Z., et al. 2022, , 928, 14, doi: 10.3847/1538-4357/ac51de

Brown, W. R. 2015, Annual Review of Astronomy and Astrophysics, 53, 15, doi: 10.1146/annurev-astro-082214-122230

Burchett, J. N., Rubin, K. H. R., Prochaska, J. X., et al. 2021, , 909, 151, doi: 10.3847/1538-4357/abd4e0

Butsky, I. S., Fielding, D. B., Hayward, C. C., et al. 2020, , 903, 77, doi: 10.3847/1538-4357/abbad2

Butsky, I. S., Hummels, C. B., Hopkins, P. F., Quinn, T. R., & Werk, J. K. 2024, , 535, 1672, doi: 10.1093/mnras/stae2459

Charlton, J. C., Ding, J., Zonak, S. G., et al. 2003, , 589, 111, doi: 10.1086/374353

Chen, H.-W., Wild, V., Tinker, J. L., et al. 2010, , 724, L176, doi: 10.1088/2041-8205/724/2/L176

Chen, H.-W., Qu, Z., Rauch, M., et al. 2023, , 955, L25, doi: 10.3847/2041-8213/acf85b

Chen, M. C., Chen, H.-W., Rauch, M., et al. 2024, , 962, 98, doi: 10.3847/1538-4357/ad1406

Cherrey, M., Bouché, N. F., Zabl, J., et al. 2025, , 694, A117, doi: 10.1051/0004-6361/202451165

Collins, J. A., Shull, J. M., & Giroux, M. L. 2004, , 605, 216, doi: 10.1086/382269

Connor, L., Ravi, V., Sharma, K., et al. 2025, Nature Astronomy, doi: 10.1038/s41550-025-02566-y

Cook, A. M., Bhardwaj, M., Gaensler, B. M., et al. 2023, , 946, 58, doi: 10.3847/1538-4357/acbbd0

Das, H. K., & Gronke, M. 2024, , 527, 991, doi: 10.1093/mnras/stad3125

Das, S., Chiang, Y.-K., & Mathur, S. 2023, , 951, 125, doi: 10.3847/1538-4357/acd764

Das, S., Mathur, S., Gupta, A., & Krongold, Y. 2021, , 918, 83, doi: 10.3847/1538-4357/ac0e8e

Das, S., Mathur, S., Gupta, A., Nicastro, F., & Krongold, Y. 2019a, , 887, 257, doi: 10.3847/1538-4357/ab5846

Das, S., Mathur, S., Nicastro, F., & Krongold, Y. 2019b, , 882, L23, doi: 10.3847/2041-8213/ab3b09

Decataldo, D., Shen, S., Mayer, L., Baumschlager, B., & Madau, P. 2024, , 685, A8, doi: 10.1051/0004-6361/202346972

Dekel, A., & Birnboim, Y. 2006, , 368, 2, doi: 10.1111/j.1365-2966.2006.10145.x

DESI Collaboration, Abdul-Karim, M., Adame, A. G., et al. 2025, arXiv e-prints, arXiv:2503.14745, doi: 10.48550/arXiv.2503.14745

Diehl, R., Halloin, H., Kretschmer, K., et al. 2006, , 439, 45, doi: 10.1038/nature04364

Donahue, M., & Voit, G. M. 2022, , 973, 1, doi: 10.1016/j.physrep.2022.04.005

Draine, B. T. 2011, Physics of the Interstellar and Intergalactic Medium (Princeton University Press)

Dutta, A., Bisht, M. S., Sharma, P., et al. 2024a, , 531, 5117, doi: 10.1093/mnras/stae977

Dutta, A., Singh Bisht, M., Sharma, P., et al. 2023, arXiv e-prints, arXiv:2310.03717, doi: 10.48550/arXiv.2310.03717

Dutta, R., Acebron, A., Fumagalli, M., et al. 2024b, , 528, 1895, doi: 10.1093/mnras/stae048

Dutta, R., Fumagalli, M., Fossati, M., et al. 2020, , 499, 5022, doi: 10.1093/mnras/staa3147

Elia, D., Evans, N. J., Soler, J. D., et al. 2025, , 980, 216, doi: 10.3847/1538-4357/adaeb2

Elia, D., Molinari, S., Schisano, E., et al. 2022, , 941, 162, doi: 10.3847/1538-4357/aca27d

Faerman, Y., Sternberg, A., & McKee, C. F. 2017, , 835, 52, doi: 10.3847/1538-4357/835/1/52

—. 2020, , 893, 82, doi: 10.3847/1538-4357/ab7ffc

Faerman, Y., & Werk, J. K. 2023, , 956, 92, doi: 10.3847/1538-4357/acf217

Faerman, Y., Zheng, Y., & Oppenheimer, B. D. 2025, , 982, L30, doi: 10.3847/2041-8213/adba51

Falomo, R., Pesce, J. E., & Treves, A. 1993, , 411, L63, doi: 10.1086/186913

Fang, T., Mckee, C. F., Canizares, C. R., & Wolfire, M. 2006, , 644, 174, doi: 10.1086/500310

Faucher-Giguère, C.-A., & Oh, S. P. 2023, , 61, 131, doi: 10.1146/annurev-astro-052920-125203

Ferland, G. J., Chatzikos, M., Guzmán, F., et al. 2017, , 53, 385, doi: 10.48550/arXiv.1705.10877

Foreman-Mackey, D., Hogg, D. W., Lang, D., & Goodman, J. 2013, , 125, 306, doi: 10.1086/670067

Fuller, C. A., Kaaret, P., Bluem, J., et al. 2023, , 943, 61, doi: 10.3847/1538-4357/acaafc

Gatuzz, E., & Churazov, E. 2018, , 474, 696, doi: 10.1093/mnras/stx2776

Gies, D. R., & Bolton, C. T. 1986, , 61, 419, doi: 10.1086/191118

Gronke, M., Oh, S. P., Ji, S., & Norman, C. 2022, , 511, 859, doi: 10.1093/mnras/stab3351

Gülzow, L., Fairbairn, M., & Schwarz, D. J. 2023, arXiv e-prints, arXiv:2306.08143, doi: 10.48550/arXiv.2306.08143

Guo, Y., Bacon, R., Bouché, N. F., et al. 2023, , 624, 53, doi: 10.1038/s41586-023-06718-w

Gupta, A., Kingsbury, J., Mathur, S., et al. 2021, , 909, 164, doi: 10.3847/1538-4357/abdbb6

Gupta, A., Mathur, S., Galeazzi, M., & Krongold, Y. 2014, , 352, 775, doi: 10.1007/s10509-014-1958-z

Gupta, A., Mathur, S., Kingsbury, J., Das, S., & Krongold, Y. 2023, Nature Astronomy, 7, 799, doi: 10.1038/s41550-023-01963-5

Gupta, A., Mathur, S., Kingsbury, J., et al. 2025, , 989, 194, doi: 10.3847/1538-4357/adf10b

Gupta, A., Mathur, S., & Krongold, Y. 2017, , 836, 243, doi: 10.3847/1538-4357/836/2/243

Gupta, A., Mathur, S., Krongold, Y., Nicastro, F., & Galeazzi, M. 2012, , 756, L8, doi: 10.1088/2041-8205/756/1/L8

Haardt, F., & Madau, P. 2012, , 746, 125, doi: 10.1088/0004-637X/746/2/125

Heger, A., & Woosley, S. E. 2010, , 724, 341, doi: 10.1088/0004-637X/724/1/341

Henley, D. B., & Shelton, R. L. 2010, , 187, 388, doi: 10.1088/0067-0049/187/2/388

—. 2013, , 773, 92, doi: 10.1088/0004-637X/773/2/92

Henley, D. B., Shelton, R. L., Cumbee, R. S., & Stancil, P. C. 2015, , 799, 117, doi: 10.1088/0004-637X/799/2/117

HI4PI Collaboration, Ben Bekhti, N., Flöer, L., et al. 2016, , 594, A116, doi: 10.1051/0004-6361/201629178

Hitomi Collaboration, Aharonian, F., Akamatsu, H., et al. 2016, , 535, 117, doi: 10.1038/nature18627

Holweger, H. 2001, in American Institute of Physics Conference Series, Vol. 598, Joint SOHO/ACE workshop "Solar and Galactic Composition", ed. R. F. Wimmer-Schweingruber (AIP), 23–30, doi: 10.1063/1.1433974

Howk, J. C., Rueff, K. M., Lehner, N., et al. 2018, , 856, 167, doi: 10.3847/1538-4357/aab105

Hsu, W. H., Putman, M. E., Heitsch, F., et al. 2011, , 141, 57, doi: 10.1088/0004-6256/141/2/57

Huang, Y.-H., Chen, H.-W., Shectman, S. A., et al. 2021, , 502, 4743, doi: 10.1093/mnras/stab360

Hummels, C. B., Rubin, K. H. R., Schneider, E. E., & Fielding, D. B. 2024, , 972, 148, doi: 10.3847/1538-4357/ad5965

Jansen, F., Lumb, D., Altieri, B., et al. 2001, , 365, L1, doi: 10.1051/0004-6361:20000036

Kaaret, P., Zajczyk, A., LaRocca, D. M., et al. 2019, , 884, 162, doi: 10.3847/1538-4357/ab4193

Kaaret, P., Koutroumpa, D., Kuntz, K. D., et al. 2020, Nature Astronomy, 4, 1072, doi: 10.1038/s41550-020-01215-w

Kalberla, P. M. W., & Dedes, L. 2008, , 487, 951, doi: 10.1051/0004-6361:20079240

Kalberla, P. M. W., & Kerp, J. 2009, , 47, 27, doi: 10.1146/annurev-astro-082708-101823

Kennicutt, Robert C., J. 1998, , 36, 189, doi: 10.1146/annurev.astro.36.1.189

Khaire, V., & Srianand, R. 2019, , 484, 4174, doi: 10.1093/mnras/stz174

Klypin, A., Zhao, H., & Somerville, R. S. 2002, , 573, 597, doi: 10.1086/340656

Kolmogorov, A. N. 1991, Proceedings of the Royal Society of London Series A, 434, 9, doi: 10.1098/rspa.1991.0075

Krongold, Y., Nicastro, F., Brickhouse, N. S., et al. 2003, , 597, 832, doi: 10.1086/378639

Kuntz, K. D. 2019, , 27, 1, doi: 10.1007/s00159-018-0114-0

Kuntz, K. D., & Snowden, S. L. 2000, , 543, 195, doi: 10.1086/317071

Lacey, C., & Cole, S. 1993, , 262, 627, doi: 10.1093/mnras/262.3.627

Lan, T.-W., & Mo, H. 2019, , 486, 608, doi: 10.1093/mnras/stz839

Lara-DI, A., Krongold, Y., Mathur, S., et al. 2024a, , 531, 3034, doi: 10.1093/mnras/stae1051

—. 2024b, , 531, 3034, doi: 10.1093/mnras/stae1051

—. 2024c, , 533, 287, doi: 10.1093/mnras/stae1845

Lara-DI, A., Mathur, S., Krongold, Y., Das, S., & Gupta, A. 2023, , 946, 55, doi: 10.3847/1538-4357/acbf40

Leahy, D. A., Merrick, F., & Filipović, M. 2022, Universe, 8, 653, doi: 10.3390/universe8120653

Lehner, N., Berek, S. C., Howk, J. C., et al. 2020, , 900, 9, doi: 10.3847/1538-4357/aba49c

Li, M., & Bryan, G. L. 2020, , 890, L30, doi: 10.3847/2041-8213/ab7304

Li, M., & Tonnesen, S. 2020, , 898, 148, doi: 10.3847/1538-4357/ab9f9f

Lian, J., Zasowski, G., Chen, B., et al. 2024, Nature Astronomy, 8, 1302, doi: 10.1038/s41550-024-02315-7

Liu, W., Chiao, M., Collier, M. R., et al. 2017, , 834, 33, doi: 10.3847/1538-4357/834/1/33

Locatelli, N., Ponti, G., Zheng, X., et al. 2024, , 681, A78, doi: 10.1051/0004-6361/202347061

Lockman, F. J. 2002, , 580, L47, doi: 10.1086/345495

Macquart, J. P., Prochaska, J. X., McQuinn, M., et al. 2020, , 581, 391, doi: 10.1038/s41586-020-2300-2

Maller, A. H., & Bullock, J. S. 2004, , 355, 694, doi: 10.1111/j.1365-2966.2004.08349.x

Martínez-Delgado, D., Román, J., Erkal, D., et al. 2021, , 506, 5030, doi: 10.1093/mnras/stab1874

Mas-Ribas, L., McQuinn, M., & Prochaska, J. X. 2025, arXiv e-prints, arXiv:2504.19562, doi: 10.48550/arXiv.2504.19562

Mathur, S. 2022, Probing the Circumgalactic Medium with X-Ray Absorption Lines (Singapore: Springer Nature Singapore), 1–36, doi: 10.1007/978-981-16-4544-0_112-1

Mathur, S., Das, S., Gupta, A., & Krongold, Y. 2023, , 525, L11, doi: 10.1093/mnrasl/slad085

Mathur, S., Nicastro, F., Gupta, A., et al. 2017, , 851, L7, doi: 10.3847/2041-8213/aa991a

McCammon, D., & Sanders, W. T. 1990, , 28, 657, doi: 10.1146/annurev.aa.28.090190.003301

McClain, R. L., Mathur, S., Das, S., Krongold, Y., & Gupta, A. 2024a, , 527, 5093, doi: 10.1093/mnras/stad3497

—. 2024b, , 527, 5093, doi: 10.1093/mnras/stad3497

McCourt, M., Sharma, P., Quataert, E., & Parrish, I. J. 2012, , 419, 3319, doi: 10.1111/j.1365-2966.2011.19972.x

McMillan, P. J. 2017, , 465, 76, doi: 10.1093/mnras/stw2759

McQuinn, M., & Werk, J. K. 2018, , 852, 33, doi: 10.3847/1538-4357/aa9d3f

Mignone, A., Bodo, G., Massaglia, S., et al. 2007, , 170, 228, doi: 10.1086/513316

Mihalas, D. 1978, Stellar atmospheres (W.H.Freeman & Co Ltd)

Miller, M. J., & Bregman, J. N. 2013, , 770, 118, doi: 10.1088/0004-637X/770/2/118

—. 2015, , 800, 14, doi: 10.1088/0004-637X/800/1/14

Mitsuda, K., Bautz, M., Inoue, H., et al. 2007, , 59, S1, doi: 10.1093/pasj/59.sp1.S1

Miyamoto, M., & Nagai, R. 1975, , 27, 533

Mo, H., van den Bosch, F. C., & White, S. 2010, Galaxy Formation and Evolution, doi: 10.1017/CBO9780511807244

Mohapatra, R., Jetti, M., Sharma, P., & Federrath, C. 2022a, , 510, 3778, doi: 10.1093/mnras/stab3603

—. 2022b, , 510, 2327, doi: 10.1093/mnras/stab3429

Mooney, S., Quinn, J., Callingham, J. R., et al. 2019, , 622, A14, doi: 10.1051/0004-6361/201833937

Morgan, J. P., & Bailin, J. 2025, arXiv e-prints, arXiv:2501.16045, doi: 10.48550/arXiv.2501.16045

Nakashima, S., Inoue, Y., Yamasaki, N., et al. 2018, , 862, 34, doi: 10.3847/1538-4357/aacceb

Navarro, J. F., Frenk, C. S., & White, S. D. M. 1997, , 490, 493, doi: 10.1086/304888

Nelson, D., Sharma, P., Pillepich, A., et al. 2020, , 498, 2391, doi: 10.1093/mnras/staa2419

Nevalainen, J., Wakker, B., Kaastra, J., et al. 2017, , 605, A47, doi: 10.1051/0004-6361/201630336

Ng, Y. V., Lan, T.-W., Prochaska, J. X., et al. 2025, arXiv e-prints, arXiv:2503.11139, doi: 10.48550/arXiv.2503.11139

Nicastro, F., Senatore, F., Krongold, Y., Mathur, S., & Elvis, M. 2016, , 828, L12, doi: 10.3847/2041-8205/828/1/L12

Nicastro, F., Zezas, A., Drake, J., et al. 2002, , 573, 157, doi: 10.1086/340489

Nicastro, F., Kaastra, J., Krongold, Y., et al. 2018, , 558, 406, doi: 10.1038/s41586-018-0204-1

Nielsen, N. M., Churchill, C. W., & Kacprzak, G. G. 2013, , 776, 115, doi: 10.1088/0004-637X/776/2/115

Nielsen, N. M., Fisher, D. B., Kacprzak, G. G., et al. 2024, Nature Astronomy, doi: 10.1038/s41550-024-02365-x

Nieuwenhuijzen, H., & de Jager, C. 1990, , 231, 134

Nomoto, K., Tominaga, N., Umeda, H., Kobayashi, C., & Maeda, K. 2006, , 777, 424, doi: 10.1016/j.nuclphysa.2006.05.008

Nori, M., Giroletti, M., Massaro, F., et al. 2014, , 212, 3, doi: 10.1088/0067-0049/212/1/3

Peebles, P. J. E. 1980, The large-scale structure of the universe

Pessa, I., Wisotzki, L., Urrutia, T., et al. 2024, , 691, A5, doi: 10.1051/0004-6361/202450547

Petroff, E., Hessels, J. W. T., & Lorimer, D. R. 2019, , 27, 4, doi: 10.1007/s00159-019-0116-6

Planck Collaboration, Aghanim, N., Akrami, Y., et al. 2020, , 641, A6, doi: 10.1051/0004-6361/201833910

Ponti, G., Zheng, X., Locatelli, N., et al. 2023, , 674, A195, doi: 10.1051/0004-6361/202243992

Poveda, A., Ruiz, J., & Allen, C. 1967, Boletin de los Observatorios Tonantzintla y Tacubaya, 4, 86

Predehl, P., Andritschke, R., Arefiev, V., et al. 2021, , 647, A1, doi: 10.1051/0004-6361/202039313

Prochaska, J. X., & Zheng, Y. 2019, , 485, 648, doi: 10.1093/mnras/stz261

Prochaska, J. X., Werk, J. K., Worseck, G., et al. 2017, , 837, 169, doi: 10.3847/1538-4357/aa6007

Qu, Z., Chen, H.-W., Rudie, G. C., et al. 2023, , 524, 512, doi: 10.1093/mnras/stad1886

Rahmani, H., Péroux, C., Augustin, R., et al. 2018, , 474, 254, doi: 10.1093/mnras/stx2726

Ramesh, R., & Nelson, D. 2024, , 528, 3320, doi: 10.1093/mnras/stae237

Ramesh, R., Nelson, D., Fielding, D., & Brüggen, M. 2025, , 699, A10, doi: 10.1051/0004-6361/202451303

Ranasinghe, S., & Leahy, D. 2023, , 265, 53, doi: 10.3847/1538-4365/acc1de

Rao, S. M., Sardane, G., Turnshek, D. A., et al. 2013, , 432, 866, doi: 10.1093/mnras/stt417

Rauscher, T., Heger, A., Hoffman, R. D., & Woosley, S. E. 2003, , 718, 463, doi: 10.1016/S0375-9474(03)00852-2

Ravi, V. 2019, , 872, 88, doi: 10.3847/1538-4357/aafb30

Ravi, V., Catha, M., Chen, G., et al. 2025, , 169, 330, doi: 10.3847/1538-3881/adc725

Rees, M. J., & Ostriker, J. P. 1977, , 179, 541, doi: 10.1093/mnras/179.4.541

Roy, M., Mathur, S., Das, S., et al. 2025, , 982, 8, doi: 10.3847/1538-4357/adb3a5

Roy, M., Su, K.-Y., Tonnesen, S., Fielding, D. B., & Faucher-Giguère, C.-A. 2024, , 527, 265, doi: 10.1093/mnras/stad3142

Rubin, K. H. R., Prochaska, J. X., Koo, D. C., & Phillips, A. C. 2012, , 747, L26, doi: 10.1088/2041-8205/747/2/L26

Salpeter, E. E. 1955, , 121, 161, doi: 10.1086/145971

Sameer, Charlton, J. C., Wakker, B. P., et al. 2024, , 530, 3827, doi: 10.1093/mnras/stae962

Sarkar, K. C., Nath, B. B., & Sharma, P. 2017, , 467, 3544, doi: 10.1093/mnras/stx314

Sarkar, K. C., Nath, B. B., Sharma, P., & Shchekinov, Y. 2015, , 448, 328, doi: 10.1093/mnras/stu2760

Savage, B. D., & Sembach, K. R. 1991, , 379, 245, doi: 10.1086/170498

Schaan, E., Ferraro, S., Amodeo, S., et al. 2021, , 103, 063513, doi: 10.1103/PhysRevD.103.063513

Schmidt, W., Schmidt, J. P., & Grete, P. 2021, , 654, A115, doi: 10.1051/0004-6361/202140920

Shaban, A., Bordoloi, R., O'Meara, J. M., et al. 2025, , 986, 190, doi: 10.3847/1538-4357/add0b9

Shapiro, P. R., & Field, G. B. 1976, , 205, 762, doi: 10.1086/154332

Sharma, P., McCourt, M., Parrish, I. J., & Quataert, E. 2012, , 427, 1219, doi: 10.1111/j.1365-2966.2012.22050.x

Sharma, P., Parrish, I. J., & Quataert, E. 2010, , 720, 652, doi: 10.1088/0004-637X/720/1/652

Shull, J. M. 2014, , 784, 142, doi: 10.1088/0004-637X/784/2/142

Silk, J. 1977, , 211, 638, doi: 10.1086/154972

Silva, M. D. V., & Napiwotzki, R. 2011, , 411, 2596, doi: 10.1111/j.1365-2966.2010.17864.x

Singh, P., Lau, E. T., Faerman, Y., Stern, J., & Nagai, D. 2024, , 532, 3222, doi: 10.1093/mnras/stae1695

Singh, P., Nath, B. B., Majumdar, S., & Silk, J. 2015, , 448, 2384, doi: 10.1093/mnras/stv155

Singh Bisht, M., Das, S., Mathur, S., et al. 2025, arXiv e-prints, arXiv:2509.02019, doi: 10.48550/arXiv.2509.02019

Smith, R. K., Brickhouse, N. S., Liedahl, D. A., & Raymond, J. C. 2001, , 556, L91, doi: 10.1086/322992

Sommer-Larsen, J. 2006, , 644, L1, doi: 10.1086/505489

Sormani, M. C., Sobacchi, E., Pezzulli, G., Binney, J., & Klessen, R. S. 2018, , 481, 3370, doi: 10.1093/mnras/sty2500

Spitzer, Jr., L. 1956, , 124, 20, doi: 10.1086/146200

Srianand, R., & Khare, P. 1993, , 413, 486, doi: 10.1086/173018

Stern, J., Fielding, D., Faucher-Giguère, C.-A., & Quataert, E. 2019, , 488, 2549, doi: 10.1093/mnras/stz1859

Stern, J., Hennawi, J. F., Prochaska, J. X., & Werk, J. K. 2016, , 830, 87, doi: 10.3847/0004-637X/830/2/87

Stone, R. C. 1991, , 102, 333, doi: 10.1086/115880

Sugiyama, H., Ueda, M., Fukushima, K., et al. 2023, , 75, 1324, doi: 10.1093/pasj/psad073

Tan, B., & Fielding, D. B. 2024, , 527, 9683, doi: 10.1093/mnras/stad3793

Tashiro, M., Kelley, R., Watanabe, S., et al. 2025, , doi: 10.1093/pasj/psaf023

Terrazas, B. A., Bell, E. F., Pillepich, A., et al. 2020, , 493, 1888, doi: 10.1093/mnras/staa374

Tinsley, B. M. 1980, , 5, 287, doi: 10.48550/arXiv.2203.02041

Toft, S., Rasmussen, J., Sommer-Larsen, J., & Pedersen, K. 2002, , 335, 799, doi: 10.1046/j.1365-8711.2002.05663.x

Tollet, E., Cattaneo, A., Macciò, A. V., & Kang, X. 2022, , 515, 3453, doi: 10.1093/mnras/stac1867

Truelove, J. K., & McKee, C. F. 1999, , 120, 299, doi: 10.1086/313176

Tüllmann, R., Rosa, M. R., Elwert, T., et al. 2003, , 412, 69, doi: 10.1051/0004-6361:20031521

Tumlinson, J., Peeples, M. S., & Werk, J. K. 2017, , 55, 389, doi: 10.1146/annurev-astro-091916-055240

Tumlinson, J., Thom, C., Werk, J. K., et al. 2011, Science, 334, 948, doi: 10.1126/science.1209840

Tur, C., Heger, A., & Austin, S. M. 2010, , 718, 357, doi: 10.1088/0004-637X/718/1/357

Vasiliev, E. O., Nath, B. B., & Shchekinov, Y. 2015, , 446, 1703, doi: 10.1093/mnras/stu2133

Verner, D. A., & Ferland, G. J. 1996, , 103, 467, doi: 10.1086/192284

Vijayan, A., & Li, M. 2022, , 510, 568, doi: 10.1093/mnras/stab3413

Vijayan, A., Sarkar, K. C., Nath, B. B., Sharma, P., & Shchekinov, Y. 2018, , 475, 5513, doi: 10.1093/mnras/sty198

Voit, G. M. 2019, , 880, 139, doi: 10.3847/1538-4357/ab2bfd

Voit, G. M., Meece, G., Li, Y., et al. 2017, , 845, 80, doi: 10.3847/1538-4357/aa7d04

Voronov, G. S. 1997, Atomic Data and Nuclear Data Tables, 65, 1, doi: 10.1006/adnd.1997.0732

Weaver, T. A., Zimmerman, G. B., & Woosley, S. E. 1978, , 225, 1021, doi: 10.1086/156569

Weinberg, S. 1972, Gravitation and Cosmology: Principles and Applications of the General Theory of Relativity

Weinberger, R., & Hernquist, L. 2023, , 519, 3011, doi: 10.1093/mnras/stac3708

Weisskopf, M. C., Tananbaum, H. D., Van Speybroeck, L. P., & O'Dell, S. L. 2000, in Society of Photo-Optical Instrumentation Engineers (SPIE) Conference Series, Vol. 4012, X-Ray Optics, Instruments, and Missions III, ed. J. E. Truemper & B. Aschenbach, 2–16, doi: 10.1117/12.391545

Werk, J. K., Prochaska, J. X., Thom, C., et al. 2012, , 198, 3, doi: 10.1088/0067-0049/198/1/3

—. 2013, , 204, 17, doi: 10.1088/0067-0049/204/2/17

Werk, J. K., Prochaska, J. X., Tumlinson, J., et al. 2014, , 792, 8, doi: 10.1088/0004-637X/792/1/8

Werk, J. K., Prochaska, J. X., Cantalupo, S., et al. 2016, , 833, 54, doi: 10.3847/1538-4357/833/1/54

Williams, R. J., Mathur, S., Nicastro, F., et al. 2005, , 631, 856, doi: 10.1086/431343

Woosley, S. E., & Heger, A. 2007, , 442, 269, doi: 10.1016/j.physrep.2007.02.009

Woosley, S. E., Heger, A., & Weaver, T. A. 2002, Reviews of Modern Physics, 74, 1015, doi: 10.1103/RevModPhys.74.1015

Woosley, S. E., & Weaver, T. A. 1988, , 163, 79, doi: 10.1016/0370-1573(88)90037-3

Yadav, J., Bharadwaj, S., Pandey, B., & Seshadri, T. R. 2005, , 364, 601, doi: 10.1111/j.1365-2966.2005.09578.x

Yadav, N., Mukherjee, D., Sharma, P., & Nath, B. B. 2017, , 465, 1720, doi: 10.1093/mnras/stw2522

Yang, H., Qu, Z., Bregman, J. N., & Ji, L. 2025, , 538, 1871, doi: 10.1093/mnras/staf407

Yoshino, T., Mitsuda, K., Yamasaki, N. Y., et al. 2009, , 61, 805, doi: 10.1093/pasj/61.4.805

Zabl, J., Bouché, N. F., Wisotzki, L., et al. 2021, , 507, 4294, doi: 10.1093/mnras/stab2165

Zhang, H., Zaritsky, D., Behroozi, P., & Werk, J. 2019, , 880, 28, doi: 10.3847/1538-4357/ab2761

Zinger, E., Pillepich, A., Nelson, D., et al. 2020, , 499, 768, doi: 10.1093/mnras/staa2607

# Appendix A

# The mist limit

It is important to recall the meaning of the mist limit within a CC. Here we extend the discussion in section 4.2 of D24, which uses cubical cloudlets (geometry only introduces order unity factors without altering the scaling relations with the parameters) of uniform size. The parameters for such a CC, also assumed to be a cubical, are the volume filling fraction $f_V$, the number of cloudlets $N_{\rm cl}$, and the CC size $L$. The column density of the cool gas in the mist limit is given by $n_{\rm cool} L f_V$, where $n_{\rm cool}$ is the physical number density of the cool gas. The area covering fraction is unity provided the average number of cloudlets along a sightline $f_V^{2/3} N_{\rm cl}^{1/3}$ exceeds unity, that is, when $N_{\rm cl} \gtrsim f_V^{-2}$.

To test the above scaling borrowed from D24, we carry out a simple Monte Carlo experiment (see Figure A.1). We divide a uniform cubical volume $L^3$ into equal cubical cells of size $l = L f_V^{1/3} N_{\rm cl}^{-1/3}$ of our cubical cloudlets. $N_{\rm cl}$ cloudlets, which occupy a volume fraction $f_V$ of the available volume, fill these available cells with uniform probability. In this arrangement, either the cell is fully occupied or unoccupied (there is no partial occupation). The number distribution of cloudlets along a LOS is Poisson, with a mean $f_V^{2/3} N_{\rm cl}^{1/3}$ and a standard deviation equaling the square root of the mean (as expected for a Poisson distribution). A Poisson distribution is expected for a uniform cloudlet distribution. These mist estimates provide a useful benchmark to compare with more sophisticated models.

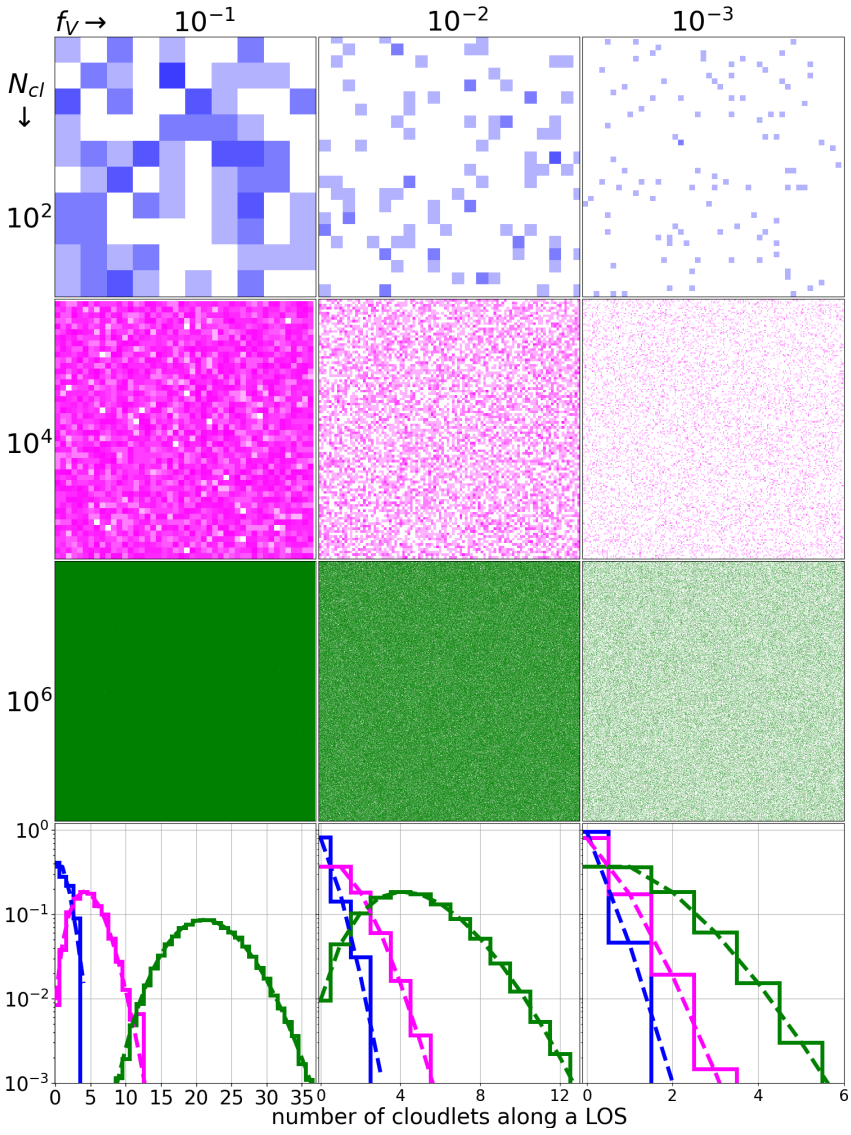



Figure A.1: Projected cloudlet distribution (top 3×3 panels) in a cubical volume with $N_{\rm cl}$ cubical cloudlets uniformly covering a volume fraction $f_V$. The size of vacancies equals the cloudlet size. As expected from simple estimates, the area covering fraction becomes of order unity when $N_{\rm cl} \gtrsim f_V^{-2}$. The panels farther from the diagonal (toward the bottom-left) are deeper into the mist limit. The bottom panels show the normalized histogram of the number of cloudlets along different sightlines. The histogram is very well fit by a Poisson distribution (shown by dashed lines) with a mean $f_V^{2/3} N_{\rm cl}^{1/3}$. Note that the number of sightlines with zero and one cloudlet becomes comparable for $N_{\rm cl} \sim f_V^{-2}$, corresponding to the approach toward the mist limit with a unity area covering fraction.

### A.0.1 Terminal velocity of cloudlets within a CC

We can estimate the terminal velocity of a cloudlet within a CC by balancing the gravitational force and the drag force experienced by a cloudlet. The standard expression in the Rayleigh/turbulent drag regime is given by

$$v_{\rm term}^{\rm cl} = \sqrt{\frac{4\chi r_{\rm cl}}{3C_D R_{\rm CGM}}} v_c$$
$$\approx 48 \text{ km s}^{-1} \left(\frac{\chi}{100}\right)^{1/2} \left(\frac{r_{\rm cl}/R_{\rm CGM}}{4\times10^{-4}}\right)^{1/2} \left(\frac{v_c}{220 \text{ kms}^{-1}}\right), \quad \text{(A.1)}$$

where $\chi \approx 100$ is the density contrast between the cool and hot CGM phases, $C_D \sim 1$ is the drag coefficient, and $v_c \approx 220$ km s$^{-1}$ is the circular velocity of a Milky Way-like galaxy. For $r_{\rm cl} = 100$ pc (best resolution achievable by current cosmological galaxy formation simulations) and $R_{\rm CGM} = 280$ kpc, the above expression gives a terminal velocity $\sim 48$ km s$^{-1}$, higher than the turbulent velocity across a CC ($\sim 35$ km s$^{-1}$; see section 4.3.4). For cloudlets to be suspended in the CGM, and for mist description to be appropriate (as motivated by observations), the cloudlet terminal velocity should be $\lesssim 35$ km s$^{-1}$ (turbulent velocity within a CC), or equivalently, the cloudlet size should be $\lesssim$ a few pc! This simple argument emphasizes the importance of phenomenological models like ours, given the computational intractability of modeling realistic suspended CGM cloudlets from first principles.

## A.1 MgII ion fraction estimates

The number density of MgII is given by

$$n_{\rm MgII} = \mu X \left(\frac{Z}{Z_\odot}\right) \left(\frac{n_{\rm Mg}}{n_{\rm H}}\right)_\odot \left(\frac{n_{\rm MgII}}{n_{\rm Mg}}\right) n_{\rm cool}, \quad \text{(A.2)}$$

where $X = 0.74$ (Asplund et al. 2009) is the hydrogen mass fraction, $\mu = 0.6$ is the mean molecular weight, $Z = 0.3Z_\odot$ (Prochaska et al. 2017) is the metallicity of the gas, $(n_{\rm Mg}/n_{\rm H})_\odot = 3.47 \times 10^{-5}$ (Ferland et al. 2017; Holweger 2001) is the solar abundance of Mg, and $(n_{\rm MgII}/n_{\rm Mg})$ is the fraction of MgII. Figure A.2 shows the MgII ion fraction as a function of the total number density. The purple line shows the ion fraction in Collisional Ionization Equilibrium (CIE). The green, blue, and orange lines show the ion fraction at three different redshifts in Photoionization Equilibrium (PIE).

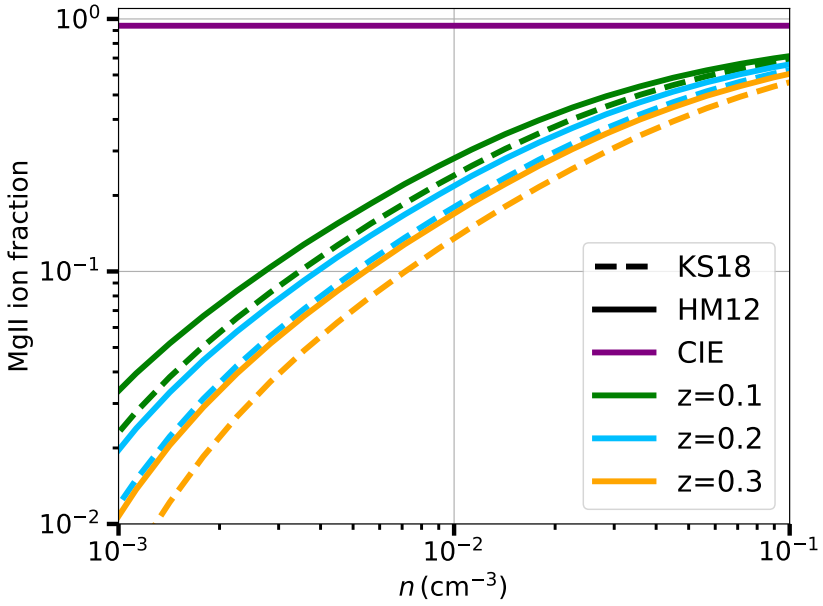



Figure A.2: MgII ion fraction as a function of total number density at $10^4$ K. The purple line shows the MgII fraction for the Collisional Ionization Equilibrium, while the green, blue, and orange colors show the values for Photoionization Equilibrium at the redshifts of 0.1, 0.2, and 0.3, respectively. The solid and dashed colored line shows the ion fraction with the HM12 (Haardt & Madau 2012) and KS18 (Khaire & Srianand 2019) background radiation field. We computed the ion fraction values using the radiative transfer code `CLOUDY` (Ferland et al. 2017). MgII ion fraction values vary by $\sim 2$ orders of magnitude from $\approx 0.01$–$0.6$ for $n \approx 10^{-3}$-$10^{-1}\,\mathrm{cm}^{-3}$ at $z \sim 0.2$.

## A.2 Standard deviation estimates

Just as we can calculate the average number of CCs along a LOS and the average path length along a CC, we can also calculate the standard deviation of these quantities.

For average CC density, which is only a function of the distance $r$ and independent of $\theta$ and $\phi$, the distribution of CCs in a radial shell is expected to be Poisson, with the variance equal to the mean number of clouds. For the number of CCs encountered along a LOS, this means that the variance in the number of CCs along a LOS equals the average number of CCs. Thus, the standard deviation in the number of CCs along a LOS is simply the square root of the average number of clouds encountered.

The deviation in the length along a single CC is given by $\sigma_L = \sqrt{\langle L^2 \rangle - \langle L \rangle^2}$, with

$$\langle L^2 \rangle = \frac{\int_0^{R_{\rm CC}} 2\pi b db \, 4(R_{\rm CC}^2 - b^2)}{\int_0^{R_{\rm CC}} 2\pi b db} = 2R_{\rm CC}^2. \tag{A.3}$$

Combining this, and Eq. 4.5 gives, $\sigma_L = \sqrt{2}R_{\rm CC}/3$.

Both the number of clouds encountered along a LOS and the path length through a CC are random variables. Thus, the variation in column density along a LOS will have contributions due to both of these random variables. Adding all the deviations in quadrature (and assuming $N_{\rm CC,LOS}$ and $L$ to be independent random variables), we can write

$$\sigma_N^2 = \sigma_{N_{\rm CC,LOS}}^2 \langle L \rangle^2 + \langle N_{\rm CC,LOS} \rangle^2 \sigma_L^2 + \sigma_{N_{\rm CC,LOS}}^2 \sigma_L^2. \tag{A.4}$$

Here, the column density $N = \sum (n_{\rm ion})_j L_j = N_{\rm CC,LOS} L n_{\rm ion}$ is a sum over CCs along the LOS. Recall that $\langle N \rangle = \langle N_{\rm CC,LOS} \rangle \langle L \rangle \langle n_{\rm ion} \rangle$, $\sigma_{N_{\rm CC,LOS}} / \langle N_{\rm CC,LOS} \rangle = 1/\sqrt{\langle N_{\rm CC,LOS} \rangle}$ and $\sigma_L / \langle L \rangle = \sqrt{2}/4$. These estimates are used to show (using dotted lines) the expected deviation from average column density in the *bottom panel* of Fig. 4.2.